UNIVERSITA' DEGLI STUDI DI NAPOLI "FEDERICO II"

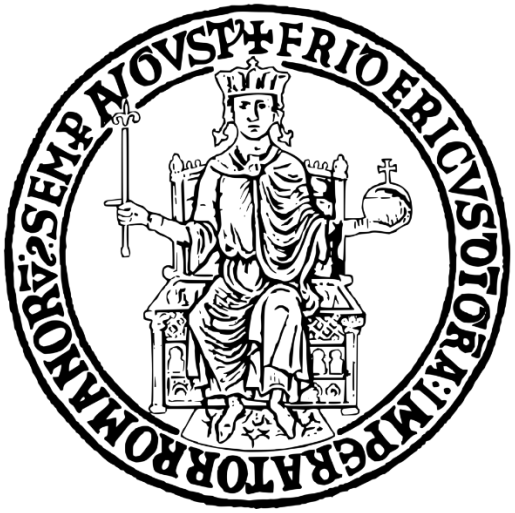

PhD thesis in Industrial products and process engineering

XXXIII cycle

Design and fabrication of advanced microfluidic *in vitro* platforms to study drug delivery systems integrating OECT-based bioelectronics sensors.

Cinzia Sgambato

Supervisor

Prof. Paolo A. Netti

Advisor

Dr. Ing. Raffaele Vecchione

Coordinator

Prof. Andrea D'Anna

January 2018 – May 2021

Motivation and outline

The way to develop and understand the cell culture systems has notably evolved since the first artificial tissue culture in 1907 [1]. Over the next century, multidisciplinary efforts in cell biology and bioengineering have led to highly functional *in vitro* culture platforms enabling the controlled presentation of microenvironmental signals [2]. The principal goal of the developed platforms is to reproduce the real environment in order to mimic human pathophysiology. Therefore, cell biology systems are moving from the conventional two-dimensional (2D) *in vitro* models [3] to more complex three-dimensional (3D) systems in order to solve the discrepancies to capture the real features of the cellular microenvironments [4]. Based on this context, the concept of Organ-On-a-Chip (OOC) platforms emerges[5] [6]. An OOC system implies a microfluidic cell culture device that contains continuously perfused chambers inhabited by living cells and arranged to simulate tissue- and organ-level physiology [7], [8]. The goal of this system is complex due to the difficulty to mimic living tissues and organs, maintaining physicochemical microenvironments like *in vivo* conditions. Besides the development of micro physiological environments of human tissue or organ recapitulating *in vivo* structure and function, the capability to analyze and monitor its real-time response to drugs or other stimulation is of utmost importance. For this reason, the incorporation of monitoring tools in the OOC systems is essential to allow the continuous improvements of these models. Currently, analysis of OOC cell culture is still mainly based on optical measurement techniques using time-lapse brightfield and fluorescence microscopy[9]. These conventional analytical methods require manual sample collection from the microfluidic systems, large working volumes, and frequent system disturbance, and thus are not suitable for miniaturized OOC platforms. Consequently, over the past few decades, tremendous progress has been initiated towards the development of sensors for cell culture applications. Great efforts are made each year for the development of miniaturized sensors thus improving their benefits. In the 1970s, the discovery of conductive polymers led to the great growth and development of bioelectronics. Since then, an enormous number of electronic devices have been explored in bioelectronic applications, in which electronic signals are converted into bio signals and vice versa, to understand various biological phenomena as well as to exploit the potential to create improved healthcare products and biomedical diagnostics. One popular theme has been to use the organic electrochemical transistor (OECT), belonging to the class of electrolyte-gated transistor [10], [11]. The key advantage of the OECT is the ease of fabrication, the local high amplification at low-voltage operation, offering excellent biocompatibility and great performances [12], [13]. As a result, the OECT has yielded a vast array of promising applications ranging from electrophysiology, by recordings of neural activity of organs, to biosensing, by the detection of analytes and

metabolites.[14] The OECT has been shown as a complementary sensor for cell barrier integrity in comparison to traditional techniques such as immunofluorescence, permeability assay and transepithelial electrical resistance measurements (TEER). In order to take advantage of the attractive properties of the OECT for biomedical applications as an improved assessment of cell layer integrity, the OECT needs to be further pushed towards greater sensitivity and efficiency to meet the requirements of high-performance biosensing. Recently, different published review articles about cell monitoring and OOC systems claim for the necessity of integrating functional and real-time monitoring tools[15], [16]. For this purpose, it must be necessary to pave the way to interface existing biomimetic OOC models to achieve in-situ monitoring of physicochemical parameters. One of the limitations of the current OECT fabrication is the difficulty to integrate them in microfluidic, and until now, to the best of our knowledge, has never been done a platform that combine Blood Brain barrier (BBB) *on chip* with OECTs. Here we propose a new fabrication technique that allows us to realize a high performance OECT that can be integrated in microfluidic device with a classical plasma O_2 bonding. We integrate them in a device that mimics the tubular shape of BBB in order to improve barrier tissue characterization and we show that this system is able to monitor formation and disruption of the brain barrier optically and electrically. We used this platform, at the end, to test the effect of gH625 peptide, which is known in literature, to be capable to cross the BBB [17]. This work is organized as followed: the theoretical background regarding the three main issues of bioelectronics, PEDOT:PSS and OECTs, associated with essentials of cell biology, is given in **Chapter 1**, establishing relevant definitions for a sufficient background knowledge for the work presented in this thesis. The **Chapter 2** describes the background of the OOC models, with an overview of the evolution of the cell culture systems and the monitoring tools for the analysis of OOC systems, with great attention on BBB. In the **Chapter 3** the development of a new microfabrication strategy for OECT is described, with electrical and theoretical models. Then, in the **Chapter 4** we introduce our idea of microfluidic device to mimic BBB combined with OECT. At the end, in the **Chapter 5,** we discuss an immune-responsive Microbiota-Intestine axis on chip as a platform able to reproduce the architecture and vertical topography of the microbiota with a complex extracellular microenvironment with a future aim to combine this model in an axis with the proposed advanced BBB model. This chapter is part of a much larger project, which aims to build a GUT-BRAIN axis. The aim is to study the effect of diseases, such as Crohn's disease, and especially the role of the microbiome on BRAIN. Chapter 5 reports the part relating to the role of the microbiome in recreating an in vitro model of Gut on chip. Future perspective to combine this advanced model with the BBB developed in chapter 4, and to study how the GUT sends signals to the brain through the OECT introduced in chapter 3.

References

[1] R. G. Harrison, M. J. Greenman, F. P. Mall, and C. M. Jackson, “Observations of the living developing nerve fiber,” *Anat. Rec.*, vol. 1, no. 5, pp. 116–128, 1907, doi: 10.1002/ar.1090010503.

[2] G. H. Underhill, G. Peter, C. S. Chen, and S. N. Bhatia, “Bioengineering methods for analysis of cells in vitro,” *Annu. Rev. Cell Dev. Biol.*, vol. 28, pp. 385–410, 2012, doi: 10.1146/annurev-cellbio-101011-155709.

[3] M. Mehling and S. Tay, “Microfluidic cell culture,” *Curr. Opin. Biotechnol.*, vol. 25, pp. 95–102, 2014, doi: 10.1016/j.copbio.2013.10.005.

[4] E. W. Esch, A. Bahinski, and D. Huh, “Organs-on-chips at the frontiers of drug discovery,” *Nat. Rev. Drug Discov.*, vol. 14, no. 4, pp. 248–260, 2015, doi: 10.1038/nrd4539.

[5] H. J. Kim, D. Huh, G. Hamilton, and D. E. Ingber, “Human gut-on-a-chip inhabited by microbial flora that experiences intestinal peristalsis-like motions and flow,” *Lab Chip*, vol. 12, no. 12, pp. 2165–2174, 2012, doi: 10.1039/c2lc40074j.

[6] H. Kimura, T. Yamamoto, H. Sakai, Y. Sakai, and T. Fujii, “An integrated microfluidic system for long-term perfusion culture and on-line monitoring of intestinal tissue models,” *Lab Chip*, vol. 8, no. 5, pp. 741–746, 2008, doi: 10.1039/b717091b.

[7] X. Li, A. V. Valadez, P. Zuo, and Z. Nie, “Microfluidic 3D cell culture: Potential application for tissue-based bioassays,” *Bioanalysis*, vol. 4, no. 12, pp. 1509–1525, 2012, doi: 10.4155/bio.12.133.

[8] L. Kim, Y. C. Toh, J. Voldman, and H. Yu, “A practical guide to microfluidic perfusion culture of adherent mammalian cells,” *Lab Chip*, vol. 7, no. 6, pp.

681–694, 2007, doi: 10.1039/b704602b.

[9] M. Vinci *et al.*, “Advances in establishment and analysis of three-dimensional tumor spheroid-based functional assays for target validation and drug evaluation,” *BMC Biol.*, vol. 10, no. March, 2012, doi: 10.1186/1741-7007-10-29.

[10] M. Berggren and A. Richter-Dahlfors, “Organic bioelectronics,” *Adv. Mater.*, vol. 19, no. 20, pp. 3201–3213, 2007, doi: 10.1002/adma.200700419.

[11] R. M. Owens and G. G. Malliaras, “Organic electronics at the interface with biology: a biologist’s perspective,” *MRS Bull.*, vol. 35, no. June, pp. 86–89, 2012, [Online]. Available: http://journals.cambridge.org/abstract_S088376940000083X.

[12] J. Rivnay *et al.*, “High-performance transistors for bioelectronics through tuning of channel thickness,” *Sci. Adv.*, vol. 1, no. 4, pp. 1–6, 2015, doi: 10.1126/sciadv.1400251.

[13] D. Khodagholy *et al.*, “High transconductance organic electrochemical transistors,” *Nat. Commun.*, vol. 4, pp. 1–6, 2013, doi: 10.1038/ncomms3133.

[14] J. Rivnay, S. Inal, A. Salleo, R. M. Owens, M. Berggren, and G. G. Malliaras, “Organic electrochemical transistors,” *Nat. Rev. Mater.*, vol. 3, 2018, doi: 10.1038/natrevmats.2017.86.

[15] J. Rogal, C. Probst, and P. Loskill, “Integration concepts for multi-organ chips: How to maintain flexibility?!,” *Futur. Sci. OA*, vol. 3, no. 2, 2017, doi: 10.4155/fsoa-2016-0092.

[16] A. Polini, L. Prodanov, N. S. Bhise, V. Manoharan, M. R. Dokmeci, and A. Khademhosseini, “Organs-on-a-chip: A new tool for drug discovery,” *Expert Opin. Drug Discov.*, vol. 9, no. 4, pp. 335–352, 2014, doi: 10.1517/17460441.2014.886562.

[17] A. Falanga *et al.*, “Enhanced uptake of gH625 by blood brain barrier compared to liver in vivo: characterization of the mechanism by an in vitro model and implications for delivery,” *Sci. Rep.*, vol. 8, no. 1, pp. 1–13, 2018, doi: 10.1038/s41598-018-32095-w.

Table of contents

List of Figures 13
CHAPTER 1 16
State of art of OECT 16
1.1 OECT literature review 19
1.1.2 Operation principles 20
1.1.3 Fabrication with Parylene C peel off Method 22
1.1.3 Direct Lithographic Patterning of Conducting Polymers 25
1.2 Model for OECTs behavior 28
1.2.1 Steady state behavior 28
1.2.2 Transient model 32
1.2.3 Equivalent circuit model with B&M model 33
1.3 Biological application 34
1.3.1 Enzymatic sensor 35
1.3.2 OECT's cells monitoring 36
1.3.3 OECT for Dopamine detection 39
1.4 Conclusion 40
Bibliography 42
CHAPTER 2 48
Organ on chip and State of art of Blood Brain Barrier in vitro models 48
2.1 Organ on chip (OOC) model 50
2.2 Organ on chip models to mimic Blood Brain Barrier 51
2.2.1 Blood Brain Barrier anatomy 51
2.2.2 Modeling Blood Brain Barrier 54
2.3 Current BBBs on chip 57
2.4 Standardization challenging 62
2.4.1 Permeability 62
2.4.2 Transendothelial electrical resistance 64
2.4.3 Cells 65
2.4.4 Shear stress 65
2.5 Conclusion 67
CHAPTER 3 76
New lithography strategy for the fabrication of a biocompatible high performing organic electrochemical transistor Parylene C-free. 76
3.1 OECT: Design and fabrication 79

3.1.1. Design 80
3.1.2. Fabrication 81
3. 2 Experimental characterizations 84
3.2.1 Morphological characterization 85
3.2.2 Cyclic Voltammetry 86
3.2.3 Cell culture and biocompatibility assay 87
3.3 Electrical characterization 88
3.3.1 Output and Transfer Curve and Transconductance measurement 88
3.3.2 Comparison with theoretical model 92
3.3.3 Statistical analysis of reproducibility 96
3.3.4 Measurement of the potential along the channel 99
3. 4 Microfluidic applications 102
3.4.1 Biocompatibility assay 102
3.4.2 Microfluidic device embedded with OECT. 103
3. 5 Conclusion 104
CHAPTER 4 110
Tubular in vitro Blood Brain Barrier Platform embedding OECTs for Optical and Electrical Monitoring of Barrier Integrity. 110
4.1 BBB: Design, Fabrication and COMSOL simulation 112
4.1.1 Design 112
4.1.2 Simulation 112
4.1.3 Fabrication 114
4.2 Cells culture and Collagen fingering method 115
4.2.1 Astrocytes and HBEC-5i 115
4.2.2 Viscous fingering method 115
4.2.3 Improving stability of collagen. 116
4.2.4 Immunofluorescence and ultrastructural analyses in physiological and reduced dynamic conditions. 117
4.3 Experimental characterization 118
4.3.1 Device characterization 118
4.3.2 Flow effect on endothelial cells 119
4. 4 Electrical characterizations 125
4.4.1 OECTS array integration in microfluidic 3D channel 125
4.4.2 Electrical Impedance spectroscopy (EIS) 126
4. 5 Morphological characterizations 128
4.5.1 Dextran 40 kDa transport across the BBB 128

4.5.2 Frap analysis with Fourier Transform. 130
4. 6 BBB in vitro crossing: gH625 peptide study 133
4.6.1 Monitoring Barrier through transient current 133
4. 6.2 Monitoring Barrier interaction with gH625 peptide 135
4. 7 Conclusion 140
Bibliography 141
CHAPTER 5 145
Immunocompetent Microbiota-gut axis on-chip reproduces barrier dysfunction, stromal reshaping and microbial species translocation under inflammation. 145
Introduction 147
5.1 Cells and microbial strains culture conditions 150
5.2. Organotypic 3D human intestine (3D-hI) model development 151
5.3. Microbiota human Intestine on chip (MihI-oC) design, assembly and operation 152
5.3.1. Microfluidic device fabrication 152
5.3.2 MihI-oC assembly: Microbiota chamber (M_C) design and application on human intestine on chip (hI-oC) 153
5.3.3. Computational model of MihI-oC 154
5.3.4. On-line Oxygen concentration measurement 156
5.4. Assessment of the M_C functionality: comparison of single strains growth into the anaerobic workstation (AW) vs MihI-oC 156
5.4.1. Total and viable count 156
5.4.2. Live/Dead assay 157
5.4.3. Ultrastructural and morphological characterization of microbiota 157
5.5 Statistical Analysis 158
5.6 Results and Discussion 158
5.6.1 Establishing hypoxic environment in Microbiota Chamber (MC) of MihI-oC 159
5.6.2 Microbiota Chamber (M_C) promotes microbial strains growth and oxygen gradient across the MihI lumen 161
5.6.3 Establishing physiological vertical localization of microbiota in MihI-oC 165
5.7 Conclusion 167
Supplementary 172
Conclusion 179

List of Figures

Figure 1.1 Typical structure for an OFET and an OECT.

Figure 1.2 OECT operation in depletion mode and molecular structure of PEDOT: PSS.

Figure 1.3 Output and transfer curves for a typical OECT

Figure 1.4 Typical fabrication step.

Figure 1.5 Patterning of conducting polymer with sacrificial layer peel-off technique.

Figure 1.6 Difference between PaC and Orthogonal patterning.

Figure 1.7 Orthogonal pattern.

Figure 1.8 Channel geometry and Circuit diagram used to construct the Bernards model.

Figure 1.9 Comparison of experimental data (circles) to model fits (solid lines) using the Bernard-Malliaras model with carrier concentration dependent mobility.

Figure 1.10 Artist's impression of the Gentile model and electrical circuit.

Figure 1.11 Barrier tissue integrity monitored with an OECT.

Figure 1.12 The OECT device for monitoring adherent cells.

Figure 1.13 Working principle of the selective all-PEDOT: PSS OECT.

Figure 2.2 Cellular constituents of the blood–brain barrier.

Figure 2.2 Paracellular and transcellular routes across the blood-brain barrier (BBB).

Figure 2.3 Schematic representation of different in vitro BBB models.

Figure 2.4 A variety of existing OOC models for the BBB.

Figure 2.5 Flow profiles at different shape channel.

Figure 3.1 Schematic representation of the Sample1 OECT.

Figure 3.2 Schematic representation of the Sample2 OECT.

Figure 3.3 Process for photolithographic patterning of PEDOT: PSS with a copper interlayer.

Figure 3.4 Illustration of different step in the fabrication of Sample1 and Sample2.

Figure 3.5 Absorbance spectra of pristine and acid treated PEDOT: PSS films on glass.

Figure 3.6 AFM images of PEDOT: PSS before and after etching.

Figure 3.7 Cyclic voltammograms recorded for PRISTINE or Untreated and Treated PEDOT: PSS.

Figure 3.8 Experimental set-up used to characterize the three-terminal device.

Figure 3.9 Output Characteristics for Sample1 and Sample2 for different value of V_{GS}.

Figure 3.10 Transfer curve and Transconductance for Sample1and Sample2.

Figure 3.11 Data fit of Output curve for Sample 1 and Sample2 with B&M model.

Figure 3.12 Data fit of Output curve for Sample 1 and Sample2 with Friedelin model.

Figure 3.13 Output Transfer Curve at V_{DS} = −0.1:0.6 V and V_{GS} = 0.1 to 0.9 V statistical analysis.

Figure 3.14 Mean Output Transfer Curve at V_{DS} = −0.1:0.6 V and V_{GS} = 0.1 to 0.9 V.

Figure 3.15 Mean Transconductance.

Figure 3.16 Potential measurement.

Figure 3.17 Normalized hole density, ion density OECT for Sample2.

Figure 3.18 Biocompatibility assessment and Immunofluorescence of Bend3 cells cultured on Glass Etched PEDOT: PSS and Si Etched PEDOT: PSS.

Figure 3.19 Microfluidic device for gradient concentration with OECT.

Figure 4.3 Schematic representation of the BBB Device.

Figure 4.4 Process used for patterning lumens through an extracellular matrix (ECM) hydrogel via viscous finger patterning.

Figure 4.3 PDMS Functionalization to increase collagen adhesion.
Figure 4.5 3D illustration, photograph, and SEM image of the fabricated microfluidic chip.

Figure 4.6 CFD simulations using COMSOL Multiphysics.

Figure 4.7 Tubular shape of Blood Brain Barrier.

Figure 4.8 Quantitative analysis of endothelial responses to shear stress.

Figure 4.9 Configuration of endothelial cells in the tubular device.

Figure 4.10 Graphical design of complete system with 8 array of OECTs combined with the microfluidic device of BBB.

Figure 4.11 Bode plot. Measured and fitted impedance spectra in the presence and absence of a confluent cell layer covering the OECT channel for physiological and reduced shear stress.

Figure 4.12 Permeability evaluated in the microfluidic device in three different cases.

Figure 4.13 Frap analysis.

Figure 4.14 Scanning Electron microscopy images.

Figure 4.15 Electrical and optical characterization of Tubular Blood brain barrier on the planar OECT.

Figure 4.16 The transient response of the OECT after the addition of 10 µM to 80 µM of an aqueous solution of gH625 and scrambled peptide in cells medium.

Figure 4.17 Monitoring barrier tissue integrity with an OECT.

Figure 4.18 Calibration of the organic electrochemical transistor device with increasing dopamine concentration.

Figure 5.1 Design and optimization of flow rate of M_C.

Figure 5.2 MihI-oC establishes the physiological oxygen gradient across the MihI tissue.

Figure 5.3 Microbiota Chamber (M_C) sustains the microbial strains viability and growth in the MihI-oC lumen.

Figure 5.4 Physioxic condition in the lumen of MihI-oC determines the physiological vertical stratification of the microbiota.

CHAPTER 1

State of art of OECT

This chapter provides background information about OECTs and their use in various applications taking information from literature. We present the fundamental physics of OECTs behaviors, and we use this information to discuss the experimental results presented in Chapter III. In the first part, OECTs are introduced as well as the specific transistor characteristics for PEDOT: PSS are explained in detail. This is followed by a short introduction to two different lithographic fabrication approaches. Then, we consider several theoretical existing models for OECT behavior, and we conclude the chapter discussing application for OECTs.

Table of contents

State of art of OECT 16
1.1 OECT literature review 19
1.1.2 Operation principles 20
1.1.3 Fabrication with Parylene C peel off Method 22
1.1.3 Direct Lithographic Patterning of Conducting Polymers 25
1.2 Model for OECTs behavior 28
1.2.1 Steady state behavior 28
1.2.2 Transient model 32
1.2.3 Equivalent circuit model with B&M model 33
1.3 Biological application 34
1.3.1 Enzymatic sensor 35
1.3.2 OECT's cells monitoring 36
1.3.3 OECT for Dopamine detection 39
1.4 Conclusion 40
Bibliography 42

1.1 OECT literature review

Organic electrochemical transistors (OECTs) are thin-film transistors with an organic semiconductor channel between source and drain electrodes. OECTs are structured much like organic field-effect transistors (OFETs) with the distinction that OECTs have an electrolyte layer between the channel and the gate electrode instead of a standard dielectric, as shown in Figure 1.1. In 1984, H. S. White et al. reported the first OECTs, demonstrating that the conductivity of a polypyrrole channel could be reversibly modulated by changing its redox state with a gate electrode in an electrolyte. Since that time, researchers have fabricated OECTs with many different materials and geometries and have demonstrated the usefulness of OECTs in a variety of applications. However, several gaps remain in the understanding of OECT behavior. Existing theoretical models have been useful for the design of OECT sensors and circuits, but they fail to properly incorporate polymer physics. This has prevented these models from predicting several widely observed characteristics of OECTs. This chapter addresses all of these gaps in the understanding of OECT behavior. It highlights the influence that material properties have on the device physics of OECTs, and it describes three original models for predicting the steady-state and transient response of OECTs. These models provide quantitative explanations for the previously unexplained characteristics described above,[1] and, although each model describes a different regime of OECT behavior, they are all consistent with each other. Ultimately, these models inform the design of OECT sensors, and they provide a way to measure the material properties of the polymer semiconductors used in OECTs, thus aiding the development of new polymers for performance optimization in different applications.

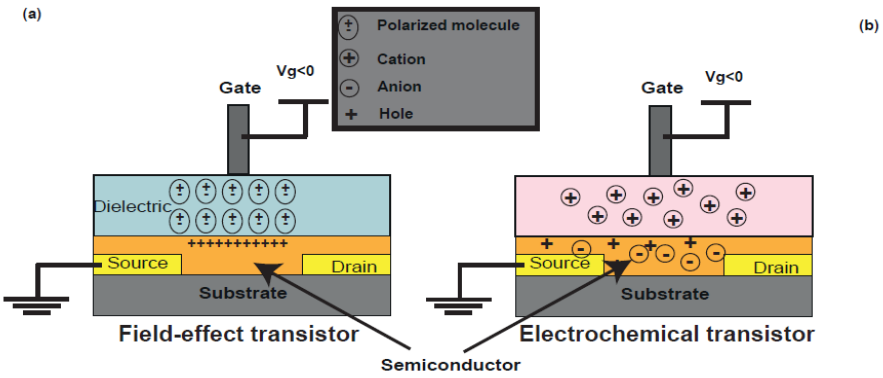

Figure 1.1 Typical structure for an OFET and an OECT. a) In the OFET, immobile molecules in the dielectric are polarized by a gate voltage. Charge transport in the semiconductor occurs at the interface of the semiconductor and dielectric. b) In the OECT, mobile ions are pushed from the electrolyte into the semiconductor by a gate voltage. These ions dope (or de-dope) the semiconductor. Charge transport occurs throughout the volume of the OECT.

1.1.2 Operation principles

As mentioned before, OECTs have a structure similar to that of OFETs, and they operate according to similar principles. When a voltage, V_{DS}, is applied between the source and drain electrodes, a current flow through the semiconductor channel and is collected at the drain. This current is the output current of the OECT and is called the drain current, I_{DS}. The gate electrode, though not directly connected to the channel, can modulate the drain current. When a voltage is applied at the gate electrode, it creates an electric field that pushes ions from the electrolyte into the semiconductor channel. The effect of these ions on channel conductivity depends on the properties of the semiconductor in the channel. In p-type semiconductors, positive gate voltages decrease channel conductivity, and negative gate voltages increase channel conductivity. Conversely, positive gate voltages increase channel conductivity in n-type semiconductors while negative gate voltages decrease channel conductivity. OECTs can also be classified as "depletion-mode" or "accumulation-mode" transistors. Depletion-mode transistors are highly conductive at V_{GS} = 0 and become less conductive when a gate voltage is applied. Accumulation-mode transistors behave in the opposite way. They are non-conductive at V_{GS} = 0 V and become more conductive in response to a non-zero gate voltage. The OECT described in this thesis works in depletion mode with the p-type semiconductor poly(3,4-ethylenedioxythiophene):poly(styrenesulfonate), or PEDOT:PSS. PEDOT is a conjugated polymer with semiconducting properties and a stable oxidized form,[1],[2] and PSS allows the PEDOT to be dispersed in water.[3] In addition to solubilizing PEDOT, the PSS also acts as an acceptor ion, forming an ionic bond with the PEDOT and withdrawing electronic charge density, as shown in Figure 1.2.[3] This gives the PEDOT positively charged electronic carriers, making it a p-type semiconductor and endowing it with conductivity greater than 800 S/cm in its oxidized form.[4], [5] Because the PEDOT:PSS is naturally in a conductive state, OECTs using PEDOT:PSS are classified as p-type, depletion-mode transistors. When a positive voltage is applied at the gate electrode, it creates a field that pushes cations from the electrolyte into the semiconductor channel, as shown in Figure 1a. These cations form ionic bonds with the PSS, displacing it from the PEDOT. Without the ionically bound PSS dopants, holes are no longer coulombically stable on the PEDOT backbone, so the $PEDOT^+$ is reduced from its conductive state to its insulating neutral state, $PEDOT^0$. This de-doping (reduction) process is described in equation (1) and is reversible; when the gate voltage, V_{GS}, returns to 0, the cations diffuse back out of the channel, and the PSS forms new ionic bonds with the PEDOT, oxidizing it to its conductive state, $PEDOT^+$.

$$PEDOT^{+}:PSS^{-} + M^{+} \leftrightarrow PEDOT^{0} + M^{+}:PSS^{-} + h^{+} \quad (1)$$

The left-hand side of equation (1) represents the situation when VGS = 0 V. In this case cations, M^{+}, are in the electrolyte, PEDOT forms an ionic bond with PSS, and holes are on the PEDOT chain. The right-hand side of equation (1) represents the situation when VGS > 0. In this case, the PEDOT chain is neutral, cations form ionic bonds with the PSS, and holes, h^{+}, are removed from the channel. Although, OECTs can use materials other than PEDOT: PSS,[6], [7] the basic principles delineated above still describe device behavior as long as appropriate adjustments are made when considering n-type or accumulation-mode OECTs. [8]

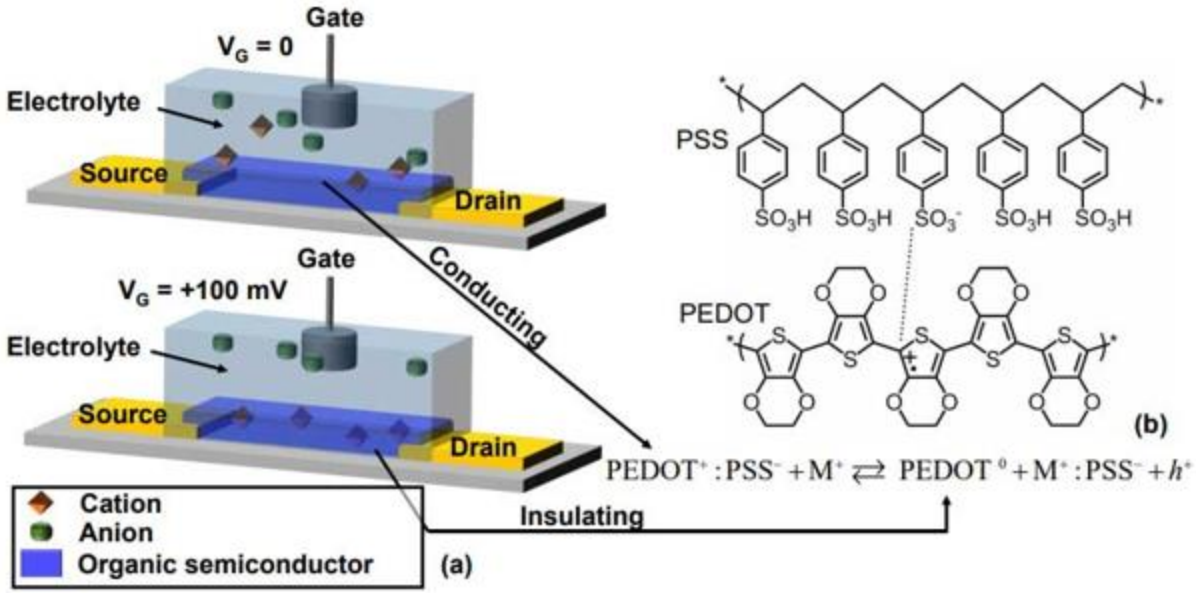

Figure 1.2 OECT operation in depletion mode and molecular structure of PEDOT:PSS. In panel (a), the top image represents the OECT in its ON state at V_{GS} = 0 V. The bottom image represents the OECT in its OFF state at V_{GS} = 100 mV. In b) the dashed line between the PEDOT and PSS represents an ionic bond that leaves a radical cation on the PEDOT chain. [9].

To characterize OECT performance, researchers usually present output and transfer curves, which show the dependence of drain current on V_{DS} and V_{GS}, respectively. An example of typical output and transfer curves is shown in Figure 1.3. The channel current has a linear dependence on V_{DS} at low voltages but saturates for higher values of V_{DS}. Also, for a fixed V_{DS}, the magnitude of the drain current decreases as V_{GS} becomes higher.

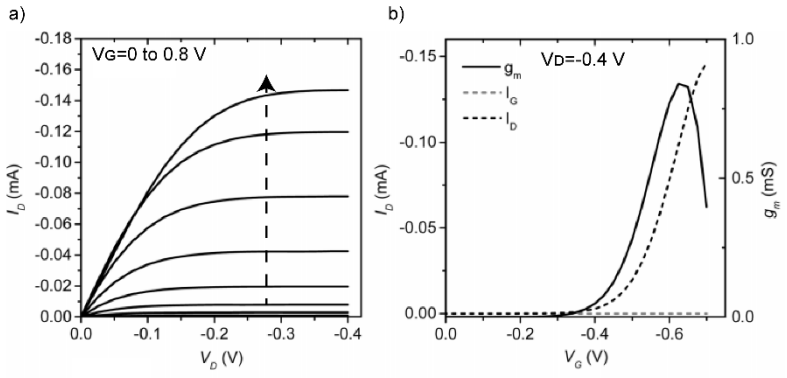

Figure 1.3 Output and transfer curves for a typical OECT. a) Output transfer. Each curve in a is for a single gate voltage between 0.6 V and -0.4 V in 0.1 V steps, as indicated in the Figure. b) Transfer curve. Each curve in (b) is for a single drain voltage between 0.2 V and -0.6 V in 0.1 V steps, as indicated in the Figure.[9]

1.1.3 Fabrication with Parylene C peel off Method

There are several ways to pattern conducting polymers and amongst the most interesting on an industrial scale are probably inkjet printing, screen printing or spray coating, due to their compatibility with roll-to-roll processing [9]. Whereas these techniques pose their own challenges regarding ink formulation, stability, or miniaturization, scientists typically exploit a lithographic approach due to an implementation with existing processing steps and to the possibility for small feature sizes currently not possible with printing techniques. The fabrication of an OECT can be broken down into two stages: first, the source, drain and gate contact as well as lead lines must be defined, patterning a highly conductive material (see Figure 1.4).

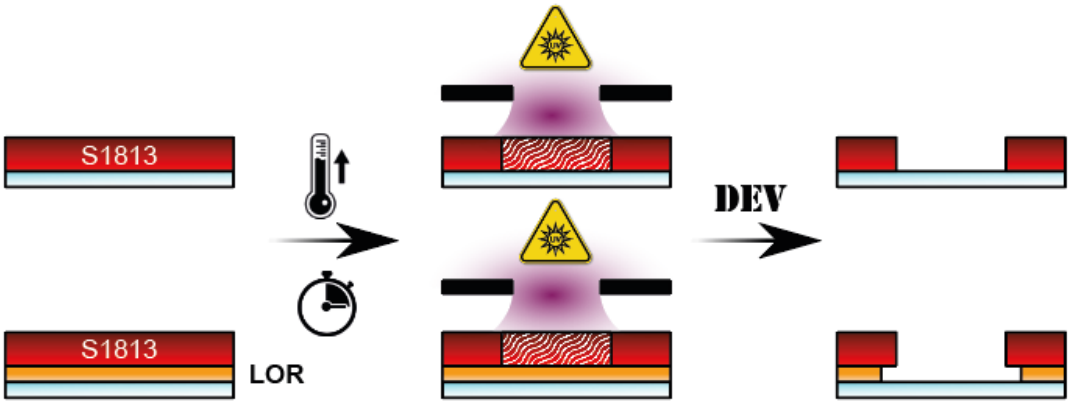

Figure 1.4 Typical fabrication step. Photolithography steps with spincoating of positive photoresist, softbaking, exposure and development (from left to right). On the top is shown the procedure with simply the photoresist and on the bottom with an additional undercut layer (LOR). The exposure to UV light alters the chemical structure of the photoresist in a way that the resist gets soluble in the developer. A photomask defines the pattern. The undercut layer helps in the subsequent metal evaporation step.

For PEDOT: PSS based devices, gold is the material of choice due to its low resistivity and a work function that lies slightly above the HOMO level of the conducting polymer. In a second stage, the conducting polymer will be patterned to bridge the source and drain contact and form the transistor channel Figure 1.5 [10].

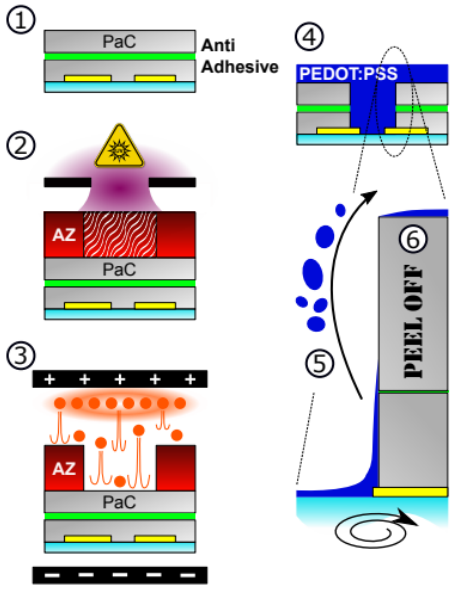

Figure 1.5 Patterning of conducting polymer with sacrificial layer peel-off technique. From top to bottom: parylene-C deposition of two layers with anti-adhesive layer in between (1), photolithography with positive thick resist AZ9620 (2), reactive ion etching to create an opening (well) in the PaC layers (3). A subsequent spin coating step with PEDOT:PSS will coat the PaC and fill the well (4). A zoom-in emphasizes the scale of the 4 µm thick double layer PaC versus 100nm PEDOT:PSS. Upon spinning, most of the PEDOT:PSS solution will be hurled out of the PaC well (5). Peeling off the outermost sacrificial PaC layer will remove the excess PEDOT:PSS (6).

PaC is a polymer that is traditionally used as hydrophobic diffusion barrier [11]. With a low dielectric constant of around $\varepsilon_r \approx 3$ this material exhibits low leakage currents, rendering it a good electrical insulator. The mechanical properties (tensile strength of about 70 MPa and yield strength of about 3 GPa) allow for the use of PaC as ultraflexible substrate and various applications are based on that approach [12], [13]. PaC is deposited in a high vacuum chamber at about 10 Pa to 100 Pa. In the deposition chamber, kept at room temperature, the monomer gas deposits on the substrate as a thin, transparent polymer film.

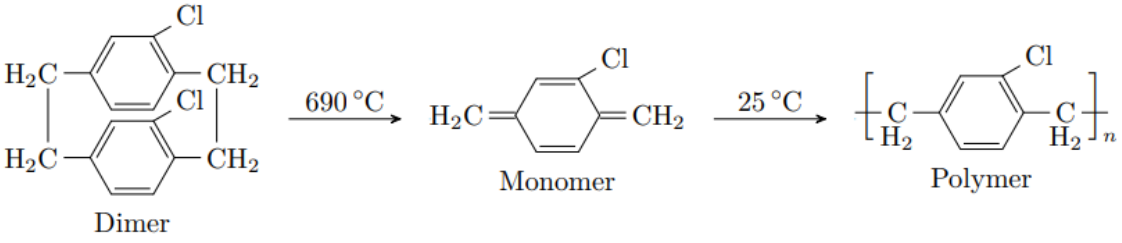

The thickness of the film is controlled by the amount of raw dimer material loaded into the deposition machine [14]. A first layer of about 1.5 µm will serve as an isolation layer. A second layer of about 2.5 µm is used as a sacrificial layer, i.e. the layer will be patterned to create openings, coated with PEDOT:PSS and mechanically removed to peel off the PEDOT:PSS in the unpatterned parts. The idea is to create openings in the PaC double layer so that a coating with PEDOT:PSS will allow the conducting polymer to reach the substrate surface and the gold contacts. Every part, which needs to be accessible in the final device (i.e. contact pads, gate electrode and transistor channel) needs to be defined during this step. For this, a thick photoresist is needed to protect the PaC double layer in the subsequent dry etching step where PaC needs to remain. After the desired features are successfully transferred to the photoresist, the whole structure (substrate, gold, double layer PaC, photoresist) is placed into a reactive ion etching chamber. As soon as the PaC is fully removed and the glass substrate and gold contacts are exposed to the plasma beam, the etching process must be stopped as an over-etching would also remove the gold from the substrate. After the etching step, the unexposed photoresist can be removed in an acetone bath. This step is optional, as the photoresist will also be removed when peeling off the sacrificial layer, but generally, there is also photoresist on the edge of the glass substrate that might have an impact on the biocompatibility of the final device. The PEDOT:PSS coating step is done using a spin-coater. For this, a solution [15] is produced according to the formula presented in Table 1.1.

PEDOT:PSS (Clevios PH1000) EG (Sigma Aldrich) DBSA (Acros Organics)	19 mL 1 mL 50 µL	(19 g) (1.11 g) (0.053 g)
	sonicate for roughly 20 min	
GOPS (Sigma Aldrich)	188 µL	(0.2011 g)
	sonicate for another 5 min	

Table 1.1 Formula for about 20 mL of spincast processable PEDOT:PSS with good film formation and best compromise between ionic and electronic conductivity.

If PEDOT:PSS is coated directly after the dry etching step, no additional steps need to be considered, as there will be already hydroxyl groups present on the surface due to the plasma treatment. The hydroxyl groups will form a chemical bond with the (3-glycidyloxypropyl) trimethoxy silane (GOPS) present in the PEDOT:PSS solution and therefore improve the adhesion of the conducting polymer layer [16]. Additionally, the hydroxyl groups alter the surface energy and render the substrate more hydrophilic which increases the wettability of the substrate and facilitates the spin coating. If the substrate has been exposed to ambient air conditions for a longer time (more than 30 min to 1 h),

water will adsorb on the surface removing the hydroxyl groups. Therefore, a quick oxygen plasma with low power is needed to re-induce those hydroxyl groups. The thickness of the conducting polymer layer can be controlled to some extend by adjusting the rotational speed of the spin coating process [17]. However, this is not comparable with coating a bare substrate, such as a glass slide or silicon wafer. The PEDOT:PSS solution needs to enter the opening in the PaC double layer, which can be seen as a well (see Figure 1.5). When the substrate is coated with PEDOT:PSS, this well will be fully filled. During the spincoating (step 1), part of the solution will be projected out of the well due to centripetal forces and the remaining solution will be smeared out inside the well and partly cover also the walls of the well, resulting in a thin film coating. A quick soft baking step ensures that the PEDOT:PSS solution is stable enough for the peel-off process, but not yet fully cross-linked as this would rupture the film during the peel-off. It has been found that an initial thin film of PEDOT:PSS (3500 rpm for about 70 nm) and several additional slower spin coatings (650 rpm) provide a more homogeneous film than one spin coating step at very slow rotational speeds, when thick PEDOT:PSS coatings are needed. With a scotch tape, the sacrificial PaC layer can be carefully peeled off (step 2), taking with it the excess PEDOT:PSS and leaving a thin film of the conducting polymer only on the exposed parts of the substrate and gold contacts. The final structure needs to be cured at about 120°C for about 1 h to ensure a full cross-linking of the GOPS in the PEDOT:PSS solution and the device is ready to use.

1.1.3 Direct Lithographic Patterning of Conducting Polymers

The peel-off process described above has been developed for the first time by Ilic and Craighead, in 2010 [10] for patterning proteins and cells on the surface of different substrates. This process was realized because regular photolithographic patterning would necessitate exposure of the conducting polymer to harsh chemicals such as photoresists or developers during the process [18]. Instead of first spin coating the conducting polymer and then performing all necessary steps (subtractive patterning), the PaC peel-off process allows the implementation of the conducting polymer at the very last processing step (additive patterning), ensuring that the delicate material remains functional (see Figure 1.6a) [10].

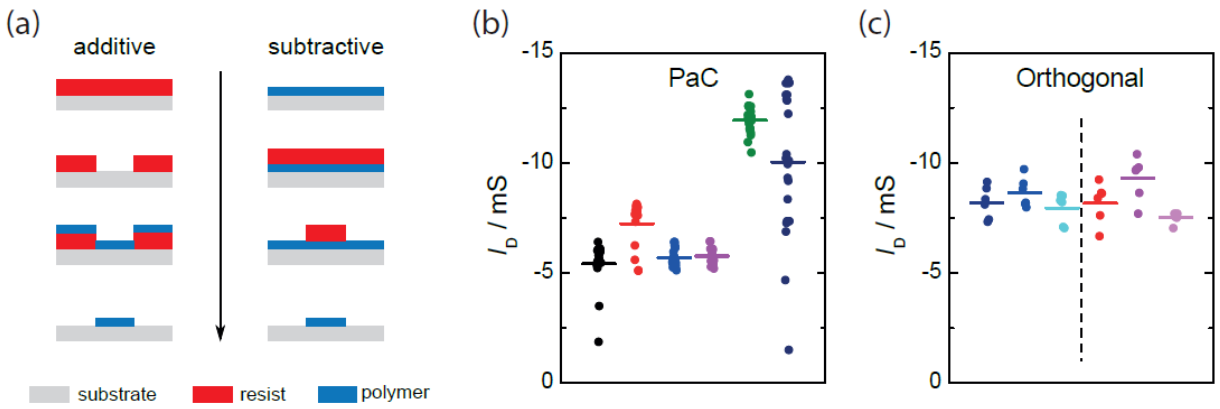

Figure 1.6 Difference between PaC and Orthogonal patterning [19]. a) For additive patterning, the conducting polymer is spuncast only at the very last step. For subtractive patterning, the conducting polymer is spincast first and exposed to both resist, developer and eventually stripper. (b) Drain current at $V_{DS} = -0.6$ V and $V_{GS} = 0$ V as an indicator for device homogeneity of OECTs fabricated with PaC peel-off technique. (c) Similar data at same bias point for devices fabricated with Orthogonal Inc. resist. The device geometry is kept the same. The mean value is indicate as horizontal bar [14].

However, despite the ease and utility of PaC peel-off patterning, this process lacks one fundamental demand for industrial application, and this is device homogeneity [14]. The very nature of this process, where the conducting polymer solution must enter a micron sized opening in the PaC double layer and be thinned down to about 100 nm with spincoating, is not well defined. Depending on the position of the opening with respect to the spin center, the centripetal forces vary. The conducting polymer solution gets smeared out on the walls of the opening and during peel-off might get ruptured as there may not be a separation between the layer on top of PaC and the layer inside the opening. Depending on how far the conducting polymer gets smeared out, the device geometry changes. In Figure 1.6b, one can see a statistical study of the device homogeneity for OECTs fabricated with the PaC peel-off technique. Here, the drain current at a defined bias point is plotted for several devices on the same glass slide and for several glass slides within the same batch. Even though, this bias point reflects only a tiny portion of the whole output characteristics of the devices, it can give an estimate about the homogeneity. For identical transistors, the drain current should be equal at equal bias points. Even though a good device homogeneity can be achieved occasionally throughout the same glass slide, the majority of times the devices show a huge discrepancy in their output characteristics Figure 1.6b. Furthermore, the mean values vary from glass slide to glass slide even within the same batch. This can be probably attributed to different channel thickness, as the thickness depends on how much of the conducting polymer remains inside the openings of the double PaC layer during the spin-coating step. This shows the need for a more reliable patterning approach. In Figure 1.6c, one can see a similar set of data for OECTs fabricated with a subtractive method using photoresist from Orthogonal Inc. especially designed not to harm organic materials. Even though this study contains

less devices per glass slide and also a different photomask layout has been used, it is evident that the slide to slide and batch to batch homogeneity is much higher. As with this method, the conducting polymer is spun cast onto the full glass slide, very homogeneous coatings can be achieved, only limited by edge effects. This allows for devices with the same channel thickness throughout the whole batch. The Orthogonal Inc. materials are based on hydrofluoroether (HFE) solvents that are "orthogonal" to nonfluorinated organic materials [20]. Here, orthogonal means that the organic material is insoluble and does not swell in HFEs. In addition, most HFEs have been evaluated as non-toxic and environmentally friendly [21]. A HFE compatible photoresist has been designed by copolymerizing a highly fluorinated monomer with a photolabile monomer, which upon UV irradiation would switch solubility in HFE solvents [22]. Such a material, especially designed for acidic organic materials, such as PEDOT:PSS, has been successfully used for submicron feature sized patterning of various organic semiconductors. The processing steps are as follows: the definition of metal lead lines is identical to the PaC peel-off method described above, up until after the metal lift-off. For the coating of the conducting polymer, the same formula of PEDOT:PSS solution is used as for the PaC peel-off process. The material is again spuncast onto the substrate and immediately cured at 125 °C for about one hour. This ensure a homogeneous coating of the film over the whole substrate. Therefore, in order to protect the organic layer in the subsequent etching step, a thickness of the photoresist of about 1200 nm should be sufficient. As the OSCoR 5001 is a negative photoresist, a post-exposure bake is necessary to fully drive the acid-initiated chemical reaction that induces the solubility switching. After the post-exposure bake, the developer (simply called "Developer 100" by Orthogonal Inc.) can be applied either by dipping the substrate in a bath or, more economically, via a double-puddle method. An image of the developed PEDOT:PSS channel of the OECT can be seen in Figure 1.7a. The etching process is similar to the PaC peel-off method described above, the difference being that in this case the conducting polymer is directly removed at the unexposed parts. After the etching, the remaining photoresist at the exposed parts needs to be removed.

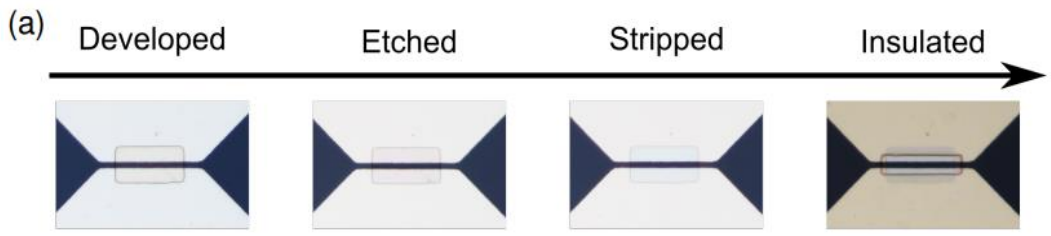

Figure 1.7 Orthogonal pattern. (a) Microscope images of a PEDOT:PSS channel (square at the center) on source and drain contacts (bright trapezoids) at different processing steps. After the development, a rectangular pattern of photoresist can be seen on a homogeneous PEDOT:PSS layer. After etching, PEDOT:PSS remains only underneath the photoresist and the gold contacts are exposed to air. A clear outline of the PEDOT:PSS channel can still be seen. After stripping, the PEDOT:PSS channel is barely visible. The insulation layer protects the gold contacts from exposure to water and only the PEDOT:PSS channel can be accessed by the ions [22].

For the passivation of the metallic lead lines, another negative orthogonal resist is used, called "OSCoR DE1" (for dielectric). In order to ensure a proper alignment of the opening in the passivation layer and the PEDOT:PSS channel, an overlap of about 10 µm is used in the mask design.

1.2 Model for OECTs behavior

Several theoretical models were proposed to quantitatively describe OECT behavior, in particular the process of doping/de-doping of the organic semiconductor. One of the first attempts to model both the steady state and transient behavior of OECTs was proposed by Daniel Bernards and George Malliaras in early 2007 [23]. The model was based on coupling an electronic circuit with an ionic one, mainly to generate an expression that describes the steady state and transient responses of OECTs (output/transfer and pulsed characteristics). The original model assumes few simplifications, such as constant charge carrier mobility, which were corrected in follow up articles [24]. In the following paragraph we give a review about the models existing in the literature until now.

1.2.1 Steady state behavior

The steady state current is defined to be the operational mode of the transistor where the ionic current, which comes from the electrolyte upon a gate voltage, remains unchanged. In other words, the channel has completely been charged with ions and doping or de-doping of the semiconducting material does no longer take place. The description of the steady state originates from the Ohm's law:

$$j(x) = \sigma E = q\mu p(x)\frac{dV(x)}{dx} \tag{1.1}$$

Where j is the current density, σ is the conductivity, q is the elementary charge, and V is the electric potential, the spatial derivative of which defines the electric field. Notice that the model assumes the electronic conductivity to be purely one-dimensional. Here, the B&M[23] model assumes that the charge carrier mobility μ is constant. The electronic conduction is correlated with the ionic flux, by proposing the following expression for the charge carrier density:

$$\rho = \rho_0(1 - \frac{Q}{q\nu\rho_0}) \tag{1.2}$$

Here, ρ_0 is the initial charge density of the polymer, Q is the total charge of the ions that penetrates the polymer film upon application a gate voltage, and ν is the volume of the transistor channel. When cations are injected into the channel Q is positive, whereas for injection of anions it is negative. Note that Equation 1.2 applies only to depletion mode OECTs, i.e., when Q=0 or, equally, V_{GS}=0, ρ=ρ_0

and the material is conductive; on the other hand, when Q=$q\rho_0 v$, ρ=0 and the polymer is fully de-doped. For accumulation mode, the charge carrier density in the polymer must be proportional to the number of injected ions in the organic film. With that, Equation 1.2 takes the form of

$$\rho = \frac{Q}{qv} \tag{1.3}$$

where Q, q and v are the same physical quantities defined in Equation 1.2. Here, we assume that the initial charge concentration ρ_0 of the undoped organic semiconductor is negligible. In order to calculate the total charge Q of ions injected upon a gate voltage V_{GS}, which enters Equations 1.2 and 1.3 equally, the model considers the channel to be an ideal capacitor with capacitance C_d. With that said, Q is given by:

$$Q(x) = C_d \nabla V = C^* WTdx[V_{GS} - V(x)] \tag{4}$$

where C^* is the capacitance of the film per unit of volume, W is the channel width, T is the film thickness, ΔV is the voltage drop in the transistor channel, and dx is a differential slice in source-drain direction, see Figure 1.8 a.

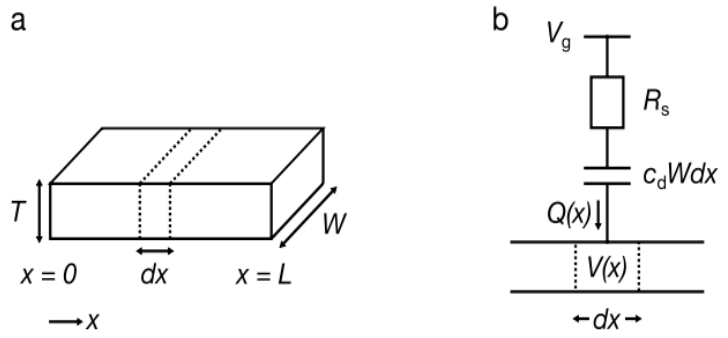

Figure 1.8 Channel geometry and Circuit diagram used to construct the Bernards model. a) Channel geometry and b) Circuit diagram used to construct the Bernards model. The double layer capacitance, cd, refers to the measured areal capacitance for the channel. The charge accumulated in a portion of the channel, dx, is coupled to the local channel potential, V(x).[23]

Also, the B&M model does not account for a possible threshold voltage V_{th}. In fact, PEDOT: PSS based OECT has practically zero V_{th} and, therefore, it would not be necessary to account for that in the original paper. In electrochemical transistors, such a quantity can be correlated to the onset potential in which the electrochemical reaction can occur (oxidation or reduction potential). Therefore, when accounting for V_{th}, Equation 1.4 becomes:

$$Q(x) = C_d \nabla V = C^* WTdx[V_{GS} - V(x) - V_{th}] \tag{1.5}$$

Combining Equations 1.2 and 1.3 for depletion or accumulation mode, respectively, with Equation. 1.1 and 1.5, it is possible to obtain the governing equation for the steady state OECTs operation. For depletion mode, this equation takes the form:

$$j = q\mu\rho_0\left[1 - \frac{\{C^*(V_{GS} - V_{th} - V(x)\}}{q\mu_0}\right]\frac{dV_x}{dx} \tag{1.6}$$

whereas for accumulation mode OECTs the expression is:

$$j = \mu C^*(V_{GS} - V_{th} - V(x))\frac{dV_x}{dx} \tag{1.7}$$

Notice that in the steady state response, the current is constant and, therefore, J=(x). Introducing a pinch-off voltage as being:

$$V_p = q\rho_0 C^* \tag{1.8}$$

the final expression for depletion mode (Equation 1.6) can be simplified to

$$j = q\mu\rho_0\left[1 - (V_{GS} - V_{th} - V(x))V_p\right]\frac{dV_x}{dx} \tag{1.9}$$

This equation can be readily integrated over the length of the transistor channel. The final analytical expression for depletion mode OECT is:

$$I_{DS} = q\mu\rho_0 WTL\left[1 - (V_{GS} - V_{th} - \frac{V_d}{2})V_p\right]V_d \tag{1.10}$$

where I_{DS} is the source-drain current and L is the channel length. For accumulation mode, integration of Equation 1.7 yields

$$I_{DS} = \mu WTLC^*\left[1 - (V_{GS} - V_{th} - \frac{V_d}{2})\right]V_d \tag{1.11}$$

Friedlein *et al.* [24] have further improved the original B&M model, accounting for the influence of charge carrier density ρ on the charge carrier mobility μ. They assumed a dependency of μ on ρ as it was proposed by the seminal work of Vissenberg and Matters [25] on the mobility in amorphous organic transistor. According to them mobility takes this form:

$$\mu(p) = \mu_0\left(\frac{\rho}{\rho_0}\right)^{\frac{E_0}{k_B\theta}-1} \tag{1.12}$$

The development of the model follows the structure of the original B&M model: Equation 1.2 and 1.12 are plugged into Equation 1.1, yielding:

$$j = q\mu\rho_0[1 - (V_{GS} - V(x))]^{\frac{E_0}{k_B\theta}-1}\frac{dV_x}{dx} \tag{1.13}$$

which resembles Equation 1.9, except for the pre-factor μ_0 and the exponent $\frac{E_0}{k_B\theta}$ which arise from Equation 1.12. It is worth mentioning that this development is exclusively for depletion mode OECT. An extension to accumulation mode OECT, however, is rather simple: one simply has to use Equation 1.3 instead of Equation 1.2 and follow the same mathematical steps. Integration of Equation 1.13 generates the final current-voltage relationship, which is valid until the saturation regime:

$$I_{DS} = p_0 e\mu_0 \frac{wd}{L}\frac{V_P}{\frac{E_0}{k_B T}+1}\left\{\left[1 - \frac{V_{GS} - V_{DS}}{V_P}\right]^{\frac{E_0}{k_B T}+1} - \left[1 - \frac{V_{GS}}{V_P}\right]^{\frac{E_0}{k_B T}+1}\right\} \tag{1.14}$$

Friedlein *et al.*[24] used this model to fit experimental data and were able to successfully recreate the output characteristics of PEDOT: PSS-based OECTs. In fact, they compared the original B&M model with the non-uniform mobility model, see Figure 1.9 which was adapted from the original publication.

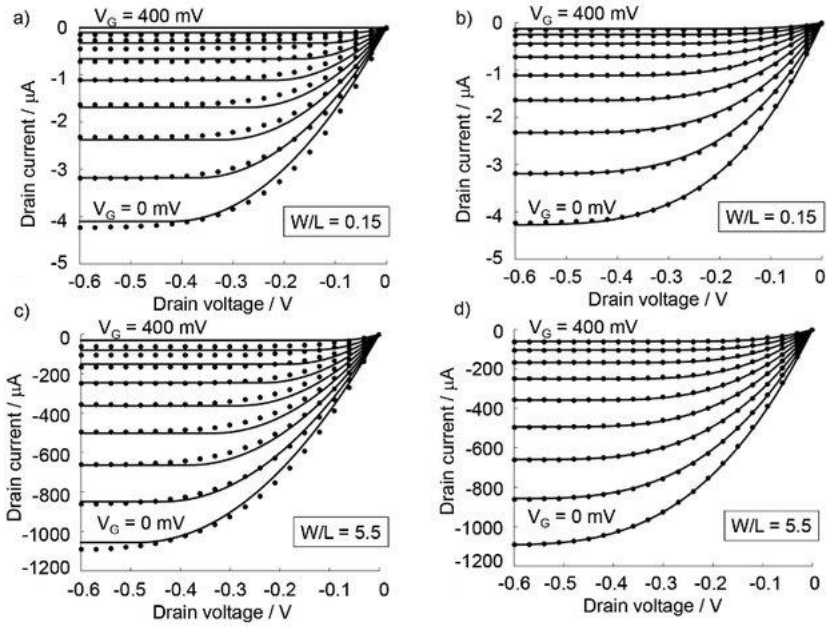

Figure 1.9 Comparison of experimental data (circles) to model fits (solid lines) using the Bernard-Malliaras model with carrier concentration dependent mobility. Graphics (a) and (b) are the data and fits for a device with width/length = 33.2 µm/238 µm. (c) and (d) are the data and fits for a device with width/length = 250 µm/45.6 µm. The Bernards–Malliaras model fits are in panels (a) and (c), while the nonuniform mobility model fits are shown in panels (b) and (d). Each curve is for a different gate voltage starting from V_{GS} = 0 mV and increasing in 50 mV steps up to 400 mV, as indicated by the labels on the top and bottom curves. This Figure was adapted from Ref [24].

1.2.2 Transient model

The transient state is defined to be the operation mode of the transistor where the ionic current coming from the electrolyte, upon a certain gate voltage application, is still changing in time. In other words, the channel has been charged by ions and doping or de-doping of the semiconducting material is still in progress. In this situation, the Ohm's law, as described in Equation 1.1, is no longer sufficient, and a time-dependent current contribution associated with the doping/de-doping process has to be added. Therefore, there will be two current contributions in the device: one coming from the injection of anions/cations from the electrolyte and another from the injection/removal of holes by the source electrode. For simplicity, the model ignores the spatial variation of the voltage and hole density, by assuming an average ionic current and hole density. Under these considerations, the Ohm' law can be written as:

$$j(t) = q\mu\rho(t)\frac{V_d}{L} + qfL\frac{dp(t)}{dt} \tag{1.15}$$

where $p(t)$ is the change in charge density with time, $\frac{\mathrm{Vd}}{\mathrm{L}}$ is the average electric field within the channel, and the f factor is a constant that accounts for the spatial non-uniformity of the doping/de-doping process. Basically, the ion flux coming from the electrolyte into the channel is split between the source and drain electrodes, depending on the magnitude of V_{DS} and V_{GS}. For V_{DS}=0, the drain and source electrodes are short-circuited, and there is no preferential potential for ionic charges to follow. Therefore, doping/dedoping of the channel is said to be uniform. That way, the f factor tends to the value of $\frac{1}{2}$. Conversely, when $V_{\mathrm{DS}}\neq 0$, there will be a preferable "potential" path for ions to follow, and doping/de-doping of the semiconducting layer will be non-uniform along the channel [26].

Using Equation 1.2 for depletion mode (or Equation 1.3 for accumulation mode OECT), one can rewrite Equation 15 as

$$I_{DS}(t) = \frac{WT}{L}q\mu\rho_0\left(1 - \frac{Q(t)}{q\rho_0 v}\right)V_{DS} - f\frac{dQ(t)}{dt} \tag{1.16}$$

where, $Q(t)$ is the number of ionic charges that the semiconducting channel uptakes over time. In this sub-section, we focus only on the development of expression to depletion mode OECT. Although the transient state B&M [23] model allows for a good estimation of semiconductors parameters, such as charge carrier mobility, the final expression does not completely fit experimental drain currents.

1.2.3 Equivalent circuit model with B&M model

Gentile *et al.* proposed a hybrid B&M-equivalent circuit model in order to better describe the transient response of OECTs [27]. The proposed equivalent circuit is the one illustrated in Figure 1.10, with a Warburg impedance element R_w that was used instead of a simple charge-transfer resistance R_d.

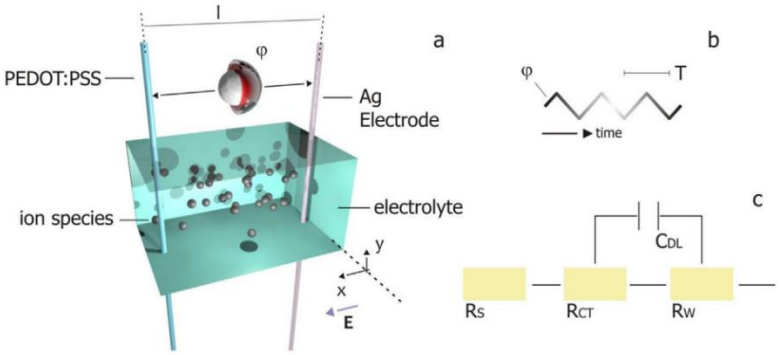

Figure 1.10 Artist's impression of the Gentile model and electrical circuit. a) A silver electrode and a PEDOT:PSS polymer are integrated in the electrolyte. Upon application of an alternate voltage at the gate (b), positive ions are transported to the PEDOT channel and a current is generated. The behavior of the device is here analyzed on dividing the system into an electronic and an ionic circuit. The ionic charge transported in the unit time to the PEDOT/electrolyte interface is determined from the analysis of the electrical equivalent circuit of the system, as in (c): R_S is the resistance of the electrolyte, R_{CT} is the charge transfer resistance, R_W is the Warburg or diffusion impedance, C_{dl} is the double layer capacitor. Taken from Gentile et al [27].

In OECTs, such impedance may account for the diffusion response of different ionic species. The Warburg impedance is a complex valued quantity given by [66]

$$Z_w = A_w \left[\frac{1}{\sqrt{\omega}} - i\frac{1}{\sqrt{\omega}}\right] \tag{1.17}$$

where $\boldsymbol{A_w}$ is known as the Warburg coefficient and $\boldsymbol{i}$ is the imaginary number. $\boldsymbol{A_w}$ is related to the diffusion coefficient through the relation

$$A_w = \frac{R\theta}{n^2F^2Ac_0}\sqrt{\frac{1}{2D}} \tag{1.18}$$

Here, $\boldsymbol{R}$ is the universal gas constant, $\boldsymbol{\Theta}$ is the temperature, $\boldsymbol{n}$ is the number of charges involved in the process, $\boldsymbol{F}$ is the Faraday constant, $\boldsymbol{A}$ is the interfacial area between the polymer and the electrolyte, $\boldsymbol{c_0}$ is the initial charge concentration, and, finally, $\boldsymbol{D}$ is the molecular diffusion coefficient of ions. Proceeding with the calculation of the equivalent impedance generates the following equation:

$$Z_{eq} = R_s + \frac{A_w}{\sqrt{w} + 2C_{DL} w {A_w}^2 + 2{C_{DL}}^2 {A_w}^2 w^{\frac{3}{2}}} - i\left[\frac{A_{w\left(2C_{DL} w A_w + {}^1/_{\sqrt{w}}\right)}}{2C_{DL}\sqrt{w}A_w + 2{C_{DL}}^2 {A_w}^2 w}\right] \quad (1.19)$$

The total amount of charge exchanged between the electrolyte and the polymer film can then be calculated using:

$$Q(t) = \int_0^t \frac{\varphi(t)}{|Z_{eq|}} \quad (1.20)$$

where $\varphi(t)$ is the time-dependent gate voltage. Here, the authors have chosen a triangular gate voltage, although such stimulation in the gate electrode is usually not used to characterize the transient response of OECTs. Finally, the time-dependent drain current is calculated by plugging Equation 1.20 into Equation 1.16. Moreover, in their work, Gentile *et al.*[27] assume that the f factor is expressed by the following relation:

$$f \sim \frac{\sqrt{\frac{D}{f_{Hz}}}}{T} \quad (1.21)$$

where, f_{Hz} is the input voltage frequency and T is the film thickness. The authors refer to this ratio as the penetration depth of ions into the organic film. It is worth mentioning that the origin of the f factor is most probably due to the spatial voltage profile across the transistor channel, due to the application of a simultaneous V_{DS} and V_{GS} potentials. Solving the combination of Equation 1.13 with Equations 1.19 and 1.20 yields an expression to the drain transient current. The authors applied the derived expression for a series of OECT measurements using a triangular gate voltage stimulus with varying frequencies. Their fit shows good agreement with experimental data. The authors claim that their model is sensitive to capture the response of individual ionic species and, therefore, allows discriminating the type of salt used.

1.3 Biological application

In this paragraph, we will discuss about the coupling of OECTs with a variety of different biological molecules and macromolecules, including ions, proteins (enzymes and antibodies). These devices have been reported for applications in basic research but particularly as new alternatives for low-cost diagnostics.

1.3.1 Enzymatic sensor

One of the first applications of the OECT interfacing with biology was an enzymatic sensor. The operating principle of an OECT-based enzymatic sensor involves either a change in a local pH coming from oxidation of species or transfer of electrons to the gate of the device. By measuring changes in pH Nishizawa et al., have used polypyrrole-based OECTs to sense penicillin[28]. In contrast, by measuring electron transfer, Zhu et al., [29] demonstrated the use of a PEDOT: PSS-based OECT for glucose sensing in a wide range of pH environments. The sensing mechanism is as follows: glucose oxidase catalyzes the conversion of glucose to gluconolactone in the presence of oxygen, forming hydrogen peroxide (H_2O_2) as a byproduct. The H_2O_2 in turn transfers an electron to the gate of the OECT. In order for charge neutrality to be maintained in the electrolyte, a positive ion penetrates the OECT and compensates the PSS anion, which in turn causes a shift of the V_{GS} and thus, a decrease of the source– drain current, logarithmically proportional to the glucose concentration.[30] Pt has been extensively used as a gate in OECT-based glucose sensors[28] because of its good catalytic performance for the oxidation and reduction of H_2O_2 and other biomolecules of interest such as dopamine and adrenaline. [31][32] The sensitivity of OECT devices, after optimization, can detect levels of glucose that exist in human saliva (as low as 8 mM), and sweat (150 mM), and have been proposed as noninvasive measurement systems.[28] The geometry of an OECT-based enzymatic sensor affect its sensitivity and a systematic study has been performed by Cicoira et al.[33], who measured the decomposition of H_2O_2, mentioned above as the byproduct of an enzymatic reaction, for devices with a constant channel area, but changing gate area. They showed that the sensitivity of the device increased as the gate size decreased. Such optimization is confirmed by modeling the behavior of the OECT and optimizing it for two types of applications: for electrochemical sensing and for ion to electron conversion.[34], [35] This can be explained by the potential drop at the two interfaces: the gate/electrolyte and electrolyte/channel interface, respectively. Redox active molecules like H_2O_2 which are produced in redox enzymatic reactions, modulate the potential drop at the metal gate/ electrolyte interface. In the case of a gate electrode which is much larger than the OECT channel, the potential drop vanishes at this interface as the overall electrode impedance is minimized, and electrochemical potential modulation cannot be detected. In case of smaller gate areas, the potential drop is maximized at the gate/electrolyte interface. In this situation, changes in the potential drop at the gate/electrolyte interface directly affect also the electrolyte/channel interface and thus, modulate the OECT current.

1.3.2 OECT's cells monitoring.

The coupling of OECTs with live mammalian cells for monitoring toxicology/diagnostics and other properties was developed in the past decade. Bolin et al. [36] firstly coupled the OECTs with cells and detected the gradients of cells on the OECT channel. They seeded Madin Darby canine kidney (MDCK) epithelial cells on an OECT channel, and the channel bias added and produced a potential gradient. The gate potential controls and modulates the potential gradient of the channel. Therefore, the MDCK cell quantity gradient on the channel depended on the gate and source voltages.

Subsequent integration of OECTs with live cells have focused on the sensitivity of the devices to changes in biological ion flux, a parameter which can be used for monitoring the integrity of mammalian cells, as the flow of ions is tightly regulated in tissues and dysregulation is often a sign of disease or dysfunction. In particular, OECTs have been used as an alternative technology for sensing barrier tissue integrity, monitoring variations in paracellular ion flux with state-of-the-art temporal resolution and high sensitivity. Barrier tissue is composed of epithelial or specialized endothelial cells whose role is to modulate ion flux between different bodily compartments. As this role is often compromised during toxic events, monitoring of this tissue is very interesting for diagnostics/toxicology. In a first instance, Jimison *et al.*,[37] integrated epithelial cells grown on filter supports with the OECT, using a model of the gastrointestinal tract Caco-2 cell line, which is established as a barrier tissue model Figure 1.11(a). This configuration is compatible with existing barrier tissue characterization and toxicology methods and protocols, which frequently use filter supports as they mimic the polarized nature of the cells *in vivo* where they separate different functional compartments (e.g., gastrointestinal tract from blood stream). The OECT ionic circuit on the addition of barrier tissue is shown schematically in Figure 1.11 (b), with the cell layer represented as a resistor and capacitor in parallel. In this way, the OECT uses the ionic to electronic transduction to measure changes in the impedance of the ionic circuit. Application of a positive gate voltage V_{GS} leads cations from the electrolyte, in this case cell culture media, into the CP channel, thus dedoping it. The transient response, which gives the time of how fast the channel will be dedoped, can be quantified by the time constant ($\tau = RC$). The τ depends on the capacitance of the channel and the resistance of the electrolyte. The presence of the barrier tissue modifies the ionic flux, due to the addition of additional capacitor and resistor, Figure 1.11 (b) and the drain current by inducing a slow response and thus an increase in the τ [38].

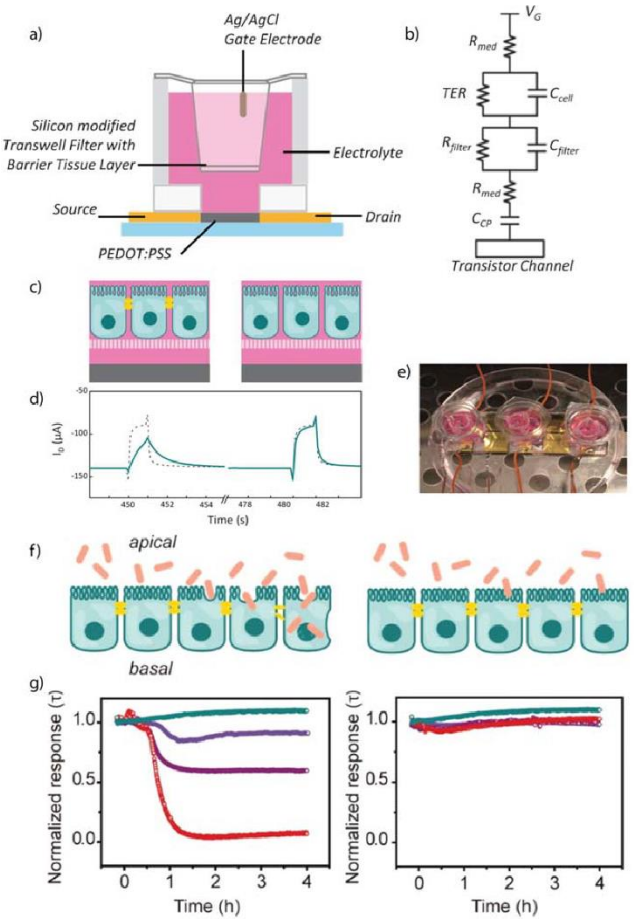

Figura 1.11 Barrier tissue integrity monitored with an OECT: a) layout of an OECT with an integrated barrier tissue, b) equivalent circuit describing ionic transport between gate electrode and transistor channel. TER refers to the transepithelial resistance of the cell layer, C_{cell} refers to the capacitance of the cell layer, R_{filter} and C_{filter} refer to the resistance and capacitance of the porous filter, respectively, R_{med} refers to the resistance of the media, and C_{cp} refers to the capacitance at the CP and electrolyte layer, c) cartoon showing polarized Caco-2 cells with tight junctions (left) and without (right), sitting on a porous cell culture membrane, above a PEDOT:PSS transistor channel. Tight junctions are shown in yellow. D) OECT I_{DS} transient response with cells before (left) and after (right) the addition of 100 mM H_2O_2,(solid lines). OECT I_{DS} response in the absence of cells is overlaid (dashed lines) (a, b, c, d, were taken from [37] e) Picture of the multiplex device shown on a Petri dish inside the cell-culture incubator. The cell culture insert is shown suspended in the plastic holder affixed to the glass slide. The Ag/AgCl gate electrode is shown immersed in the apical media, while source and drain cables are attached to their respective positions on the glass slide, f) cartoon illustrating infection with wildtype (WT) (left) and noninvasive S. typhimurium (right). G) Mean normalized response (τ) of the OECT in the presence of WT (left) and noninvasive S. typhimurium (right) at different MOI over 4 h, bacteria were added at t = 0. Noninfected represents OECT + cells with no added bacteria. Noninfected cells are in cyan, MOI: 10 in blue, MOI: 100 in purple, and MOI: 1000 in red. (e, f, g, taken from [39]).

The disruption of barrier tissue in Figure 1.11(c), related to the destruction of protein complexes between the cells, was also demonstrated on addition of hydrogen peroxide (H_2O_2), a known toxin. Figure 1.11(d) illustrates the high temporal resolution of the OECT in monitoring barrier tissue disruption, from one pulse to the next. Monitoring of the I_{DS} response to the gate voltage was normalized as a function of time in the presence of both H_2O_2 and a second toxin, ethanol, and shown to have greater sensitivity than traditional methods. The effect of EGTA (Ethylene glycol-bis(beta-aminoethyl ether)- N,N,N0,N0-tetra acetic acid) known to affect paracellular ion transport pathways and trans epithelial resistance of cells has also been demonstrated with the OECT.[40] Dose dependent responses to addition of EGTA were detected and validated against existing commercially available electrical impedance spectroscopy shown significant advantages of the OECT in terms of

temporal resolution. A visual demonstration of the OECT fabrication and operation for monitoring barrier tissue disruption by EGTA has also been reported.[41] For nonacute diagnostics applications where time scales for readouts exceed minutes and may actually extend to days or even weeks, not only the stability of the sensor, but also the environmental conditions for measurement must be required. To test the stability of the OECT and assess suitability for long term measurements of an OECT, Tria et al., transitioned the device to a format compatible with operation in physiological conditions, and to cope with the many varying parameters inherent to biological systems, the number of devices operated simultaneously was scaled-up, Figure 1.11(e).[41] This system was used to successfully monitor the kinetics of integrity of the same gastrointestinal model after infection with the pathogenic organism Salmonella typhimurium in Figure 1.11(f), while a nonpathogenic Salmonella bacterium showed no response regardless of the concentration added Figure 1.11(g).

Ramuz et al. [39] found that barrier tissue cells adhered on the polymer surface can be deprived of function in calcium switch assay, and re-addition of calcium lead to improvement of the cells function. The process is monitored both electronically and optically, enabling the capture of cells images while simultaneously recording electronic information Figure 1.12.

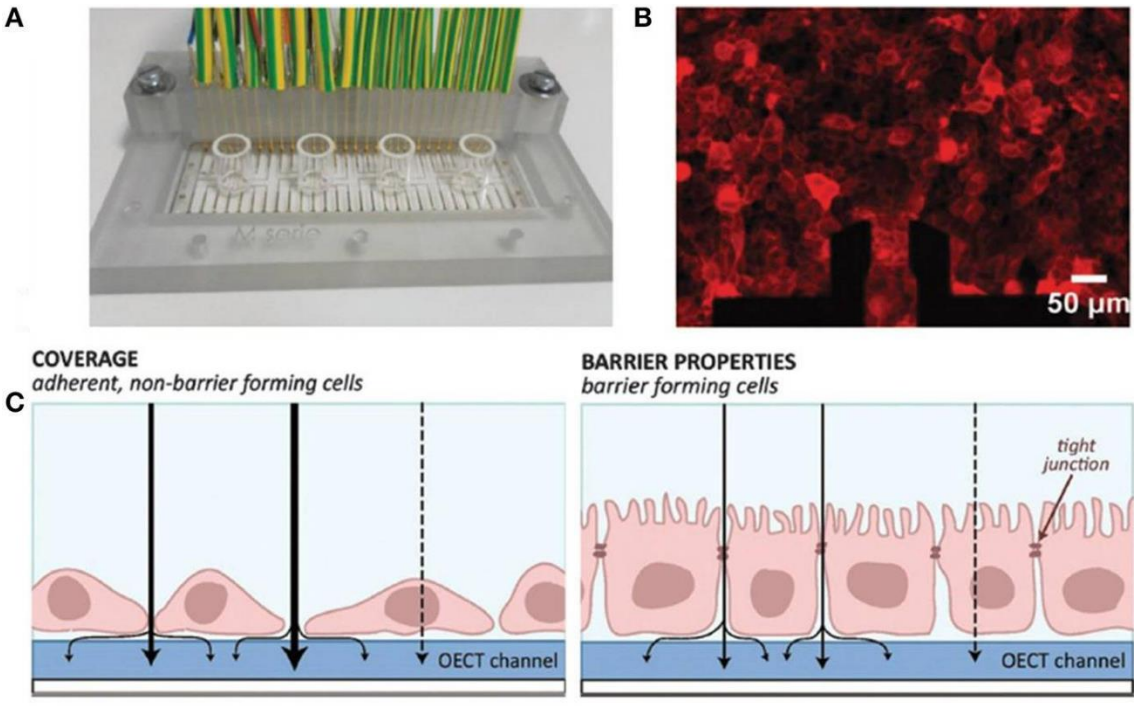

Figure 1.12 The OECT device for monitoring adherent cells. (A) Measurement platform consisting of 24 OECTs divided between four glass wells. (B) MDCK II cells transfected with RFP actin construct seeded on device for fluorescence imaging. (C) Schematic diagram of the cell coverage with low ion flow through barrier (right) or high ion flow through non-barrier (left). [39]

The OECT uses the ionic to electronic transduction to measure changes in the impedance of the ionic circuit. Application of a positive gate voltage V_{GS} leads cations from the electrolyte, in this case cell culture media, into the CP channel thus dedoping it. The transient response, which gives the time of how fast the channel will be dedoped, can be quantified by the time constant (τ=RC). The τ depends on the capacitance of the channel and the resistance of the electrolyte. The presence of the barrier tissue modifies the ionic flux, due to the addition of additional capacitor and resistor and the drain current by inducing a slow response and thus an increase in the τ. The disruption of barrier tissue, schematically illustrated in Figure 11c, related to the destruction of protein complexes between the cells, was also demonstrated on addition of hydrogen peroxide (H_2O_2), a known toxin induces a correspondent decrease in the τ. Wei et al. [36] presented the first report to apply OECTs for detecting the microalgae *H. pluvialis* cell. The constructed OECT array is a platform with advantages of convenience, and efficiency, and is able to monitor the real-time signals induced by settling *H. pluvialis* cells on the active conducting polymers. The results can help to approximately estimate the time point for producing the maximum astaxanthin in the commercial fermentation. Rivnay et al. [39], combined OECT with the impedance sensing technique by applying gate current to generate complicate low error impedance signals. They applied the method *in vitro* to sense a layer of epithelial tissue and concluded that the data is suitable to an equivalent circuit, allowing the resistance of trans-epithelial, and capacitance values of cell layer in accordance with literature.

1.3.3 OECT for Dopamine detection

Fraboni et al [42], explored a new approach to selectively identify and determine the contributions of different analytes to the OECT electrical output signal through a linear scan of the gate potential. They used OECTs entirely made of PEDOT:PSS (both conductive channel and gate) in order to take advantage of the peculiar electrochemical properties of the conducting polymer. By cyclic voltammetry and differential pulse voltammetry (CV and DPV) characterizations in a 3-electrode cell set-up, they achieved a deeper insight into the electrochemical processes that occur at the polymer gate electrode, showing that: (i) the oxidation of different analytes occurs at different potentials and (ii) the scan rate affects the separation between the redox waves by influencing the kinetics of charge transfer reactions. They assessed how OECTs can profit from PEDOT:PSS electrochemical features by selectively detecting the electro-oxidation of three different analytes (ascorbic acid, uric acid and dopamine). Figure 13 shows that they occur at different gate potentials. The signal related to each one of the three different analytes can be individually detected and resolved by recording the trans-conductance, obtaining a linear response for all the analytes.

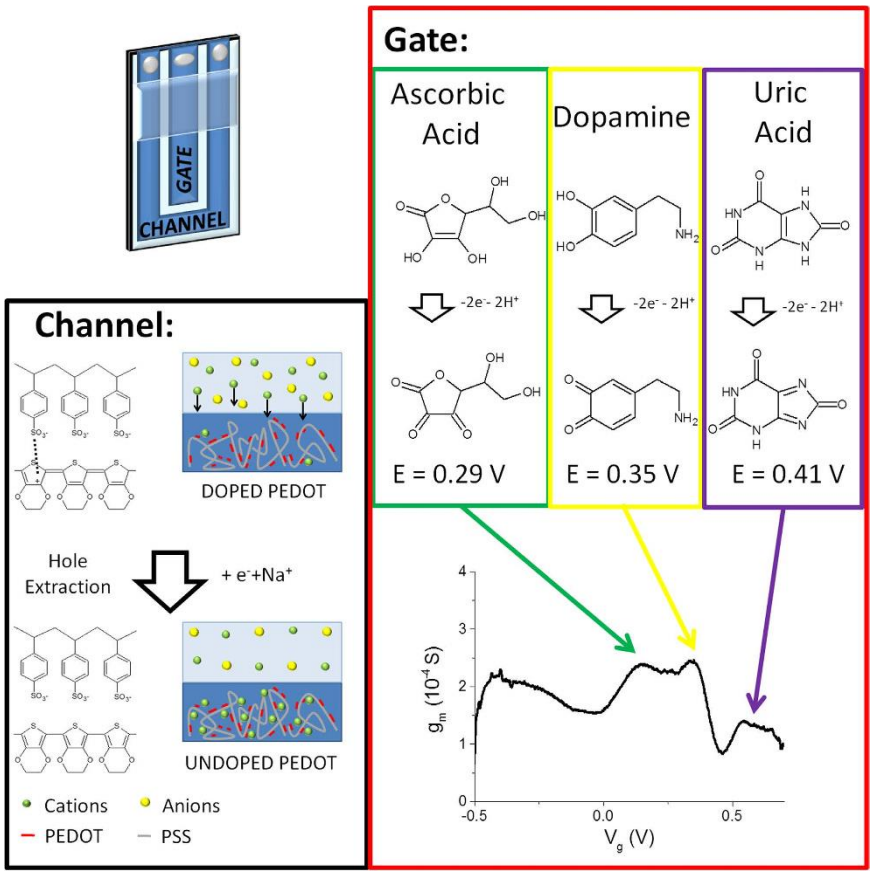

Figure 1.13 Working principle of the selective all-PEDOT:PSS OECT. The oxidation reactions of ascorbic acid, uric acid and dopamine (AA, DA and UA) take place at different electrochemical potentials and, consequently, also at different gate potentials in an OECT. When a faradic process occurs at the gate electrode, more cations are injected in the PEDOT:PSS of the channel leading to an extraction of holes from the conductive polymer. Consequently, the gate effect is enhanced by a rise of the trans-conductance value. The OECT sensor identifies the contributions of different analytes as peaks in the trans-conductance plot [42].

The validity of the proposed approach has been assessed by using all-PEDOT:PSS OECTs as sensors for dopamine in presence of ascorbic acid and uric acid. The resulting interference of both compounds was very low, even if the concentrations of the interfering agents were noticeably higher than the dopamine's one. They are able to reach a limit of detection of 6 μM, which is higher than the value desirable for DA detection in biological samples.

1.4 Conclusion

OECTs have become a well-established standard device for application in several branches within electronics and bioelectronics. Understanding the device working mechanism and the fundamentals behind the ion-electron transducing mechanisms is the key for rational and fast device optimization. Here, a review of several seminal works on modeling both the steady state and transient response regimes of OECTs is proposed. It is focused on the operating principle but above all on the two fundamental manufacturing techniques, which will then be resumed in Chapter 3 where I propose a

novel technique to pattern the PEDOT: PSS suitable for OECT integration to microfluidics assessed in terms of irreversible bonding, absence of leakage, reproducible OECTs electrical response. Furthermore, the multiple applications of OECT are introduced, focusing on their versatility which will be relevant in Chapter 4 where a tubular model of blood brain barrier *in vitro* combined with OECT is presented.

Bibliography

[1] L. Groenendaal, F. Jonas, D. Freitag, H. Pielartzik, and J. R. Reynolds, "Poly(3,4-ethylenedioxythiophene) and its derivatives: past, present, and future," *Adv. Mater.*, vol. 12, no. 7, pp. 481–494, 2000, doi: 10.1002/(SICI)1521-4095(200004)12:7<481::AID-ADMA481>3.0.CO;2-C.

[2] A. Rostami and M. S. Taylor, "Polymers for anion recognition and sensing," *Macromol. Rapid Commun.*, vol. 33, no. 1, pp. 21–34, 2012, doi: 10.1002/marc.201100528.

[3] F. Jonas, W. Krafft, and B. Muys, "Poly(3, 4-ethylenedioxythiophene): Conductive coatings, technical applications and properties," *Macromol. Symp.*, vol. 100, no. 1, pp. 169–173, 1995, doi: 10.1002/masy.19951000128.

[4] K. Lim *et al.*, "The enhancement of electrical and optical properties of PEDOT:PSS using one-step dynamic etching for flexible application," *Org. Electron.*, vol. 15, no. 8, pp. 1849–1855, 2014, doi: 10.1016/j.orgel.2014.04.014.

[5] V. Kaphle, S. Liu, A. Al-Shadeedi, C. M. Keum, and B. Lüssem, "Contact Resistance Effects in Highly Doped Organic Electrochemical Transistors," *Adv. Mater.*, vol. 28, no. 39, pp. 8766–8770, 2016, doi: 10.1002/adma.201602125.

[6] A. Giovannitti *et al.*, "Erratum: N-type organic electrochemical transistors with stability in water (Nature Communications (2016) 7 (13066) DOI: 10.1038/ncomms13066)," *Nat. Commun.*, vol. 7, pp. 1–9, 2016, doi: 10.1038/ncomms13066.

[7] S. Inal *et al.*, "A high transconductance accumulation mode electrochemical transistor," *Adv. Mater.*, vol. 26, no. 44, pp. 7450–7455, 2014, doi: 10.1002/adma.201403150.

[8] T. Stöcker, A. Köhler, and R. Moos, "Why does the electrical conductivity in PEDOT:PSS decrease with PSS content? A study combining thermoelectric measurements with impedance spectroscopy," *J. Polym. Sci. Part B Polym. Phys.*, vol. 50, no. 14, pp. 976–983, 2012, doi: 10.1002/polb.23089.

[9] C. B. Nielsen *et al.*, "Molecular Design of Semiconducting Polymers for High-Performance Organic Electrochemical Transistors," *J. Am. Chem. Soc.*, vol. 138, no. 32, pp. 10252–10259, 2016, doi: 10.1021/jacs.6b05280.

[10] B. Ilic and H. G. Craighead, "Topographical patterning of chemically sensitive biological

materials using a polymer-based dry lift off," *Biomed. Microdevices*, vol. 2, no. 4, pp. 317–322, 2000, doi: 10.1023/A:1009911407093.

[11] C. P. Tan and H. G. Craighead, "Surface engineering and patterning using parylene for biological applications," *Materials (Basel).*, vol. 3, no. 3, pp. 1803–1832, 2010, doi: 10.3390/ma3031803.

[12] M. Sessolo *et al.*, "Easy-to-fabricate conducting polymer microelectrode arrays," *Adv. Mater.*, vol. 25, no. 15, pp. 2135–2139, 2013, doi: 10.1002/adma.201204322.

[13] K. Fukuda *et al.*, "Fully-printed high-performance organic thin-film transistors and circuitry on one-micron-thick polymer films," *Nat. Commun.*, vol. 5, no. May, pp. 5–12, 2014, doi: 10.1038/ncomms5147.

[14] S. Ouyang *et al.*, "Surface Patterning of PEDOT:PSS by Photolithography for Organic Electronic Devices," *J. Nanomater.*, vol. 2015, 2015, doi: 10.1155/2015/603148.

[15] M. ElMahmoudy, S. Inal, A. Charrier, I. Uguz, G. G. Malliaras, and S. Sanaur, "Tailoring the Electrochemical and Mechanical Properties of PEDOT:PSS Films for Bioelectronics," *Macromol. Mater. Eng.*, vol. 302, no. 5, pp. 1–8, 2017, doi: 10.1002/mame.201600497.

[16] A. Håkansson *et al.*, "Effect of (3-glycidyloxypropyl)trimethoxysilane (GOPS) on the electrical properties of PEDOT:PSS films," *J. Polym. Sci. Part B Polym. Phys.*, vol. 55, no. 10, pp. 814–820, 2017, doi: 10.1002/polb.24331.

[17] D. H. Han *et al.*, "Effects of aging on the thickness of a homogeneous film fabricated using a spin coating process," *J. Coatings Technol. Res.*, vol. 18, no. 3, pp. 641–647, 2021, doi: 10.1007/s11998-020-00429-x.

[18] S. Y. Kim, K. Kim, K. Hong, and J.-L. Lee, "Investigation of Metal Peel-Off Technique for the Fabrication of Flexible Organic Light-Emitting Diodes," *J. Electrochem. Soc.*, vol. 156, no. 9, p. J253, 2009, doi: 10.1149/1.3158804.

[19] B. Piro *et al.*, "Fabrication and use of organic electrochemical transistors for sensing of metabolites in aqueous media," *Appl. Sci.*, vol. 8, no. 6, 2018, doi: 10.3390/app8060928.

[20] C. Zhang *et al.*, "Hydrofluoroethers as orthogonal solvents for all-solution processed perovskite quantum-dot light-emitting diodes," *Nano Energy*, vol. 51, no. April, pp. 358–365, 2018, doi: 10.1016/j.nanoen.2018.06.056.

[21] W. T. Tsai, "Environmental risk assessment of hydrofluoroethers (HFEs)," *J. Hazard.*

Mater., vol. 119, no. 1–3, pp. 69–78, 2005, doi: 10.1016/j.jhazmat.2004.12.018.

[22] P. G. Taylor *et al.*, "Orthogonal patterning of PEDOT:PSS for organic electronics using hydrofluoroether solvents," *Adv. Mater.*, vol. 21, no. 22, pp. 2314–2317, 2009, doi: 10.1002/adma.200803291.

[23] D. A. Bernards and G. G. Malliaras, "Steady-state and transient behavior of organic electrochemical transistors," *Adv. Funct. Mater.*, vol. 17, no. 17, pp. 3538–3544, 2007, doi: 10.1002/adfm.200601239.

[24] J. T. Friedlein, S. E. Shaheen, G. G. Malliaras, and R. R. McLeod, "Optical Measurements Revealing Nonuniform Hole Mobility in O[1] J. T. Friedlein, S. E. Shaheen, G. G. Malliaras, and R. R. McLeod, 'Optical Measurements Revealing Nonuniform Hole Mobility in Organic Electrochemical Transistors,' Adv. Electron. Mater., vol," *Adv. Electron. Mater.*, vol. 1, no. 11, pp. 1–9, 2015, doi: 10.1002/aelm.201500189.

[25] M. C. J. M. Vissenberg and M. Matters, "PhysRevB.57.12964.pdf," *Phys. Rev. B*, vol. 57, no. 20, pp. 12964–12967, 1998.

[26] R. Colucci, H. F. D. P. Barbosa, F. Günther, P. Cavassin, and G. C. Faria, "Recent advances in modeling organic electrochemical transistors," *Flex. Print. Electron.*, vol. 5, no. 1, 2020, doi: 10.1088/2058-8585/ab601b.

[27] F. Gentile *et al.*, "A theoretical model for the time varying current in organic electrochemical transistors in a dynamic regime," *Org. Electron.*, vol. 35, pp. 59–64, 2016, doi: 10.1016/j.orgel.2016.05.001.

[28] M. Nishizawa, T. Matsue, and I. Uchida, "Penicillin Sensor Based on a Microarray Electrode Coated with pH-Responsive Polypyrrole," *Anal. Chem.*, vol. 64, no. 21, pp. 2642–2644, 1992, doi: 10.1021/ac00045a030.

[29] Z. Zhu, J. T. Mabeck, C. Zhu, N. C. Cady, A. Batt, and G. G. Malliaras, "A simple PEDOT:PSS transistor for glucose sensing at neutral pH," *Mater. Sci.*, pp. 1556–1557, 2004.

[30] N. Nakatsuka *et al.*, "Aptamer-field-effect transistors overcome Debye length limitations for small-molecule sensing," *Science (80-.).*, vol. 362, no. 6412, pp. 319–324, 2018, doi: 10.1126/science.aao675.

[31] J. W. Onorato and C. K. Luscombe, "Morphological effects on polymeric mixed ionic/electronic conductors," *Mol. Syst. Des. Eng.*, vol. 4, no. 2, pp. 310–324, 2019, doi:

10.1039/c8me00093j.

[32] A. M. Pappa *et al.*, “Polyelectrolyte Layer-by-Layer Assembly on Organic Electrochemical Transistors,” *ACS Appl. Mater. Interfaces*, vol. 9, no. 12, pp. 10427–10434, 2017, doi: 10.1021/acsami.6b15522.

[33] F. Cicoira, M. Sessolo, O. Yaghmazadeh, J. A. Defranco, S. Y. Yang, and G. C. Malliaras, “Influence of device geometry on sensor characteristics of planar Organic electrochemical transistors,” *Adv. Mater.*, vol. 22, no. 9, pp. 1012–1016, 2010, doi: 10.1002/adma.200902329.

[34] O. Parlak, S. T. Keene, A. Marais, V. F. Curto, and A. Salleo, “Molecularly selective nanoporous membrane-based wearable organic electrochemical device for noninvasive cortisol sensing,” *Sci. Adv.*, vol. 4, no. 7, 2018, doi: 10.1126/sciadv.aar2904.

[35] A. M. Pappa *et al.*, “Direct metabolite detection with an n-type accumulation mode organic electrochemical transistor,” *Sci. Adv.*, vol. 4, no. 6, pp. 1–8, 2018, doi: 10.1126/sciadv.aat0911.

[36] M. H. Bolin *et al.*, “Active control of epithelial cell-density gradients grown along the channel of an organic electrochemical transistor,” *Adv. Mater.*, vol. 21, no. 43, pp. 4379–4382, 2009, doi: 10.1002/adma.200901191.

[37] L. H. Jimison *et al.*, “Measurement of barrier tissue integrity with an organic electrochemical transistor,” *Adv. Mater.*, vol. 24, no. 44, pp. 5919–5923, 2012, doi: 10.1002/adma.201202612.

[38] X. Strakosas *et al.*, “A facile biofunctionalisation route for solution processable conducting polymer devices,” *J. Mater. Chem. B*, vol. 2, no. 17, pp. 2537–2545, 2014, doi: 10.1039/c3tb21491e.

[39] M. Ramuz, A. Hama, J. Rivnay, P. Leleux, and R. M. Owens, “Monitoring of cell layer coverage and differentiation with the organic electrochemical transistor,” *J. Mater. Chem. B*, vol. 3, no. 29, pp. 5971–5977, 2015, doi: 10.1039/c5tb00922g.

[40] S. Tria, L. H. Jimison, A. Hama, M. Bongo, and R. M. Owens, “Sensing of EGTA mediated barrier tissue disruption with an organic transistor,” *Biosensors*, vol. 3, no. 1, pp. 44–57, 2013, doi: 10.3390/bios3010044.

[41] X. Strakosas, M. Bongo, and R. M. Owens, “The organic electrochemical transistor for

biological applications," *J. Appl. Polym. Sci.*, vol. 132, no. 15, pp. 1–14, 2015, doi: 10.1002/app.41735.

[42] I. Gualandi, D. Tonelli, F. Mariani, E. Scavetta, M. Marzocchi, and B. Fraboni, "Selective detection of dopamine with an all PEDOT:PSS Organic Electrochemical Transistor," *Sci. Rep.*, vol. 6, no. October, pp. 1–10, 2016, doi: 10.1038/srep35419.

CHAPTER 2

Organ on chip and State of art of Blood Brain Barrier in vitro models

Microfluidic organs-on-chips (OOC) systems have been used to model the blood-brain barrier (BBB) and these systems have started to manifest physiological or pathological properties akin to *in vivo* findings. In this chapter, we will first introduce the structure of the blood brain barrier, in order to understand the anatomy and the function. Then, we discuss the existing compelling research work in the microfluidic OOC field as well as its applications for modeling the BBB. Finally, we will provide to summarize the aspects that need to be taken into consideration when designing and testing BBBs-on-chips that we will use in the Chapter 4.

Table of contents

CHAPTER 2 48
Organ on chip and State of art of Blood Brain Barrier in vitro models 48
2.1 Organ on chip (OOC) model 50
2.2 Organ on chip models to mimic Blood Brain Barrier 51
2.2.1 Blood Brain Barrier anatomy 51
2.2.2 Modeling Blood Brain Barrier 54
2.3 Current BBBs on chip 57
2.4 Standardization challenging 62
2.4.1 Permeability 62
2.4.2 Transendothelial electrical resistance 64
2.4.3 Cells 65
2.4.4 Shear stress 65
2.5 Conclusion 67

2.1 Organ on chip (OOC) model

OOC models are *in vitro* cell culture platforms that are realized by microchip manufacturing methods to house living cells in relevant multicellular architectures within a perfusable culture chamber. OOC models aim to bridge the gap between static cell culture systems and animal models by leveraging advances in microfluidic technology and 3D tissue engineering to provide simple, but predictive, screening platforms that better recapitulate innate *in vivo* physiology while readily facilitating detailed mechanistic observations. By allowing researchers to combine human cell lines with relevant chemical and mechanical cues *in vitro*, OOC models provide a means to better balance simplicity and physiological relevance when conducting mechanistic studies. To combine the advantages of *in vivo* and current *in vitro* models of tissues and organs, a new class of *in vitro* models has recently been introduced: organs-on-chips [1]. These so-called chips are microfluidic devices in which tissues can be cultured in an environment that is engineered in such a way that it better replicates the *in vivo* microenvironment of that tissue [2]. This more physiologically relevant microenvironment can be achieved by engineering geometrical, mechanical and biochemical factors from the *in vivo* environment into a microfluidic device [3]. Another advantage of these organ-on-chip platforms is that imaging systems and sensors with real-time readouts can also be integrated [2]. Like in conventional *in vitro* methods, human cells or tissues can be included in organs-on-chips. Furthermore, these devices can be used for personalized (or precision) medicine when cells from a specific donor or group of donors are used. Both healthy and diseased tissues can be mimicked and tested in the same controlled environment. Moreover, organs-on-chips promise to replicate organ-level functions and allow the study of (patho)physiology on a higher level than could be achieved by conventional *in vitro* models. The comparison of organs-on-chips with current *in vivo* and *in vitro* methods is summarized in Table 2.1. The first organ-on-chip papers have provided proof-of-principle allowing better replication of the microenvironment mimicking the physiological behavior of the tissues inside the organ-on-chip device and thus providing better predictive value. More examples of such organ-on-chip applications are emerging rapidly.

	In vivo	In vitro	Organ on chip
Human tissue	No	Yes	Yes
Personalized/precision medicine	No	Yes	Yes
Realistic microenvironment	Yes	No	Yes
Control over microenvironment	No	Yes	Yes
Organ-level function	Yes	Limited	Potentially
Real-time readouts	No	Limited	Yes
High-throughput, parallelized testing	No	Yes	Possible
Pharmacodynamics / -kinetics	Yes	No	Potentially

Table 2.1 Comparison of organs-on-chips to current in vivo and in vitro methods.

2.2 Organ on chip models to mimic Blood Brain Barrier

2.2.1 Blood Brain Barrier anatomy

The BBB is formed by the brain capillary endothelial cells (BCECs). These cells line the cerebral microvasculature. Compared to endothelial cells of other organs, BCECs have a set of unique features, including a robust expression of tight junction proteins, lack of fenestrations and a low number of cytoplasmic vesicles, resulting in low vesicular trafficking across the BCECs compared to capillary endothelial cells in many other organs of the body [4,5]. Pericytes and astrocytes form intimate contact with the BCECs and both are important for the formation and maintenance of the BBB phenotype. Together with the BCECs, pericytes and astrocytes are referred to as the neurovascular unit (NVU) [5]. Pericytes are embedded in the basement membrane, which they share with the BCECs. Pericytes are distributed discontinuously along the length of the capillaries, and there is about one pericyte for every two to four endothelial cells. Astrocytic endfeet form a complex network surrounding more than 99 % of the capillaries (Figure 2.1).

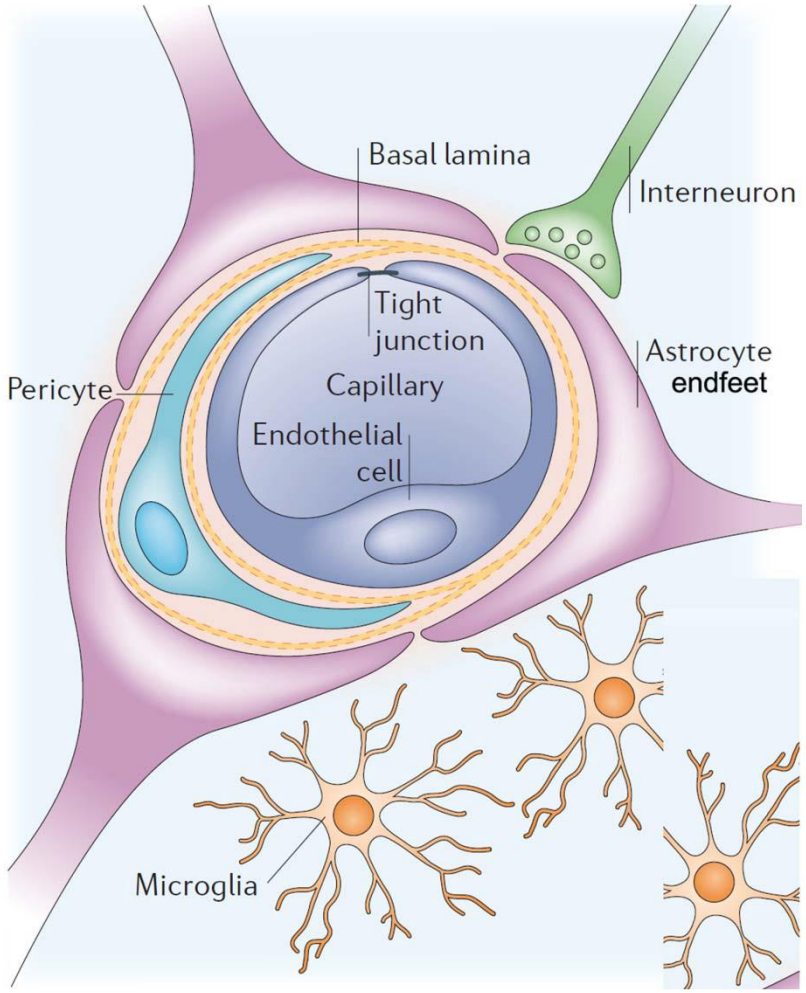

Figure 2.1 Cellular constituents of the blood–brain barrier. The barrier is formed by capillary ECs, surrounded by basal lamina and astrocytic perivascular endfeet. Astrocytes provide the cellular link to the neurons. The figure also shows pericytes and microglial cells.[6]

Astrocytes secrete important factors like transforming growth factor β (TGF-β), basic fibroblast growth factor (bFGF), leukaemia inhibitory factor and glia cell-derived neurotrophic factor (GDNF) that regulate the BBB phenotype [7]. Cultured astrocytes implanted into areas with normally leaky vessels have been found to increase the tightness of the endothelium [8], emphasizing the important role of astrocytes in establishing and maintaining the BBB phenotype. BCECs are thin and non-fenestrated cells that are closely joined together by adherens- and tight junction proteins [9]. Adherens junction's proteins are primarily responsible for holding the cells together and consequently giving the BCECs structural support. Adherens junctions are necessary for the formation of tight junctions, since the lack or disruption of adherens junction leads to disruption of the tight junctions and thereby a disruption of the barrier properties [10]. Tight junction proteins are mainly responsible for the polarisation of BCECs, which results in the clear definition of a luminal and abluminal membrane. The tight junction proteins force most molecules to take a transcellular route across the BBB, rather

than a paracellular route [11]. Adherens junction proteins include vascular endothelial cadherin (VE-cadherin) and platelet endothelial cell adhesion molecule (PECAM). These proteins span the intracellular cleft and are linked to the cell cytoplasm by scaffolding proteins. The tight junctional complex is primarily composed of proteins like occludin and claudin, with claudin 3 and 5 being the most important barrier forming proteins. The membrane spanning region of two tight junction proteins from two neighboring cells interacts and binds each other across the intercellular cleft. They are linked to a number of cytoplasmic scaffolding proteins, called zonula occludens (ZO1-3), that are further linked to the cells actin skeletal system [12]. The presence of the tight junction proteins results in a high *in vivo* trans-endothelial electrical resistance (TEER) above 1000 $\Omega*cm^2$ in rats [13]. Therefore, tight junctions are important in regulating the paracellular transport of polar substances into the brain. Finally, junctional adhesion molecules (JAMs) are also expressed at the intercellular junction between two adjacent BCECs. These are believed to be important cell adhesion molecules for leukocytes [14]. The restricted paracellular transport across the BBB creates a demand for specific transport mechanisms that can supply the brain with required nutrients. A functional BBB expresses a number of active transport mechanisms that ensure the transport of essential nutrients into the CNS. These include passive diffusion of small lipophilic molecules, carrier mediated transport, receptor mediated transport and absorptive mediated transport. Small molecules like O_2, CO_2 and ethanol passively diffuse across the BBB due to their lipophilic nature, while glucose and amino acids are carried via specific solute transporters expressed on both the luminal and abluminal side of the BCECs. Macromolecules, like insulin and transferrin enter the brain via binding to their respective receptors expressed on the BCECs, which triggers an endocytic event and subsequently transport across the BBB. Positively charged macromolecules like albumin can also be absorbed by the BCECs via a non-specific transcytosis mechanism (Figure 2.2) [15].

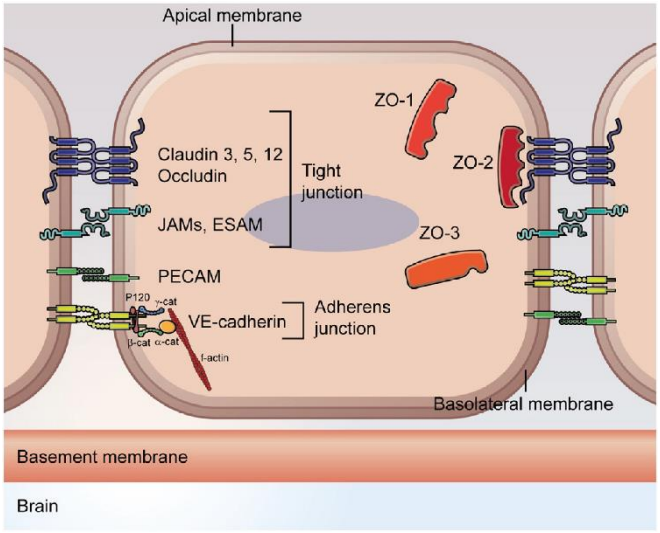

Figure 2.2 Paracellular and transcellular routes across the blood-brain barrier (BBB). Two adjacent brain capillary endothelial cells (BCECs) are tightly connected by the membrane spanning tight junction proteins, claudin-5 and occludin and the adherens junction proteins, platelet endothelial cell adhesion molecule (PECAM) and vascular endothelial cadherin (VE-cadherin). These proteins force most molecules to take a transcellular route into the brain. Junctional adhesion molecules (JAMs) are believed to be important for cell adhesion of leukocytes. There are four different transcellular transport routes across the BCECs. Small lipophilic molecules can access the brain via passive diffusion across the BCECs, while molecules like glucose, amino acids and nucleotides are carried across the BCECs via specific solute carriers. Macromolecules like transferrin and insulin enter the brain via receptor mediated transcytosis, while positively charged molecules like albumin enter the brain via absorptive mediated transcytosis [15].

2.2.2 Modeling Blood Brain Barrier

To speed up brain research, and the development of novel drugs for numerous neurological diseases, different types of *in vitro* BBB models have been established. However, as none of these *in vitro* models entirely reproduces the *in vivo* conditions, there is no perfect *in vitro* BBB model. Therefore, it is important to carefully choose the *in vitro* BBB model according to the requirement of the study and interpretation of the data, efficiently [16]. In the following paragraphs, we have summarized the commonly used *in vitro* BBB models, including the recently developed microfluidic BBB models, along with their advantages and disadvantages. Based on the simulation of shear stress, in vitro BBB models are classified into static and dynamic BBB models.

Static model

Static BBB models are commonly used, but they do not imitate the shear stress, which is usually generated *in vivo* due to the blood flow. Static BBB models are further divided into monolayer and co-culture models, based on the type of cells involved in the BBB design.

Monolayer BBB models

A monolayer of endothelial cells grown in the Transwell insert is used as a simple *in vitro* BBB model (Figure 2.3A-i). The insert mimics the blood (luminal) side, whereas the well in which the insert fits, mimics the parenchymal (abluminal) side. The microporous membrane support (0.2–0.4 μm) allows the exchange of small molecules and cell-secreted growth factors but prevents the migration of cells between the two compartments. To mimic the unique properties of BMECs, primary or low passage number cells are used for the BBB model preparation. Human cells are used for the studies focusing on human-specific transporters/ receptors or immunological aspects, but they are generally difficult to source because of ethical issues. To overcome this, many immortalized human cell lines, such as human cerebral microvascular endothelial cell line (hCMEC/D3) and immortalized human cerebral endothelial cells, have been produced, which are useful but have lower expression of some of the BBB specific transporters and enzymes, leading to decreased generation of a tight monolayer and thus, having inadequate barrier function [17]. Monolayer models are employed in studying signaling pathways, transporter kinetics, binding affinity, and high-throughput screenings. However, the monolayer model is not ideal for BBB integrity studies, as it has only one type of cells (BMECs) and lacks to imitate the brain microenvironment in which cell to cell communication is essential between different cell CNS cell types [17,18]. Therefore, for the study of BBB integrity, more vivid and complex BBB models are required, such as co-culture and dynamic models.

Co-culture BBB models

In order to mimic the anatomic structure of BBB *in vivo*, BMECs are co-cultured with other CNS cells that directly contribute to the barrier properties of BBB. Interaction between BMECs and other brain cells increases the expression of transporters, TJs in BMECs, and induces the cell polarity in BMECs, promoting a phenotype closely mimicking the BBB *in vivo* [20]. In this co-culture model (Figure 2.3A-ii) BMECs are seeded in the transwell insert, and astrocytes are grown on the undersurface of the transwell insert. Since pericytes also have a key role in BBB regulation, a BMEC–astrocyte pericyte co-culture model has also been developed, which is termed as a triple co-culture system (BMEC–pericyte–astrocyte). Addition of pericytes enhances the quality of the co-culture model compared to the monolayer model. In this model, BMECs are plated in the transwell insert with astrocytes at the bottom of the well and pericytes on the underside of the insert (Figure 2.3A-iii). Although it lacks the direct cell-cell to communication between BMECs, astrocytes, and pericytes, this arrangement utilizes indirect cell-to-cell communication via secreted soluble factors,

which promotes BBB regulation. BMEC–pericyte–astrocyte triple co-culture model is a more reliable *in vitro* BBB model due to the higher transendothelial electric resistance (TEER) value and lower permeability, which generates tighter BBB, ideal for permeability studies [19,20]. The cone-plate apparatus was used initially to construct shear force, in which a rotating cone produces shear force, and the angular velocity and the angle of the cone regulate the produced shear stress. The shear stress then reaches the endothelial monolayer via the medium (Figure 3B), but it is not uniformly dispersed along the radius of the plates, and therefore the endothelial monolayer receives varying shear stress depending upon the location. This model does not include astrocytes and pericytes; therefore, it has a limited application, low reliability, and less significant to be used in the BBB studies.

Dynamic model

To incorporate both the components, i.e., shear stress and various cell types, microporous hollow fibers are used (Figure 2.3C). In this model, BMECs and astrocytes are implanted in the inner (luminal) and outer (abluminal) sides of the porous hollow fibers, respectively [23]. The culture medium is pushed into the system through a variable-speed pump to produce shear stress equivalent to that of physiological conditions *in vivo* (5–23 dynes/cm^2). To maintain the stable microenvironment, a gas-permeable tubing system is used for the exchange of O_2 and CO_2. This dynamic *in vitro* BBB model has been used to study the pathophysiology of various CNS diseases, including ischemia-reperfusion-induced injury and epilepsy. Recently, an updated model with hollow fibers with transmural microholes of 2–4 μm has been developed to facilitate transmigration/trafficking studies. However, the dynamic BBB model has many disadvantages like, i) it does not allow direct visualization of the endothelial morphology in the luminal side; ii) the cell numbers ($>1 \cdot 10^6$) required to build this model are relatively high, and iii) the time required to reach steady-state TEER is quite longer (9–12 days) than in the case of co-culture models (3–4 days). These shortcomings prevent the use of dynamic *in vitro* BBB model in large-scale screens. This model, however, is useful in lead compound validation/optimization in new drug research and development [24].

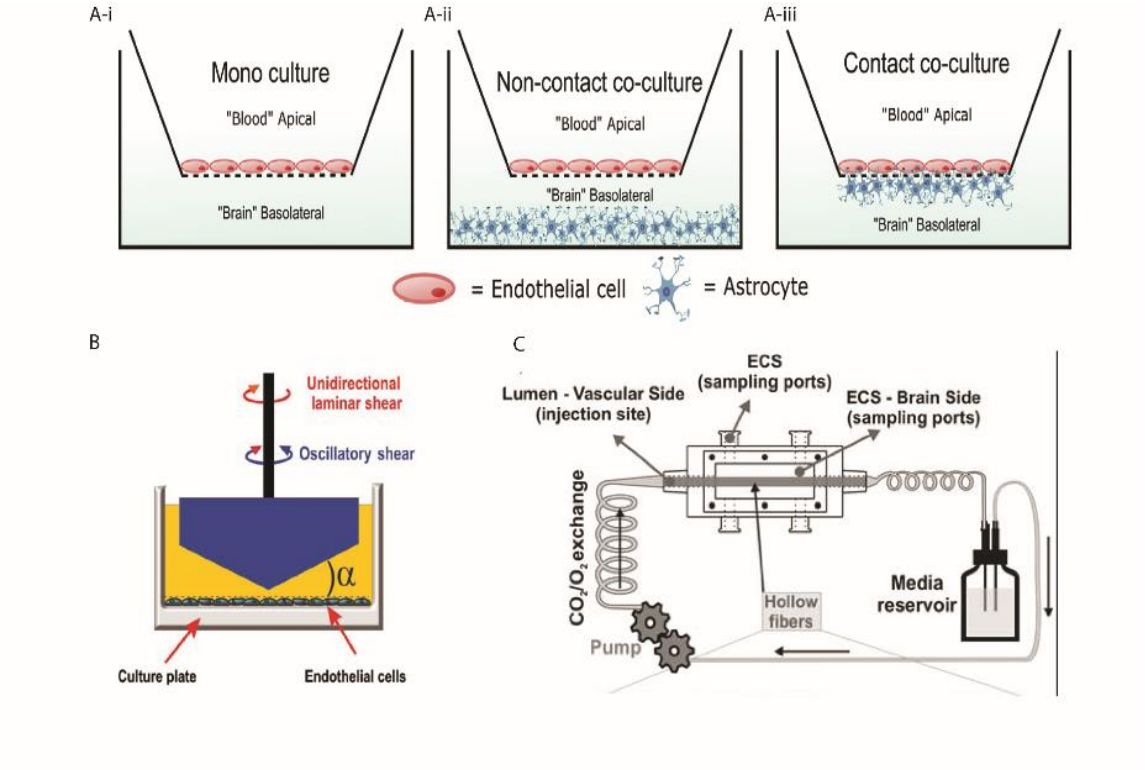

Figure 2.3 Schematic representation of different in vitro BBB models. (A) Configurations for in vitro static BBB Models using brain capillary endothelial cells (BCECs) (i) Monolayer models: are constructed using BCECs on the upper side of microporous semipermeable membrane (transwell), (ii) Non-contact co-culture: Astrocytes seeded at the bottom of the culture wells with BCECs; (iii) 2D co-culture contact models: endothelial cells are grown on porous cell culture inserts and co-cultured with primary astrocyte[25]. (B) The cone-plate apparatus was used initially to construct shear force, in which a rotating cone produces shear force, and the angular velocity and the angle of the cone regulate the produced shear stress[26].(C) Dynamic in vitro blood–brain barrier (DIV-BBB) model: The endothelial cells (ECs) are cultured inside the fibronectin-coated surface of hollow fibers made up of polypropylene. This system allows co-culture because astrocytes can be cultured on the outer surface of the hollow fibers [27].

2.3 Current BBBs on chip

In this section, it is provided a summary of the BBB microfluidic-based models that are the most relevant for this thesis. In Figure 2.4, representative images of such models are shown.

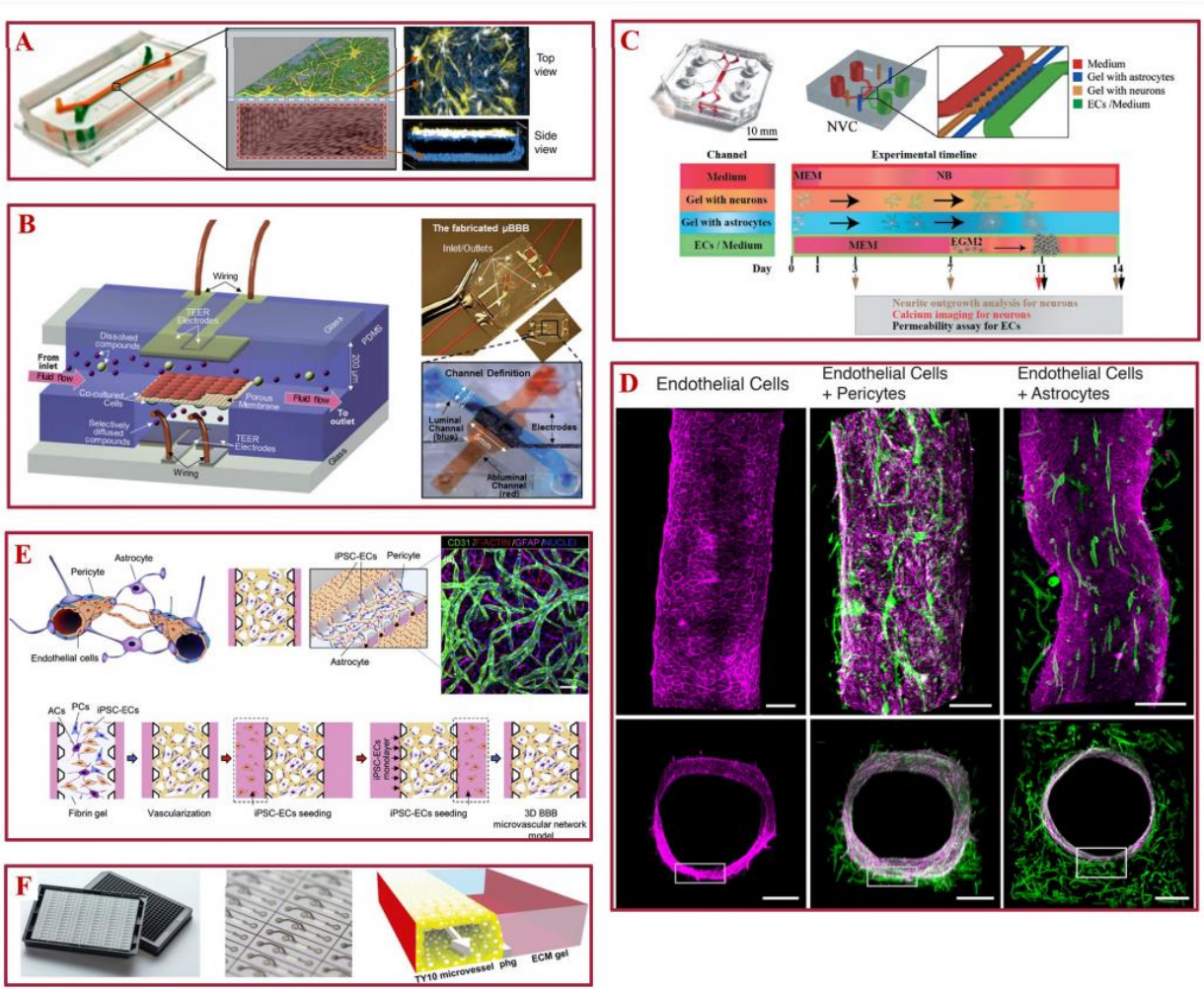

Figure 2.4 A variety of existing OOC models for the BBB. A) A 2-channel microfluidic organ chip with iPS-BMVECs cultured on all surfaces of the basal vascular channel, and primary human brain astrocytes and pericytes on the upper surface of the central horizontal membrane, which was coated on both sides with collagen type IV and fibronectin [28]. B) Shear stress can be applied to the endothelial monolayer in the OOC system to allow dynamic microenvironment and improved analysis of test compounds and controlled delivery compared to static models [29]. C) Precise cellular spatial location defined by microfluidic channels. Two central hydrogel regions for co-culturing astrocytes (blue) and neurons (orange) and two side channels for hosting endothelial cells and media (green and red, respectively) [30]. D) A cylindrical hollow structure can be created for endothelial cells lining. The surrounding gel can be embedded with astrocytes or lined with pericytes on the surface. The microstructure created in this model resembles in vivo organizations [31]. E) A BBB model created using iPSC-ECs, pericytes and astrocytes in a 3D gel environment. EC self-assembled into microvascular network [32]. F) The two-lane OrganoPlate which consists of 96 tissue culture chips. ECM gel is added to the gel channel and a phase guide prevents it from flowing into the adjacent microvessel channel. The microvessel lined by TY10 cells has a lumen that is perfused [33].

Park's model

In 2019, Park et al proposed a human BBB Chip realized using iPS-BMVECs exposed to developmentally inspired hypoxic differentiation conditions and cultured under physiological flow when interfaced with human brain pericytes and astrocytes (Figure 2.4A). This model, using human cells, exhibits enhanced functionalities relative to past human BBB models including long-term improvements resulting in the formation of a stable BBB with high, *in vivo*-like permeability restriction that lasts up to 2 weeks; high levels of expression of tight junction, SLC and ABC proteins; proper function of efflux proteins, as well as drug, peptide, nanoparticle, and antibody transcytosis

capabilities that are dependent on TfR and LRP1 surface proteins. This enhanced human BBB Chip provides a significant advance as it allows for improved drug screening by better recapitulating the *in vivo* environment of the BBB. It may therefore prove useful for development of drugs or delivery vehicles that selectively cross the BBB and target the CNS, as well as for modeling CNS diseases in vitro using patient-derived iPSCs to investigate improved brain therapies and advance personalized medicine. This model belongs to the compartmentalized models that are useful, since they permit to evaluate a lot of parameters of BBB *in vitro* but they are disadvantaged by artificial barrier interphases that limit direct neurovascular coupling. These systems often consist of cell monolayers that do not recapitulate 3D ECM and heterotypic cell interactions, also using rectangular channel cross sections that result in poor cell coverage and flow dead zones at the corners [28].

Booth and Kim's model

Booth and Kim published about their BBB in 2012, which is shown in Figure 2.4B [29]. Their device consists of poly(dimethylsiloxane) (PDMS) parts with two channels (2 mm (luminal) and 5 mm (basal) wide, 200 µm deep), that are separated by a porous polycarbonate (PC) membrane (10 µm thick, 0.4 µm pores). The PDMS parts are sandwiched between two glass slides with sputtered thin-film silver chloride (AgCl) electrodes in a four-point sensing structure to measure transendothelial electrical resistance (TEER) at near direct current (DC) conditions. A mouse brain endothelial cell line (bEnd.3) was co-cultured with a murine astrocytic cell line (C8D1A) on the opposite side of the membrane, which was coated with fibronectin. Both channels were perfused at 2.6 µl/min, which corresponds to a shear on the endothelial cells of approximately 2 mPa (calculated using the method presented in section 2.3.4), which is low compared to the physiologically found shear of 0.3-2 Pa in brain capillaries. However, the small height-to-width ratio ensured a mostly uniform shear stress across the channel width and TEER measurements yielded values of 180-280 $\Omega \cdot cm^2$, indicating the presence of a functional barrier. Apart from measuring the TEER, also permeability measurements of fluorescein isothiocyanate (FITC)-dextrans (4, 20, 70 kDa) and propidium iodide were used to confirm barrier function. Immunofluorescence showed the presence of tight junction protein ZO-1. In addition, the physiological effects of exposure to histamine and high pH were recorded. The TEER was higher and permeability lower inside the µBBB compared to conventional Transwell models, and co-culture with astrocytes resulted in even more improved barrier functionality. The transient barrier disruption caused by histamine was monitored continuously by measuring TEER. One limitation of the proposed model was in the use of non-human cells, which makes the device not really suitable as a platform for drug testing, despite mimicking the characteristics of the BBB *in vivo* very well. Additionally, it does not reproduce a physiological tubular shape.

Adriani's model

In 2017, Adriani et al. published on their neurovascular chip shown in Figure 2.4C. Their device comprises a single layer of PDMS on glass with four parallel channels (190 µm high), separated by pillar structures. The inner two channels (both 580 µm wide) are filled with primary rat astrocytes in a collagen I gel (7 mg/ml) and primary rat neurons (2.5 mg/ml gel), respectively. The outer two channels (920 µm wide) are fluidic channels used to provide neurobasal culture media to the cells. After seven days of culture, the fluidic channel next to the astrocyte channel was coated with collagen and subsequently lined with human endothelial cells (HUVECs or hCMEC/D3 cells) that were maintained in endothelial growth medium 2 (EGM-2). Immunofluorescence confirmed the formation of a monolayer of endothelial cells expressing VE-cadherin and tight junction protein ZO-1. The barrier permeability coefficient of fluorescently labeled dextrans (10 and 70 kDa), as measured with fluorescence microscopy, was lower for hCMEC/D3 than for HUVEC. Co-culture with astrocytes and neurons decreased the permeability coefficient of HUVEC barriers, but slightly increased the permeability of hCMEC/D3 barriers. Neuronal development was confirmed by examining morphology (neurite outgrowth) and functionality (calcium imaging) of the neurons in the 3D matrix. Furthermore, the availability of the neurotransmitter glutamate at the neurons was decreased in the presence of an endothelial barrier, indicating both functional neurons and endothelial cells in their device [30]. This model displayed size-selective barrier permeabilities and an active neuronal network. While the permeability coefficients were supraphysiological, likely due to combining cells from different species and the absence of pericytes, it advantageously provided functionally coupled 3D NVUs (neuronal vascular unit) for assessing the effects of perfused drugs on neuronal activity. As in the case of the previous model, also this one does not reproduce a physiological tubular shape.

Herland's model

The 3D BBB-on-chip of Herland et al., published in 2016, is shown in Figure 2.4D [50]. Their device consists of a single PDMS layer with a channel of 1 mm width and 1 mm height, bonded onto PDMS-coated glass. The channel was filled with 5 mg/ml collagen I and subsequently medium was flown through the viscous collagen solution prior to gelation to form a hollow lumen of 600-800 µm diameter ("viscous fingering"). Primary human brain endothelial cells were introduced and lined the lumen. They were allowed to form a monolayer and cAMP and RO were added to the culture medium to tighten the resulting barrier. For co-cultures, primary human astrocytes were mixed in the gel and pericytes were seeded in the lumen prior to endothelial cell introduction. As evidenced by immunofluorescence, the endothelial cells showed ZO-1 (tight junctions) and VE-cadherin (adherens junctions) expression and also secreted collagen IV along the cell-gel interface. Using Alexa 488-

labeled dextran (3 kDa), time-lapse microscopy and image analysis the apparent permeability coefficients of BBBs with and without co-cultured cells could be quantified. The presence of astrocytes or pericytes resulted in lower permeability coefficients, indicating improvement of barrier function. Furthermore, the same cultures in Transwell plates gave significantly higher permeability coefficients, indicating that the microenvironment in the 3D BBB chip positively influenced the barrier function. Lastly, they measured the cytokine release profiles upon exposure to TNF-α to mimic neuroinflammation. The chip cultures showed more physiologically relevant changes in cytokine release than Transwell cultures (normalized to culture area) [31]. Although reproducing a tubular shape, no electrical measurement could be integrated in this simple configuration.

Campisi's model

Campisi et al published in 2018 (Figure 2.4E) a highly functional 3D BBB *in vitro* model produced by vasculogenesis that incorporates human iPSC-ECs microvascular network (mVN) in contact interaction with human brain PCs (pericytes) and ACs (astrocytes) within a single 3D ECM/fibrin gel region, Figure 4E. 3D BBB mVN model incorporating three cell-types expressed both functional and morphological characteristics present in the human BBB, with stable and perfusable mVNs, comprising small lumens with circular cross-section comparable with *in vivo* human microcirculation (arterioles and venules 10-90 μm; capillaries 7-10 μm). AC endfeet were directly attached to the surface of vascular networks in the 3D matrix. This morphological feature of ACs recapitulates their physiological arrangement in the brain and provides mutual biochemical support for those cells, helping to maintain the integrity of the neurovascular networks. Vascular perfusability and permeability were measured using fluorescent probes. The vessel networks in their tri-culture BBB model attained permeability values of 10^{-8}cm/s and 10^{-7} cm/s for 40 kDa and 10 kDa FTIC-labeled dextran, respectively, confirming barrier selectivity depending on their molecular weight. Importantly, these values are comparable to those measured in vivo in rat cerebral microcirculation ($3.1 \pm 1.3\ 10^{-7}$ cm/s for a 10 kDa FITC-dextran), ($1.37 \pm 0.26\ 10^{-7}$ cm/s for a 40 kDa FITC-dextran), similar to specific models that employ brain ECs derived from iPSCs (IMR90-4) by co-culturing with astrocytes and/ or neurons, and lower than previously reported 3D, or 2D BBB models. Also in this case, despite the tubular shape no electrical measurements could be embedded [32].

Wevers's model

Wevers et. al, in 2018, described a significant advancement in the development of a novel BBB model that incorporates human brain endothelial cells, astrocytes, and pericytes in a high-throughput microfluidic platform that can be used for screening purposes, Figure 2.4F. The TY10 brain endothelial cell line used in this study has been shown to express relevant junctional markers and

transporters, independent of the passage number. These cells have been shown to express relevant junctional proteins and transporters, respond well to cues from supporting cell types. Perfusion is generated by placing the entire plate on a rocker platform, allowing medium to flow from medium inlet to outlet and back, creating a bidirectional flow. Fluid flow is controlled by regulating the inclination angle and the interval with which the rocker platform switches sides. Although direct *in vivo* measurements of shear stress in BBB vessels and venules of different diameters are lacking, it is likely that the shear stress established in the presented model (~1.2 dyne/cm^2) is low compared to the shear stress experienced by vessels of similar diameter and curvature *in vivo* [33].

2.4 Standardization challenging

As evidenced by the body of literature summarized in the previous section, significant steps have been taken toward developing physiological BBBs-on-chips. These recently reported chips show promising improvements when compared to conventional Transwell models: the exposure to fluid flow resulted in better barrier function [34] and dynamic drug permeability studies in chips were found to be more predictive than in conventional static models. However, there are still challenges ahead for developing BBB-on-chip models that will become widely available for BBB-related research applications. One of them is to arrive at commonly accepted standards for quantitative evaluation of the functionality of a BBB-on-chip model. In the following sections an overview is provided of aspects that need to be taken into consideration when designing and testing BBBs-on-chips and aspects that require consensus among researchers.

2.4.1 Permeability

As it was mentioned in the introduction, the key function of the BBB is to provide homeostasis in the brain, and more specifically to protect the brain from harmful substances in the blood[35]. The performance of BBBs-on-chips should therefore be evaluated by measuring the permeability of the cell barrier. If this permeability is in agreement with physiological levels, then a valuable BBB-on-chip has been obtained which can be used for testing drug candidates. In general, large and hydrophilic molecules, for example dextran and ions, are physically blocked by the tight junctions between endothelial cells. Ions and essential nutrients such as glucose, amino acids, peptides and hormones are transported actively into the brain by carriers and receptor mediated transport [36]. However, it is important to quantify this permeability in such a way that it can be compared to in vivo and other in vitro data. For passive transport, this can be done by calculating the permeability

coefficient of an analyte (cm/s), which is independent of the used analyte concentration, flow rate and device size, and can also be determined *in vivo* [37]. When an analyte is added to the luminal channel under constant flow and transport takes place toward the basal channel through the cell barrier on a membrane, the permeability coefficient can be determined with the following formulas:

$$P_{meas} = \frac{\dot{m}_a}{A \cdot (C_l - C_b)} = \frac{C_b \cdot Q}{A \cdot (C_l - C_b)} \quad [cm/s]$$

In these formulas, P_{meas} is the measured (or apparent) permeability coefficient (cm/s), $\dot{m}_a$ is the mass transport rate (mol/s) across the membrane which – when analyzing the sample flowing out of the basal compartment – can be quantified by multiplying the basal concentration C_b (mol/ml) with the applied flow rate in the basal channel Q (ml/s), A is the membrane area through which the transport takes place (cm^2) and $C_l$is the luminal concentration (mol/ml). The permeability coefficient of the endothelial barrier, P_{endo}, can be calculated from this measured permeability coefficient P_{meas} and the permeability coefficient measured in a device without endothelium P_0 (blank) as follows [38]:

$$\frac{1}{P_{endo}} = \frac{1}{P_{meas}} - \frac{1}{P_0} \quad [\frac{s}{cm}]$$

This endothelial permeability coefficient can then be compared to permeability coefficients found with the same analyte in other platforms. If there are more complex channel geometries the transport of analytes can also be modeled mathematically to arrive at a permeability coefficient. An advantage of measuring the permeability in microfluidic devices over Transwell systems is that the analyte can be supplied to the luminal channel at a constant flow rate and the transported analyte can also be collected from the basal channel with a constant flow rate. In this way, the assumption that the concentration difference across the membrane stays constant throughout the measurement is met, while in static Transwell systems this difference decreases over time. Another factor that can influence permeability measurement is the presence of e.g., astrocytes at the basal side of the membrane, we show the effect of the presences of astrocytes in the Chapter 4 with Fourier Frap analysis. These are reported to have a tightening effect on the BBB, but they will also form a physical barrier against diffusion by themselves. So, one should always check for the contribution of the presence of extra cells to the total barrier function. Summarizing, the permeability of the cell layer is a very important readout of BBBs-on-chips. To validate physiological relevance, different analytes that are either passively or actively transported, excreted or metabolized should be tested with a suitable protocol.

2.4.2 Transendothelial electrical resistance

Next to permeability, TEER is a widely used quantity to assess barrier tightness [38]. TEER mostly represents the electrical resistance against paracellular transport: the tighter the cell layer is packed, the less gaps there will be in the cell barrier through which ions and other charged species can move, resulting in a higher resistance [38]. Only when the cell barrier is tight enough and the contribution of paracellular ion transport pathways is low, the ion transport through paracellular channels formed by tight junction proteins and the transcellular transport of ions (via transporters) is measured [39]. It means that, there is a strong correlation between the TEER measurements and permeability analysis., When the TEER is high, so the cell barrier is tight enough, you can perform permeability, in order to study the passages of ions (e.g., Dextran) that use a paracellular pathways or proteins, such gH625, that use a transcellular transport. Measuring the TEER has the great advantage over the permeability measurements described before that it is a quick, non-invasive, and label-free way to assess barrier tightness. In addition, if a suitable electrode material and measurement method are chosen and the measurement electrodes are integrated into a microfluidic BBB-on-chip device, the measurements can be performed in real-time. The measured resistance of the endothelial barrier (R in V, if needed corrected for the resistance of e.g., channels and membranes) is normalized by multiplying it with the area through which the resistance has been measured (A in cm^2), resulting in the

$$TEER = R_{endo} \cdot A \ \ [\Omega \cdot cm^2]$$

Electrically, the inverse of TEER corresponds to the conductance per unit area. In such configurations, one has to take into account that microfluidic channels can have a high electrical resistance when they have small dimensions: the resistance scales inversely to the cross-sectional area of the channel. Therefore, the electrodes need to be positioned smartly and preferably be fixed in place to prevent measurement errors by variations in electrode placement. Another possible issue that was pointed out by Odijk et al. is that the distribution of the electrical current may not be uniform across the membrane interface in microfluidic devices, resulting in an overestimation of the TEER [40]. Measuring TEER with impedance spectroscopy (using AC) is preferred over measuring the ohmic resistance with DC. Using AC at the proper frequencies prevents electrode and concentration polarization, and other DC-related effects on the cells [39]. Furthermore, measuring the impedance at different AC frequencies gives more information about the cell culture and even enables direct measurement of the TEER without having to correct for the resistance of the device without cells. Next to device characteristics, for which can be compensated mathematically, also other factors will influence electrical resistance measurements. Analogously to the permeability measurements

specified above, TEER measurements will be influenced by the presence of co-cultured cells. The presence of extra cells will provide an extra obstacle for ion transport, resulting in a higher resistance than what would result from the tight endothelium alone. In addition, TEER measurements are sensitive to temperature and the ionic composition of the culture medium. These factors have to be kept constant in TEER measurement protocols. In conclusion, TEER is a very valuable indicator of barrier tightness that can be measured quickly, non-invasively, label-free and real-time.

2.4.3 Cells

The cells used are important for the physiological relevance of the BBB-on-chip. The more closely the cells mimic the human BBB, the more predictive the model is expected to be. Until now, many of the BBB-on-chip models and other *in vitro* BBB models use cells from animal sources. Using these cells can provide valuable information for validation purposes, because the *in vitro* results can be more easily compared to *in vivo* results from the same species. However, human cells would be the most predictive and would thus be the cells of choice for future drug development applications. Endothelial cells derived from brain capillaries already have the appropriate expression profile, so these will be the first choice. However, retaining this phenotype *in vitro* after several passages has been challenging. In addition, human brain tissue and therefore primary human brain endothelial cells are scarce. Although challenging to make, brain-derived endothelial cell lines are more readily available and provide less batch-to-batch difference, but they also lost part of their phenotype (and possibly genotype) during the immortalization process [41]. In contrast, advances have been made in deriving brain-specific endothelial cells from hiPSCs. This development holds great promise for personalized (or precision) medicine, since brain endothelium can be derived from both “healthy” cells and “diseased” cells (e.g., with genetic defects resulting in BBB pathology *in vivo*), as well as from cells originating from different people or populations. As it was mentioned in the introduction, next to endothelial cells also other cells from the NVU, such as astrocytes and pericytes, are important for the formation and maintenance of the barrier [23]. However, the use of human cells in BBBs-on-chips would be most informative for drug development studies or studies of human BBB physiology and pathology, although the tissue source has limited availability. Recent advances show that deriving brain endothelium from hiPSCs potentially provides a more accessible source of relevant cells.

2.4.4 Shear stress

Exposing the endothelium to fluid flow and the associated wall shear stress is reported to have positive effects on endothelial differentiation and cell function, which is expected as such shear flow occurs in the natural environment. Microfluidic devices are especially suited for incorporation of fluid flow

and shear stress, which is difficult in conventional *in vitro* (Transwell) models, thus presenting a real operational advantage of microfluidic models. The positive effect of shear stress on BBB tightness has already been demonstrated in several BBBs-on-chips, but shear stress is not yet standardly applied. Furthermore, as it was already mentioned before, the wall shear stress is not always of physiological level, which is 0.3-2 Pa for brain capillaries [42]. For a channel with a rectangular cross-section and with a steady laminar flow of a Newtonian fluid, the shear stress is calculated as:

$$\tau = \frac{6 \cdot \mu \cdot Q}{w \cdot h^2} \cdot \left(1 + \frac{h}{w}\right) \cdot f^*\left(\frac{h}{w}\right) \quad [Pa]$$

in which τ is the shear stress (Pa), μ is the viscosity of the fluid used in the microfluidic channel (Pa·s), Q is the volumetric flow rate (ml/s), and w and h are the channel width (at the surface of endothelial culture; cm) and height (cm), respectively [42]. The function f^* is an infinite summation series of which the output values for most common input values. If the channel width is much larger than the channel height ($w \gg h$) and the aspect ratio h/w approaches zero, this equation reduces to:

$$\tau = \frac{6 \cdot \mu \cdot Q}{w \cdot h^2} \quad [Pa]$$

To approximate the viscosity of culture medium the viscosity of water at 37°C can be used, which is 0.7 mPa·s. In a tube with a circular cross-section the wall shear stress will be equal along the entire inner wall because of the cylindrical symmetry. However, inside a rectangular channel the shear stress will not be uniform across the channel width because of the presence of the side walls. Therefore, to achieve a mostly uniform shear stress on all cells across the channel width, the width should be much larger than the height ($w \gg h$), resulting in a flat flow profile. This situation is illustrated in Figure 2.5 for different aspect ratios (channel height over channel width). The flow profile in a channel with a rectangular cross-section can be approximated with the following equations:

$$\frac{u_{x,y}}{u_{max}} = \left[1 - \left(\frac{2x}{h}\right)^2\right]\left[1 - \left|\frac{2y}{w}\right|^m\right]$$

$$m = \frac{w}{h}\sqrt{2} + 0.89\frac{h}{w}$$

In these equations $u_{x,y}$ is the fluid velocity at a given position (x, y) inside the channel cross-section, which is scaled to the maximum velocity, u_{max}; h is the channel height and w is the channel width (with $w > h$). In Figure 2.5C, the flow profiles for more aspect ratios are shown as two-dimensional (2D) projections, clearly demonstrating that a smaller aspect ratio h/w results in a more uniform flow profile. All flow profiles were modeled and displayed using MATLAB R2013a (The MathWorks,

Inc.). The result of a non-uniform flow profile is that the cells near the side walls will always experience a lower shear than the cells in the middle of the chip, Figure 2.5B. In addition, this lower flow rate at the edges results in longer retention times of paracrine signaling agents and analytes for permeability measurements at the edges. Different, instead, is the case of circular channel. For this condition, the flow profile results uniform, and also the profile of velocity is always parabolic (Figure 2.5C). The mechanisms mentioned above can result in differences in cell behavior or measured permeability across the channel width. Moreover, the growth of cells in a channel can influence the flow profile and the associated shear stress. If the cells form a thick layer compared to the channel height, the average shear stress on the cells will be higher compared to the shear stress on an empty surface at the same volumetric flow rate. Epithelia are more likely to pose such problems than endothelia because of their relative thickness. In conclusion, physiologically relevant shear stress is an important stimulus for endothelial cells. This can be applied easily on cells in a microfluidic device. However, the channel geometry influences the shear stress distribution on the cells. In a rectangular channel the most uniform shear stress is achieved if the channel height is much smaller than the channel width, instead in a circular channel the shear stress is always uniform.

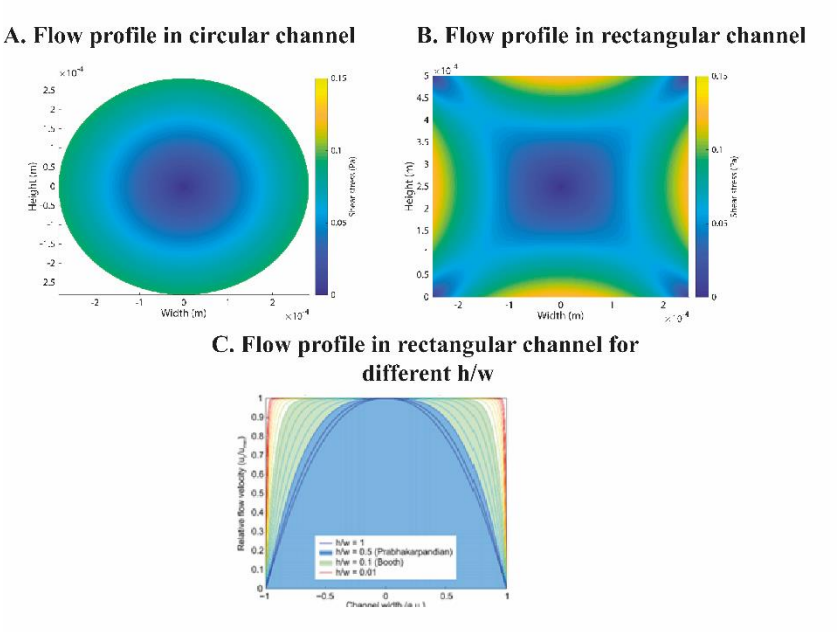

Figure 2.5 Flow profiles at different shape channel. A) 2D flow profile inside the BBB chip ofcircular shape B. 2D flow profile inside the BBB chip for rectangular shape C. 2D projections of flow profiles at different aspect ratios Prabhakarpandian [43] and BBB chip of Booth [29]. All flow profiles were modeled with MATLAB R2013a.

2.5 Conclusion

The use of BBBs-on-chips has great potential to further the field of BBB research. In microfluidic platforms the advantages of *in vivo* and *in vitro* models are combined: organ-on-chip technologies

enable the study of organ-level function like *in vivo* models, while still being robust, reproducible, and easy to analyze like *in vitro* models. There are already a number of reports of BBBs-on-chips in literature that show novel approaches and promising results. These examples already show some benefits of the use of microfluidics for BBB research applications. In addition, organ-on-chip technologies provide flexibility in the design and control over microenvironments, as well as readout protocols. This enables the development of a wide range of BBB-on-chip models that can each answer specific research questions. However, to accelerate the development and enable comparison and validation of the BBB-on-chip models, it is beneficial to have some standardization and consensus among researchers. In these chapter four aspects are highlighted:

- Determining the BBB permeability is an important readout of any BBB model.
- Human cells are more informative for BBB research though brain microvascular endothelial cells from animal sources are more widely available.
- The endothelial cells inside BBBs-on-chips can be exposed to physiologically relevant shear stress.
- Suitable channel geometries are required to achieve mostly uniform shear stress across the cell barrier.

To this end, having reviewed all the existing BBB models in the literature, our aim is to realize a 3D model of BBB with human cells, also integrating astrocytes and with potentiality to include neurons later on. Our project lies between the Herland's and Campisi's models with the advantage of being able to electrically monitor the changes in the formation of the barrier by integrating electrochemical sensors, known as OECTs with the aim to mimic degenerative diseases and represent a platform for drug screening.

Bibliography

[1] Y. Chen and L. Liu, “Modern methods for delivery of drugs across the blood-brain barrier,” *Adv. Drug Deliv. Rev.*, vol. 64, no. 7, pp. 640–665, 2012, doi: 10.1016/j.addr.2011.11.010.

[2] S. N. Bhatia and D. E. Ingber, “Microfluidic organs-on-chips,” *Nat. Biotechnol.*, vol. 32, no. 8, pp. 760–772, 2014, doi: 10.1038/nbt.2989.

[3] A. D. Van Der Meer and A. Van Den Berg, “Organs-on-chips: Breaking the in vitro impasse,” *Integr. Biol.*, vol. 4, no. 5, pp. 461–470, 2012, doi: 10.1039/c2ib00176d.

[4] N. J. Abbott, A. A. K. Patabendige, D. E. M. Dolman, S. R. Yusof, and D. J. Begley, “Structure and function of the blood-brain barrier,” *Neurobiol. Dis.*, vol. 37, no. 1, pp. 13–25, 2010, doi: 10.1016/j.nbd.2009.07.030.

[5] N. J. Abbott, L. Rönnbäck, and E. Hansson, “Astrocyte-endothelial interactions at the blood-brain barrier,” *Nat. Rev. Neurosci.*, vol. 7, no. 1, pp. 41–53, 2006, doi: 10.1038/nrn1824.

[6] M.-F. Lang, “A transgenic strategy to define SLCO1C1-expressingstructures during brain development,” no. November, 2008.

[7] Y. Igarashi *et al.*, “Glial cell line-derived neurotrophic factor induces barrier function of endothelial cells forming the blood-brain barrier,” *Biochem. Biophys. Res. Commun.*, vol. 261, no. 1, pp. 108–112, 1999, doi: 10.1006/bbrc.1999.0992.

[8] R. C. Janzer and M. C. Raff, “Astrocytes induce blood-brain barrier properties in endothelial cells,” *Nature*, vol. 325, no. 6101. pp. 253–257, 1987, doi: 10.1038/325253a0.

[9] J. Lichota, T. Skjørringe, L. B. Thomsen, and T. Moos, “Macromolecular drug transport into the brain using targeted therapy,” *J. Neurochem.*, vol. 113, no. 1, pp. 1–13, 2010, doi: 10.1111/j.1471-4159.2009.06544.x.

[10] C. Schulze and J. A. Firth, “Immunohistochemical localization of adherens junction components in blood-brain barrier microvessels of the rat,” *J. Cell Sci.*, vol. 104, no. 3, pp. 773–782, 1993, doi: 10.1242/jcs.104.3.773.

[11] W. Neuhaus, “In Vitro Models of the Blood-Brain Barrier,” *Handb. Exp. Pharmacol.*, vol. 265, pp. 75–110, 2021, doi: 10.1007/164_2020_370.

[12] U. Kniesel and H. Wolburg, “Tight junctions of the blood-brain barrier,” *Cell. Mol.*

Neurobiol., vol. 20, no. 1, pp. 57–76, 2000, doi: 10.1023/A:1006995910836.

[13] B. Y. A. M. Butt, H. C. Jones, and N. J. Abbott, "BY ARTHUR M. BUTT, HAZEL C. JONES* AND N. JOAN ABBOTT From the Physiology Group, Biomedical Sciences Division, King's College London, Campden Hill Road, London W8 7AH (Received 22 March 1990)," *Blood Vessels*, pp. 47–62, 1990.

[14] A. Del Maschio *et al.*, "Leukocyte recruitment in the cerebrospinal fluid of mice with experimental meningitis is inhibited by an antibody to junctional adhesion molecule (JAM)," *J. Exp. Med.*, vol. 190, no. 9, pp. 1351–1356, 1999, doi: 10.1084/jem.190.9.1351.

[15] C. D. Troletti, P. de Goede, A. Kamermans, and H. E. de Vries, "Molecular alterations of the blood-brain barrier under inflammatory conditions: The role of endothelial to mesenchymal transition," *Biochim. Biophys. Acta - Mol. Basis Dis.*, vol. 1862, no. 3, pp. 452–460, 2016, doi: 10.1016/j.bbadis.2015.10.010.

[16] and K. D. Cathrin J. Czupalla , Stefan Liebner, "In Vitro Models of the Blood–Brain Barrier," *Methods Mol Biol.*, vol. 1135, pp. 205–211, 2014, doi: 10.1007/978-1-4939-0320-7.

[17] E. S. Lippmann, A. Al-Ahmad, S. P. Palecek, and E. V. Shusta, "Modeling the blood-brain barrier using stem cell sources," *Fluids Barriers CNS*, vol. 10, no. 1, pp. 1–14, 2013, doi: 10.1186/2045-8118-10-2.

[18] S. Hori, S. Ohtsuki, K. I. Hosoya, E. Nakashima, and T. Terasaki, "A pericyte-derived angiopoietin-1 multimeric complex induces occludin gene expression in brain capillary endothelial cells through Tie-2 activation in vitro," *J. Neurochem.*, vol. 89, no. 2, pp. 503–513, 2004, doi: 10.1111/j.1471-4159.2004.02343.x.

[19] T. Toimela, H. Mäenpää, M. Mannerström, and H. Tähti, "Development of an in vitro blood-brain barrier model - Cytotoxicity of mercury and aluminum," *Toxicol. Appl. Pharmacol.*, vol. 195, no. 1, pp. 73–82, 2004, doi: 10.1016/j.taap.2003.11.002.

[20] V. V. A. Steven M. Singer#, Marc Y. Fink, "乳鼠心肌提取 HHS Public Access," *Physiol. Behav.*, vol. 176, no. 3, pp. 139–148, 2019, doi: 10.1161/STROKEAHA.114.005427.Cell-Culture.

[21] S. Nakagawa *et al.*, "Pericytes from brain microvessels strengthen the barrier integrity in primary cultures of rat brain endothelial cells," *Cell. Mol. Neurobiol.*, vol. 27, no. 6, pp. 687–694, 2007, doi: 10.1007/s10571-007-9195-4.

[22] S. Nakagawa *et al.*, “A new blood-brain barrier model using primary rat brain endothelial cells, pericytes and astrocytes,” *Neurochem. Int.*, vol. 54, no. 3–4, pp. 253–263, 2009, doi: 10.1016/j.neuint.2008.12.002.

[23] Y. He, Y. Yao, S. E. Tsirka, and Y. Cao, “Cell-culture models of the blood-brain barrier,” *Stroke*, vol. 45, no. 8, pp. 2514–2526, 2014, doi: 10.1161/STROKEAHA.114.005427.

[24] L. Cucullo, N. Marchi, M. Hossain, and D. Janigro, “A dynamic in vitro BBB model for the study of immune cell trafficking into the central nervous system,” *J. Cereb. Blood Flow Metab.*, vol. 31, no. 2, pp. 767–777, 2011, doi: 10.1038/jcbfm.2010.162.

[25] E. Tornabene and B. Brodin, “Stroke and Drug Delivery - In Vitro Models of the Ischemic Blood-Brain Barrier,” *J. Pharm. Sci.*, vol. 105, no. 2, pp. 398–405, 2016, doi: 10.1016/j.xphs.2015.11.041.

[26] S. Bagchi, T. Chhibber, B. Lahooti, A. Verma, V. Borse, and R. D. Jayant, “In-vitro blood-brain barrier models for drug screening and permeation studies: An overview,” *Drug Des. Devel. Ther.*, vol. 13, pp. 3591–3605, 2019, doi: 10.2147/DDDT.S218708.

[27] E. Tornabene and B. Brodin, “Stroke and Drug Delivery - In Vitro Models of the Ischemic Blood-Brain Barrier,” *J. Pharm. Sci.*, vol. 105, no. 2, pp. 398–405, 2016, doi: 10.1016/j.xphs.2015.11.041.

[28] T. E. Park *et al.*, “Hypoxia-enhanced Blood-Brain Barrier Chip recapitulates human barrier function and shuttling of drugs and antibodies,” *Nat. Commun.*, vol. 10, no. 1, pp. 1–12, 2019, doi: 10.1038/s41467-019-10588-0.

[29] R. Booth and H. Kim, “Characterization of a microfluidic in vitro model of the blood-brain barrier (μBBB),” *Lab Chip*, vol. 12, no. 10, pp. 1784–1792, 2012, doi: 10.1039/c2lc40094d.

[30] G. Adriani, D. Ma, A. Pavesi, R. D. Kamm, and E. L. K. Goh, “A 3D neurovascular microfluidic model consisting of neurons, astrocytes and cerebral endothelial cells as a blood-brain barrier,” *Lab Chip*, vol. 17, no. 3, pp. 448–459, 2017, doi: 10.1039/c6lc00638h.

[31] A. Herland, A. D. Van Der Meer, E. A. FitzGerald, T. E. Park, J. J. F. Sleeboom, and D. E. Ingber, “Distinct contributions of astrocytes and pericytes to neuroinflammation identified in a 3D human blood-brain barrier on a chip,” *PLoS One*, vol. 11, no. 3, pp. 1–21, 2016, doi: 10.1371/journal.pone.0150360.

[32] M. Campisi, Y. Shin, T. Osaki, C. Hajal, V. Chiono, and R. D. Kamm, “3D self-organized

microvascular model of the human blood-brain barrier with endothelial cells, pericytes and astrocytes," *Biomaterials*, vol. 180, pp. 117–129, 2018, doi: 10.1016/j.biomaterials.2018.07.014.

[33] N. R. Wevers *et al.*, "A perfused human blood-brain barrier on-a-chip for high-throughput assessment of barrier function and antibody transport," *Fluids Barriers CNS*, vol. 15, no. 1, pp. 1–12, 2018, doi: 10.1186/s12987-018-0108-3.

[34] J. G. DeStefano, Z. S. Xu, A. J. Williams, N. Yimam, and P. C. Searson, "Effect of shear stress on iPSC-derived human brain microvascular endothelial cells (dhBMECs)," *Fluids Barriers CNS*, vol. 14, no. 1, pp. 1–15, 2017, doi: 10.1186/s12987-017-0068-z.

[35] N. Weiss, F. Miller, S. Cazaubon, and P. O. Couraud, "The blood-brain barrier in brain homeostasis and neurological diseases," *Biochim. Biophys. Acta - Biomembr.*, vol. 1788, no. 4, pp. 842–857, 2009, doi: 10.1016/j.bbamem.2008.10.022.

[36] N. J. Abbott, "Physiology of the blood-brain barrier and its consequences for drug transport to the brain," *Int. Congr. Ser.*, vol. 1277, pp. 3–18, 2005, doi: 10.1016/j.ics.2005.02.008.

[37] F. Yuan, M. Leunig, D. A. Berk, and R. K. Jain, "Microvascular permeability of albumin in Human Adenocarcinoma in SCID Mice." 1993.

[38] G. Li *et al.*, "Permeability of endothelial and astrocyte cocultures: In vitro Blood-brain barrier models for drug delivery studies," *Ann. Biomed. Eng.*, vol. 38, no. 8, pp. 2499–2511, 2010, doi: 10.1007/s10439-010-0023-5.

[39] K. Benson, S. Cramer, and H. J. Galla, "Impedance-based cell monitoring: Barrier properties and beyond," *Fluids Barriers CNS*, vol. 10, no. 1, pp. 1–11, 2013, doi: 10.1186/2045-8118-10-5.

[40] M. Odijk *et al.*, "Measuring direct current trans-epithelial electrical resistance in organ-on-a-chip microsystems," *Lab Chip*, vol. 15, no. 3, pp. 745–752, 2015, doi: 10.1039/c4lc01219d.

[41] A. Reichel, D. J. Begley, and N. J. Abbott, "for Blood – Brain Barrier Studies," no. April 2015, 2014, doi: 10.1007/978-1-4614-9105-7.

[42] S. Y. Desai *et al.*, "Mechanisms of endothelial survival under shear stress," *Endothel. J. Endothel. Cell Res.*, vol. 9, no. 2, pp. 89–102, 2002, doi: 10.1080/10623320212004.

[43] Y. Son, "Determination of shear viscosity and shear rate from pressure drop and flow rate relationship in a rectangular channel," *Polymer (Guildf).*, vol. 48, no. 2, pp. 632–637, 2007,

doi: 10.1016/j.polymer.2006.11.048.

CHAPTER 3

New lithography strategy for the fabrication of a biocompatible high performing organic electrochemical transistor Parylene C-free.

Organic electrochemical transistors (OECTs) are hybrid ionic/electronic devices capable of high-gain signal amplification useful in numerous applications such as logic circuits, neuromorphic elements, and biosensing platforms. To date there are two techniques used to fabricate these electronic devices: (i) the first one involves the use of photolithography with hydrofluoroether (HFE) solvents and fluorinated photoresists to pattern the conductive polymer channel that is a product solution provided only by Orthogonal Inc; (ii) the second one, instead, involves the use of Parylene-C (PaC) and is considered as the standard fabrication technique since it allows the realization of the most performing OECTs available a the moment [1]. Despite considerable advances in microfluidics, particularly in the organ-on-a-chip technology, there is still a need for tools that can perform real-time multi-parameter monitoring of live cells and be easily combined with a microfluidic system. To address this need, Róisín Owens et al, in 2017 [2] integrated an electronic sensor based on an organic electrochemical transistor (OECT) within a microfluidic device. In their work, as part of OECT fabrication, they use a thin layer of PaC to insulate the gold contact and have a PMMA microfluidic devices irreversible bonded to a PaC-coated glass slide through a pressure sensitive adhesive (PSA) layer. However, in case of PDMS microfluidic devices, the integration of PaC with the PDMS is still an open issue and, it is not possible to achieve permanent bonding by O_2 plasma activation or other methods. The poor adhesion between the two substrates results in leakages and eventually delamination of the PDMS structure from the substrate. To circumvent the PaC/PDMS adhesion problem it has been proposed the use of a medical tape to exploit the adhesive component of the tape but the proposed method is limited from the resolution point of view as it requires the use of a cutting plotter to pattern the tape, which does not allow to realize highly resolved devices [3]. Until now, some strategies have been proposed for the irreversible bonding of PDMS and other plastic substrates

involving surface modification [4], however, it was not possible to achieve stable adhesion of PDMS and PaC using these protocols. Here, we propose a simple and high-resolution patterning method of conductive polymer films, namely PEDOT:PSS, as transparent electrodes for the fabrication of organic devices on glass and silicon substrate. With the technique proposed, we can obtain high performance OECTs, with transconductance and trans characteristic curves comparable with the standard ones. Moreover, we are able to bond the obtained device with PDMS microfluidic devices without leakages, and more reliable patterning approach of PEDOT:PSS in terms of homogeneity. This process results to be a good technique for combining bioelectronics with microfluidics for monitoring *in vitro* tissue or organ on chip.

The Chapter is presented as follows: we first discuss two designs of the OECT and we introduce the fabrication technique. In the second part, we present the characterization of the device focusing on their electrical performance. Last, we compare the results obtained to the theoretical models described in Chapter 1.

Table of contents

CHAPTER 3 76

New lithography strategy for the fabrication of a biocompatible high performing organic electrochemical transistor Parylene C-free. 76

3.1 OECT: Design and fabrication 79

3.1.1. Design 80

3.1.2. Fabrication 81

3. 2 Experimental characterizations 84

3.2.1 Morphological characterization 85

3.2.2 Cyclic Voltammetry 86

3.2.3 Cell culture and biocompatibility assay 87

3.3 Electrical characterization 88

3.3.1 Output and Transfer Curve and Transconductance measurement 88

3.3.2 Comparison with theoretical model 92

3.3.3 Statistical analysis of reproducibility 96

3.3.4 Measurement of the potential along the channel 99

3. 4 Microfluidic applications 102

3.4.1 Biocompatibility assay 102

3.4.2 Microfluidic device embedded with OECT 103

3. 5 Conclusion 104

3.1 OECT: Design and fabrication

OECTs are based on the principle of electrochemical gating, which employs a conducting polymer film in contact with a gate electrode via an electrolyte. The application of a gate voltage induces a reversible redistribution of ions within the electrolyte. Some of these ions enter the polymer film, and the resulting electrochemical doping/de-doping leads to a modulation in the current that flows between the source and drain electrodes. The working mechanism of OECTs requires the conducting polymer to be electrochemically active and ion permeable [5]. The device structure of OECTs resembles that of organic electrical double layer transistors [6], which also exploit gating through an electrolyte. However, in electrical double layer transistors, the ions do not enter the polymer layer, and the operation of these devices relies on a field effect rather than on electrochemical doping/de-doping.

A unique feature of OECTs, associated with electrochemical gating, is that the gate electrode does not need to be positioned at a small distance from the channel [7]. This allows planar device architectures in which the area, shape, and relative position of the channel and gate electrode can be varied independently. In particular, in order to increase the sensitivity of the device, the surface of the gate needs to be bigger than the one of the channel [7]. Another important aspect of OECTs is the relation between the transconductance and the geometrical properties of the transistors. Several authors, in fact, have shown that OECT transconductance is directly proportional to the ratio Wd/L, in which W is the width of the channel, d is the thickness of the polymer layer and L is the length of the channel. The fact that transconductance scales with thickness, and not just W/L distinguishes OECTs from FETs. This distinction arises because field-effect doping only modulates carrier density at the semiconductor-insulator interface [8], whereas electrochemical doping modulates carrier density throughout the bulk of the semiconductor. This bulk doping effect leads to the proportionality $g_m \sim d$, where g_m being the transconductance of the OECT allows engineers to design high transconductance OECTs without expanding the W (width) of the devices. In conclusion, the geometrical properties that need to be considered when designing OECTs are:

- The ratio between the area of the channel and the one of the gate, which needs to be bigger than 1 to increase sensitivity ($A_c/A_g<1$) [7].
- The thickness of PEDOT:PSS layer which affects the transconductance of the device and needs to be tuned according to desired application [9].

3.1.1. Design

We consider two different designs for this work. The first one (Sample1) consists in a standard three-terminal device while the second one (Sample2) is a seven-terminal device. The choice for the realization of Sample2 is motivated by the fact that in order to perform a better characterization of the device, a measurement of the potential along the channel is needed. This allows us to compare our experimental results to the theoretical models described in literature and presented in Chapter 1.

Sample1

Sample1 consists in three terminal devices (Figure 3.1). We decided to realize a device with a thickness of 100 nm, width of 270 µm and length of the channel of 750 µm and a gate with width of 450 µm and length of 1000 µm and the same thickness. The gate in PEDOT:PSS is designed so to have an area larger than channel area ($A_c/A_g<1$), such that, the electrolyte is at the same potential of the gate, as it typically happens in transistors with big gates. Therefore, the potential drop between the electrolyte and the channel is large and, in turn, this leads to a strong modulation of the drain current.

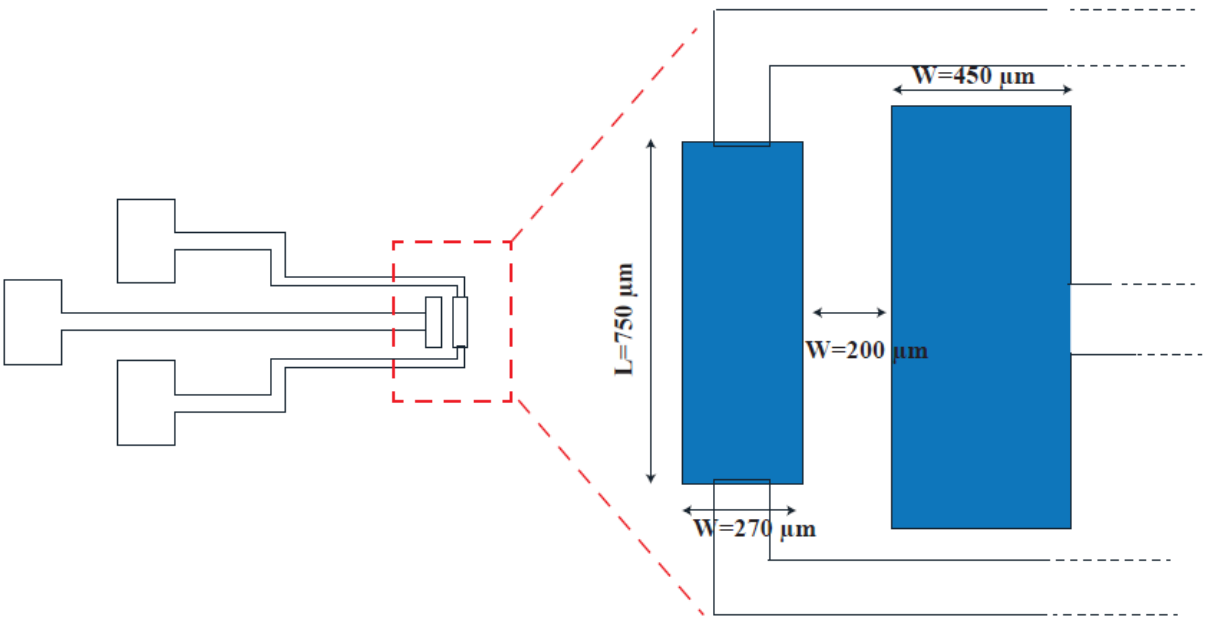

Figure 3.1 Schematic representation of the Sample1 OECT. In blue is designed the channel and the gate made of PEDOT: PSS, while the lines represent the gold contacts. In particular, the channel (the smallest in blue) has a length L=250 µm and a width W=270 µm, while for the gate L=1000 µm and W=450 µm.

Sample2

The Sample2 consists in seven terminal devices (Figure 3.2) and, as for Sample1, the gate (1284 µm x 320 µm) is designed to be larger than the channel (284 µm x 1284 µm). The thickness of the PEDOT:PSS layer is 100 nm. The larger size of the device allowed us to put different pads along the channel with an interspace of 150 µm.

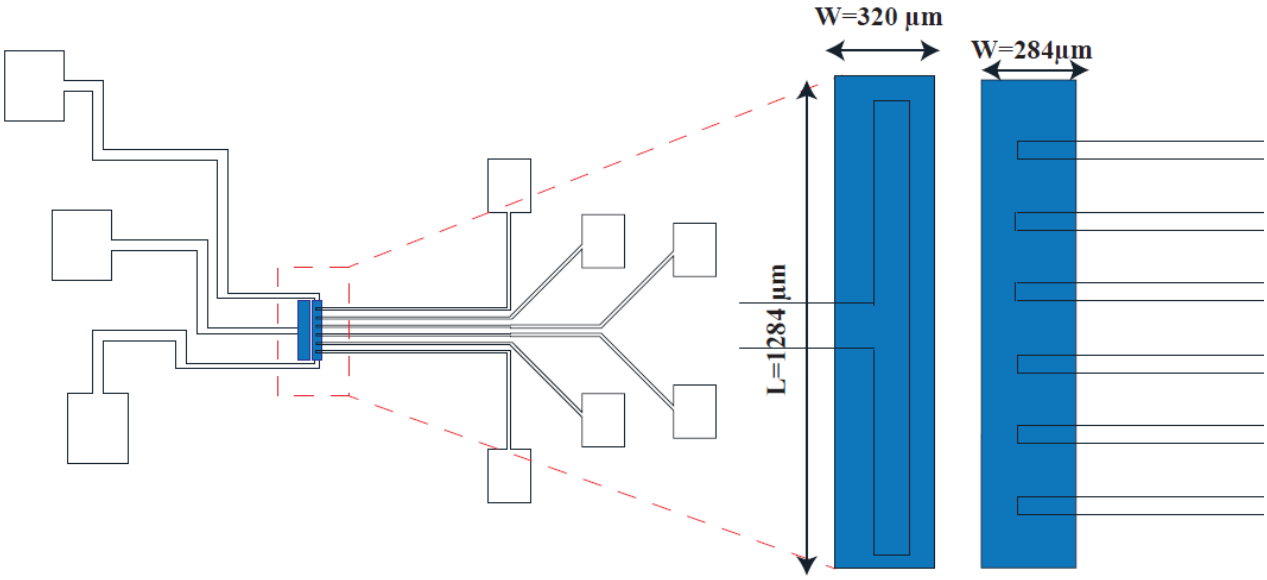

Figure 3.2 Schematic representation of the Sample2 OECT. In blue is designed the channel and the gate made of PEDOT: PSS, while the lines represent the gold contacts. Both the length of the gate and the channel is L=1284 µm while the width of the gate is 320 µm while the one of the channel is W=284 µm.

3.1.2. Fabrication

We now describe in detail all the steps of the fabrication process that are summarized schematically in Figure 3.3.

On a clean glass substrate (30 mm in radius), we patterned gold source and drain contacts via photolithography, thermal evaporation, and subsequent lift-off. For the photolithography, performed with Laser 2D Heidelberg, we used photoresist AZ1505 (MicroChem Corp.) spin-coated at 2000 rpm for 30 s (Figura 3.3a). The samples were developed using AZ 351 B (1:4 v/v) (Figure 3.3b) and then, 5 nm and 100 nm of chromium and gold respectively, were evaporated (Figure 3.3c). Finally, the photoresist was lifted-off in an acetone bath under sonication for 10 min, which left the substrate with the source and drain Au contacts only (Figure 3.3d). PEDOT:PSS (Heraeus, Clevios PH 1000), with ethylene glycol (Sigma–Aldrich, 0.25 mL for 1 mL PEDOT:PSS solution), 4,dodecylbenzenesulfonic acid (DBSA) (0.5 µL/mL) and 3-glycidoxypropyltrimethoxysilane (GOPS) (10 mg/mL) was spin

coated at 1000 rpm for 60 s, in order to obtain a thickness of 100 nm (Figure 3.3e). Polymer channels were patterned using a copper mask layer. Briefly, 150 nm of copper were evaporated (Figure 3.3f), and the patterns for the channel and for the gate were defined again by photolithography, following a very precise process of alignment (Figure 3.3g). In this case, we used a negative photoresist AZ 125 nXT with the same developer used before (Figure 3.3h). At this point, Cu was removed using a slightly modified Cu etchant, based on a method described by Ouyang et al. [10]. The etchant used consisted of fuming nitric acid, phosphoric acid (90 wt%), glacial acetic acid (99.8 wt%) and de-ionized water in a ratio of 1:18:18:1 by volume. The duration of the 150 nm Cu etching was 36 s at room temperature until the full metal removal yielded the substrate patterned with a highly conductive PEDOT:PSS (Figure 3.3i). Next, in order to remove exposed and unprotected PEDOT:PSS, reactive ion etching was performed at 100 W for 8 min (Figure 3.3j). In the final steps of the process, we first completely removed the photoresist from the channel and the gate (Figure 3.3k) and then we removed the copper that served as a protective layer (Figure 3.3l). The substrate was washed using isopropanol, water and followed by nitrogen blow-drying as the final step.

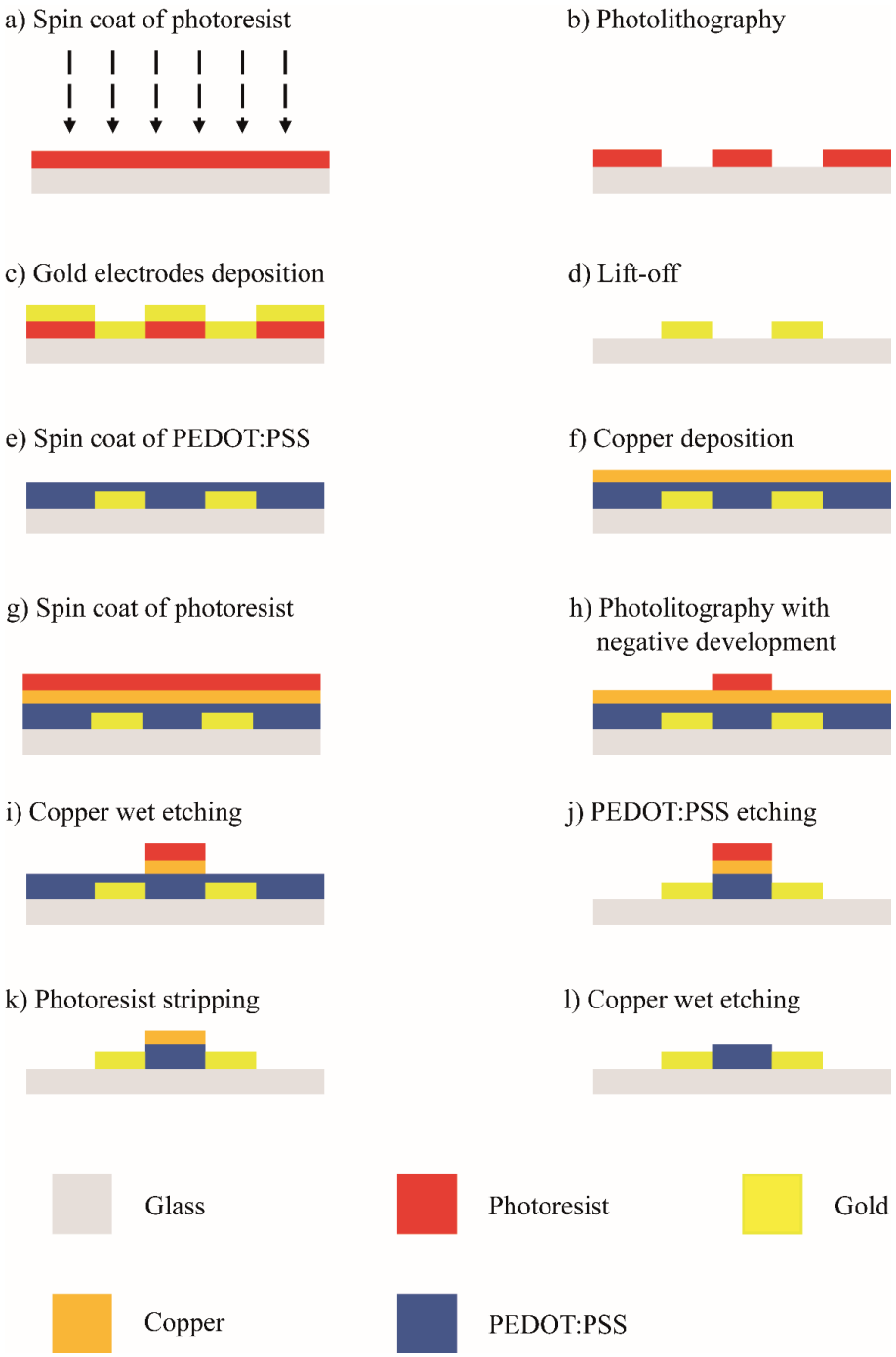

Figure 3.3 Process for photolithographic patterning of PEDOT:PSS with a copper interlayer. The patterning of gold contacts is realized following the steps from a to d. Following that, PEDOT:PSS is spin coated (e), the copper interlayer deposited and patterned(f to h). Finally the protective copper layer and the PEDOT:PSS are etched (i to l).

In Figure 3.4, we show the most delicate steps of fabrication for both Samples. In particular, in Figure 3.4a and 3.4d we show an optical picture of the two samples after the patterning of the copper. Figure 3.4 b and 3.4e shows the same samples after the etching of the PEDOT in the areas outside the channel and the gate. Finally in Figure 3.4c and 3.4f we show the final samples, in which channel and gate are in PEDOT:PSS, the contacts in gold and the passivation is made by a layer of photoresist left (step

k) in Figure 3.3 to prevent the electrolyte form coming in contact with the source and drain creating a further capacitive effect.

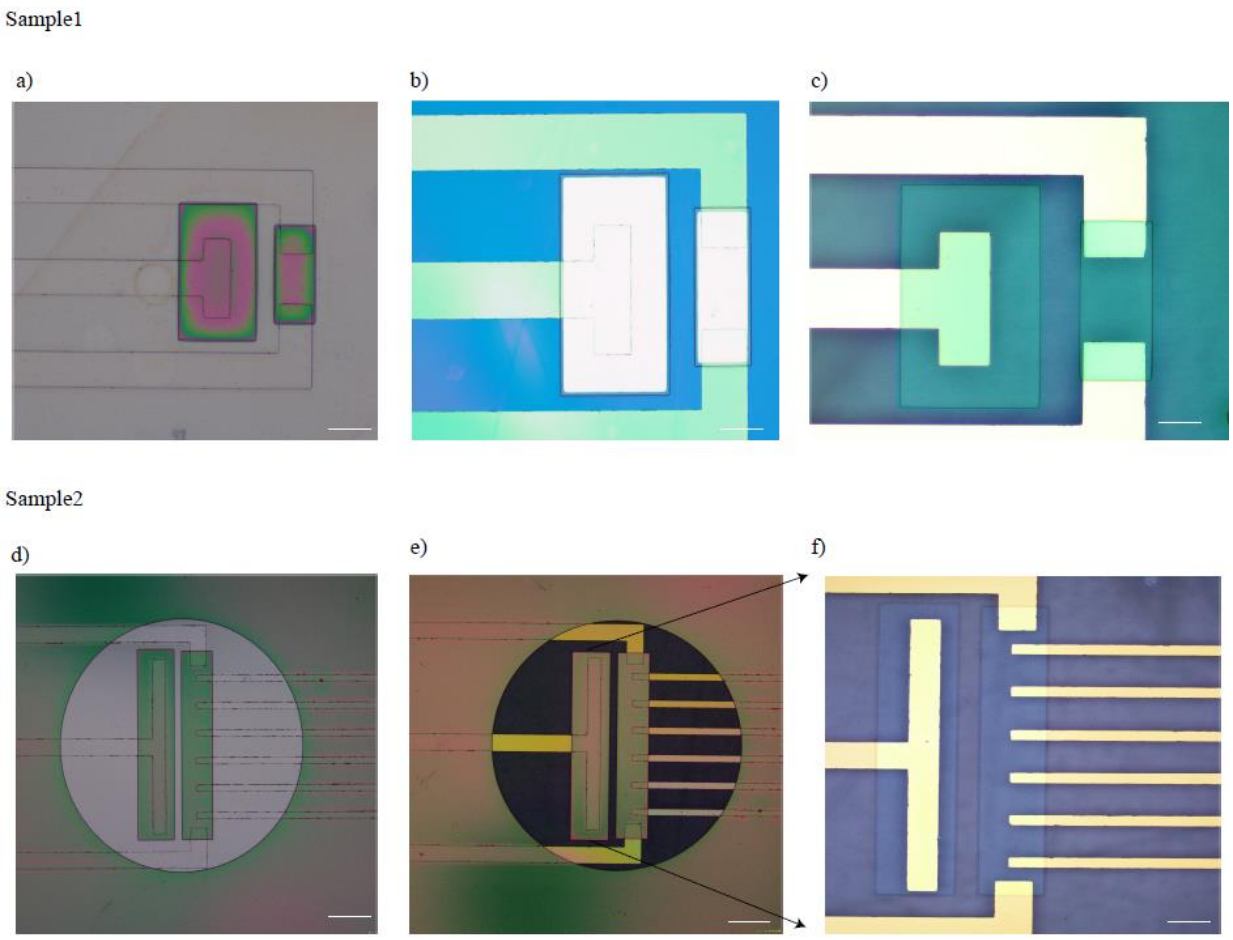

Figure 3.4 Illustration of different step in the fabrication of Sample 1 and Sample 2. *In particular:* 4 a-d show the pattern of the copper layer. Figure 4 b-e show the etching of the PEDOT in the areas outside the channel and the gate, and Figure 4 c-f show the final sample, in which channel and gate are in PEDOT:PSS *(color blue in the images).* Scale bar 100 µm.

3. 2 Experimental characterizations

In this section we discuss the experimental characterization of the fabricated devices. We first investigate the morphology of the PEDOT:PSS after the etching process by performing an AFM analysis as suggested in [10]. We then focus on the cyclic voltammetry in order to verify that no changing in doping and dedoping polymer (PEDOT:PSS) occurs after etching treatment. And we then discuss biocompatibility with cells, showing that this fabrication technique can be applied for devices that are used for cells sensing.

3.2.1 Morphological characterization

The influence of acid treatment used during the fabrication process was carefully investigated. In order to verify if the copper interlay was completely removed from the substrate, we decided to perform an absorbance spectra analysis. Since copper is sensitive to the absorption of visible light, the transmission spectrum can be used to investigate the copper residuals on the PEDOT:PSS surface. Fresh PEDOT:PSS films with thickness of 100 nm and patterned PEDOT:PSS films with same thickness were investigated, as shown in Figure 3.5. Their transmittance spectra were nearly identical. No apparent absorption was observed coming from potential existence of residual copper on PEDOT:PSS films. This analysis confirms that through immersion in the copper etchant, copper mask can be fully removed. This analysis was performed on three different samples for Sample1 and three for Sample2.

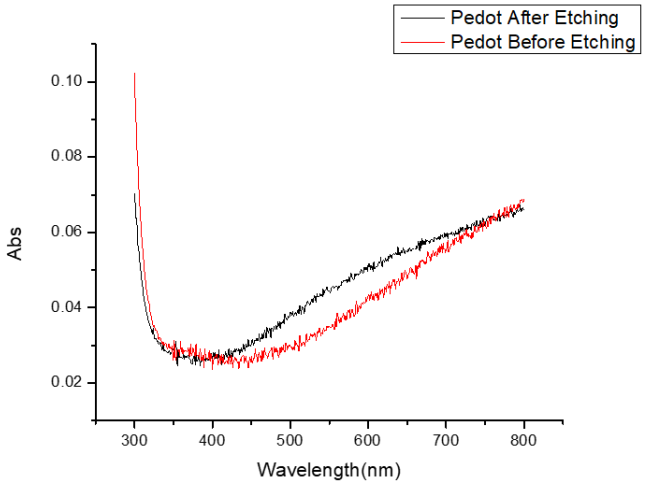

Figure 3.5 Absorbance spectra of pristine and acid treated PEDOT: PSS films on glass: Black line denotes pristine PEDOT: PSS (100 nm) and red lines denotes 15 s etching time (105 nm). No apparent absorption is observed that confirms that through immersion in the copper etchant all the copper layer is successfully removed. Analysis performed on three different samples of Sample1 and three different sample of Sample2.

The PEDOT:PSS structure is characterized by highly conductive and hydrophobic PEDOT rich core which are surrounded by insulating and hydrophilic PSS rich shell grains [11]. To study the morphology of the PEDOT:PSS layer used for OECT, an AFM analysis was performed [12]. Figure 3.6a shows the surface of PEDOT:PSS before the etching process while Figure 3.6b shows the same surface once the etching is applied. In term of roughness the untreated PEDOT:PSS showed a roughness of 31±2.01 nm instead the treated one 28 ±1.8 nm. This difference, obtained by examining 10 treated and 10 untreated samples, is minimal but it results compatible with those of the article [10]

from which the measurement is taken, and it means that with this procedure we do not change surface morphology of the conductive polymers, so the acid treatment is safe for the PEDOT:PSS.

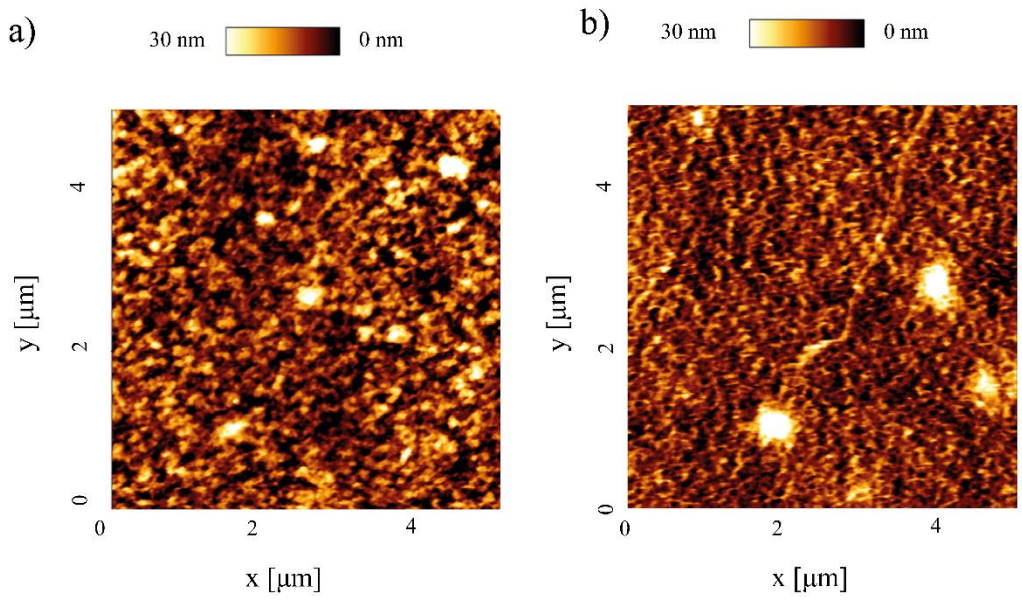

Figure 3.6 AFM images of PEDOT: PSS before (a) and after etching (b). Roughness of the untreated PEDOT:PSS results of approximately 31± 2.01 nm (a), while the treated one is close to 28 ±1.8 nm (b). No changing in the morphology is visible, so the treatment is safe for the conductive layer of PEDOT:PSS, according to what has already been reported in the literature [10].

3.2.2 Cyclic Voltammetry

Cyclic voltammetry (CV) is a common technique to measure the charge/discharge process of PEDOT:PSS. It consists in measuring the current, flowing in the material under study, at a given potential and set scan rate (mV s− 1). During oxidation or reduction, ions move in and out of the PEDOT:PSS layers, and current is being measured at the electrode through transduction [13]. During the repeated charge/discharge process, the film undergoes volume change (swelling, shrinkage, cracking) as a result of dopant entering and leaving of the film. Thus, the ability of the film to withstand repeated charge-discharge cycle without degeneration in the CV profile and the mechanical integrity of the film are indicators of the film's ability to withstand prolonged measurements in aqueous media [14]. Besides adhesion of the PEDOT:PSS film to the electrode surface and the charge/discharge cycles, it is important to note that the morphology of PEDOT:PSS at the nanometer scale has a significant effect electrochemically. Figure 3.7 shows the cyclic voltammograms (CV) obtained for pristine as well as etched PEDOT: PSS substrates. The data were acquired from the sample treated with the highest tested potentials, V = 1V (oxidized) and V = -1 V (reduced). Oxidation

peaks appeared at around 0.75 V corresponding to monomer oxidation leading to cation radical formation [15]. The oxidized waves were less defined which probably was due to a high electrical resistance [16]. In this case, diffusion was not the limiting step of the electrochemical processes and thus that the whole film thickness was involved in the electrochemical reaction. Therefore, the charge flowing during the CV scans corresponded to the electrons that were needed to change the redox state of the whole PEDOT:PSS volume. Since the oxidation potential did not change substantially it could be concluded that the electronic structure of PEDOT was not changed after treatment with acid. The different current values observed for two voltammograms might be due to different amounts of two samples used for voltammetry.

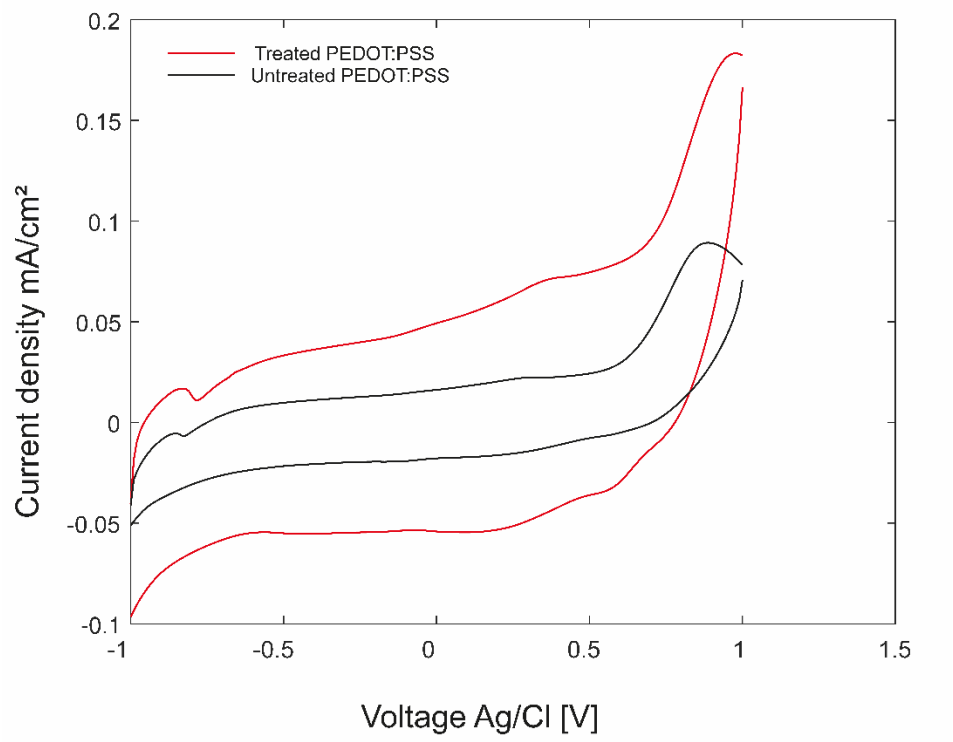

Figure 3.7 Cyclic voltammograms recorded for PRISTINE or Untreated and Treated PEDOT: PSS. (Scan rate = 50 mV/s). The PEDOT:PSS Treated (red line) exhibited around 0.93 times higher current response than that of untreated one (black line), and the current density is 2 times superior than the pristine. The oxidation potential did not change, in fact for both the case it appears at 0.75 V, so it could be concluded that the electronic structure of PEDOT was not changed after treatment with acid.

3.2.3 Cell culture and biocompatibility assay

Here we introduce the cells choosen to test biocompatibility and the method used to perform the analysis for the cells. We want to verify that this treatment does not release substances harmful to the cells which can therefore modify their morphology and induce differentiation.

Cell culture.

BEND3 (Brain endothelial cells) cells were cultured in DMEM medium (Sigma-Aldrich) supplemented with 10% of fetal bovine serum (specific for HL-1 cell line, Merck Millipore), 1% of penicillin-streptomycin (10 000 U mL^{-1}, Sigma-Aldrich), 1% of GlutaMAX (Thermo Fisher Scientific). Cells were gently seeded on each substrate at a density of 30 000 cells cm^{-2} and incubated at 37 °C with 5% CO_2.

Cytotoxicity assay

Cytotoxicity was evaluated after 1 DIV by fluorescently labeling alive and dead cells with Calcein-AM (Thermo Fisher Scientific) and propidium iodide (Thermo Fisher Scientific), respectively. Cells plated on to Si/SiO_2 substrate were set as negative control. The staining solution (1 µg mL^{-1} for Calcein AM and 10 µg mL^{-1} for propidium iodide) was added to cell media and incubated for 10 min. Samples were then rinsed in phosphate-buffered saline (PBS) and mounted on glass coverslip for imaging. Images were collected with epifluorescence microscope (Axio Observer Z1, Zeiss) using Planar Apocromat 20× 0.8 dry objective. % Viability quantification (n = 3) was evaluated using the following formula

$$\%\ Viability = \frac{Live\ Cells}{Live\ cells + Dead\ cells} \times 100$$

3.3 Electrical characterization

In the following paragraph we examine the electrical characteristics of the OECTs manufactured with the mentioned technique, in order to identify their main characteristics and verify their correct functioning.

3.3.1 Output and Transfer Curve and Transconductance measurement

OECTs have proven to exhibit the highest transconductance (g_m) among electrolyte gated transistors of comparable geometry [9]. It is defined as $g_m = \frac{\partial I_{DS}}{\partial V_{GS}}$. Transconductance is the figure of merit for biosensing applications as it sensitively quantifies the current flowing in the channel (I_{DS}, drain

current), in response to a change (V_{GS}, gate voltage), and is thus a measure of the "efficiency" of transduction of a biological event.

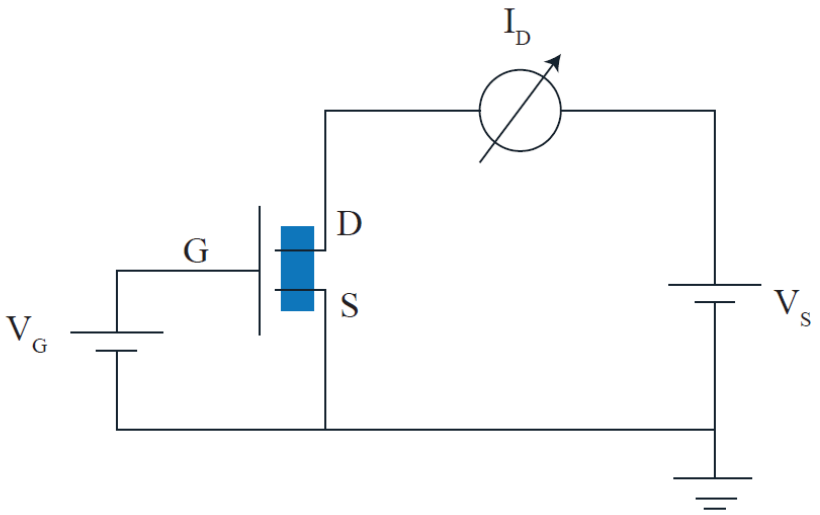

Figure 3.8 Experimental set-up used to characterize the three-terminal device.

Using a commercial apparatus (Arkeo-Ariadne, Cicci research s.r.l) based on a double channel source meter, whose scheme is shown in Figure 8, we measured the variation of the drain current as function of the drain voltage for Sample1 and Sample2. The gate voltage ranged between 0 mV and 1 V (Figure 3.9). The output curves showed in Figure 3.9, are for Sample1 and Sample2. It can be noticed that, by applying a negative bias between source and drain, holes act as charge carrier and by increasing V_{DS}, current increases till it reaches a maximum and then saturates. This saturation is more evident at higher V_{GS}. This behavior is typical for a depletion mode transistor normally ON. When the gate voltage is equal to 0 V (first curve in blue from the top) the OECTs behave like a linear resistor, since the corresponding curve is a straight line, with a constant slope and therefore a constant conductance (or equivalently a constant resistance). This is because, according to the trans-characteristic curve, the OECT is deeply in the ON state at this gate voltage, independently from the drain voltage applied. By applying positive voltage to the gate electrode, cations from electrolyte enter the channel, compensate hole and therefore reduce the current I_{DS}. It is observed from Figure 3.9, that for the same value of $V_{GS,}$ the Sample2 tends to turn off faster than Sample1.

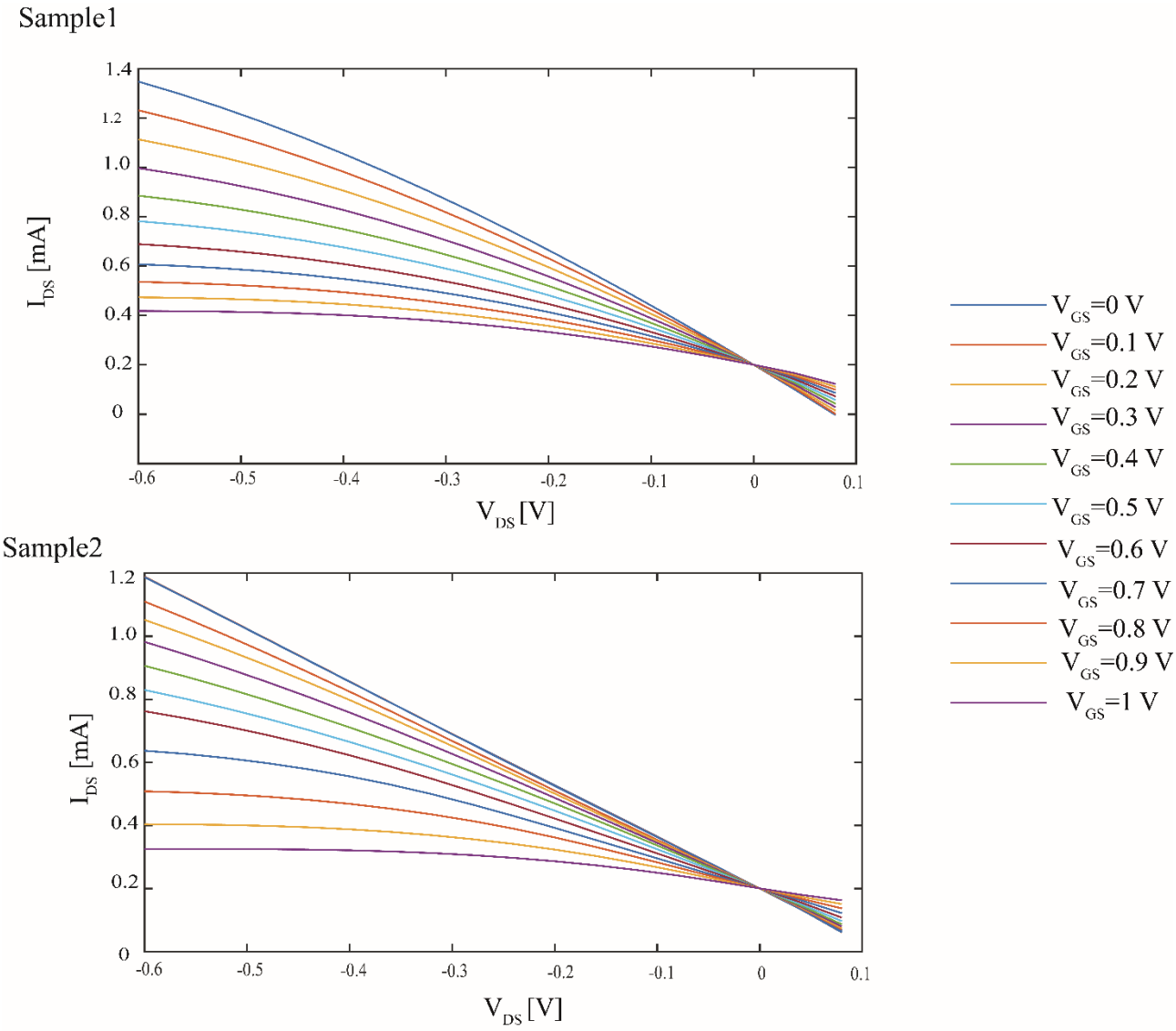

Figure 3.9 Output Characteristics for Sample1 and Sample2 for different value of V_{GS}. In depletion mode, under the application of a positive gate voltage (V_{GS}) cations penetrate the polymer, dedoping the channel and switching the transistor to its "off" state. The blue lines represent the "maximum" value of current for Sample1 and Sample2, while the violet ones the "off" state.

Since the transconductance, is indicative of the efficiency of the transistor in transducing electrical signals into biological information, we perform electrical analysis in order to evaluate transfer characteristics, shown in Figure 3.10 a-c and more interesting the value of g_m calculated using $g_m = \frac{\partial I_{DS}}{\partial V_{GS}}$, shown in Figure 3.10 b-d. for two distinct values of V_{DS}. The electrical measurements are made for Sample1 and for Sample2 geometries, evaluating the results for three devices different, reporting only one for simplicity of observation. The statistical analysis are reported in the paragraph 3.3.3. Transfer curves of OECT Figure 3.10 a-c show that increasing drain voltage from 0 V to -0.8 V, the current between source and drain shifted to larger values. However, by decreasing V_{DS} more and more, the amount of change in current decreased. Also, by increasing gate voltage, OECT tends to turn "OFF" as the charge carrier concentration is decreased. Therefore, increasing gate bias more and

more, I_{DS} will not change. Transconductance relates to change in source-drain current with V_{GS} and its curve in Figure 3.10b-d shows typical transistor behavior for both the samples. By increasing gate voltage, transconductance reaches a maximum and above certain limit, transistor tend to turn OFF. Here, the above mentioned Sample1, reaches its maximum transconductance (0.7 mS) at V_G=0.2V and V_D=-0.8V while for Sample2 at the same value for V_G=0.2V and V_D=-0.8V the maximum value for transconductance is 1 mS. This behavior is extremely important as it tells us that OECT's transconductance value depends on gate electrode and channel geometry. By changing device geometry one can tune transconductance and reach a maximum transconductance value at low gate voltage.

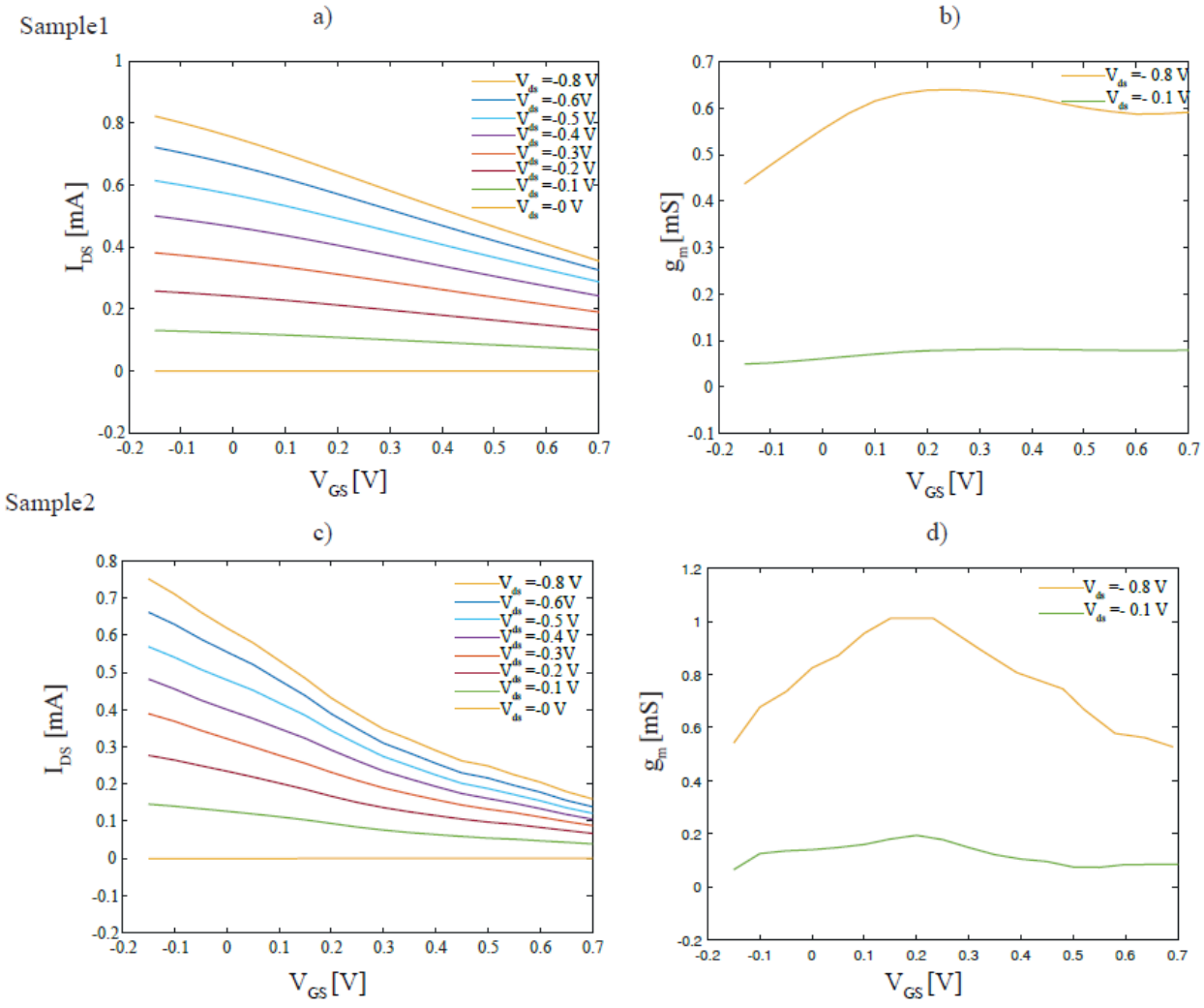

Figure 3.10 Transfer curve and Transconductance for Sample1and Sample2. Transfer curve (a-c) for V_{DS} changing from 0 (bottom curve) to -0.8 V (top curve) and OECT transconductance (b-d) for V_{DS} of -0.8 V (top curve) and -0.1V (bottom curve) of the 2 OECTs in depletion mode.

This value of transconductance of OECT makes them good candidate for biosensing applications [17] where, small change in gate voltage cause large change in current. We know that, by changing

geometry, or thickness of conducting layer [7], it is possible to increase or reduce the performance of the OECT. The OECTs, fabricated with this procedure, show a good performance that can be tuned to achieve different working regimes depending on the applications. In this part of the work, we are not interested in obtaining the best performance for the OECT, but we want to show that with the proposed photolithography pattern with sacrificial layer, we are able to realize a sensor embeddable in the standard PDMS microfluidic device, maintaining all the characteristics that make it a goos biological transductor.

3.3.2 Comparison with theoretical model

Modelling of OECT is an important instrument that allows us not only to understand the device working principle, but also to model its performance. There exist several OECT models with different degree of complexity, each of them looking at OECT from its own perspective. In the next paragraph we apply the models previously discussed in Chapter 1 to our experimental data, to demonstrate the success of our fabrication technique, and to better understand the physical principles of our OECTs and predict the behavior of the OECT that we will use in Chapter 4.

We begin the analysis starting with the Bernards and Malliaras model[18] (equation 1.10), which we report only for ease of observation:

$$I = q\mu\rho_0 WTL\left[1 - (V_g - V_{th} - \frac{V_d}{2})V_p\right]V_d \tag{3.1}$$

We used this equation to fit the data showed in Figure 3.9. The data, together with the corresponding fit are reported in Figure 3.11.

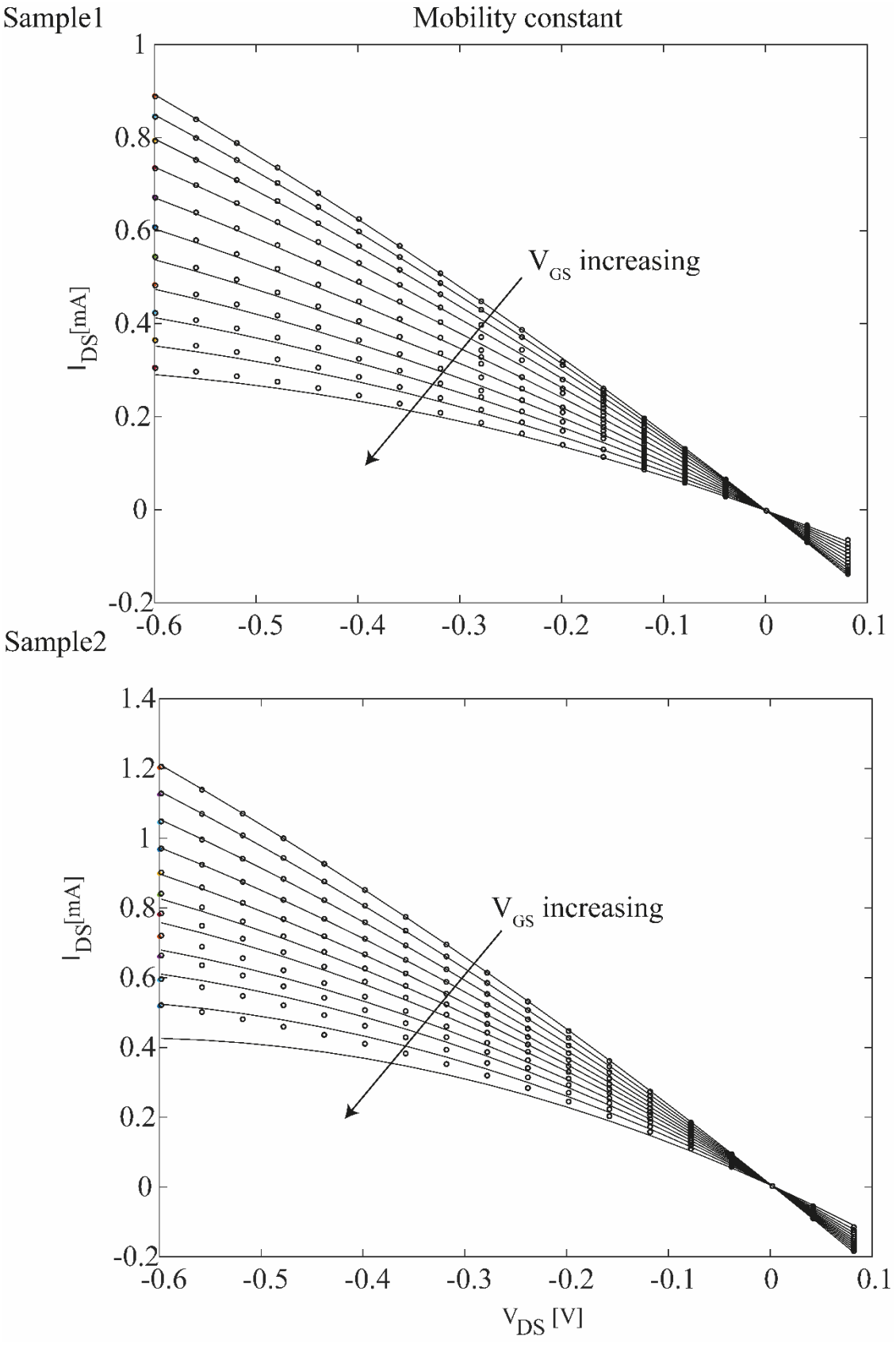

Figure 3.11 Data fit of Output curve for Sample 1 and Sample2 with B&M model [18], assuming constant mobility. The dots show the measurement from Arkeo Set-up while the lines stay for the fit. V_{GS} increases from 0 to 1 [V]. According to the results, considering electron mobility constant, we see that only for few values of V_{GS} the data and fit correspond.

The fit formula provides two parameters: the pinch-off voltage $V_P = \frac{qp_0}{c_G}$ and the material conductance $G = \frac{q\mu_0\rho_0 WT}{L}$. From our measurements shown in Figure 3.11a, the fit yielded G~0.0015 mS and Vp~0.78 V for Sample1 while G~0.0016 S and Vp~0.7315V for Sample2. The model proposed by Bernards and Malliares [18] is based on the limiting assumption of constant electron mobility within the polymer film. In 2015, Friedelin et al. [19], after performing optical measurements on the properties of OECTs, extended the B&M model to the case of non-constant mobility. We fit the same data of Figure 3.8 with the formula that we report for simplicity.

$$I_{DS} = p_0 e\mu_0 \frac{WT}{L} \frac{V_P}{\frac{E_0}{k_B T} + 1} \left\{ \left[1 - \frac{V_{GS} - V_{DS}}{V_P} \right]^{\frac{E_0}{k_B T}+1} - \left[1 - \frac{V_{GS}}{V_P} \right]^{\frac{E_0}{k_B T}+1} \right\} \tag{3.2}$$

The substantial difference between the two models is in the term $\frac{E_0}{k_B T}$, . The fit is showed in Figure 3.12.

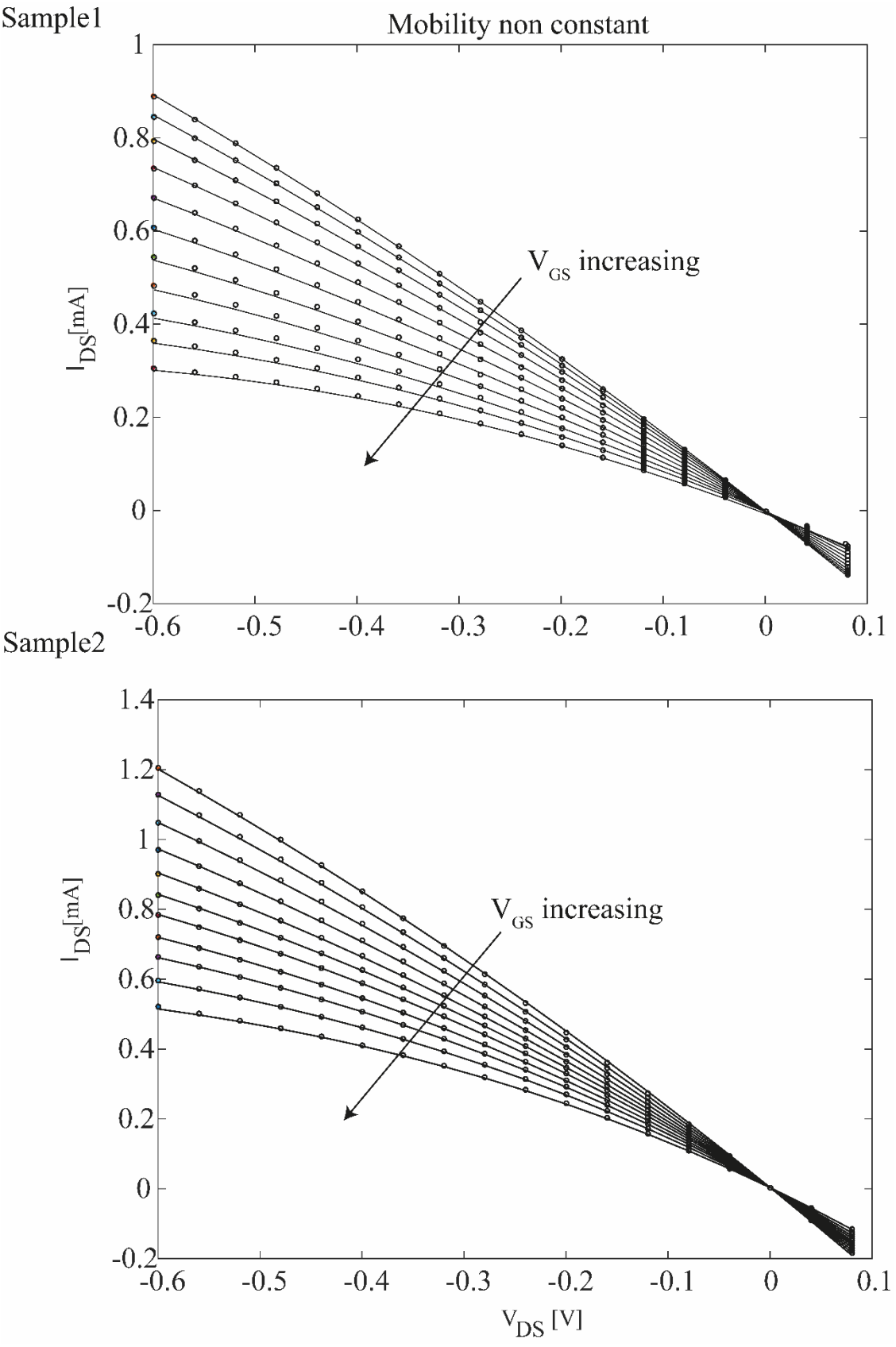

Figure 3.12 Data fit of Output curve for Sample 1 and Sample2 with Friedelin model [19], assuming non constant mobility. The dots show the measurement from Arkeo Set-up while the lines stay for the fit. V_{GS} increases from 0 to 1 [V]. According to the results, considering electron mobility non constant, we see a better overlap between measurements and mathematical model.

Also, in this case the free parameters of the fit are Vp and G. The values extracted by the second model were G= 0.0030 S and Vp~1.6 V for Sample1 while G=0.0021 S and Vp~1.59V for Sample2. While the G term, does not undergo excessive changes from the change from constant to non-constant mobility, the pinch off voltage, increases considerably. This discrepancy has significant implications for the use of OECTs as biosensors. We have already seen how transconductance increases monotonically as the drain voltage decreases, up to the saturation voltage. Because many OECT-based sensing platforms use a fixed drain voltage, the optimal V_D is chosen such that it maximizes the signal to noise ratio (SNR). Setting the drain voltage at V_D=$V_{D,sat}$ maximizes the transconductance while minimizing bias stress on the device and damage to any biological systems being measured [18]. Because $V_{D,sat} = V_G - V_P$, an underestimate of V_P translates to an underestimate of $|V_{D,sat}|$ (for $V_P > V_G$) and leads to suboptimal transconductance. Comparing the two models we see that the assumption of constant mobility, given by Bernards–Malliaras model can lead an underestimation of V_p and to a suboptimal transconductance.

3.3.3 Statistical analysis of reproducibility

In this paragraph we discuss the reproducibility and homogeneity of our fabrication technique. To verify it, we fabricated 12 identical transistors having the design of Sample1 and we measured their electrical properties as discussed in section 3.3.1. The measured devices were fabricated on 4 different batches (3 transistors per batch) and under the same conditions (see section 3.1.2).

We started the analysis by comparing the output transfer curve of the devices that we report in Figure 3.13 for 5 samples and 3 different values of gate voltage.

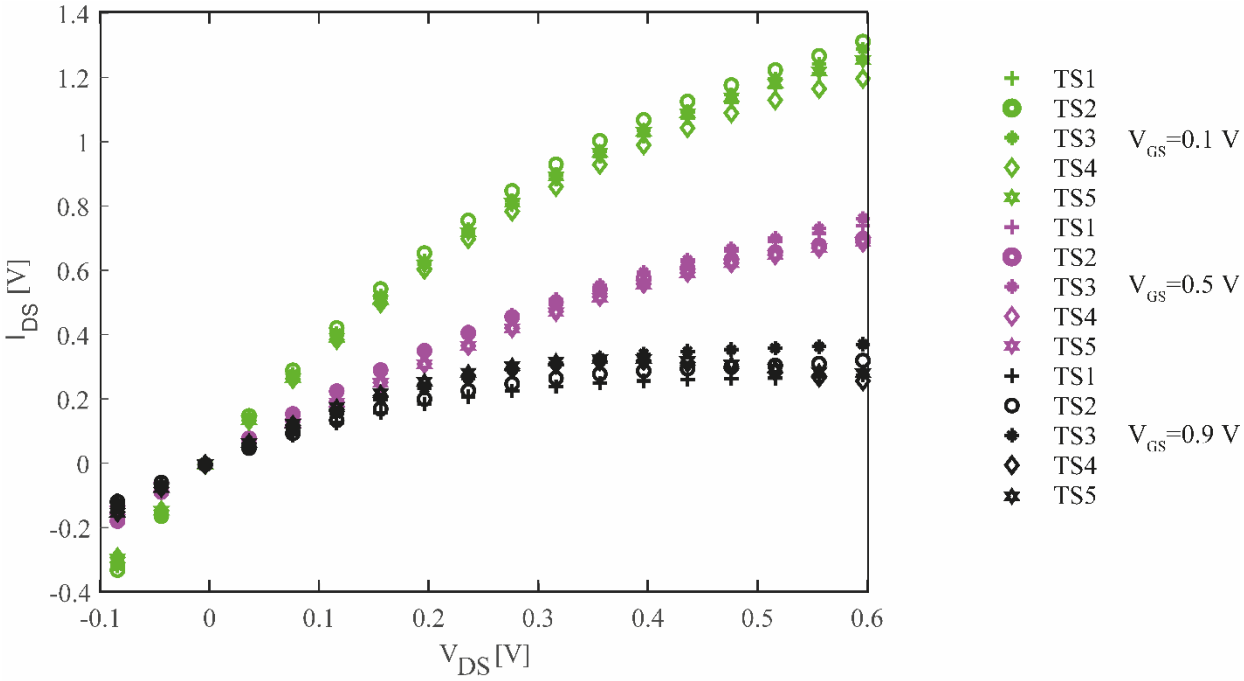

Figure 3.13 Output Transfer Curve at V_{DS} = −0.1:0.6 V and V_{GS} = 0.1 to 0.9 V statistical analysis. We report only the values for 5 of the 12-transistor measured. Here we show the overlap of the measurements for different device as an indicator of the homogeneity of OECTs fabricated with the technique here proposed.

In green we report the current of 5 transistors, for V_{GS}=0.1V, in magenta for V_{GS}=0.5 V and in black for V_{GS}=0.9 V. The overlap of the measurement of the different OECTs is an indicator of the good reproducibility we can achieve using the presented fabrication technique.

In Figure 3.14, we show the average output curve obtained by averaging the measurement of the 12 devices. The error bars correspond to the standard deviation of the data. This confirms the good reproducibility achieved.

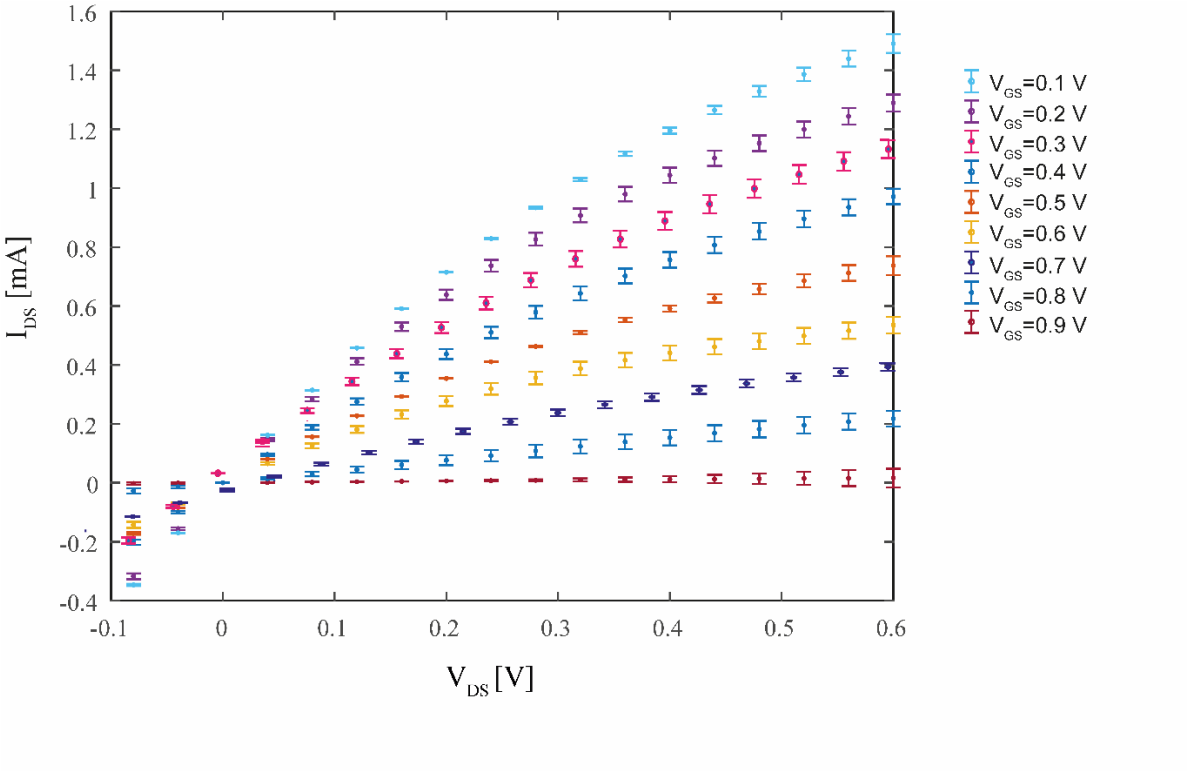

Figure 3.14 Mean Output Transfer Curve at V_{DS} = −0.1:0.6 V and V_{GS} = 0.1 to 0.9 V. The data are obtained by averaging the measurement of the 12 devices (belonging to 4 difference batches) while the error bars correspond to the standard deviation. The small deviation is an indicator of the device homogeneity of OECTs fabricated with the technique here proposed.

Moreover, as transconductance is one of the key parameters of OECTs, since it indicates the sensitivity of the sensor, we report, also statistical analysis of these parameters for the different transistors. In Figure 3.15a, we show the transconductance, calculated as discussed in 3.3.1, for 4 transistors. The g_m is evaluated for V_{DS}= -0.3, -0.1 and 0 V and for V_{GS} ranging from -0.3 to 0.6 V. The highest value is around 700 µS, and is given for V_{DS}= -0.3 V. In Figure 3.15 b a statistical analysis for the 15 devices is shown.

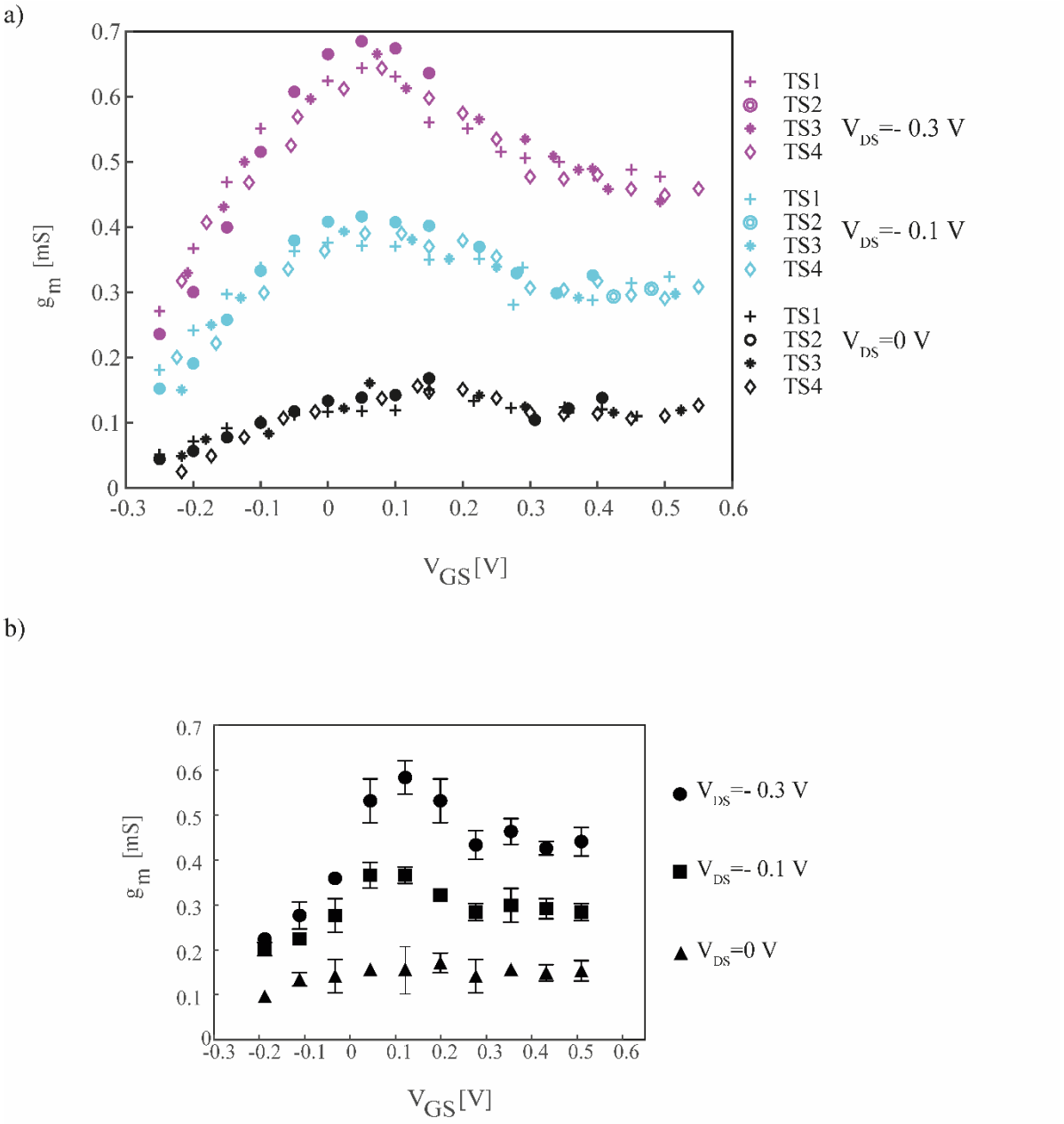

Figure 3.15 Mean Transconductance. (a) Transconductance value at V_{DS} = −0.3, -0.1 and 0 V and V_{GS} = -0.3 to 0.6 V. For simplicity we show in (a) the values for 4 TS fabricated on the glass on 4 different batches. Then, in (b) we show data analysis at same bias point for 15 devices. The data points correspond to the mean transconductance while the error bars are the standard deviation of the data.

3.3.4 Measurement of the potential along the channel

Once verified that our transistors fit suitably the theoretical models of literature and that they are highly reproducible, in order to extract additional information, we proceeded to measure the potential Φ(x) along the channel of our transistor. For this type of measurement, we referred only to Sample2, whose geometry was chosen to allow the addition of 6 probes along the channel, for the purpose to

evaluate the potential at different position x as we shown in the section fabrication and design in Figure 3.2.

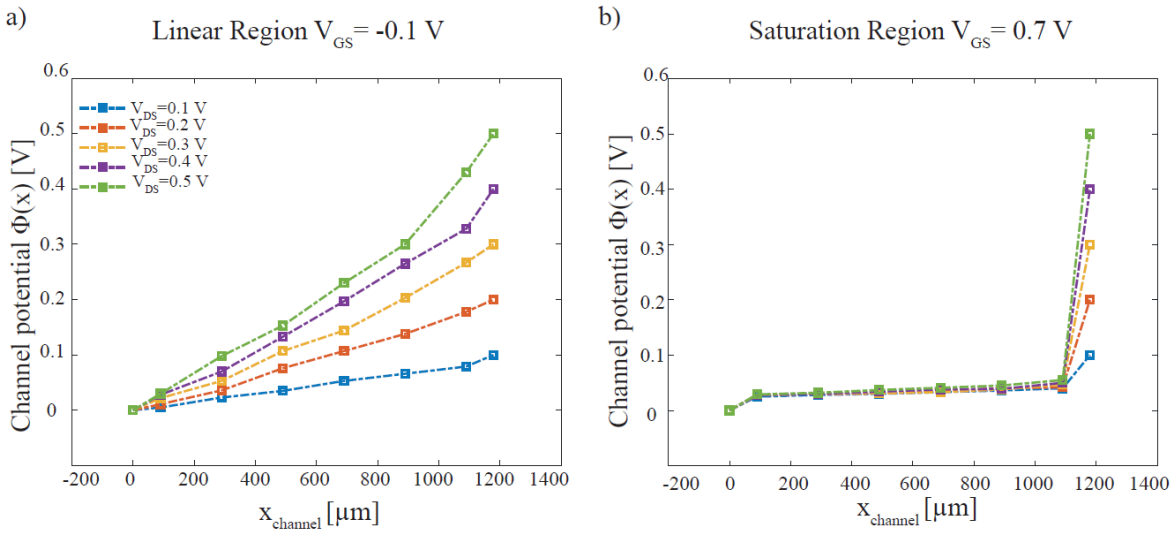

Figure 3.16 Potential measurement. a) Potential along the transistor channel in the linear regime (at V_{GS} = −0.1 V). b) Potential in the saturation regime (at V_{GS} = 0.7 V). The measurements are performed on the OECTs with the Sample2 geometry.

In Figure 3.16, we report the potential measured in the channel of the Sample2. At $V_{GS} = -0.1\ V$ the transistor was operated in the linear regime (Figure 3.16a). Consequently, the potential profile increased steadily towards the drain contact according to the model proposed by Mariani et al [20], who used scanning electrochemical microscopy to determine the electrochemical potential in the OECT channel. In their macroscopic study, a linear dependency of the electrochemical potential inside the channel was found, with potential changes at the drain contacts. While the transistor is in saturation at $V_{GS} = 0.7\ V$ (Figure 3.16b), the potential remains almost constant inside the channel and most of the potential drops at the drain contact, which reflects the pinch-off of the channel close to the drain. For intermediate values of V_{GS}, while the transistor is always in the linear region, ranging from -0.1 to 0.6 we did not notice trends different from those presented (Figure 3.16a), and likewise for values greater than 0.7 (Figure 3.16b), for the OECT in saturation regime [21].

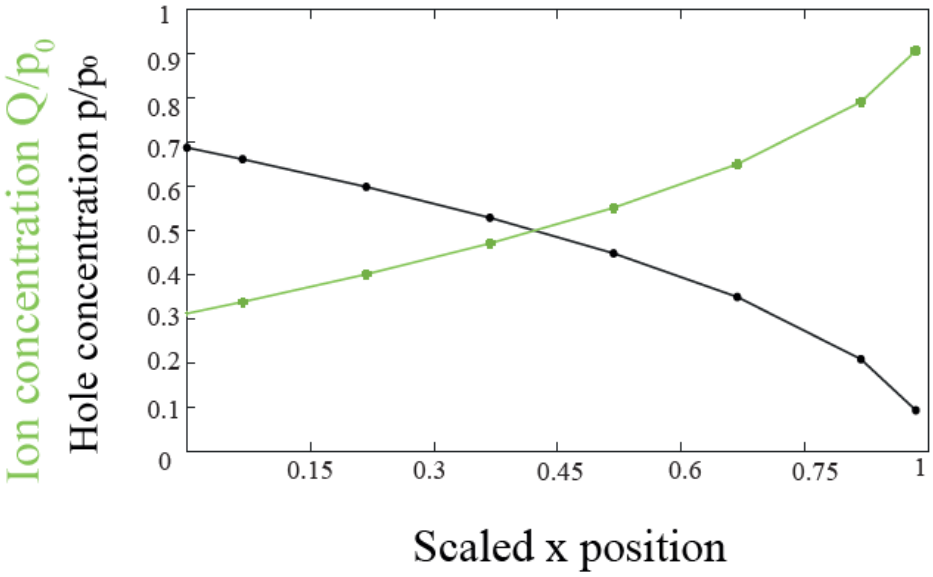

Figure 3.17 Normalized hole density, ion density OECT for Sample2. (W = 270 µm, d = 100 nm, L = 1400 µm, p_0 = 1020 cm^{-3}, μ_{hole} = 0.25 cm^2 $(Vs)^{-1}$, V_{GS} = 0.2 V, V_{DS} = −0.1 V). We show an increase in ion concentration (green lines) given by the difference between the gate and drain potential, and in the meantime, the decrease of hole density (black line).

The normalized hole density p(x)/p0 and the normalized density of cations Q/p0 inside the channel, obtained for OECT Sample2, of channel width W = 270 µm, channel thickness d = 100 nm, channel length L = 1400 µm, doping concentration inside the PEDOT:PSS layer of p_0 = 1020 cm^{-3}, mobility μ_{hole} = 0.25 cm^2 $(Vs)^{-1}$, gate voltage, V_{GS} = 0.2 V, and drain voltage V_{DS} = −0.1 V are plotted. In particular using Equation 3.3

$$Q(x) = p_0 - p_{ion}(x) = p_0 - \frac{C_G}{e}(V_{GS} - \Phi(x)) \tag{3.3}$$

we calculate the hole density as a function of the position x along the channel. Here p_{ion} is the density of ions along the channel and is calculated using:

$$p_{ion}(x) = \frac{C_G}{e}(V_{GS} - \Phi(x))$$

We report the normalized ion (Q) and hole (p) concentration respect to p_0 in Figure 3.17. We can see that p(x) decreases from the source at x = 0 to the drain at x=L=1400 µm.

Like the hole concentration, the ion concentration Q(x) increases from the source at x = 0 to the drain electrode at x= L (calculated from Equation 3.4). This increase in Q(x) concentration is caused by the increasing difference between the gate and the channel potential. The calculation of the ion current

discussed above implicitly assumes that the PEDOT: PSS layer is homogeneous, that is, ions and holes experience an identical electric field E(x) [21].

3. 4 Microfluidic applications

In this section, we report two results for the OECTs fabricated with the mentioned technique: the first is the biocompatibility with the cells and the second one is the application of OECT in a microfluidic device. These results explain the reason for introducing this new fabrication technique and makes them good candidates in the field of bioelectronics.

3.4.1 Biocompatibility assay

To validate that etched PEDOT: PSS materials did not affect cells' functionalities, we evaluated the Ca^{2+} flow across a confluent monolayer of Bend3. Figure 3.18a show the results of the viability experiment for two different substrates. In particular, we performed this analysis on a classical opaque substrates of silicon coated with silica and on transparent substrates typical of cell cultures (Glass), both with PEDOT:PSS patterned with the procedure described in this chapter. The glass is the king of substrate used in the proposed work while silicon is a commonly used substrate in the electronic field due the possibility to use its conductive behavior if properly patterned and doped. The percentage of live cells is positive for both substrates, showing that the treatment leaves no toxic residues on the cells, which therefore survive, especially in the case of glass substrates. However, it is possible to notice a better predisposition of the cells to adhere to the glass and not to the silicon. This depends mainly on the substrate and not on the treatment performed. This result allows us to use these devices even in contact with cells, without changing their appearance or causing differentiation.

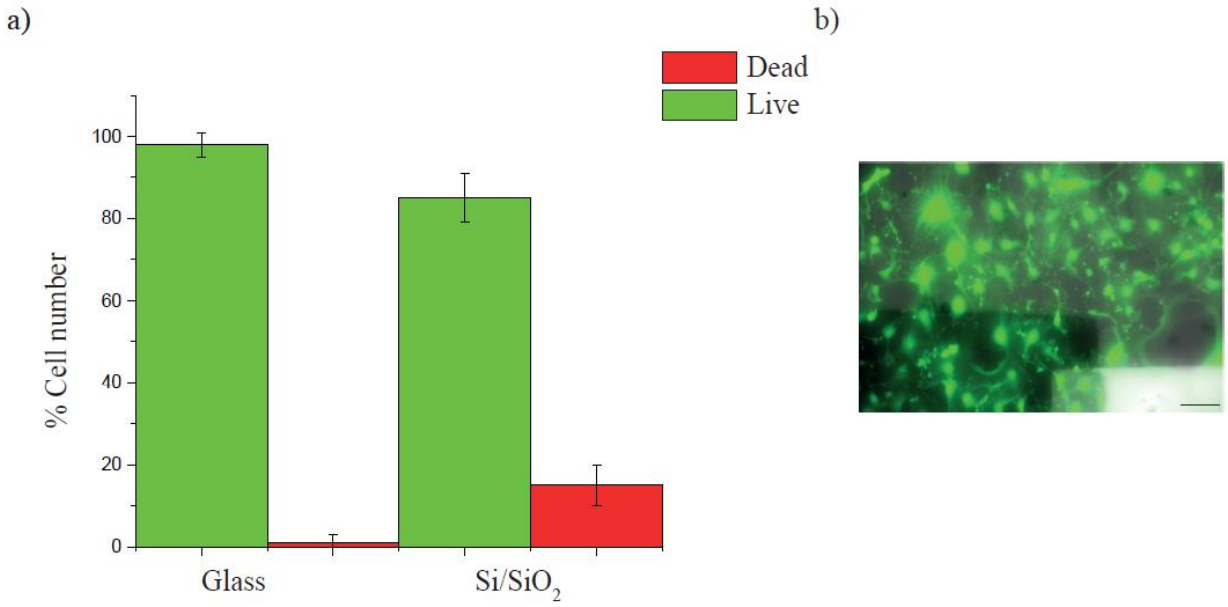

Figure 3.18 Biocompatibility assessment and Immunofluorescence of Bend3 cells cultured on Glass Etched PEDOT: PSS and Si Etched PEDOT:PSS. a) Percentage of live and dead cell represented as mean ± SD (*n* = 3); a) Cell vitality assay (in case of glass substrate) through live (green) and dead (red) cell labeling with Calcein AM and propidium iodide, respectively. b) Immunofluorescence image taken from Leica Confocal Multiphoton. Scale bar 50 µm.

3.4.2 Microfluidic device embedded with OECT.

In Figure 3.19, we show the effective bonding between microfluidic PDMS device and OECTs. In particular, we show a gradient concentration device with a colored fluid flowing in the channels without any leakage. This proof open the doors to many possible microfluidic applications including detection of protein, enzyme, or bacteria as well as in principle the GUT on chip application reported in Chapter 5.

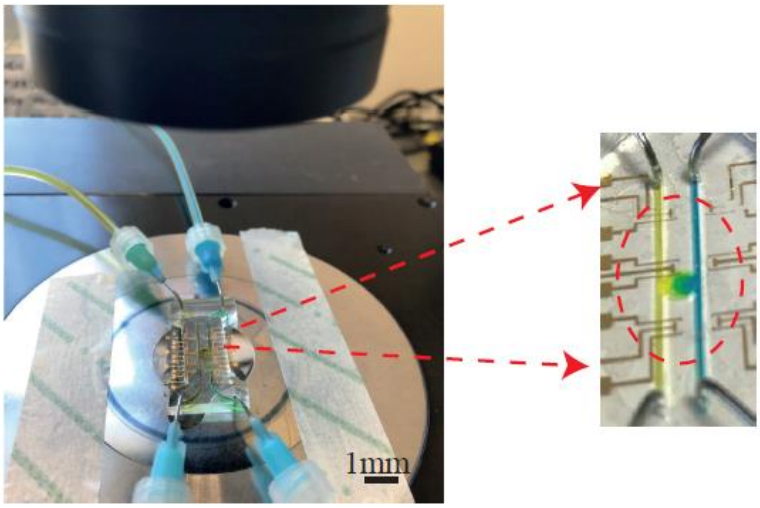

Figure 3.19 Microfluidic device for gradient concentration with OECT. No leakage is seen after bonding with plasma O_2. In the zoom image we show the gradient inside the microfluidic device.

3. 5 Conclusion

In this chapter, we presented a fabrication technique for PEDOT: PSS patterning to be exploited for the realization of OECTs channel and gate. This technique together with guarantying high resolution OECTs, conversely to the conventional high performing OECTs using Parylen C can be irreversibly bonded to PDMS microchannels paving the way for a possible exploitation of OECTs in the wide field of microfluidics. From the presented results, we showed how the technique is versatile to the point of being able to realize very small devices but also macroscopic structures. In principle, the technique can be applied to all the substrates on which PEDOT:PSS has been deposited up to now. The morphological characterization and cyclo-voltammetry curves were performed to assess that the polymer film was not damaged. Actually, PEDOT:PSS conductivity was even improved maybe due to the rounding effect of the acidic treatment. Finally, the theoretical modeling carried out, served as a further validation of proposed OECTs.

Bibliography

[1] S. Ouyang *et al.*, "Surface Patterning of PEDOT:PSS by Photolithography for Organic Electronic Devices," *J. Nanomater.*, vol. 2015, 2015, doi: 10.1155/2015/603148.

[2] V. F. Curto *et al.*, "Organic transistor platform with integrated microfluidics for in-line multi-parametric in vitro cell monitoring," *Microsystems Nanoeng.*, vol. 3, no. March, pp. 1–12, 2017, doi: 10.1038/micronano.2017.28.

[3] T. E. Winkler, M. Feil, E. F. G. J. Stronkman, I. Matthiesen, and A. Herland, "Low-cost microphysiological systems: Feasibility study of a tape-based barrier-on-chip for small intestine modeling," *Lab Chip*, vol. 20, no. 7, pp. 1212–1226, 2020, doi: 10.1039/d0lc00009d.

[4] W. Wu, J. Wu, J. H. Kim, and N. Y. Lee, "Instantaneous room temperature bonding of a wide range of non-silicon substrates with poly(dimethylsiloxane) (PDMS) elastomer mediated by a mercaptosilane," *Lab Chip*, vol. 15, no. 13, pp. 2819–2825, 2015, doi: 10.1039/c5lc00285k.

[5] J. Nissa, P. Janson, D. T. Simon, and M. Berggren, "Expanding the understanding of organic electrochemical transistor function," *Appl. Phys. Lett.*, vol. 118, no. 5, 2021, doi: 10.1063/5.0039345.

[6] H. Du, X. Lin, Z. Xu, and D. Chu, *Electric double-layer transistors: a review of recent progress*, vol. 50, no. 17. Springer US, 2015.

[7] P. C. Hütter, T. Rothländer, A. Haase, G. Trimmel, and B. Stadlober, "Influence of geometry variations on the response of organic electrochemical transistors," *Appl. Phys. Lett.*, vol. 103, no. 4, 2013, doi: 10.1063/1.4816781.

[8] M. J. Donahue *et al.*, "High-Performance Vertical Organic Electrochemical Transistors," *Adv. Mater.*, vol. 30, no. 5, pp. 1–5, 2018, doi: 10.1002/adma.201705031.

[9] D. Khodagholy *et al.*, "High transconductance organic electrochemical transistors," *Nat. Commun.*, vol. 4, pp. 1–6, 2013, doi: 10.1038/ncomms3133.

[10] S. Ouyang *et al.*, "Photolithographic patterning of PEDOT:PSS with a silver interlayer and its application in organic light emitting diodes," *Org. Electron.*, vol. 15, no. 8, pp. 1822–1827, 2014, doi: 10.1016/j.orgel.2014.05.004.

[11] M. N. Gueye, A. Carella, J. Faure-Vincent, R. Demadrille, and J. P. Simonato, “Progress in understanding structure and transport properties of PEDOT-based materials: A critical review,” *Prog. Mater. Sci.*, vol. 108, no. September 2019, p. 100616, 2020, doi: 10.1016/j.pmatsci.2019.100616.

[12] P. D’Angelo *et al.*, “PEDOT:PSS Morphostructure and ion-to-electron transduction and amplification mechanisms in organic electrochemical transistors,” *Materials (Basel).*, vol. 12, no. 1, pp. 1–13, 2018, doi: 10.3390/ma12010009.

[13] N. Zhao *et al.*, “Hierarchical porous carbon with graphitic structure synthesized by a water soluble template method,” *Mater. Lett.*, vol. 87, pp. 77–79, 2012, doi: 10.1016/j.matlet.2012.07.085.

[14] Z. Wang *et al.*, “Facile preparation of highly water-stable and flexible PEDOT:PSS organic/inorganic composite materials and their application in electrochemical sensors,” *Sensors Actuators, B Chem.*, vol. 196, pp. 357–369, 2014, doi: 10.1016/j.snb.2014.02.035.

[15] A. R. Gonalves, M. E. Ghica, and C. M. A. Brett, “Preparation and characterisation of poly(3,4-ethylenedioxythiophene) and poly(3,4-ethylenedioxythiophene)/poly(neutral red) modified carbon film electrodes, and application as sensors for hydrogen peroxide,” *Electrochim. Acta*, vol. 56, no. 10, pp. 3685–3692, 2011, doi: 10.1016/j.electacta.2010.11.056.

[16] T.-S. Choi and D. W. Hess, “Chemical Etching and Patterning of Copper, Silver, and Gold Films at Low Temperatures,” *ECS J. Solid State Sci. Technol.*, vol. 4, no. 1, pp. N3084–N3093, 2015, doi: 10.1149/2.0111501jss.

[17] S. Badhwar and K. S. Narayan, “Optimum Design of Organic Electrochemical Type Transistors for Applications in Biochemical Sensing,” *J. Sensors*, vol. 2008, pp. 1–5, 2008, doi: 10.1155/2008/702161.

[18] D. A. Bernards and G. G. Malliaras, “Steady-state and transient behavior of organic electrochemical transistors,” *Adv. Funct. Mater.*, vol. 17, no. 17, pp. 3538–3544, 2007, doi: 10.1002/adfm.200601239.

[19] J. T. Friedlein, S. E. Shaheen, G. G. Malliaras, and R. R. McLeod, “Optical Measurements Revealing Nonuniform Hole Mobility in O[1] J. T. Friedlein, S. E. Shaheen, G. G. Malliaras, and R. R. McLeod, ‘Optical Measurements Revealing Nonuniform Hole Mobility in Organic Electrochemical Transistors,’ Adv. Electron. Mater., vol,” *Adv. Electron. Mater.*, vol. 1, no.

11, pp. 1–9, 2015, doi: 10.1002/aelm.201500189.

[20] F. Mariani *et al.*, “Microscopic Determination of Carrier Density and Mobility in Working Organic Electrochemical Transistors,” *Small*, vol. 15, no. 42, pp. 1–10, 2019, doi: 10.1002/smll.201902534.

[21] V. Kaphle, P. R. Paudel, D. Dahal, R. K. Radha Krishnan, and B. Lüssem, “Finding the equilibrium of organic electrochemical transistors,” *Nat. Commun.*, vol. 11, no. 1, 2020, doi: 10.1038/s41467-020-16252-2.

CHAPTER 4

Tubular in vitro Blood Brain Barrier Platform embedding OECTs for Optical and Electrical Monitoring of Barrier Integrity.

Mechanisms of Blood brain barrier (BBB) induction, maintenance and dysfunction are for the large part still unknown. To enable the development of new drugs and therapeutics to combat BBB impairments and brain diseases we need to gain more knowledge of how the complex cellular interactions at the BBB modulate different aspects of barrier behavior. It is known that, due to its high selectivity, the BBB represents a major obstacle to the efficient delivery of large molecules for the treatment of brain diseases[1], [2]. Recent advancements in nano- and microtechnology used in the fabrication of BBB devices enable complex *in vitro* models that more closely mimic the human BBB. In particular, microfluidic based models can easily integrate sensors for cell culture health monitoring, real-time electrical measurements, biomarker detection, etc.[3]. Here, we set out to develop a 3D microfluidic model of a hollow human brain micro-vessel that contains primary endothelial cells and astrocytes isolated from human brain. Then, to monitor real time the evolution of the proposed 3D model, we integrated in this platform OECTs, capable to convert biological signals in electrical ones. At the end, we used this platform to predict gH625 peptide transport to the brain. This platform is a promising real-time monitoring tool for blood brain barrier disruption augmented drug delivery.

The chapter is presented as follows: first we discuss the design, the fabrication and Comsol validation of the microfluidic platform to understand the geometry and the effect of the physiological shear stress on the endothelial cells. In the second part, we present the characterization of the device focusing on electrical performance using the OECTs. At the end, we verify, electrically and optically, the ability of gH625, a membranotropic peptide, to cross the BBB layer under flow conditions that mimic the blood flow rate.

Table of contents

CHAPTER 4 110

Tubular in vitro Blood Brain Barrier Platform embedding OECTs for Optical and Electrical Monitoring of Barrier Integrity. 110

4.1 BBB: Design, Fabrication and COMSOL simulation 112

4.1.1 Design 112

4.1.2 Simulation 112

4.1.3 Fabrication 114

4.2 Cells colture and Collagen fingering method 115

4.2.1 Astrocytes and HBEC-5i 115

4.2.2 Viscous fingering method 115

4.2.3 Improving stability of collagen. 116

4.2.4 Immunofluorescence and ultrastructural analyses in physiological and reduced dynamic conditions. 117

4.2.5 Statistical analysis. 118

4.3 Experimental characterization 118

4.3.1 Device characterization 118

4.3.2 Flow effect on endothelial cells 119

4. 4 Electrical characterizations 125

4. 4.1 OECTS array integration in microfluidic 3D channel 125

4. 4.2 Electrical Impedance spectroscopy (EIS) 126

4. 5 Morphological characterizations 128

4.5.1 Dextran 40 kDa transport across the BBB 128

4.5.2 Frap analysis with Fourier Transform. 130

4. 6 BBB in vitro crossing: gH625 peptide study 133

4.6.1 Monitoring Barrier through transient current 133

4. 6.2 Monitoring Barrier interaction with gH625 peptide 135

4. 7 Conclusion 140

Bibliography 141

4.1 BBB: Design, Fabrication and COMSOL simulation

In this paragraph we introduce the fabrication technique used in this work in order to realize the mold for us microfluidic device. Then, in order to assess the good performance of the device, Comsol physics simulation are performed to identify the best flow rate, in relation with the geometry for our 3D model of BBB *in vitro*.

4.1.1 Design

The microfluidic device consists in three channels (Figure 4.1). The central one with width of 2300 µm for the hydrogel with astrocytes, and two fluidic lateral channels 800 µm wide are for tubular shape of endothelial cells. Inside the device, there are 18 pillars of parallelepiped shape that separate the hydrogel from the lateral fluidic channels in order to create a side-by-side compartment to mimic brain part (central channel) and blood ones (lateral channels). The height of the device is 300 µm.

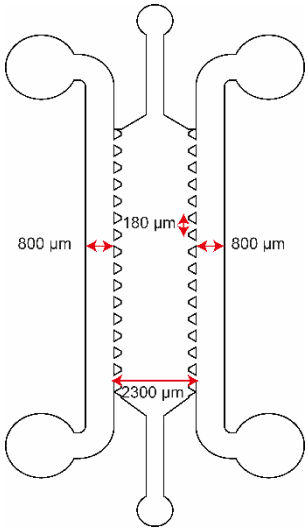

Figure 4.1 Schematic representation of the BBB Device. We show the parameters chosen for the fabrication: 18 pillars, 2 fluidic channels 800 µm wide, and a central channel of 2300 µm. The height is of 300 µm.

4.1.2 Simulation

The oxygen gradient and the nutrient supply velocity were measured by using commercial CFD COMSOL Multiphysics vers. 5.0. CFD analysis was performed dividing the entire device into two different domains, a fluid domain, which identified the region filled with culture medium, namely the lateral channels with the endothelium, and a tissue domain, which identified the region filled with the collagen and astrocytes. Simulations within the fluid domain were performed by using the steady

state Navier-Stokes equation (4.1). No slip boundary conditions were set on the walls, and the fluid was considered to have the same physical characteristics as water. A specific laminar flow was set at the inlet and reference pressure was set at the outlet (p_{ref}=1atm):

$$\rho(v_1 \cdot \nabla)v_1 = \nabla \cdot [-pI + \mu(\nabla v_1 + (\nabla v_1)^T)] + F \qquad (4.1)))$$
$$\rho(v_1 \cdot \nabla) = 0$$

where μ is the dynamic viscosity, *v* is the fluid velocity, *p* is the hydrostatic pressure, and *ρ* is the fluid density. Brinkman equation (4.2) was used to describe the flow through a porous medium, that is the flow through collagen with astrocytes:

$$\left(\frac{\mu}{k} + Q\right) v = \nabla \cdot \left(-pl + \left(\frac{1}{\varepsilon}\right)\left(\mu(\nabla v + (\nabla v)^T)\right)\right) - \left(\frac{2\mu}{3} - k_{dv}\right)(\nabla \cdot v)^l)) + F, \qquad (4.2)$$
$$\rho(v \cdot \nabla) = 0,$$

where *k* is the hydraulic permeability, *μ* is the viscosity of the tissue, *p* is the pressure, *ε* is the porosity of the material, k_{dv} is the dynamic permeability. The oxygen concentration within the system was calculated by means of the following mass balance equation (4.3):

$$\mathrm{D}\nabla^2 C - \nabla(Cv) = -R \qquad (4.3)$$

where *C* is the oxygen concentration, *v* is the fluid velocity field, and *D* is the diffusion coefficient of the oxygen. *R* is the volumetric oxygen consumption rate expressed by the Michelis-Menten law, according to the following equation (4.4):

$$\mathrm{R}=\rho \frac{v_{max} c}{k_m + c} \qquad (4.4)$$

where v_{max} is the maximum oxygen consumption rate, k_m is the concentration at which the oxygen consumption rate is half of v_{max} and *ρ* is the cell density in the perfusion chamber obtained by taking into account the number of cells present in the Collagen. The parameters are presented in Table 4.1.

Table 4.1. Mathematical modeling parameters

Variable	Description	Value	Source
μ^f	Dynamic viscosity of the fluid (culture media) (Pa s)	0.001	[8]
μ^t	Effective viscosity of the fluid in the tissue domain (Pa s)	0.0016	[8]
ε	Porosity of the tissue	0.7	[8]

κ^t	Effective hydraulic conductivity (m^2)	10^{-11}	[8]
D^f	Oxygen diffusivity in the culture media ($m^2 s^{-1}$)	10^{-9}	[8]
D^t	Oxygen diffusivity in the tissue ($m^2 s^{-1}$)	10^{-10}	[8]
C_0	Equilibrium oxygen concentration in the culture media (μM)	0.22	[8]
ρ	Cells per hydrogel (cell m^{-3})	$0.1\ 10^{11}$	[9]
V_{max}	Maximum rate of oxygen consumption (mol $cell^{-1}\ s^{-1}$)	10^{18}	[10]
K_m	Oxygen concentration at 0.5 (V_{max}) (μM)	10^3	[10]
K_{dv}	Dynamic permeability (m^2)	0	[10]
R	Oxygen consumption rate (μM s^{-1})	$\rho \frac{V_{max} C}{K_m + C}$	[10]

4.1.3 Fabrication

The 3D microfluidic system was composed of polydimethylsiloxane (PDMS; Sylgard 184; Dow Corning, MI, USA) with a single layer microchannel and two fluid channels, fabricated by soft lithography. In particular, mold fabrication involves 2D photolithography (maskless lithography HEIDELBERG DWL66FS) and ICP-RIE (BOSCH process OXFORD PlasmaPro). Elastomer and curing agent were mixed (10:1 vol ratio), degassed and poured onto a silicon master and cured overnight at 60 °C. I/O holes were created with biopsy punches, then the device was taped to remove dust and sterilized. The PDMS micro devices were treated with oxygen plasma 100 (Plasma Etch,Inc.), then bonded to a glass coverslip (Fisher Scientific). After baking at 80°C for 2 h, devices were again treated with NaOH solution (3 min) and just after with Fluorolink (1 h at 100°C). Devices were then flushed with 100% ethanol, followed by water and ethanol and subsequently dried at 80°C for 2 h. Subsequently, the surfaces were further functionalized by filling the devices with 2.5% glutaraldehyde (Electron Microscopy Services, Inc.) as described in the following paragraph. After incubating for 15 min, the devices were rinsed extensively with deionized water and were baked for 2 h at 80°C.

4.2 Cells culture and Collagen fingering method

Here we put attention on the different cell lines used in our thesis in order to recreate the BBB. Next, we introduce the method of the viscous fingering pattern of collagen or hydrogel in general, in order to recreate a tubular structure in the microfluidic device. In the end immunofluorescence and ultrastructural analysis are introduced like technique used to characterize the system here developed.

4.2.1 Astrocytes and HBEC-5i

The model proposed in this thesis is composed of HBEC-5i endothelial cells (from ATCC-Manassas, VA, USA) and the Human Astrocyte cell line (HA from ScienCell Research Laboratories, Carlsbad, CA, USA). Initially, HBEC-5i are cultured in Dulbecco's Modified Eagle Medium: nutrient Mixture F-12 (DMEM-F12 HAM), supplemented with 10% FBS, 40 µg/mL endothelial cell growth supplement (ECGS), and 1% antibiotic antimycotic solution and HA are grown in AM Medium containing 2% FBS, 1% AGS and 1% penicillin-streptomycin solution according to manufacturer's instructions. A coculture model with endothelial cell line and cooperation with astrocytes is evaluated with astrocytes embedded in a collagen matrix. Endothelial cells are seeded at a density of $1x10^6$ cells/cm^2 while astrocytes are seeded at density of $5x10^5$ cells/cm^2. The flow condition discussed in the following paragraph (4.3.2) supply oxygen and nutrient for the cells.

4.2.2 Viscous fingering method

To obtain a 3D BBB chip with lumen we used a viscous fingering pattern via surface tension-driven pumping (aka passive pumping) to flow a less viscous fluid through an unpolymerized ECM hydrogel in a microchannel. The less viscous fluid displaces the hydrogel along the length of a microchannel, leaving behind a continuous lumen after the hydrogel has fully polymerized. A summary of the procedure is shown in Figure 4.2. Automated liquid handling systems can be employed to perform all steps required to generate arrays of physically independent lumens in a high-throughput manner [11].

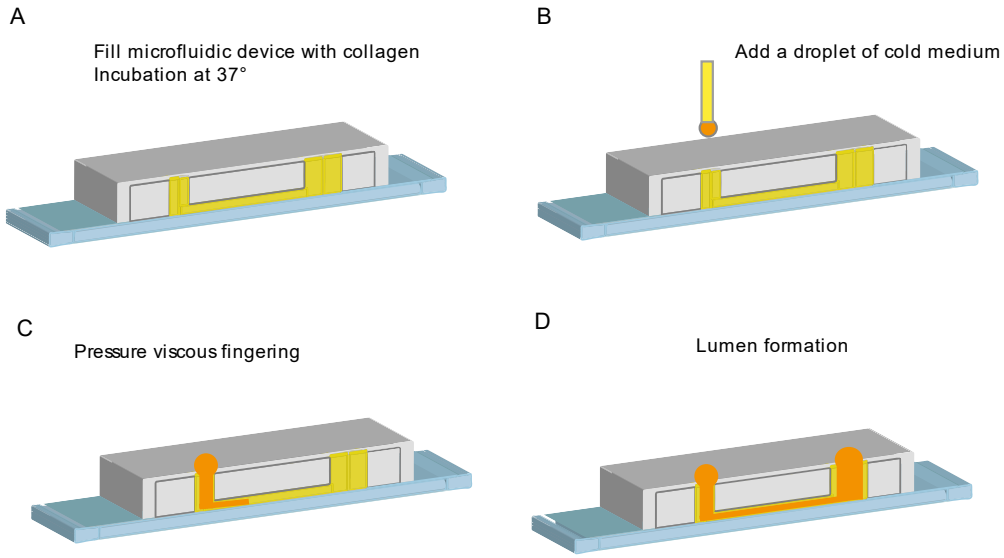

Figure 4.2 Process used for patterning lumens through an extracellular matrix (ECM) hydrogel via viscous finger patterning. First a microchannel is filled with an ECM hydrogel solution (A). The microchannels are incubated at 37 °C for a period of time depending on desired lumen dimensions, channel geometry, and ECM composition (B). Then passive pumping is performed by placing a droplet of culture media on the inlet (B), flushing out the ECM solution in the center of the microchannel (C), and leaving a continuous lumen through the ECM hydrogel (D).

4.2.3 Improving stability of collagen.

With the previous method the collagen gel tended to delaminate from the PDMS microchannel surface, and so we functionalized the PDMS surface in a three-step process involving NaOH treatment, Fluorolink treatment and glutaraldehyde derivatization [11] (Figure 4.3).

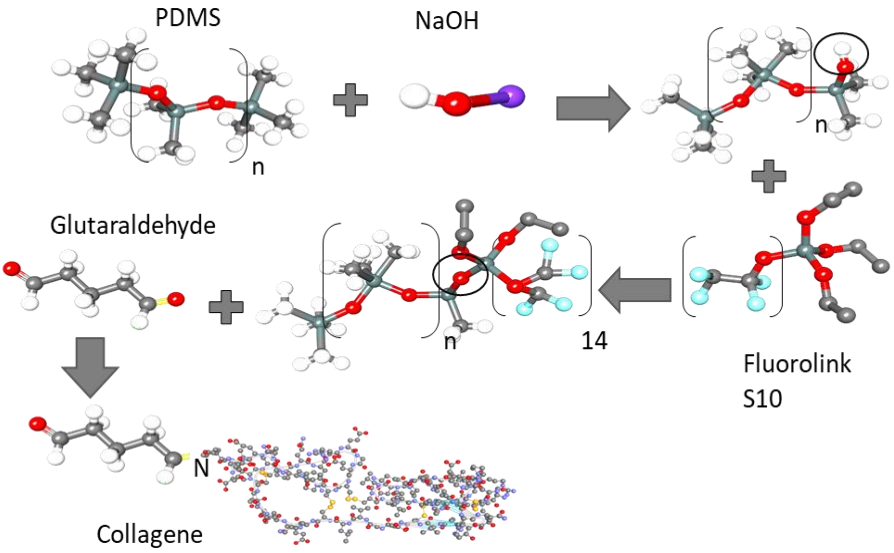

Figure 4.3 PDMS Functionalization to increase collagen adhesion.

With this treatment no delamination was observed, and this protocol allowed the chips to remain stable for more than 7 days with no apparent degradation. All devices pre-treated in this manner were kept on ice and filled with ice-cold 2 mg/ml rat-tail collagen I (Corning), mixed and neutralized as per the manufacturer's instructions. After filling the device with the collagen solution, a 200 µl pipette tip with 80 µl of ice-cold culture medium was inserted in the inlet. The medium could flow through the viscous collagen solution by hydrostatically driven flow and the devices were subsequently incubated at 37°C to allow the formation of collagen gels. The pressure values presented here were calculated as the difference in height between the meniscus of the liquid in the reservoir and the inlet of the chip. After collagen gelation by incubating for 30 min at 37°C, the devices were rinsed extensively with pre-warmed culture medium and stored in a cell culture incubator for 18 h.

4.2.4 Immunofluorescence and ultrastructural analyses in physiological and reduced dynamic conditions.

For immunofluorescence staining of 3D tubular BBB all samples are fixed with paraformaldehyde (PAF) at 4% for 20 min at room temperature and washed for three times in PBS 1%. Then, all samples are washed with PBS containing 0.2% Triton X-100, blocked in a standard blocking for 1 hr at RT, and incubated with rabbit anti-human GFAP (AbCam 1:50), Claudin 5 (1:100; Sigma-Aldrich), VE-Cadherin (1:100; Sigma Aldrich) and ZO-1 (1:50; Abcam) overnight at 4°C. Then, secondary antibody incubation, goat anti rabbit 568 and goat anti rabbit 488 (1:500; Alexa Fluor) was performed, and cell nuclei were detected by Draq5 staining (1:10,000; Sigma-Aldrich). Phalloidin staining (1:1000, Sigma-Aldrich) was performed to mark the astrocytes. Each type of experiment was repeated in triplicate. For scanning electron microscopy (SEM) analysis, all samples are fixed with 2.5% (vol/vol) glutaraldehyde in cacodylate buffer and then washed twice in 100 mM cacodylate buffer, pH 7.2, for 10 min at RT. A second fixation in 1% (wt/vol) osmium tetroxide, buffered in 100 mM cacodylate, pH 7.2, is done overnight at 4°C. Then, dehydration is carried out, and all samples are treated with liquid carbon dioxide using a Critical Point Dryer (Emitech K850), mounted onto metal stubs using double-sided adhesive tape and then gold-coated using a sputter coater at 15 mA for 20 min. Coated samples were then examined by Leica S400. Each type of experiment was repeated in triplicate. For electron transmission microscopy (TEM) analysis, all samples are fixed in glutaraldehyde and post-fixed in osmium tetroxide. After dehydration, tissue samples were embedded in Epon. Ultrathin sections were mounted on copper grids and stained with uranyl acetate and lead citrate and examined by TEM. Each type of experiment was repeated in triplicate.

4.2.5 Statistical analysis.

Data are expressed as mean ± standard deviation and show the results from three independent experiments. All results were then statistically analyzed by Student's *t* test. Statistical significance was set at a value of $p < 0.05$.

4.3 Experimental characterization

In the next section we start with the experimental characterization of the device. First of all, we put attention on the fabricated device in order to assess his geometrical description. Then, an analysis of shear stress on cells is performed showing the results in two different cases:

- Physiological shear.
- Reduced shear.

4.3.1 Device characterization

In Figure 4.4a we show a 3D illustration of the final device, with three channels. The patterned sample was etched with the inductively coupled plasma reactive ion etching technology (ICP-RIE); the system used here was the PlasmaPro 100 Cobra (OXFORD Instruments). The sample was fixed on an 8 inches silica wafer by means of high vacuum grease and etched with a Bosh process to obtain vertical walls [12]. After the dry etching, the sample was immersed in acetone for the photoresist stripping, rinsed with 2-propanol and dried with nitrogen (Figure 4.4b). To characterize the etching results the sample was analyzed by SEM (FESEM ULTRAPLUS ZEISS) (Figure 4.4c).

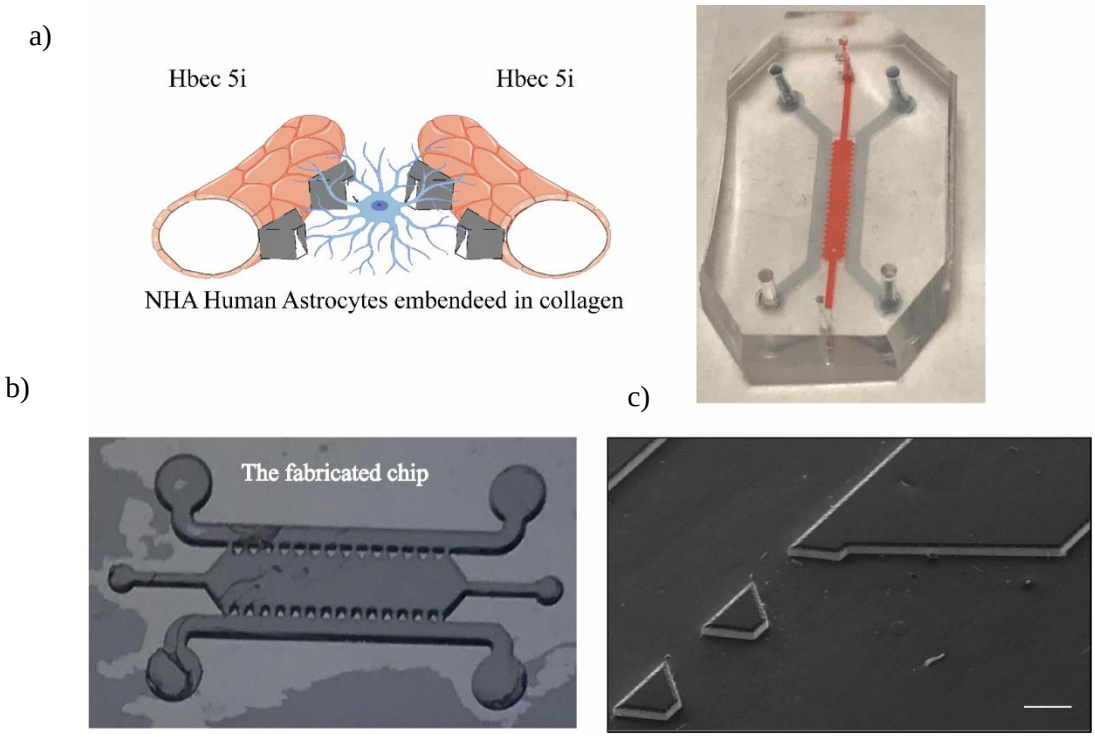

Figure 4.4 3D illustration, photograph and SEM image of the fabricated microfluidic chip. Scheme of the structure and design of the developed BBB microfluidic system(a). Picture of the fabricated chip (b) and SEM image of a section of the device (c) (scale bar 1 mm).

4.3.2 Flow effect on endothelial cells

The integrity of structure and function of the BBB plays a central role in maintaining the homeostasis of the central nervous system. Patients with severe cerebrovascular stenosis often undergo cerebrovascular bypass surgery. However, the sharply increased fluid shear stress (FSS) after cerebrovascular bypass disrupts the physiological function of brain endothelial cells (hBECs) at the lesion site, damaging BBB and inducing intracerebral hemorrhage eventually [12]. At present, there is great interest in cerebral vascular flow regulating the structure and function of BBB under physiological and pathological conditions, and most of studies have highlighted the importance of hBECs in BBB under shear stress. Understanding of how FSS regulates BBB can promote the development of new protective and restorative cerebral vascular interventional therapy.

With the objective to choose the optimal flow rate to perform the dynamic culture, we carried out CFD simulations. We coupled Navier- Stokes's Equations (4.1) with Brinkman Equation (4.2), in the fluid compartment and in the "tissue" compartment (3D collagen), respectively. Oxygen consumption, by the cells contained into the 3D collagen, was calculated using a Michelis-Menten Equation (4.4), considering the diffusive/convective oxygen transport. These numerical simulations were performed using flow rate of 20 μL/min that we named as physiological shear and 5 μL/min that we named as reduced stress. In Figure 4.5, we report the color map of the oxygen profile (Figure

4.5B); the light blue line represents the streamline of velocity field (Figure 4.5C). The simulations show that at flow rate Q=20 μL/min, the oxygen concentration was higher than in the case of 5 μL/min in all the parts of the sample due to the increased contribution of convective transport, since the velocity field was higher. Increased evidence illuminated that elevated FSS impaired the BBB barrier phenotype, causing structural and functional abnormalities of the brain microvascular endothelium. Garcia-Polite et al. (2017) [12] showed that high FSS (40 dyn/cm^2) and pulsatile flow down-regulated the expression of (tight-junction) TJ markers, translocated ZO-1 into the cytoplasm and nucleus and decreased the efflux activity of P-gp. The nuclear localization of ZO-1 is inversely related to the extent and/or maturity of cell contact. As a rapid trigger of barrier phenotype loss, ZO-1 protein level down-regulated instantaneously after exposing to non-physiological flow, which was consequently followed by Claudin-5 down-regulation [13]. In our case, the shear stress (τ), given by $\tau = 6\mu S/WH^2$, where μ is the fluid viscosity, S is the flow rate, and W and H are the width and height of the channel, is 0.1-5 (dyn/cm^2) consistent with the one present in the blood brain barrier capillary[12]. In this way, we can assure the right amount of oxygen for the astrocytes embedded in the collagen matrix, but we are sure that there is no delamination of the collagen and cells from the surface of our device due to too much high FSS[14].

Instead, operating in the reduced shear, flow rate of 5 μL/min, the convective contribution was the lowest and the safest, but the diffusive contribution is not adequate to perfuse and feed all the parts of the sample. In fact, the amount of oxygen that reaches the compartment with collagen and astrocytes is not sufficient to ensure their survival. Additionally, in terms of shear stress (0.025-0.1 dyn/cm^2) we saw that the value does not guarantee the alignment of endothelial cells, as shown later.

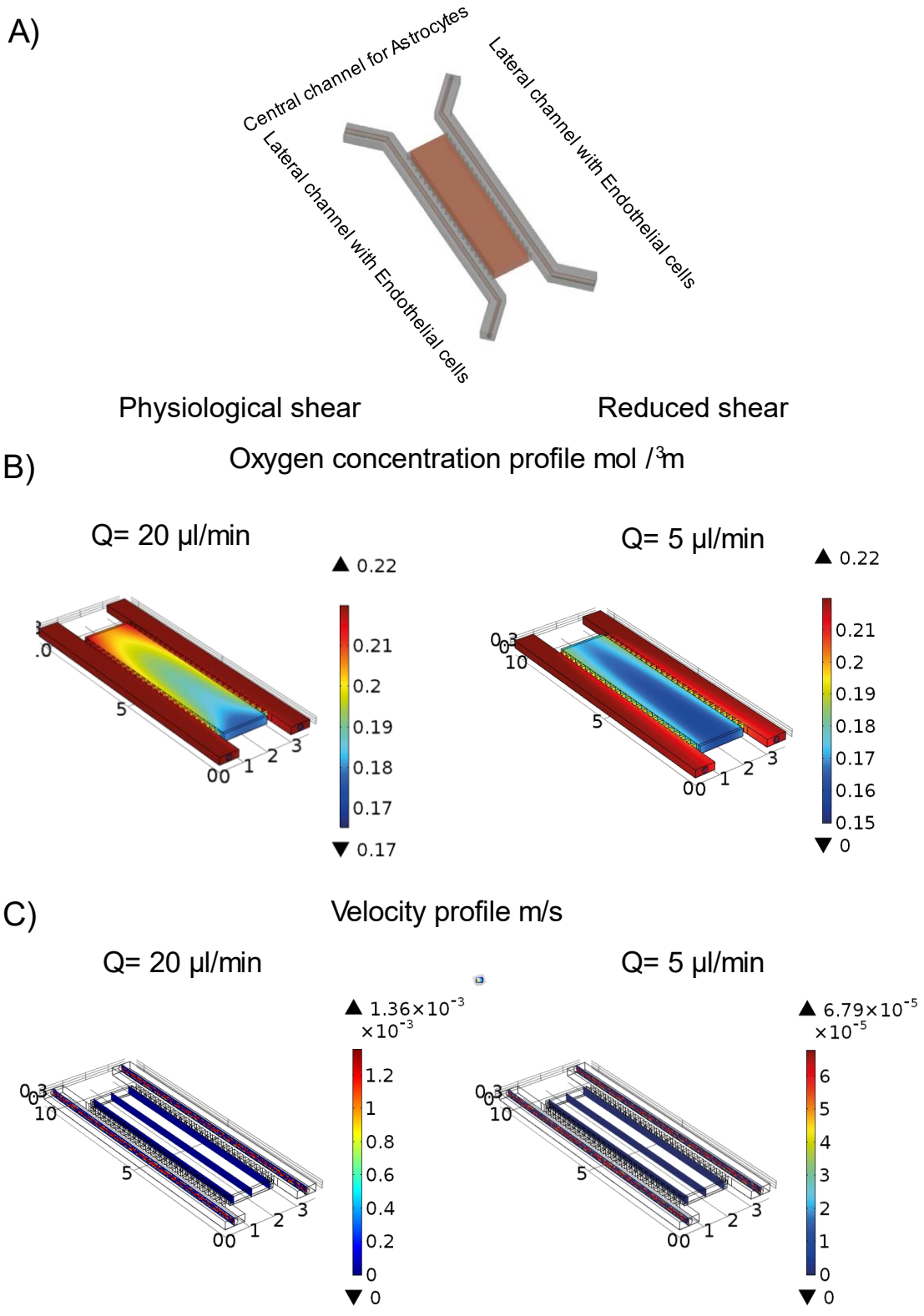

Figure 4.5 CFD simulations using COMSOL Multiphysics. In A are reported the design of microfluidic device, while in B and C are reported simulations for convective, diffusive flux and the streamline of the velocity field for the reduced shear (Q= 5 µL/min), and physiological shear Q=20 µL/min.

In Figure 4.6, we show the final result of the viscous fingering pattern and flow effect on the endothelial cells, that results in a tubular shape of the blood brain barrier. An immunofluorescence analysis show, in Figure 4.6a, the 3D reconstruction on the tubular shape of our BBB in vitro with

the cross section showing the diameters of 85 µm. More interesting, we show in Figure 4.6b the direct contact between the brain part (astrocytes in red) and blood part (endothelial cells). Immunofluorescence show in red GFAP for astrocytes, in blue nuclei with HOECHT and in green, VE-Cadherin to mark tight junction.

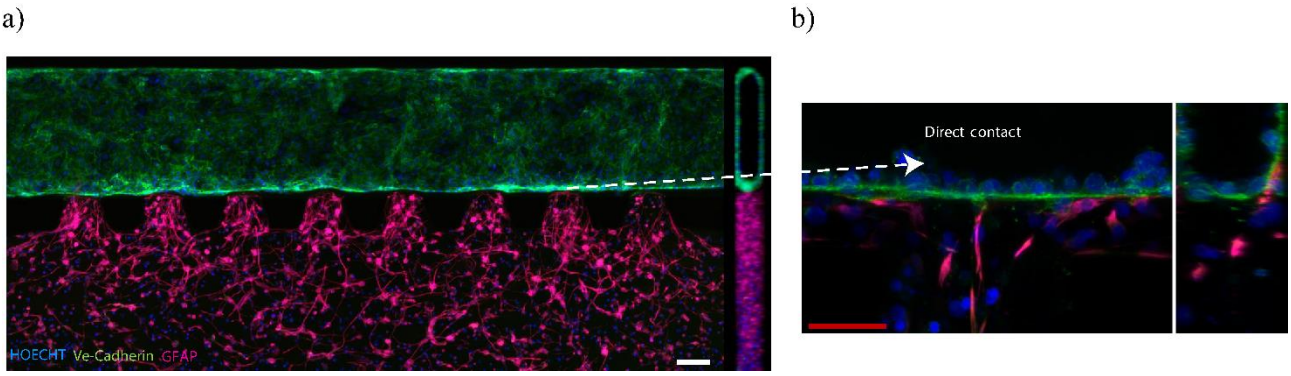

Figure 4. 6Tubular shape of Blood Brain Barrier. Immunofluorescence show in green VE-Cadherin for tight junction of Hbec-5i, in red GFAP to mark astrocytes and in blue nuclei. In a) a 3D reconstruction of the tubular shape and the cross section showing the diameter of the vessel ~85 µm. In b) a zoom of the image (scale bar 100 µm), we show direct contact between the brain part (astrocyte in red) and the blood part (endothelial cells in green) All the experiments were performed in triplicate (n = 3). Scale bar 50 µm

Once identified the flow value through simulations, in order to investigate the response of the microfluidic endothelium to physiological and reduced shear stress, we carried out image analysis of cell morphology and evaluated the Shape Index (SI) defined by the following equation (4.5)

$$SI = 4\pi \frac{A}{p^2} \tag{4.5}$$

where A and p are the area and perimeter of the cell, respectively. In Figure 4.7 we report morphological responses to physiological and reduced shear and also the analysis of flow-induced reorientation and alignment of the cultured endothelial cells. Specifically, in Figure 4.7a we show that, while with reduced flow the cell's shapeis more circular, so the shape index is very close to 1, in case of physiological a better elongation is visible, and the shape index is reduced. Moreover, cell alignment was quantified by measuring the positive angle between the major axis of the cell body and the vertical axis. The cell was considered aligned when this angle lied between 60 and 120 degrees (Figure 4.7). In Figure 4.7B we show an increase in aligned cells as the flow condition improves.

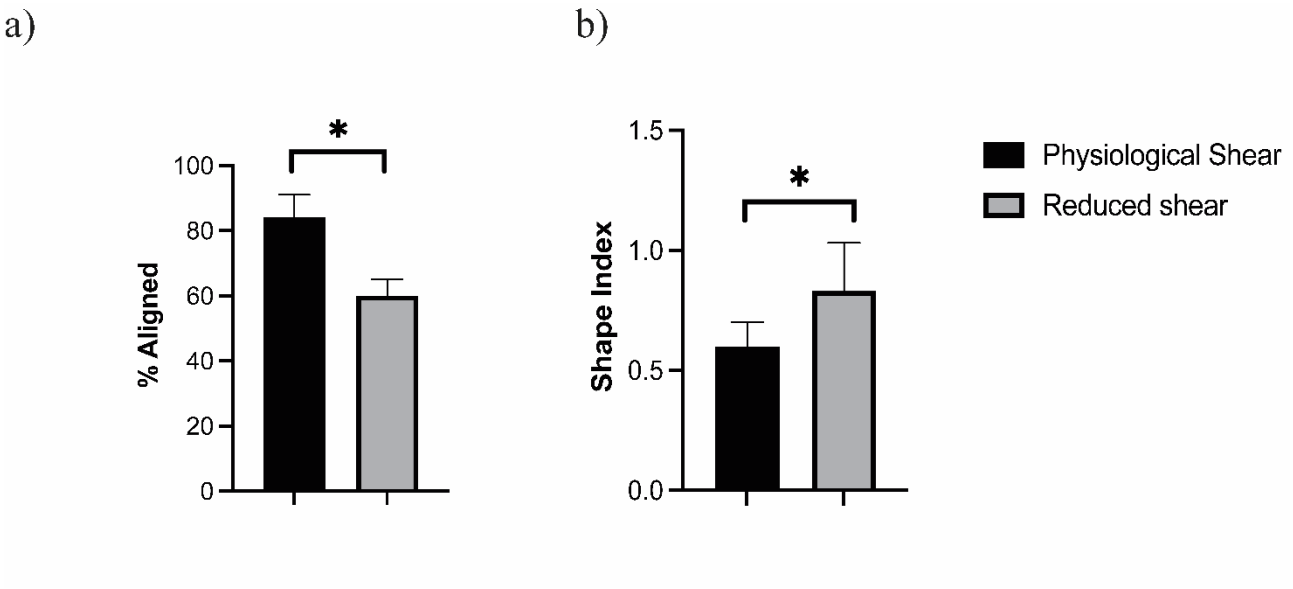

Figure 4.7 Quantitative analysis of endothelial responses to shear stress. When SI=1, the shape of cells is circular, that means no shear stress is used. A better elongation is visible in case of physiological shear SI ~0.6 compared with the reduced one SI~0.8 (Figure 4.6 a). On the other hand, when cells are subjected to a physiological stress, the number of aligned cells is higher than those subjected to a reduced one. (Figure 4.6 b) *p < 0.001, (n=10).

As a well-documented differentiating influence on endothelium, the flow has a corresponding critical modulatory role in BBB phenotype through modulating the expression of TJs and transporters [6]. As further proof of the increase in the paracellular resistance of the cell layer, we performed fluorescence immunostaining of the ZO-1 tight junction protein in order to understand how the reassembly of the intercellular junctions in the cells takes place. In Figure 4.8, we report the evaluation of expression of TJs and Occludin for both cases. First of all, we evaluated the intensity of ZO-1 in case of physiological and reduced shear stress, and we show an increase in the intensity of the ZO-1 signal when the cells are subjected to the physiological shear stress (Figure 4.8C). This is confirmed, also by Scanning electron microscopy, and immunofluorescence analysis for Claudin 5 Figure (4.8 bottom). We also show ZO-1 fluorescence images captured in the two conditions, when cells are exposed to physiological and to reduced shear stress. Although in both cases, a certain amount of ZO-1 protein is present in the cytosol of the cells, the exposure to the FSS induced a significant reorganization of the ZO-1 protein on the borders of the cells. With respect to morphology, hBECs exposed to physiological shear stress become flatter and larger, and displayed a manifest increase in endocytotic vesicles, microfilaments, and clathrin-coated pits, thereby more closely resembling that of BBB phenotype *in vivo* (Figure 4.8).

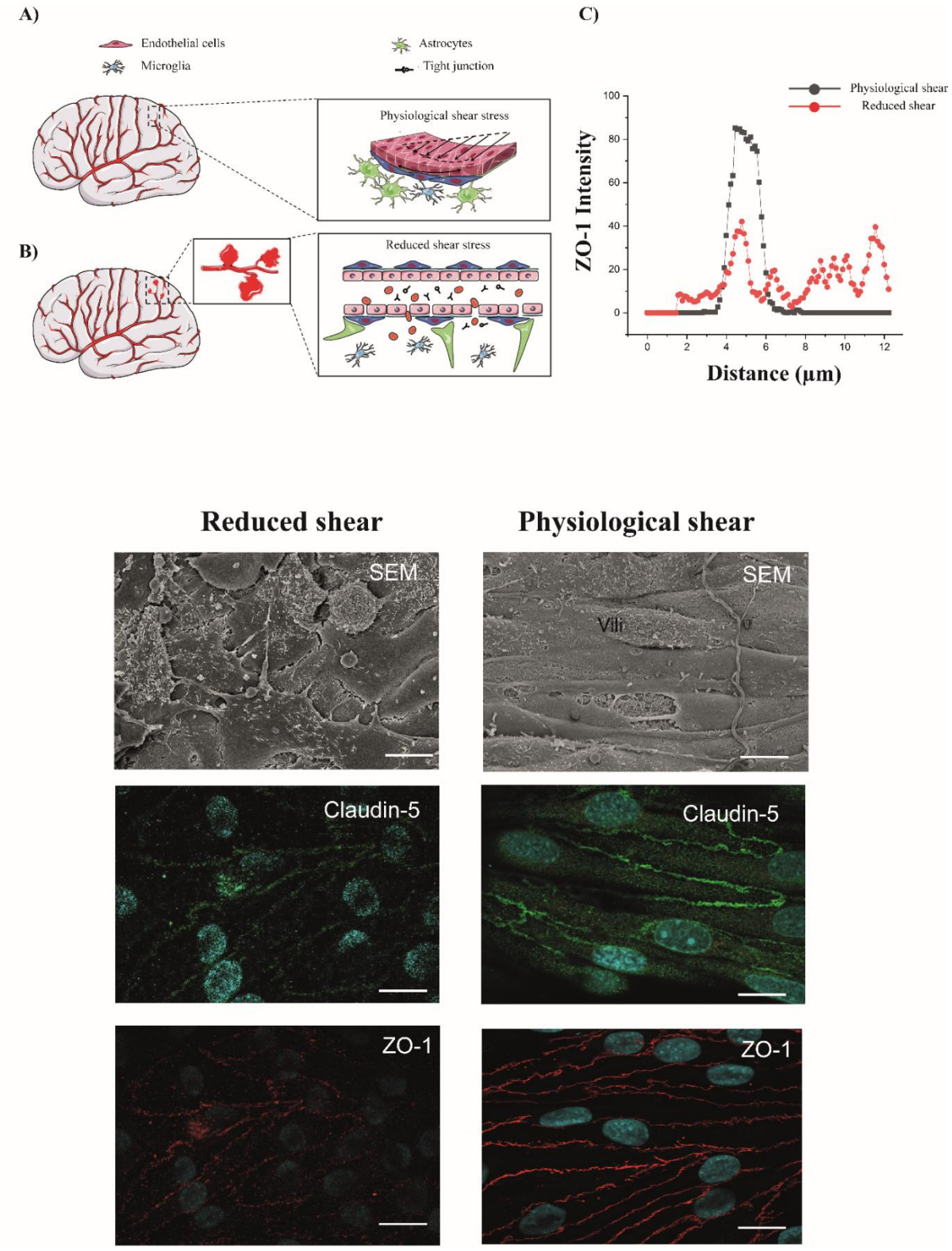

Figure 4.8 Configuration of endothelial cells in the tubular device. (a) Typical configuration of physiological effect of flow rate on the endothelial cells in the tubular device. (b) Typical configuration of reduced effect of flow rate on the endothelial cells [14] (c) ZO-1 fluorescence images of a confluent cell layer in the presence of physiological and reduced FSS stimulation (scale bar, 20 µm) . We report also, Scanning Electron microscopy, ZO-1 and Claudin immunofluorescence showing the effect of physiological and reduced shear stress. All the experiments were performed in triplicate (n = 3).

4. 4 Electrical characterizations

In this part of the work, we combine OECTs fabricated with the technique introduced in the Chapter 3 with the 3D tubular platform. In this part of work, a great attention is given on the planar configuration of the OECTs, because this configuration allows us not to damage the cylindrical structure made but at the same time to have important electrical information.

4.4.1 OECTS array integration in microfluidic 3D channel.

Following these initial results and validation of the microfluidic device, we proceeded to the integration of OECTs as in-line impedance sensors embedded in the microfluidics, to allow electrical monitoring of the optical changes observed. We previously developed a planar all polymer transistor (OECT) based on poly(3,4-ethylenedioxythiophene) :(poly(styrenesulfonate)(PEDOT:PSS) (Chapter 3). The planar OECT used for these studies is illustrated in Figure 4.9. In order to have the major amount of information along the channel, we decided to realize an array of OECTs, and monitor in different zones of the device the cellular behavior and barrier integrity.

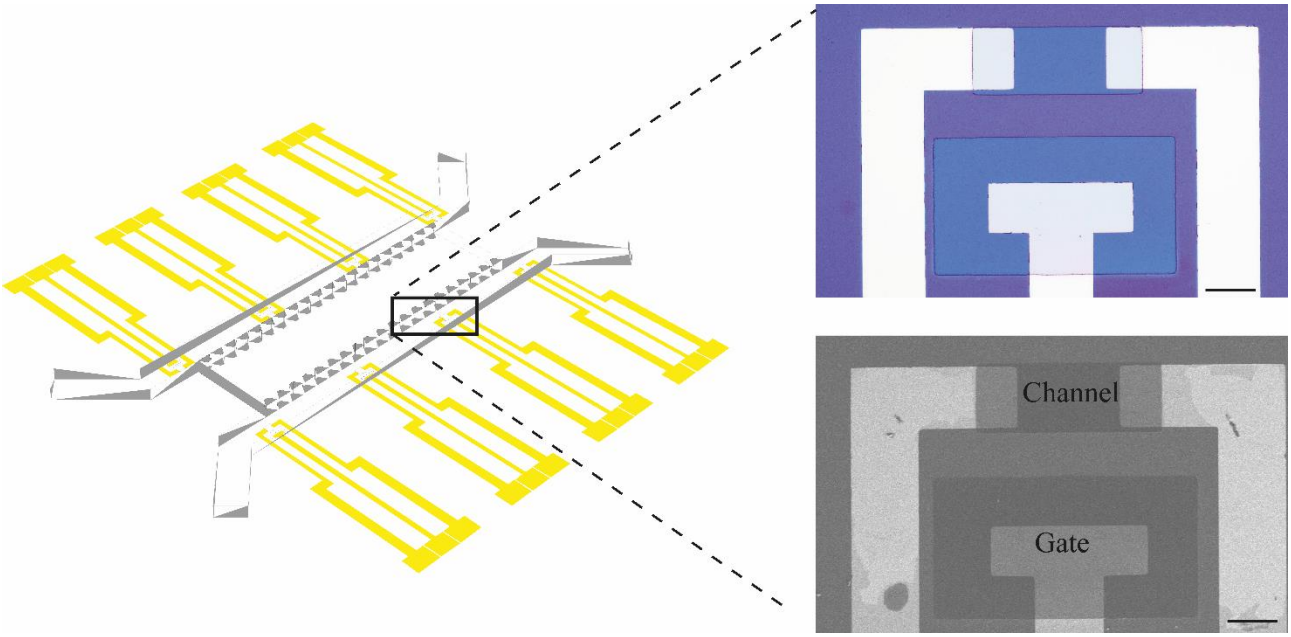

Figure 4.9 On the left a graphical design of complete system with 8 array of OECTs combined with the microfluidic device of BBB. On the right: Top) Brightfield image; Bottom) Scanning Electron Microscopy geometry of OECT, showing PEDOT: PSS used for channel and for Gate. Scale bar 100 µm.

The OECT comprises a degenerately doped CP channel in contact with an electrolyte. Upon application of a positive gate voltage (V_{GS}), cations from the electrolyte enter the channel, thus, de-doping the CP and decreasing the drain current (I_{DS}). The steady state I_{DS} is linearly proportional to the total number of ions that have entered the polymer film, and the ionic flux determines the speed at which the transistor reaches steady state. Thus, the OECT acts as a transducer of ionic signal to electronic current [15].

4.4.2 Electrical Impedance spectroscopy (EIS)

The first analysis that we performed to validate the effect of physiological shear stress on endothelial cell is the TEER. Since our tubular platform does not allow the integration of electrodes, we measured the frequency response of a planar OECT. This kind of analysis was performed with the use of Ag/Cl external gate.

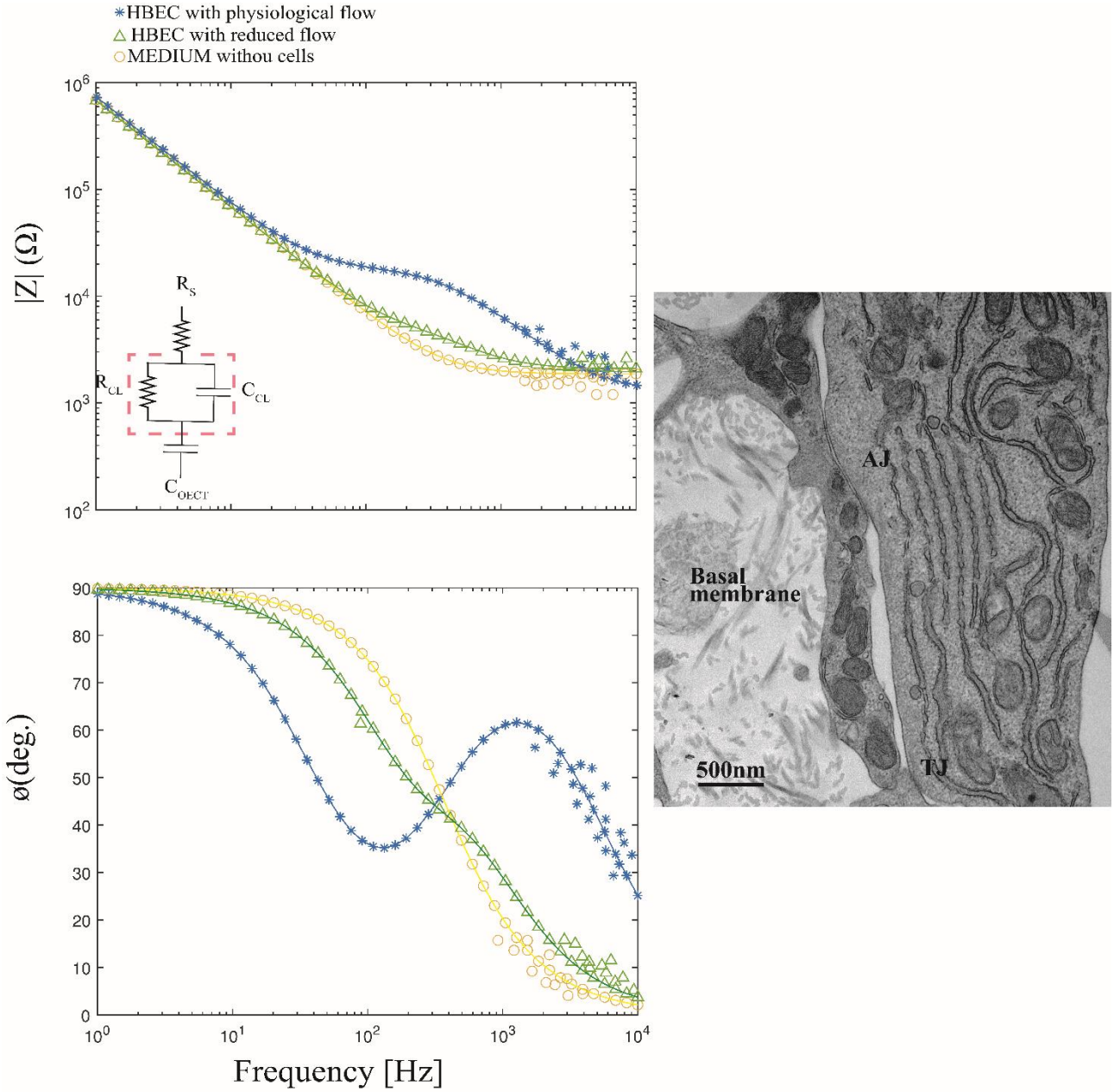

Figure 4.10 Bode plot. Measured and fitted impedance spectra in the presence and absence of a confluent cell layer covering the OECT channel for physiological and reduced shear stress. Representative impedance spectra recorded with and without a confluent layer lining the bottom substrate of the microfluidics/OECT platform. In the presence of a confluent layer of cells under physiological shear stress, the impedance spectrum shows a plateau region (f(Hz) ≤ 400 Hz) attributed to the paracellular resistance of the cell covering the active area of the device. The equivalent fitting curves calculated using an equivalent circuit model, previously show a discrete difference in the plateau region below 400 Hz attributed to changes in the cell layer resistance R_{cl}. On the right side, TRASMISSION ELECTRON SCANNING (TEM), show the coculture of NHA, and HBEC, in physiological conditions with a great interest in the formation of TJ (tight junction) and AJ (Adherent junction). Scale bar 500 nm.

Using the OECT, we determined electrically whether the cell layers form a tight barrier by means of a frequency-dependent measurement which shows the temporal evolution of the cell layer resistance (R_{cl}) and cell layer capacitance (C_{cl}) while cells were exposed to the physiological shear stress. Figure 4.10 reports measured impedance spectra in presence and absence of cells, and in case of physiological and reduced shear stress. To demonstrate that we have an increase of paracellular resistance in case of physiological shear stress we did fit the complex impedance data in Figure 4.10

to a simple model (inset of Figure 4.10). We chose to use an equivalent circuit for the no cell data of the media resistance (Rs) in series with a capacitor representing the charge storage in the OECT channel, C_{OECT}, which resulted in $R_s = 1.872\ k\Omega$, and $C_{OECT} = 230$ nF. Using these results, since the same OECT was then used with the cells, we did fit to a model that adds in series an R_{cl} and C_{cl} in parallel each other (the cell layer trans-epithelial electrical resistance (TEER) and capacitance). From the fit it was possible to calculate the values of $R_{cl} = 2.5\ k\Omega$ and $C_{cl} = 390$ nF after 5 day of reduced shear stress, and $R_{cl} = 4.1969\ k\Omega$ and $C_{cl} = 74$ nF after 5 days of physiological shear stress. Indeed, we performed this experiment up to a maximum of 6 days and observed that it was possible to reach the steady state EIS in 3-4 days, which is a lesser time if compared with culture transwell system (6-7 days). The resulting stronger increase in the R_{cl} in case of physiological shear stress can be attributed to the more effective reassembly of intercellular tight and adherent junctions due to FSS-induced mechano-transduction as compared to the case of reduced shear. This result suggests that the monitored increase in R_{cl} during and after FSS is possibly given by an increase in the density of the tight junction network, thus increasing cell layer resistance R_{cl} as observed from the electrical measurement. The cell layer resistance provides information on the ionic paracellular pathways, while the cell layer capacitance provides indirect information on the size and possibly shape of the cell. In fact, if we assume the cell membrane to be the equivalent of a capacitor insulator, changes in cell membrane area will affect the amount of stored electrical charge. The larger the cell membrane, the higher the capacitance of the cell layer. Importantly, the measurements are simultaneous and non-invasive, requiring a low gate voltage modulation. This is critical since a prolonged, excessive voltage bias across a tissue layer can be detrimental, causing rupture of membrane and cell death. [16]

4. 5 Morphological characterizations

Considering that another important parameter about the BBB *in vitro* is the permeability, in the next section we validate our system through the study of Dextran 40 kDa transport across our system, and a good analysis on the diffusion coefficient is performed with FRAP technique.

4.5.1 Dextran 40 kDa transport across the BBB

As further validation of the BBB microfluidic device, we performed transcytosis experiments to test the capability of FITC-Dextran 40 kDa to cross the endothelial layer. Dextran is known to cross the BBB through adsorptive transcytosis; therefore, it can be used as a valid standard to measure the system functionality under flow conditions. Dextran transport experiments were performed after 6

days of cell culture under dynamic conditions. The device was connected to a syringe pump and the cells were subjected to a flow rate of 2 µl/min comparable to others reported in literature [17].

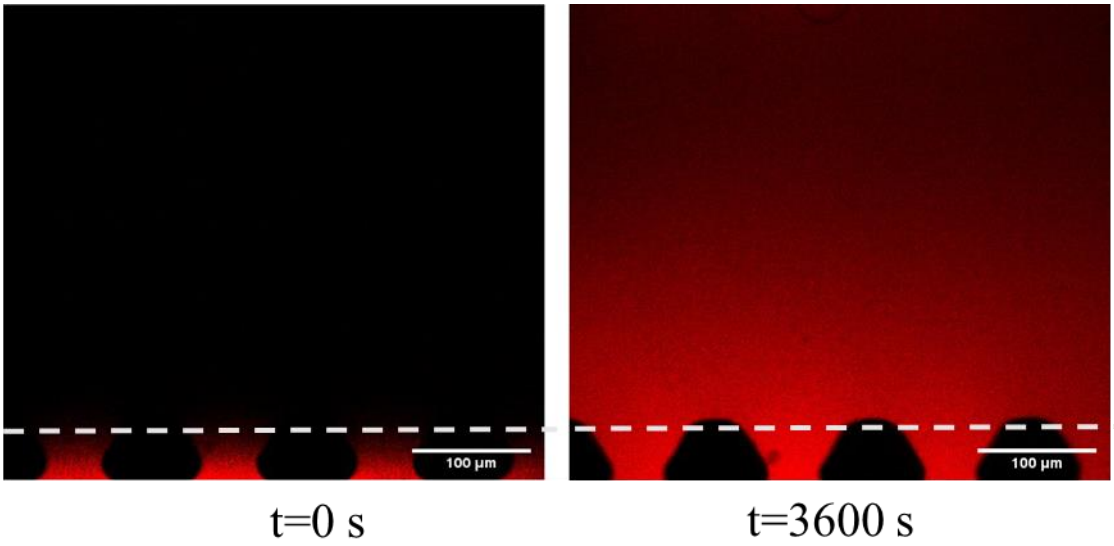

As shown in the Figure, we defined a line and calculated the amount of dextran accumulated on the other side of the line in the case of collagen, collagen with endothelium, and finally astrocytes embedded in the collagen with the endothelium. We performed the analysis according to the one described in the Chapter 2 for permeability analysis.

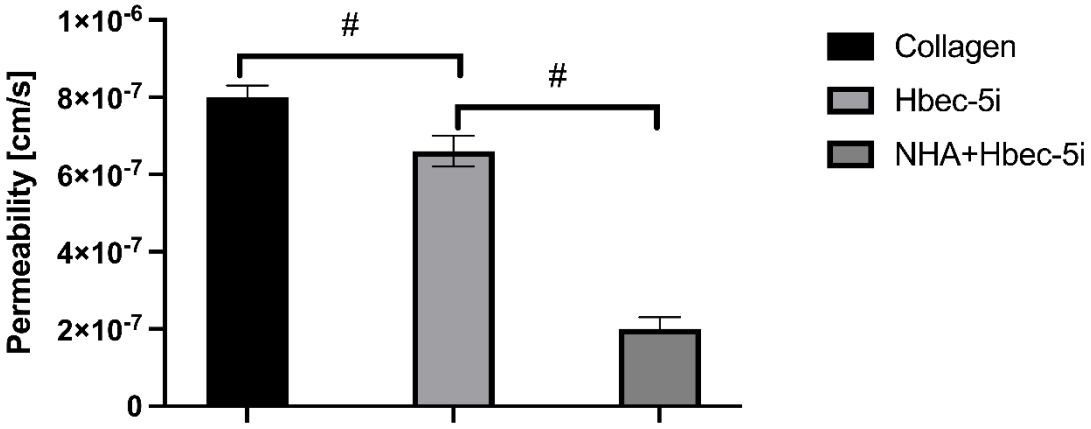

Figure 4.11 Permeability evaluated in the microfluidic device in three different cases. Only collagen, collagen with endothelial layer, and astrocytes embedded in collagen (to recreate the brain compartment) with endothelial cells. All the experiments were performed in triplicate (n = 3); values represent the mean and the standard deviation (# $p < 0.05$).

In Figure 4.11 we show the results of permeability measurement. In absence of cells, i.e for the microchannels that contained the cylindrical collagen gel without any cells almost 90% Dextran was transported by 3600 s. Conversely, in the case of microfluidic system with the confluent endothelial layer and astrocytes embedded in collagen with endothelial layer, there was a significant decrease in the Dextran permeation. In fact, after 1 h of Dextran flow we see that about 40 % of Dextran for

collagen with endothelium and 16 % of Dextran for collagen with astrocytes and endothelium is transported. We found that the presence of the human brain endothelium significantly restricted transfer of the fluorescent probe compared to control microchannels that contained the cylindrical collagen gel without any cells. Importantly, the permeability of the endothelium-lined vessel was reduced even further when astrocytes were co-cultured with the endothelium, thus synergistically improving barrier function and producing apparent permeability in the range of 2 to 3 $\times 10^{-6}$ cm/s (Figure 4.10), which are similar to values previously measured in other *in vitro* BBB models that have been realized with rat, mouse, bovine or immortalized human cells [18].

4.5.2 Frap analysis with Fourier Transform.

Since from the previous analysis we have seen that the permeability of tissue *in vitro* decreases in case of coculture of astrocytes embedded in the collagen matrix with endothelial cells, to assess the role of astrocyte in our microfluidic system we studied the diffusion coefficient in our co-culture system through a published method of Tsay and Jacobson, [19] for the video image analysis of fluorescence recovery after photobleaching (FRAP). In this approach, the diffusion coefficient is calculated from the decay of Fourier transform coefficients in successive fluorescence images, to make the diffusion coefficient independent of sample thickness. We performed this analysis in order to understand the effect of astrocytes on the diffusion coefficient of collagen.

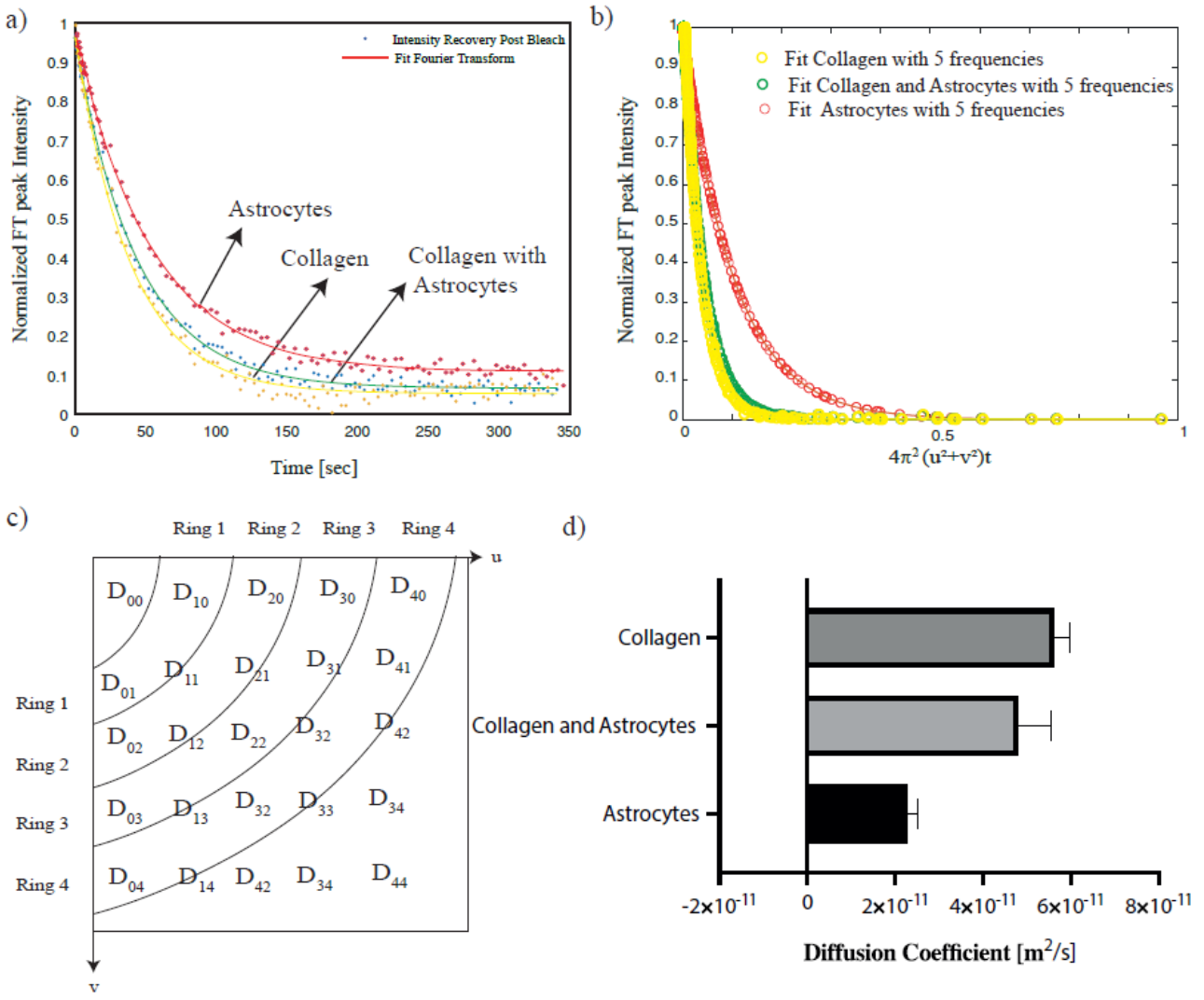

Figure 4.12 Frap analysis. In a) we show the Frap conventional photobleaching with Fit with Fourier Transform. In b) we show the evaluation of the Diffusion Coefficient in Fourier space, evaluating 5 frequencies with an error of 0.68%. In c) the Spatial frequency (u, v) assignment to "rings" for azimuthal averaging. In d) we show the results in terms of coefficient value in different cases (Water, Collagen and Collagen with Astrocytes). All the experiments were performed in triplicate (n = 3).

We decided to perform this kind of FT-FRAP in order to have a high signal noise ratio (SNR). Relative to conventional point-bleach FRAP, FT-FRAP has the advantages of mathematical simplicity, higher SNR, representative sampling, and multi-photon compatibility.

So, we calculated Diffusion coefficient's (D) by the decay of individual spatial frequency components as recovery proceeds (Figure 4.12 a). High-frequency components decay more quickly than the low-frequency components and are subject to more noise contamination (Figure 4.12 b). We averaged the D's obtained from approximately equivalent spatial frequencies defined by "rings" in Fourier space to provide some data smoothing for the case of isotropic diffusion. This amounts to an azimuthal averaging in the transform space to obtain more precise results. The assignment of spatial frequencies (u, v) to defined rings (1, 2, 3, 4, . . .) is illustrated in Figure 4.12c. For example, D2, represents the diffusion coefficient calculated at the spatial frequency defined by u = 2, v = 1, and D2, is assigned

to Ring 2. At the end we evaluated D for dextran diffusion in collagen and in collagen with astrocytes. As shown in Figure 4.12d, we found that the diffusion of dextran in the collagen matrix is slightly slower when astrocytes are present, but no relevant difference is seen. In fact, the calculated values are approximately $6.3 \cdot 10^{-11}$ m^2/sec for collagen and $5.5 \cdot 10^{-11}$ m^2/sec for collagen with astrocytes. Instead, when the frap is made on the cells, a great reduction of diffusion coefficient is seen ($2 \cdot 10^{-11}$ m^2/sec). This reduction is given by other cellular contributions such as cytoskeleton, etc. which is not the object of study in this work.

The slight difference between the two values ($6.3 \cdot 10^{-11}$ m^2/sec for collagen and $5.5 \cdot 10^{-11}$ m^2/sec for collagen with astrocytes) can be explained by a further reassembly of the collagen fibers in the presence of astrocytes. Indeed, as shown by the Scanning Electron microscopy images, the orientation of collagen fiber is isotropic and does not seem particularly dense (Figure 4.12A); conversely, when astrocytes are embedded in the matrix of collagen the collagen fiber seem denser and more compact. (Figure 4.12B).

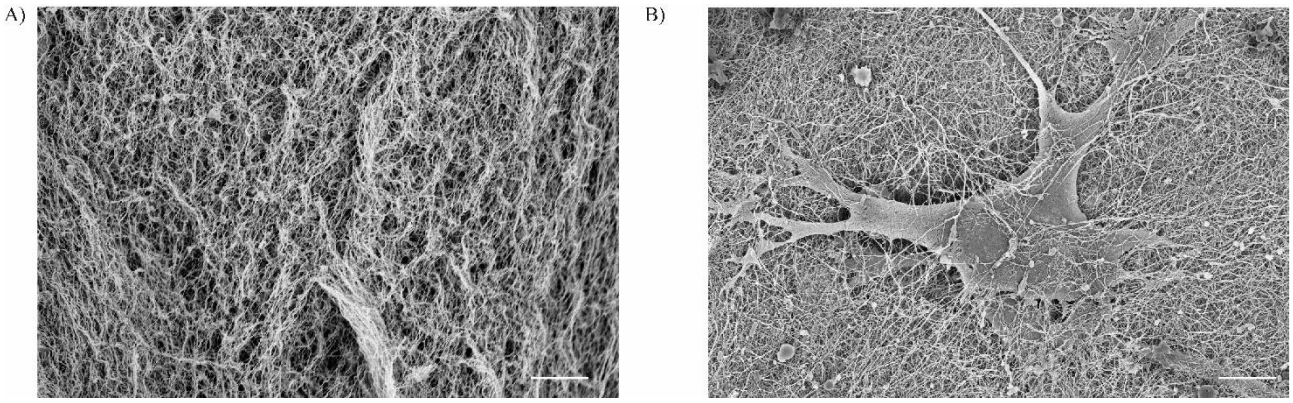

Figure 4.12 Scanning Electron microscopy images. A) the orientation of collagen fiber is isotropic and does not seem particularly dense B) with astrocytes collagen fiber seem more dense and more compact. Scale bar (10 μm)

Therefore, taking into account the slight difference in the coefficient diffusion between collagen and collagen embedding astrocytes, we can conclude that the reduction in BBB permeability measured in the previous section is essentially due to the improved robustness of the endothelial barrier in the presence of astrocytes.

4. 6 BBB in vitro crossing: gH625 peptide study

Since our goal is to realize a platform that *in vitro* mimics the blood brain barrier, having all the typical characteristics of the *in vivo* system to be used as a drug screening platform, we need to use sensors, in this case OECTs, to capture even the smallest change of construction and disruption of the barrier and the measurement itself should not alter at all barrier condition. For this reason, since the EIS measurements have a very good temporal resolution, we decided to monitor the integrity of barrier, using OECTs as ions sensor. In this case, when the barrier is completely formed, there is a reduction of cation flow that results in slower de-doping of the channel and consequently a change in the drain current (I_{DS}) that we can measure [20]. In the next section we perform experiment using transient response of OECT.

4.6.1 Monitoring Barrier through transient current

In case of OECT, there is no direct measurement of the ion conductance (or resistance) across the cell monolayer. Rather, the current through the OECT channel is linearly proportional to the number of ions that have entered the channel, which in turn determine the speed at which the transistor reaches steady state.[21] The time constant, τ, is used as a figure of merit for the electrical characterization of the ion flow through endothelial as measured by the OECT. For electrical characterization of hBEC cells seeded onto the OECT, the channel current was measured upon application of a positive square-pulse gate voltage. Similar to the charge and discharge of a capacitor in an RC electronic circuit, the channel current can be fit by an exponential equation 4.6 :

$$I_D = \alpha \left\{ \left[1 - e^{-\frac{(t-t_0)}{\tau}} \right] + \left[1 - e^{-\frac{(t-t')}{\tau'}} \right] \right\} \tag{4.6}$$

where α is a constant scaling term describing the magnitude of the current response, t_0 is the time at which the pulse starts, and τ is the time constant discussed above. Equation 4.6 is found to fit the experimental data well, both with and without cells, we report in Figure 4.13a the electrical behavior of the circuit where the increasing in the resistance causes the descending curve of the current (dashed part in Figure 4.13a). The second exponential term, described by a time offset and time constant t' and τ', is incorporated to describe the long-time evolution of the drain current, so since our interest in is the rapidly response of OECT, we can exclude this second term from our study. A background is subtracted by considering the time response with no cells. The data are then normalized using the following equation: $NR = (T_{no\ cells} - T)/ (T_{no\ cells} - T_{cells})$, where T_{cells} refers to the τ value in response

to the application of the gate voltage of a barrier forming monolayer, and τ_{no} cells refers to the τ value in response to the application of the gate voltage of no barrier [20].

After seeding hBEC cells, the rise of τ (Figure 4.13 B) started as early as at first day and plateaued between the fourth and fifth days. In order to assess that the measurements were connected with tight junction, immunofluorescence analysis have been performed at some corresponding times (i.e. 1, 4, 6 days) and showed the presence of tight junction marked in green increased over time (Figure 4.13 C).

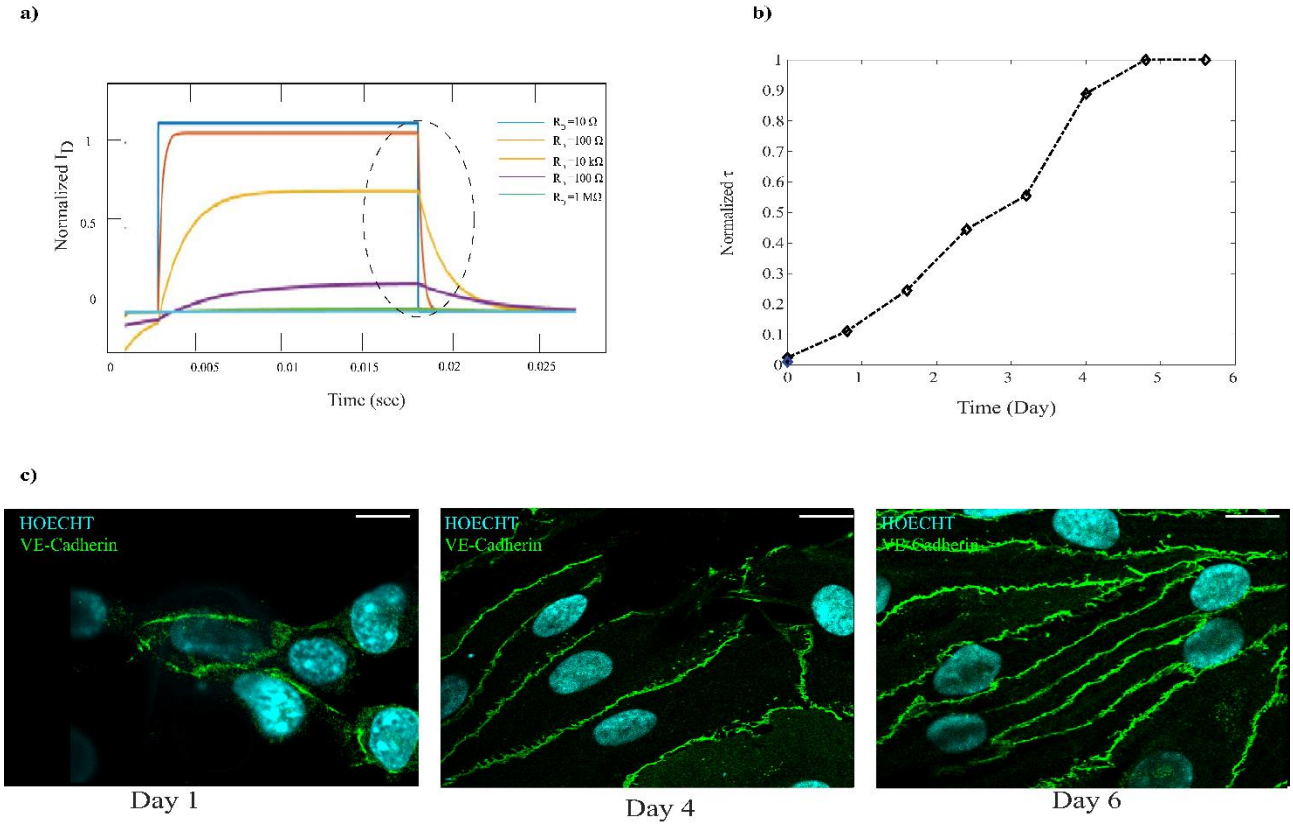

Figure 4.13 Electrical and optical characterization of Tubular Blood brain barrier on the planar OECT. Endothelial cells (EC) were seeded at 10^5 cells/cm^2 and monitored for 6 days. Electrical characteristics with a measurement taken every 3 h for 6 days. In A) we show the electrical behavior of the channel current of the OECT, in which the descending part of current was fit with the equation I_{DS}. This graphic is only a Simulink simulation performed in order to show the changing in the pulsed current I_{DS}. B) From the fit data with the equation (2), we plot normalized Tau, that gives information about the integrity and tightness of the barrier formed by EC. In particular normalized value of tau=1 [20] corresponds to the high value of integrity of barrier, value reached around 5 days, confirmed by the immunofluorescence.C) Immunofluorescence images shows the quality of tight junctions assessed by means of VE-Cadherin stainingconfirming the correspondence between the measurements and the behavior of cells. The images were examined with Leica (Confocal Leica TCS SP5 II femtosecond laser scanning system, Leica) confocal microscope. with Leica Multiphone. Experiment was performed on three different device, for 6 days while 18 electrical measurement were performed (3 every single day). Scale bar 20 µm

4. 6.2 Monitoring Barrier interaction with gH625 peptide

Advances in molecular biology, nanotechnology, and pharmaceutical chemistry have led to the rapid evolving interdisciplinary field of nanomedicine, with the production of several new classes of imaging agents and highly potent drugs. Drugs are often characterized by physicochemical and/or biological features that make their use not ideal in humans; however, nanosized delivery systems (liposomes, micelles, and polymeric systems) can circumvent these problems by improving the therapeutic index.[22] Apart from a few exceptions, nanocarriers have met with moderate success, mainly because of their behavior in vivo [22]. Free diffusion of circulating molecules from the blood into the brain is made difficult by the presence of the blood–brain barrier (BBB), which is, as we just say until now, a complex physiological checkpoint in the central nervous system, preventing passage of both beneficial drugs and potentially toxic molecules.[23] For this reason, many diseases affecting the brain still cannot be treated effectively. Therefore, development of novel systems that can significantly enhance the delivery of therapeutic agents across the BBB represents a fundamental challenge for the treatment of several brain diseases.[24] Taking advantage from our assessed model, we decided to investigate the response of the OECT to the crossing of our 3D blood brain barrier (BBB) *in vitro* by the gH625 peptide. It is known that gH625 is a membranotropic peptide that *in vivo* allows the transcellular crossing of the BBB. The process of incorporating a healthy cell layer and rupturing its integrity by gH625, has been monitored by the change of the OECT output voltage in the transfer characteristics to see the moment in which we can have the breakdown of the barrier. First of all, we assessed the OECT electrical behavior of the two compounds. Different gH625 concentrations have been used to evaluate the effect on the transfer characteristics as well as on the response times and compared to the scramble peptide (Figure 4.14). It is observed that the transconductance changes as the concentrations of the two components increase. Since no redox reactions occur between the medium and the components, these changes are due to the pH changes that occur at the interface between the gate and gH625 or scrambled peptide. We performed pulsed measurement of the device under flow condition of medium solution at varying concentrations of gH625 and scrambled peptide. In Figure 4.14 a-c) we report the conductance changes versus voltage pulses with the increase of biomolecule concentration, and in Figure 4.14 c-d) we show the same behavior seen with pulsed measurement also in the steady state for both compounds by looking at the developed I_{DS}. All this allows us to calibrate the response of our OECT, to the minimum variation of concentration, and attribute different responses to different phenomena that may occur. We performed this measure in order to identify a blank behavior (different concentration in solution without cells) that we subtracted to be sensitive in this way only to the change of gH625/scrambled peptide with

cells and removing other ionic interactions. According to Guarnieri et al [17], the gH625, is able to traverse the membrane bilayer and transport a cargo (quantum dots, liposomes, and dendrimers) into the cytoplasm and across an *in vitro* model of the BBB. Uptake studies suggested a non-active translocation mechanism in crossing the lipid bilayer, which may vary depending on the cargo.[25] Penetration by gH625 occurs in a rapid, concentration-dependent fashion that appears to be independent of receptors and transporters and instead is thought to target the lipid bilayer component of the cell membrane.

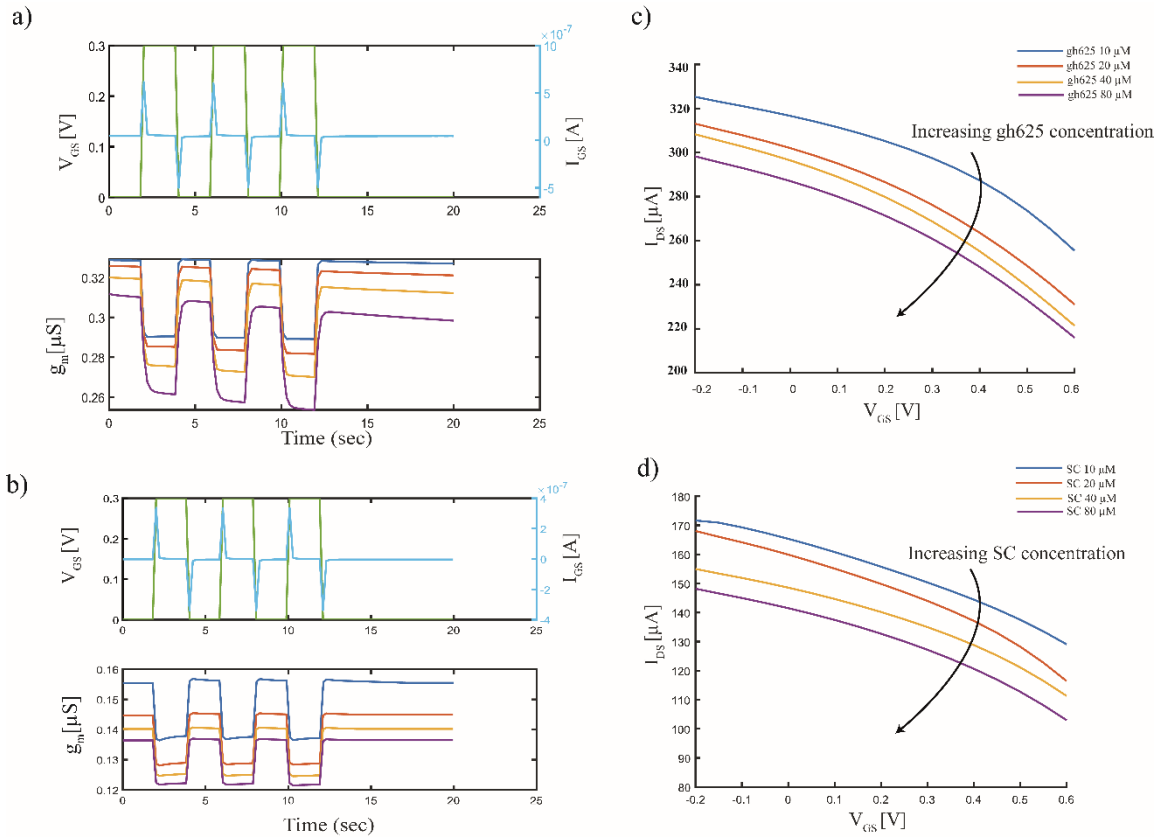

Figure 4.14 The transient response of the OECT after the addition of 10 µM to 80 µM of an aqueous solution of gH625 and scrambled peptide in cells medium. a -b) Pulsed measurements of the device under microfluidic flow of medium solution at varying concentrations showing the conductance change versus voltage pulses upon increasing biomolecule concentration. This change is visible also in the stationary behavior of the OECTs (c-d).

Therefore, we show how our system is capable to detect the rapid and continuous penetration of gH625 in the endothelial layer through the OECTs working principle (Figure 4.15); moreover, the system records over time the variation of the drain current which provides us information both on the integrity and destruction of the barrier. Specifically, through our system we are able to detect the instantaneous entrance of gH625 and – more interesting – we can also detect the instant in which the barrier rebuilds itself. According to the Figure 4.15a, we can monitor different instant in which the

peptide enters the barrier: these different instants are due to the continuous flow of peptide at the interface with the endothelial cells. In order to verify the real presence of the peptide in the endothelial barrier, an immunofluorescence was performed. We show, in Figure 4.15 b, the accumulation of the peptide (green), so the breakdown, and the presence in the form of Claudin 5 (pink) of the barrier within endothelial cells (the reconstruction). Simultaneously, in order to control the effect of gH625, we performed the same experiment with a scrambled, i.e., a peptide with the same number of amino acids of gH625, that we consider as our control. As showed in Figure 4.15c, we did not observe changes in I_{DS} when we introduce the scrambled peptide; furthermore, immunofluorescence analyses demonstrated that the scrambled peptide did not accumulate in the endothelial cells. In fact, the signal linked to the scrambled peptide (green) was not found in the negative control for the immunofluorescence technique, while for the same analyses tight junctions (pink) are always present (Figure 4.15d).

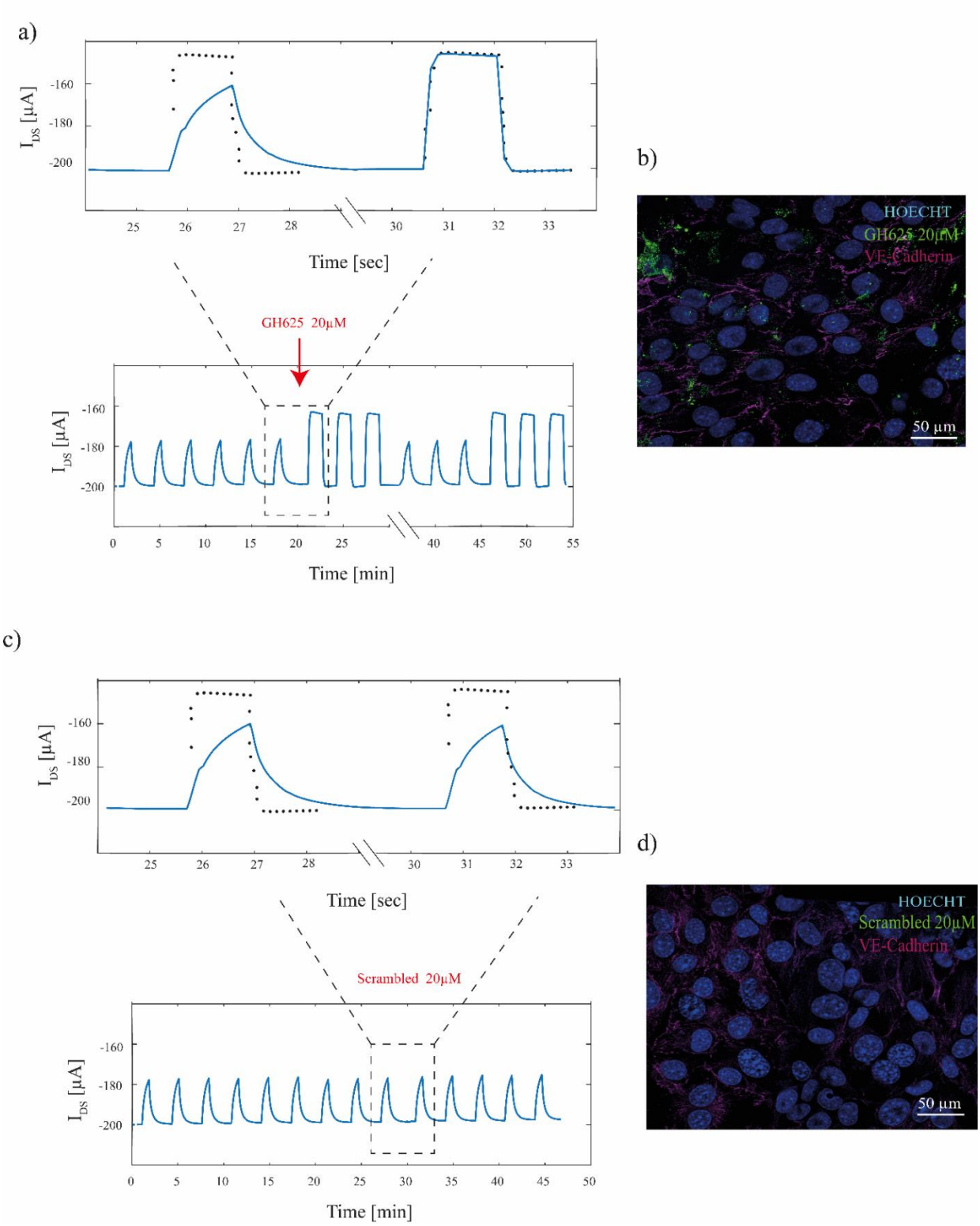

Figure 4.15 Monitoring barrier tissue integrity with an OECT. a) e c) OECT I_{DS} transient response with cells before (left) and after (right) the addition of 20 µM GH625 and 20 µM Scrambled, (solid lines). OECT I_{DS} response in the absence of tight junction is overlaid (dashed lines). In situ OECT response to periodic square V_{GS} pulses. As indicated, data here correspond to the same measurement as shown in, but for an expanded time scale. The red arrow indicates the point of gH625 and Scrambled introduction. The immediate change in OECT response to the addition of gH625 is evident by the drastic change in ΔI_{DS} while no changing is visible in case of Scrambled. b) e d) Immunofluorescence analysis showing the presence of peptide inside the endothelial cells (green) while no signal is evident in the negative control (Scrambled). The quality of tight junctions was assessed by means of VE-Cadherin staining (magenta). The results show the entrance of gH625 peptide, regarding by the electrical signal, and its presence with immunofluorescence analysis. Experiment was performed on three different device while 10 electrical measurements were performed.

Furth more, another interesting application of our organic device is to use it as a neurotransmitter sensor combined with 3D model of BBB. We show in Figure 4.16 that when dopamine (DA), (but in principle any type of neurotransmitters) is added to the medium, an increasing of transconductance is seen according to the concentration of dopamine. This behavior can be explained by considering that an electrochemical process, i.e. dopamine oxidation, takes place at the gate electrode.[25] This process occurs exclusively at an electrochemical potential that is characteristic of dopamine, in our case 0.1 V and it affects the gate current, and consequently I_{DS}, only at a specific V_{GS}. Since DA oxidation leads to an I_{GS} increase, likewise the gate action increases and more charge carriers are extracted from the channel with respect to the blank solution, leading to a higher I_{DS} decrease. Since the redox current is directly proportional to DA concentration, the I_{DS} decrement increases by increasing DA concentration.

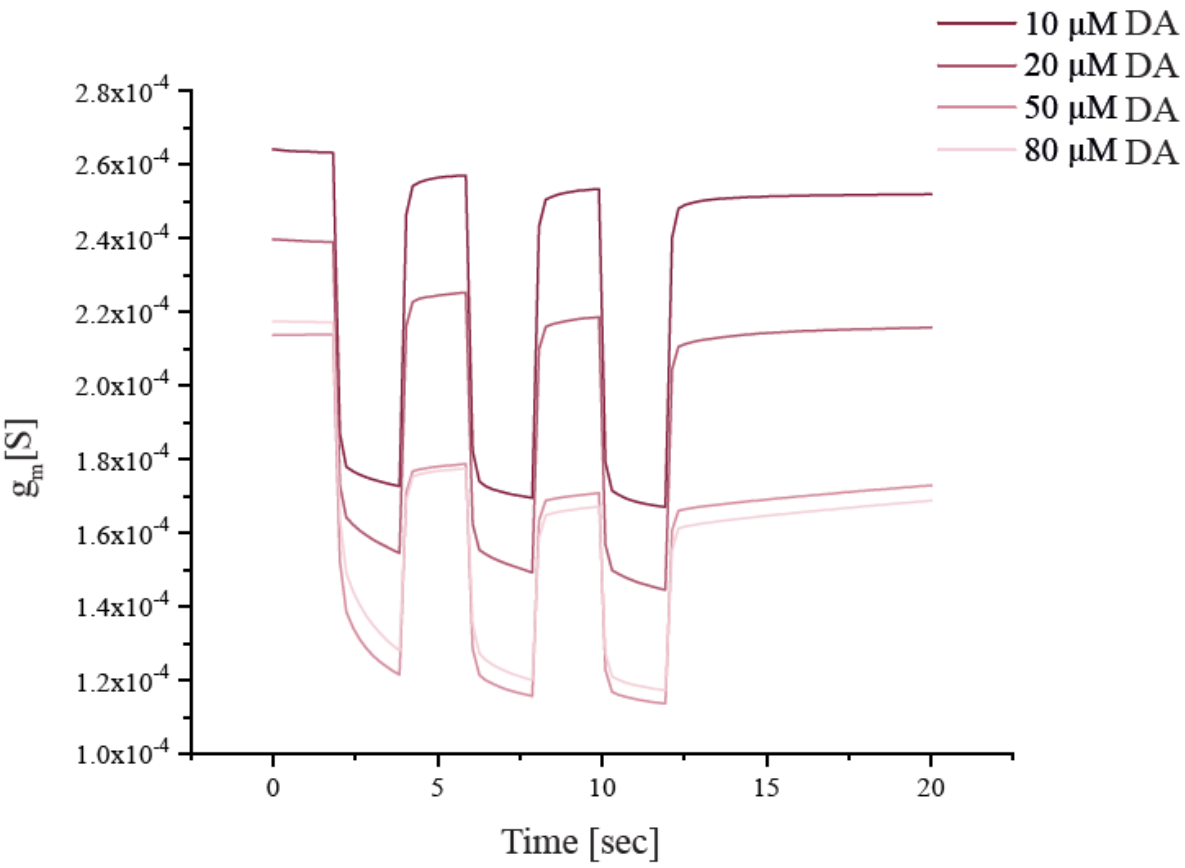

Figure 4.16 Calibration of the organic electrochemical transistor device with increasing dopamine concentration. Pulsed measurements of the device under microfluidic flow of medium solution at varied dopamine concentrations showing the conductance change following voltage pulses with increasing dopamine concentration.

4. 7 Conclusion

Motivated by the strong need in the microfluidic fields for circular blood brain barrier *in vitro*, we propose an advanced 3D BBB model which replicates the tubular shape of the BBB and integrates an OECT sensor capable to monitor real time BBB integrity.

We assessed the ability of our system to mimic the BBB model by morphological and electrical analysis. It has been demonstrated that the integrated OECT allows monitoring the formation of the brain barrier, and more interestingly the breakdown caused by interaction with gH625, a membranotropic peptide known to cross the BBB. These results open different perspectives for applications in the field of drug delivery. It would be possible, in fact, with this model, to study the effect of drug delivery in the case of neurodegenerative pathologies which are typically associated with the damaging of the blood brain barrier. Moreover, since OECTs are a valid detector of neurotransmitters such as dopamine, this platform could be used to realize an *in vitro* model involving the addition of neurons. In this way it would be possible to study the behavior of cells in presence of oxidative stress and evaluate the effect of drugs. Our next goal is to create a damage model of BBB to mimic neurodegeneration in Parkinson's Disease and screen antioxidant free and nano-encapsulated drugs by monitoring the system with the integrated OECT from one side and a specific pathological biomarker from the other side.

Bibliography

[1] U. Nanomaterials, “Drug Delivery to the Brain across the Blood – Brain Barrier,” vol. 1701921, pp. 1–17, 2017, doi: 10.1002/smll.201701921.

[2] Y. Zhou, Z. Peng, E. S. Seven, and R. M. Leblanc, “Crossing the blood-brain barrier with nanoparticles,” *J. Control. Release*, vol. 270, no. October 2017, pp. 290–303, 2018, doi: 10.1016/j.jconrel.2017.12.015.

[3] M. M. Modena, K. Chawla, P. M. Misun, and A. Hierlemann, “Smart Cell Culture Systems: Integration of Sensors and Actuators into Microphysiological Systems,” 2018, doi: 10.1021/acschembio.7b01029.

[4] N. J. Abbott, A. A. K. Patabendige, D. E. M. Dolman, S. R. Yusof, and D. J. Begley, “Structure and function of the blood-brain barrier,” *Neurobiol. Dis.*, vol. 37, no. 1, pp. 13–25, 2010, doi: 10.1016/j.nbd.2009.07.030.

[5] N. J. Abbott, “Physiology of the blood-brain barrier and its consequences for drug transport to the brain,” *Int. Congr. Ser.*, vol. 1277, pp. 3–18, 2005, doi: 10.1016/j.ics.2005.02.008.

[6] L. Cucullo, M. Hossain, V. Puvenna, N. Marchi, and D. Janigro, “The role of shear stress in Blood-Brain Barrier endothelial physiology,” pp. 1–15, 2011.

[7] M. W. van der Helm, A. D. van der Meer, J. C. T. Eijkel, A. van den Berg, and L. I. Segerink, “Microfluidic organ-on-chip technology for blood-brain barrier research,” *Tissue Barriers*, vol. 4, no. 1, 2016, doi: 10.1080/21688370.2016.1142493.

[8] A. Manuscript, “Lab on a Chip,” 2016, doi: 10.1039/C5LC01481F.

[9] A. Herland, A. D. Van Der Meer, E. A. FitzGerald, T. E. Park, J. J. F. Sleeboom, and D. E. Ingber, “Distinct contributions of astrocytes and pericytes to neuroinflammation identified in a 3D human blood-brain barrier on a chip,” *PLoS One*, vol. 11, no. 3, pp. 1–21, 2016, doi: 10.1371/journal.pone.0150360.

[10] F. Urciuolo *et al.*, “Biophysical properties of dermal building-blocks affect extra cellular matrix assembly in 3D endogenous macrotissue Biophysical properties of dermal building-blocks affect extra cellular matrix assembly in 3D endogenous macrotissue,” 2016.

[11] L. L. Bischel, S. Lee, and D. J. Beebe, “A Practical Method for Patterning Lumens through ECM Hydrogels via Viscous Finger Patterning,” 2012, doi: 10.1177/2211068211426694.

[12] T. Bourouina, “DRIE TECHNOLOGY : FROM MICRO TO NANOAPPLICATIONS DRIE TECHNOLOGY : FROM MICRO TO NANOAPPLICATIONS,” no. May, 2014.

[13] O. Tornavaca *et al.*, “ZO-1 controls endothelial adherens junctions, cell–cell tension, angiogenesis, and barrier formation,” vol. 208, no. 6, pp. 821–838, 2015, doi: 10.1083/jcb.201404140.

[14] X. Wang *et al.*, “Advances on fluid shear stress regulating blood-brain barrier,” *Microvasc. Res.*, vol. 128, no. September 2019, p. 103930, 2020, doi: 10.1016/j.mvr.2019.103930.

[15] M. Berggren, R. Forchheimer, J. Bobacka, P. Svensson, and D. Nilsson, “PEDOT : PSS-Based Electrochemical Transistors for Ion-to-Electron Transduction.”

[16] M. Ramuz, A. Hama, J. Rivnay, P. Leleux, and R. M. Owens, “Monitoring of cell layer coverage and differentiation with the organic electrochemical transistor,” *J. Mater. Chem. B*, vol. 3, no. 29, pp. 5971–5977, 2015, doi: 10.1039/c5tb00922g.

[17] A. P. Falanga *et al.*, “Shuttle-Mediated Nanoparticle Transport Across an In Vitro Brain Endothelium Under Flow Conditions,” doi: 10.1002/bit.26221.

[18] P. J. Gaillard and A. G. De Boer, “Relationship between permeability status of the blood-brain barrier and in vitro permeability coefficient of a drug,” *Eur. J. Pharm. Sci.*, vol. 12, no. 2, pp. 95–102, 2000, doi: 10.1016/S0928-0987(00)00152-4.

[19] T. T. Tsay and K. A. Jacobson, “Spatial Fourier analysis of video photobleaching measurements. Principles and optimization,” *Biophys. J.*, vol. 60, no. 2, pp. 360–368, 1991, doi: 10.1016/S0006-3495(91)82061-6.

[20] L. H. Jimison *et al.*, “Measurement of barrier tissue integrity with an organic electrochemical transistor,” *Adv. Mater.*, vol. 24, no. 44, pp. 5919–5923, 2012, doi: 10.1002/adma.201202612.

[21] M. Ramuz, A. Hama, M. Huerta, J. Rivnay, P. Leleux, and R. M. Owens, “Combined optical and electronic sensing of epithelial cells using planar organic transistors,” *Adv. Mater.*, vol. 26, no. 41, pp. 7083–7090, 2014, doi: 10.1002/adma.201401706.

[22] F. ud Din *et al.*, “Effective use of nanocarriers as drug delivery systems for the treatment of selected tumors,” *Int. J. Nanomedicine*, vol. 12, pp. 7291–7309, 2017.

[23] S. Bang *et al.*, “A Low Permeability Microfluidic Blood-Brain Barrier Platform with Direct Contact between Perfusable Vascular Network and Astrocytes,” *Sci. Rep.*, vol. 7, no. 1, pp.

1–10, 2017, doi: 10.1038/s41598-017-07416-0.

[24] S. Valiante *et al.*, “Peptide gH625 enters into neuron and astrocyte cell lines and crosses the blood–brain barrier in rats,” *Int. J. Nanomedicine*, vol. 10, pp. 1885–1898, 2015, doi: 10.2147/IJN.S77734.

[25] Y. Chen and L. Liu, “Modern methods for delivery of drugs across the blood-brain barrier,” *Adv. Drug Deliv. Rev.*, vol. 64, no. 7, pp. 640–665, 2012, doi: 10.1016/j.addr.2011.11.010.

CHAPTER 5

Immunocompetent Microbiota-gut axis on-chip reproduces barrier dysfunction, stromal reshaping and microbial species translocation under inflammation.

The following chapter is extrapolated from an article currently in submission, made in collaboration with the researcher Vincenza De Gregorio at University of Naples Federico II. The work aims to recreate the typical microenvironment of the microbiota-gut (gastrointestinal tract). The elaborate is presented only in the part of my competence, relating to the fabrication and characterization of the microfluidic device MihI-oC, simulations and oxygen measurements inside the microbiota-gut on chip. At the end we report the assessment of the MC functionality with the comparison of single strains growth into the anaerobic workstation (AW) vs MihI-oC in order to verify the good performance of this microfluidic device. This work is only part of a larger project that aims to recreate a GUT-BRAIN axis model. The concept of gut-brain axis is being actively explored, and many studies have confirmed that alterations in gut microbiota composition are associated with certain clinical conditions. Existence of a biological link among microbiota, immune signaling, and CNS (Central nervous system) indicates that both neurological and immunological activities in brain could be determined either directly by microbial metabolites or indirectly by microbiota-derived systemic signals [20]. The applications of therapeutic modulators have already shown promising results in various mood disorders, such as autism and depression [21]. However, as the details of gut-brain axis are still unclear, it is critical for future studies to clarify specific mechanisms by which gut microbes contribute to the progression or regression of certain pathological conditions. In this perspective, our final project is to use the two models of organs proposed so far, namely BBB and Gut, (the first discussed in the Chapter 4 and the latter which will be discussed in this chapter), and through the OECT try to identify the information that the Gut exchanges with the BRAIN both from the electrical and biochemical point of view. These studies may provide a basis for advanced therapeutic approaches, along with current therapeutic modalities as well as the identification of novel biomarkers, for early diagnosis and intervention of CNS disorders.

Introduction

The development of novel and reliable human intestinal in vitro models able to replicate the crosstalk between living microbial components, intestinal mucosa and immune system, is a fundamental technological tool to aid researchers in elucidating the role of microbiota in maintaining intestinal health and immune regulation [1]. To fully understand the functionality of the intestinal microbiota, greater attention must be paid to the microhabitats within the intestinal ecosystem and the spatial relationships among microorganisms and between microorganisms and the host. Moving inward along the crypt-villus axis the surface of the macrovilli and crypts is colonized by adherent species [2] and the epithelium colonized by obligate anaerobic bacteria completely embedded within the mucus at the lumen side [3]. This bacterial stratification is strictly related to the intraluminal oxygen gradient and has been extensively shown to have profound effects on population dynamics and ecosystems that in turn affect the intestinal tissue functionality [4]. Recently, great attention has been given to the integration of tissue engineering approaches with microfluidics techniques to mimic in vitro the paracrine and endocrine crosstalk between gut microbiota and intestinal mucosa. Some models have been proposed in which intestinal gut microbiota and intestinal mucosa are separated in different modules [5] or by porous membranes coated with synthetic mucus [6] or posed in direct contact in double layer model (epithelial, endothelial cells) introducing the mechanical stretch to mimic the peristalsis motion [7]. However, all these models, are still based on intestinal epithelial cells grown on synthetic substrates non-considering the key role of the lamina propria, in terms of molecular composition and mechanical properties, in affecting epithelium morphogenesis, immunological response, microbial behavior as well as disease progression [8, 9]. Here, we developed an immune-responsive Microbiota-human Intestine axis on chip in which microbiota species, vertically stratified, are in direct contact with a complex intestinal environment consisting of a responsive 3D basal lamina, a fully differentiated epithelium and circulating peripheral blood mononuclear cells (PBMCs). The chapter is organized as follow, first of all, we show the develop model of a 3D human intestine, then we fabricate a custom-made Microbiota chamber in order to recreate in vitro a luminal serosa oxygen gradient. At the end, we prove the role of microbiota on stromal reshaping of collagen fiber orientation.

Table of contents

CHAPTER 5 145

Immunocompetent Microbiota-gut axis on-chip reproduces barrier dysfunction, stromal reshaping and microbial species translocation under inflammation. 145

Introduction 147

5.1 Cells and microbial strains culture conditions 150

5.2. Organotypic 3D human intestine (3D-hI) model development 151

5.3. Microbiota human Intestine on chip (MihI-oC) design, assembly and operation 152

5.3.1. Microfluidic device fabrication 152

5.3.2 MihI-oC assembly: Microbiota chamber (M_C) design and application on human intestine on chip (hI-oC) 153

5.3.3. Computational model of MihI-oC 154

5.3.4. On-line Oxygen concentration measurement 156

5.4. Assessment of the M_C functionality: comparison of single strains growth into the anaerobic workstation (AW) vs MihI-oC 156

5.4.1. Total and viable count 156

5.4.2. Live/Dead assay 157

5.4.3. Ultrastructural and morphological characterization of microbiota 157

5.5 Statistical Analysis 158

5.6 Results and Discussion 158

5.6.1 Establishing hypoxic environment in Microbiota Chamber (MC) of MihI-oC 159

5.6.2 Microbiota Chamber (M_C) promotes microbial strains growth and oxygen gradient across the MihI lumen 161

5.6.3 Establishing physiological vertical localization of microbiota in MihI-oC 165

5.7 Conclusion 167

Supplementary 172

Conclusion 179

5.1 Cells and microbial strains culture conditions

Human colonic epithelial cell lines (Caco-2) were purchased by American Type Culture Collection (ATCC) and cultured in High-glucose DMEM (Hg-DMEM, GIBCO) supplemented with 10 % of fetal bovine serum (FBS), 2 mM L-glutamine, and 100 U mL^{-1} penicillin and streptomycin (Sigma Aldrich) and grown at 37 °C in a 5% CO_2 humidified incubator. Human intestinal subepithelial myofibroblasts (hISEMFs) were isolated from the human ileal mucosa obtained by endoscopic duodenal biopsies after informed consent as previously reported [10] and cultured in DMEM supplemented with 10% heat-inactivated FBS, 2 mM L-glutamine, and 100 U mL^{-1} penicillin and streptomycin (Sigma Aldrich). Cells at the passages 6-8 were used for the experimental phase. Human peripheral blood mononuclear cells (PBMCs) were isolated by using buffy coat separation from whole blood; 30 mL of peripheral human blood taken from healthy donors were collected, after informed consent, into BD Vacutainer™ Plastic Blood Collection Tubes with K2EDTA to avoid coagulation. The whole blood volume was diluted 1:1 with phosphate-buffered saline (PBS, Sigma Aldrich) and put on an equal volume of a density gradient media (Ficoll, Sigma Aldrich) in standard 50 mL plastic tubes. The samples were centrifuged at 250 g × 30 min without using the machine brake. Subsequently, the resulting PBMC ring was collected using a standard glass Pasteur pipette and washed twice with Red blood cell lysis buffer to exclude the erythrocyte contaminations of the sample. Afterward, PBMC were concentrated at 10^6 cells/mL and flowed into the serosal compartment (S_C) of the microfluidic device. Two strains of probiotic bacteria were obtained in commercial lyophilized form, namely Lactobacillus rhamnosus (L. rhamnosus) GG strain (ATCC 53103) and Bifidobacterium longum (B. longum) (subspp infantis) (ATCC 15697). The first one was grown 18-24 h in static de Man-Rogosa-Sharpe broth (MRS, Oxoid) in microaerophilic condition based on an atmosphere of 10 % H_2, 10 % CO_2 (Concept plus anaerobic workstation (AW), Ruskinn technology limited) at 37 °C, while the second one was cultured in M151 medium (Oxoid) for 24-48 h in an anaerobic incubator with an anaerobic gas mixture 10 % H_2, 10 % CO_2, and 80 % N_2 or in 100% N_2 (Concept plus AW, Ruskinn technology limited). For each bacterial strain, five colonies were collected, inoculated into the previously degased selective broth media, and incubated at 37°C for 18-24 h in microaerophilic (L. rhamnosus) or in anaerobic conditions (B. longum). For the experimental phase, aliquots (50 µl) of the bacterial suspensions were refreshed into 20 mL of fresh growth media and cultured for 2 h at the optimal culture conditions. The optical density was read at 600 nm (OD600) by turbidimetric analysis (BioPhotometer Eppendorf, Milan, Italy) and bacterial suspensions at the exponential phase were selected.

5.2. Organotypic 3D human intestine (3D-hI) model development

Gelatine porous microscaffolds (GPMs) having a diameter of 75-150 µm, stabilized by 4% of glyceraldehyde were fabricated by means of a modified double emulsion technique (O/W/O) as previously reported [10]. Briefly, gelatine (type B, Sigma Aldrich, Bloom 225, Mw 176,654 Da) was dissolved into 10 ml of water containing TWEEN 85 (6% w/v) (Sigma Aldrich) at 60 °C. A mixture of toluene and SPAN 85 (3% w/v; Sigma Aldrich) was constantly added to the aqueous gelatin solution (8% w/v; Sigma Aldrich) to obtain primary oil in water emulsion. GPMs containing droplets of toluene were produced through the addition of excess toluene (30 ml) and then cooled at 4 °C. Subsequently, in order to extract toluene and stabilize the GPMs, 20 ml of ethanol were added and the newly produced microspheres were filtered, washed with acetone, and dried at room temperature. To make the human Intestine-µTPs (hI-µTPs), a suspension containing hISEMFs (1 x 10^5 hISEMFs/mL) and 2 mg/ml of microbeads (10 cells per bead) was transferred to a spinner flask bioreactor (250 ml, CELLSPIN, Integra Biosciences) for at least 10 days. The culture suspension was stirred intermittently at 10 rpm (5 min stirring and 40 min in static condition) for the first day in order to promote cell adhesion; then the stirring velocity was increased to 20 rpm for the further 10 days. All cultures were maintained at 37 °C in a humidified 5% CO_2 incubator. Three times per week the media was replaced and 2-O-alpha-D-Glucopyranosyl-L-ascorbic Acid 0.5 mM (TCI Europe) was added. Then, the hI-µTPs were harvested from spinner cultures and transferred into a suitably designed assembling chamber, which contains a silicon mold with disc-shaped spaces (1 mm in thickness, 10 mm in diameter), where the hI-µTPs biological assembling takes place. Stainless steel rigid grids are posed directly on both sides of the system. Then, two polytetrafluoroethylene (PTFE) rings are located on the grids on both system sides and are fastened to each other by means of stainless steel screws, which close the system to ensure that the hI-µTPs are retained. The system is autoclavable in each part. Additionally, after accommodating the assembling chamber, the spinner flask has been set to operate at 60 rpm to ensure the continuous media stirring and the medium was changed three times per week. After 3 weeks of culture, the assembling chamber was opened and the 3D Intestinal stroma (3D-ISs) samples were collected, rinsed twice with PBS solution, and accommodated in transwell insert (diameter, 6.5 mm; Corning) allowing to dry for 5 min under laminar flow. Subsequently, 50 µL of the Caco-2 suspension was seeded to the center of each 3D-IS, corresponding to 2 x 10^5 cells/3D-IS in order to obtain the three-dimensional human intestine models (3D-hIs). The transwell insert was incubated for at least 2 h in an incubator at 37 °C with 5% CO_2 to allow cell adhesion onto the 3D-IS surface. Then, the complete medium (200 µL) was added in the apical chamber of the transwell insert and the basolateral chamber was filled with 600 µL of DMEM,

to achieve a submerged culture promoting Caco-2 polarization. The submerged culture lasted approximately 7 d. Then, an optimized air-liquid interface culture lasting 2 weeks took place in order to induce the epithelial tissues to polarize and differentiate. The culture medium was replaced on the first day and three times for week until the end of the experiments. At the end of the culture, 3D-hIs were inserted on the bottom of the snapwell insert and the entire setup was loaded into the Intestine compartment (I_C) of the microfluidic device and microbial strains were added on the apical side in order to develop the Microbiota human Intestine on chip (MihI-oC). The 3D-hIs and MihIs were then collected and processed for histological analysis (Hematoxylin and Eosin (H&E), Alcian blue staining), immunofluorescent staining, and ultrastructural analysis.

5.3. Microbiota human Intestine on chip (MihI-oC) design, assembly and operation

5.3.1. Microfluidic device fabrication

We designed and developed a handy and manageable Microbiota human Intestine on chip (MihI-oC) platform by using replica molding of polydimethylsiloxane (PDMS; Sylgard 184; Mascherpa) from a poly (methyl methacrylate) (PMMA, Goodfellow) master. The latter was designed by AutoCAD and carved with Micromilling machine (Minithech CNC Mini-Mill). It was used to obtain by direct replica a PDMS layer consisting of a central microchannel (1 mm wide × 5 mm long × 1 mm high) with an opened central chamber (13 mm diameter × 5 mm high) meant for the housing of a commercial Snapwell® polycarbonate insert (pore size 12 μm) defining two different compartments: anaerobic (apical-luminal) and aerobic (basal-serosal). The ratio of PDMS pre-polymer and curing agent was 10:1 (w/w); then, the mixture was degassed under vacuum for 20 min to remove air bubbles and poured on the PMMA master. The PDMS slab was left at 80 °C for 60 min, then peeled off from the master. Inlet and outlet holes were punched with a 1 mm biopsy punch (from DifaCooper). The micro-channel was closed by bonding the PDMS device to a glass coverslip (24 mm wide × 60 mm long) by oxygen plasma treatment for 1 min at 50 W in an oxygen plasma oven (Plasma Femto, Diener). Subsequently, the whole setup was left at 80 ºC overnight to achieve irreversible bonding of the PDMS and the glass. Before tissue culture, devices, tubes, and connectors were sterilized by autoclaving. 2-Stop Tygon sterilized tubes were inserted into the inlet and outlet channel of the MihI-oC using sterilized male luer lock connectors (Harvard Apparatus). MihI-oC was mounted by accommodating the 3D-hI model into the openable luminal intestinal compartment I_C that was, then, sealed with a silicon gasket to co-culture the bacterial strains on the luminal side of the 3D-hI, avoiding basal contamination. The gasket was made-up by punching 1 mm thick silicon layer, first

with a 6.5 mm puncher (for the inner hole) and then with a 13 mm puncher (for the outer hole) and sterilized under UV light. At last, for preventing the bacterial contaminations and to ensure the gas exchange without the evaporation issue of the medium, the I_C was closed laying a thin layer of PDMS (100 µm thickness) fabricated by PDMS precursor spin coating (1000 rpm × 30 s) as depicted in the Results section. At last, the micro-channel of MihI-oC was connected to a syringe pump (Ismatec) and the specific flow rates were assayed in order to ensure the optimal deliver of nutrients (5, 30 and 100 µL/min).

5.3.2 MihI-oC assembly: Microbiota chamber (M_C) design and application on human intestine on chip (hI-oC)

In order to obtain MihI-oC, a 3D M_C was fabricated using PMMA that possesses a very low oxygen diffusion coefficient (2.7×10^{-8} $cm^2 \cdot s^{-1}$), compared to PDMS (3.25×10^{-5} $cm^2 \cdot s^{-1}$), or polycarbonate (1×10^{-5} $cm^2 \cdot s^{-1}$). In order to establish the best geometry of the M_C to provide the optimal flow of N_2 into the luminal compartment of I_C, different heights of the M_C were fabricated and tested by modulating the N_2 flow rate at the inlet of the M_C. The final geometry chosen for the experimental phase of the M_C was a circular chamber with a diameter of 22 mm and 15 mm in height and a handmade PMMA lid provided by an inlet for N_2 entry and an outlet for exit. The integration of the M_C onto the hI-oC took place in two manufacturing steps. In detail, a PMMA snapwell-like structure was glued on the central chamber in order to give the right height to the device, and a first layer of PDMS (~ 2 cm in height) was poured and left at 80 °C for 2 h. Then, a PMMA ring was put around the central chamber, and another PDMS layer (3 cm) was fabricated on it. At the end, the ring was removed to have a geometric structure used as a guide for the accommodation of the M_C, guaranteeing its adhesion to the MihI-oC (Supplementary Figure. S1). The handmade PMMA lid of the M_C was connected to a pressure pump (Dolomite) at the inlet and N_2 was flushed at different flow rates to completely eject the oxygen. Furthermore, since the N_2 comes out in the M_C at 24°C temperature, whereas the temperature for the optimal growth of the microbiota is 37°C, a pre-warmed microbiota suspension was loaded into the apical side of MihI-oC into the anaerobic bacterial glove box, then the entire setup was transferred into a cell incubator and the temperature was monitored with a hand-made Arduino set-up to evaluate the time required from the system to reach the optimal microbiota growth temperature (37°C). Once obtained the anoxic condition, the N_2 flux was maintained at 5 µl/min with a very low Reynolds number ($4 \cdot 10^{-6}$) to ensure laminar flow on the liquid interface which hosts the microbial species into the I_C, obtaining the complete MihI-oC set up. Comsol Multiphysics was used to simulate the oxygen concentration in a given point of the M_C at various N_2 flow rates

flushed inside the M_C by a pressure pump, in order to determine the amount of time necessary to eject free oxygen outside the M_C to produce an anoxic environment as reported in the paragraph below.

5.3.3. Computational model of MihI-oC

The oxygen gradient and the nutrient supply velocity were evaluated by using commercial CFD COMSOL Multiphysics vers. 5.0. CFD analyses were performed dividing the entire device into two different domains: a fluid domain, which identified the region filled with culture medium, and a tissue domain, which identified the region filled with the intestine sample. Simulations within the fluid domain were performed by using the steady state Navier-Stockes equation Equation (5.1). No slip boundary conditions were set on the walls, and the fluid was considered to have the same physical characteristics as water. A specific laminar flow was set at the inlet and reference pressure was set at the outlet (p_{ref} = 1atm):

$$\rho(v_1 \cdot \nabla)v_1 = \nabla \cdot [-pI + \mu(\nabla v_1 + (\nabla v_1)^T)] + F \qquad (5.1)$$
$$\rho(v_1 \cdot \nabla) = 0$$

Where μ is the dynamic viscosity, v_1 is the fluid velocity, p is the hydrostatic pressure, and ρ is the fluid density. Brinkman Equation (5.2) was used to describe the flow through a porous medium:

$$\left(\frac{\mu}{k}\right)v_1 = \nabla \cdot \left(-pI + \left(\frac{1}{\varepsilon}\right)\left(\mu(\nabla v_1 + (\nabla v_1)^T)\right)\right) - \left(\frac{(2\mu)}{3} - k_{dv}\right)(\nabla \cdot v_1)^I)) + F \qquad (5.2)$$
$$\rho(v_1 \cdot \nabla) = 0$$

Where k is the hydraulic permeability, μ is the viscosity of the tissue, p is the pressure, ε is the porosity of the material, k_{dv} is the dynamic permeability. The oxygen concentration within the system was calculated by means of the following mass balance equation Equation (5.3):

$$D\nabla^2 C - \nabla(Cv_1) = -R \qquad (5.3)$$

Where C is the oxygen concentration, $v_1$is the fluid velocity field, and D is the diffusion coefficient of the oxygen. R is the volumetric oxygen consumption rate expressed by the Michelis-Menten law, according to the following Equation (5.4):

$$R = \rho \frac{v_{max,1} c}{k_m + c} \qquad (5.4)$$

Where $v_{max,1}$ is the maximum oxygen consumption rate, k_m is the concentration at which the oxygen consumption rate is half of $v_{max,1}$ and ρ is the cell density in the perfusion chamber obtained by taking into account the number of cells present in the Intestine. R was set to 0 in the fluid domain, as cells are present only in the tissue domain. To model the N_2 flow and O_2 transport within the M_C we used

a code implemented in COMSOL "Transport of diluted species for compressible fluid with a low Mach". No slip boundary conditions were set on the walls, and the fluid was considered to have the physical characteristics of nitrogen.

Table 1. Mathematical modeling parameters

Variable	*Description*	*Value*	*Source*
μ^f	Dynamic viscosity of the fluid (culture media) (Pa s)	0.001	[11]
μ^t	Effective viscosity of the fluid in the tissue domain (Pa s)	0.0016	[11]
ε	Porosity of the tissue	0.7	[11]
κ^t	Effective hydraulic conductivity (m^2)	10^{-11}	[11]
D^f	Oxygen diffusivity in the culture media ($m^2 s^{-1}$)	10^{-9}	[11]
D^t	Oxygen diffusivity in the tissue ($m^2 s^{-1}$)	10^{-10}	[11]
C_0	Equilibrium oxygen concentration in the culture media (µM)	0.22	[11]
ρ	Cell per μTPs (cell m^{-3})	$0.2\ 10^{14}$	[11]
V_{max}	Maximum rate of oxygen consumption (mol $cell^{-1}\ s^{-1}$)	10^{18}	[11]
K_m	Oxygen concentration at 0.5 (V_{max}) (µM)	10^3	[11]
K_{dv}	Dynamic permeability (m^2)	0	[11]
R	Oxygen consumption rate (µM s^{-1})	$\rho \frac{V_{max} C}{K_m + C}$	[11]
D^a	Oxygen diffusivity in the PMMA ($cm^2 s^{-1}$)	10^{-8}	[12]
C_{0-a}	Equilibrium oxygen concentration in the anaerobic chamber (µM)	0.01	[13]

5.3.4. On-line Oxygen concentration measurement

During the culture, the oxygen consumption profile inside the M_C was measured by using an optical detector (OXY-4 PreSens) located in the center of the M_C wall on the opposite side of N_2 flow inlet for 30 min by flowing at a constant rate (200 µL/min).

5.4. Assessment of the M_C functionality: comparison of single strains growth into the anaerobic workstation (AW) vs MihI-oC

5.4.1. Total and viable count

For the M_C functionality assessment, a 12-well Snapwell insert (insert diameter 13 mm, pore size 0.4 µm, Merk Millipore) was accommodated into the hI-oC in order to evaluate the single bacterial strains viability in microaerophilic conditions in the AW (micro-AW), anaerobic conditions in the AW (ana-AW) or hypoxic environment generated into the M_C of the MihI-oC (M_C-MihI-oC). First of all, snapwell insert was coated with an appropriate volume of bovine type I collagen (Sigma-Aldrich) prepared at a concentration of 5 mg/ml and neutralized by dropwise addition of 0.1 NaOH. The solution was added into a Snapwell insert and placed in an incubator at 37°C for 45 min to allow the polymerization of the collagen, resulting in a disc-shaped gel that covered the pores and avoided the bacterial crossing through the porous membranes. To compare the bacterial growth into the AW or MihI-oC, 500 µL of refreshed suspension of each bacterial strain (OD 600 = 0.5 nm), grown in selective broth media, was placed on the apical side of the MihI-oC, covered with a thin PDMS layer and placed in the ana- or micro-AW or connected to a pressure pump to flow nitrogen into the M_C. Furthermore, the S_C of MihI-oC was connected to a syringe pump (Ismatec) and a specific flow rate (5 □L/min) was imposed. All samples were incubated at 37 °C under different culture conditions (micro-AW, ana-AW and M_C-MihI-oC), three for each condition. Subsequently, in order to determine the total counts of each bacterial suspension, aliquots of 10 µL were collected every 15 min over a 32-36 h period, leading to volume of 1 mL, and the optical density at 600 nm (OD600) were read by turbidimetric analysis (BioPhotometer Eppendorf, Milan, Italy). Meantime, in order to define the total number of surviving bacteria, a viable count assay for each culture condition was also performed. The 10-fold serial dilutions of the bacterial suspension were prepared in PBS and 3 drops of 10 µL from each were plated on selective media (MRS or CM151) and incubated at 37°C for 24-48 h in above-mentioned hypoxic conditions. After the incubation time, the colonies that grew on these plates were counted and the colony-forming units CFU/mL were calculated to quantify bacteria surviving.

At last, turbidimetric measurement was correlated with growth curves of viable bacteria. Each test was performed in triplicate and repeated at least three times.

5.4.2. Live/Dead assay

The total count of viable/not-viable bacteria was assessed by using the Live/Dead BacLight Bacterial Viability Stain Kit (Molecular Probes, Eugene, OR). First of all, the best concentration of the viability kit stain mixture (SYTO9 and propidium iodide -PI-) was selected, which allowed us to distinguish the live bacterial cells from dead (SYTO9: PI, 1:2 v/v). Briefly, freshly grown bacteria suspensions (*L. rhamnosus* or *B. longum*) were opportunely diluted and harvested by centrifugation (3200 × g, for 15 min) and washed three times with NaCl 0.85% solution. Then, 3 μL of a mixture of SYTO9 and PI (1:2) were diluted in 0.5 mL of bacterial suspension directly on the apical side of the MihI-oC and incubated in darkness for 15 min at room temperature according to the manufacturer's instructions. Non-viable bacteria were prepared by 95% ethanol treatment of the bacteria for 30 min. The bacteria were washed twice with NaCl 0.85% after the treatments and examined under Leica confocal microscope (Confocal Leica TCS SP5 II femtosecond laser scanning system, Leica). Filters were set to 493-522 nm for SYTO9 and 618-676 nm for PI. CLSM images were obtained with 40x objective (optical zoom 1.5). Each sample was scanned at randomly selected areas as a series of vertical optical sections, each one 0.50 μm thick. Quantitative analyses of each bacterial strain was carried out by analyzing the digital images of live (green) and dead (red) bacteria with Image J software. Each image was divided in ROIs with comparable areas, and the thresholding was performed. The fluorescence intensity per unit area was measured and calculated as percentage of viable cells.

5.4.3. Ultrastructural and morphological characterization of microbiota

For SEM analysis, the bacterial suspension of each strain, collected from the M_C of MihI-oC, was seeded on 0.1% gelatin-coated glass accommodated into petridish of 3.5 cm^2 and fixed with 2.5% (v/v) glutaraldehyde for 2 h at room temperature and washed twice in 100 mM cacodylate buffer pH 7.2, for 10 min at room temperature. A second fixation in 1% (w/v) osmium tetroxide, buffered in 100 mM cacodylate pH 7.2, was done overnight at 4°C. Dehydration was carried out in a graded ethanol series (30, 50, 70, 90 and 100%) for 10 min each and samples were then treated with liquid carbon dioxide using a Critical Point Dryer (Emitech K850). Dried samples were mounted onto metal stubs, sputter coated with gold-palladium at 10 mA. Coated samples were then, examined by scanning electron microscopy (SEM) (Leica S400). For morphological characterization the bacterial suspensions were collected from the I_C of MihI-oC by removing the M_C and then loaded on 0.1%

gelatin-coated glass, heat-fixed and let it dry for 1 h and stained by using standard protocol as described by the manufacturer (Gram staining, Biooptica).

5.5 Statistical Analysis

This work involved at least two replicate hI-oC or MihI-oC per experiment. Each experiment was repeated two or three times for analyses of Live/Dead, ROS, TEER, and inflammatory cytokine (ELISA) measurements. The results were expressed as mean ± standard deviation (s.d.) from duplicate, triplicate or more independent experiments ($n \geq 3$). In detail, for total and viable count quantification analyses, turbidimetric measurement or viable counts of bacterial suspensions was performed in triplicate and repeated at least three times for each time point. For Live/Dead quantitative analysis, 5 digital images were divided in at least 5 region of interests (ROIs) with comparable areas for each images. For section staining (histological, SHG) three samples were used for each experimental phase and 10 and 20 sections, respectively, were used per sample, then about five ROIs were examined for each section. For molecular analyses the quantification was expressed as total rDNA amount expressed as ng/mL or normalized to 100% (for bacteria) or as a fold-change relative to gene expression of the control groups (for epithelial cells). Three independent experiments in triplicate were performed. For the villi thickness, 10 images were selected each data point. For TEER measurements, the analysis was performed on three hI-oC and MihI-oC. About 5 ROIs were examined for each section. All results were then statistically analyzed by the Student's t-test. The differences between two or more groups were evaluated by using one-way analysis of variance (ANOVA) followed by the Tukey's post-test. Statistical significance was set at a value of $p < 0.05$. The values are outlined in the Figure legends.

5.6 Results and Discussion

Here we reproduced the mucosal-associated microbiota-cell interactions into the complex microenvironment of an immune-responsive Microbiota-human Intestine axis on-chip (MihI-oC) in which microaerophilic and obligate anaerobic microbiota species are vertically stratified within the mucus overlying the epithelium of the three-dimensional human intestine model (3D-hI). In contrast to the intestinal epithelium model grown on the exogenous membrane, here, the 3D-hI presents an instructive and histologically competent ECM and a well-differentiated epithelium with mucus-covered microvilli. This physiological context allows to investigate the impact of microbiota on MihI's morphology and functional performance in terms of barrier protein and mucus production as

well as the microbiota-epithelial/stromal-immune system cross-talk. The complex ECM featuring the intestinal lamina propria has a fundamental role in dictating the epithelium morphogenesis as well as the microbiota adhesion and stratification. Moreover, we replicated the microenvironmental anaerobic condition of the human intestinal lumen by fabricating a custom-made M_C on the apical side of the MihI-oC. In these conditions, we established the physiological hypoxic environment in the lumen and, for the first time, the physiological oxygen dissipation along the thickness of the human small intestine model from the serosal side of the lamina propria to the luminal side where microbiota was grown. Furthermore, we improved the complexity of the intestinal extracellular microenvironment by integrating cell populations that are directly involved in the inflammatory response (two species of the intestinal commensal microbiota on the lumen side and PBMCs on the serosal side). We evaluated the geographical change as well as the protective role, immunomodulation, and immune-tolerance maintenance of the microbiota in LPS-induced barrier impairment and the indirect role of the microbiota on stromal reshaping in response to the inflammatory stimulus. Finally, we evidenced the synergistic contribution of different cell populations such as epithelial, stromal, blood, and microbial species on the release of the key immune-mediators (pro- and anti-inflammatory cytokines, ROS).

5.6.1 Establishing hypoxic environment in Microbiota Chamber (MC) of MihI-oC

Healthy intestinal mucosa is able to sustain physiological oxygen concentrations much lower than atmospheric conditions causing a horizontal steep oxygen gradient along the length of the intestine and a vertical gradient from the severely oxygen deficient lumen to the highly vascularized and oxygenated serosa [14], [15]. Commensal facultative anaerobic and microaerophilic bacteria inhabiting the lumen and epithelial mucosa are strictly involved in the establishment of the luminal physiological hypoxia condition called “physioxia”[16]. On the other hand, obligate anaerobic bacteria colonize the near anoxic microenvironment at the midpoint of the lumen establishing a stratification of the bacterial communities along the radial axis of the small intestine [16]. Therefore, any attempts to recapitulate *in vitro* the gut-microbiota axis have to mimic the anoxic-oxic interface of the intestinal lumen that is a key element of the gut microenvironment for the survival of the commensal microbiota as well as for the formation of a functional epithelial barrier. Here, we replicated the microenvironmental anaerobic condition of human intestinal lumen by fabricating a custom-made M_C on the apical side of the I_C, establishing the physiological near-anoxia microenvironment (< 0.0013% O_2) existing at the midpoint of the intestinal lumen that is the

mandatory condition for the colonization of the obligate anaerobic bacteria [16]. Comsol Multiphysics was used to simulate the oxygen concentration, in a given point of the M_C, by changing the flow rates at which N_2 was flushed inside the M_C (Figure 5.1a, 5.1b), in order to determine the amount of time necessary to eject free oxygen outside the M_C to produce a near-anoxia environment. A picture of the real device is depicted in Figure 5.1c. The results of the simulations displayed that the highest tested N_2 flow rate (400 µL/min) generated a near-anoxia environment inside the chamber within just 5 min. However, this flow rate created turbulent flow with visible formation of surface waves, which invalidated the bacterial viability. Conversely, lowering N_2 flow rate at 200 µL/min, the turbulent flow was prevented and the near-anoxia environment, as calculated by Comsol simulation, was reached in 15 min (Figure 5.1d-f). Remarkably, this value is still a lower time as compared to other intestinal on-chip models in which the time to reach the opportune near-anoxia environment have almost doubled [7]. Real-time and non-invasive measurements of the oxygen concentration were carried out (Figure 5.1c) by using an oxygen optical detector [7] and confirmed the Comsol simulation (Figure 5.1a, purple empty circles in the graph). According to Einstein-Smoluchowski equation for diffusion of gases in solution ($t = 0.5 \cdot r^2 \cdot D^{-1}$), where *r* equals the height of 200 µL of microbiota side into the device (5 mm) and *D* is the diffusion coefficient of O_2 ($2.46 \cdot 10^{-9}\ m^2s^{-1}$), the expected time required for oxygen to diffuse across microbiota was calculated as ~ 85 min. So, in order to prevent the re-oxygenation of the M_C, instead of completely stopping N_2 flow after reaching near-anoxia microenvironment, N_2 was kept flushing at very low flow rate such as 5 µl/min for the entire duration of the experimental phase. Even if N_2 comes in the M_C at 24°C, the time required from the system to reach the optimal temperature of 37°C is in order of few minutes (8 min) as measured by a hand-made Arduino set-up (Supplementary Figure. S2). Therefore, no troublesomeness for the bacterial viability and growth occurred. Then, a flow of oxygenated medium was streamed into the serosal channel (S_C) of the MihI-oC to provide the stromal side of the 3D-hI with the necessary nutrient and oxygen.

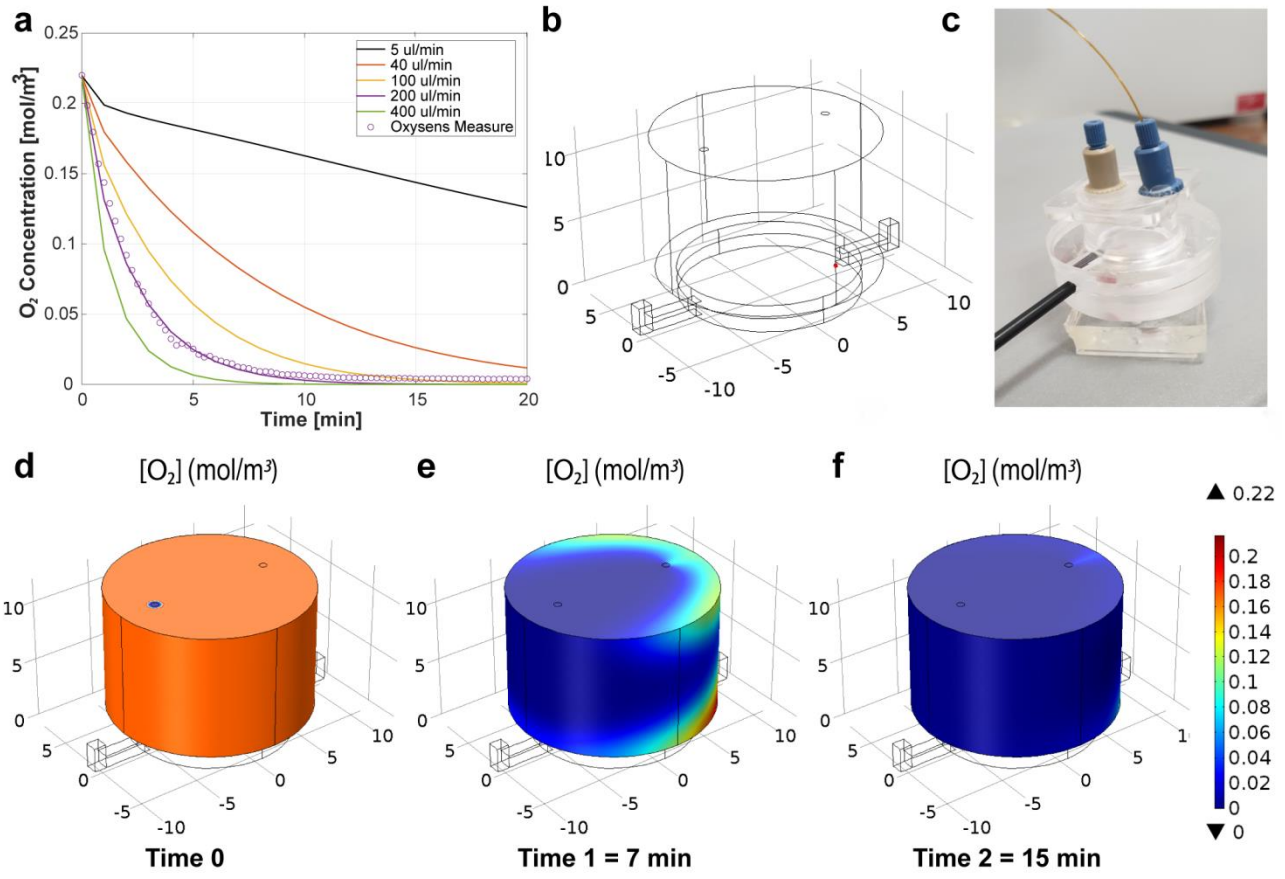

Figure 5.1 Design and optimization of flow rate of M_C. Continuous lines indicate oxygen concentration at various N_2 flow rates calculated by Comsol simulation, purple empty circles indicate the values of the real-time measurements obtained by using an oxygen optical detector (a); schematic representation of M_C, the red mark indicates the point at which the oxygen concentration was measured by Comsol simulation (b); experimental setup of on-line measurement shows a support for optical fiber accommodation (c); Comsol simulation indicates the reduction of the oxygen concentration in the whole volume of the M_C at a flow rate of 200 µL/min at different time points: Time 0 (d), Time 7 min (e), Time 15 min (f).

5.6.2 Microbiota Chamber (M_C) promotes microbial strains growth and oxygen gradient across the MihI lumen

Of note, the microbiota is biogeographically stratified within the gastrointestinal tract on different spatial scales and axes and its viability is strictly dependent on the luminal-serosal oxygen gradient. To fully understand the functionality of the intestinal microbiota, great attention must be paid to the microhabitats within the intestinal ecosystem and the spatial relationships among microorganisms and between microorganisms and the host [2, 3]. This bacterial stratification is strictly related to the intraluminal oxygen gradient that influences the spatially heterogeneous growth of the microorganisms as well as the intestinal tissue functionality. Studies reported the optimal O_2 profile at various locations along the radial axis of the intestinal lumen ranging from the normoxic submucosa

(0.15 mol/m^3), to the low oxygen environment along the crypt villous axis (0.07-0.03 mol/m^3) with a hypoxic environment at the tip of the villi (0.03 mol/m^3) to the near anoxia at the distant lumen as reported in Table. 2 [17]. In this perspective, in order to assess the capability of M_C to guarantee microbiota viability and growth as well as to reproduce its correct topographical vertical distribution on the intestinal lumen (Figure 5.2a), anaerobic (*B. longum*) or microaerophilic (*L. rhamnosus*) strains were cultured on the luminal side of the 3D-hI model, housed on the apical I_C of the compartmentalized microfluidic MihI-oC. While continuous N_2 flow assures the anaerobic condition into M_C, the oxygenated antibiotic-free medium was flowed into the S_C of the MihI-oC to provide the adequate oxygen supply to allow human intestinal cells viability (Figure 5.2b and c). In this way, an oxygen gradient across the MihI model was established, so providing a physiological microenvironment with a functional host-microbiota interface and vertical bacteria stratification.

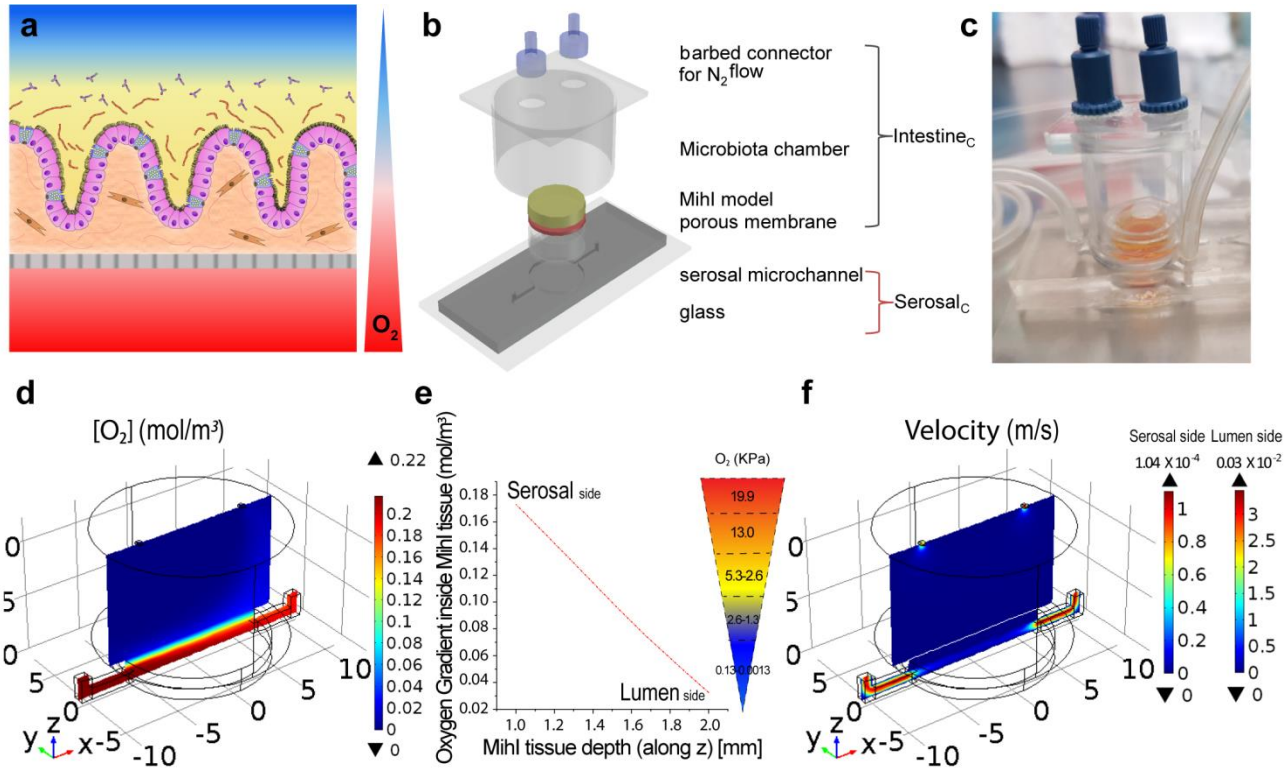

Figure 5.2 MihI-oC establishes the physiological oxygen gradient across the MihI tissue. Schematic representation of the transversal section of MihI-oC with fibroblasts embedded into the auto-produced ECM overlaid by a polarized and differentiated epithelium and the vertically distributed microbial strains into the luminal side; triangular color map indicates the oxygen gradient from the Serosal to the Lumen side (a); rendering of the MihI-oC show the I_C and S_C separated by a porous membrane (b); experimental setup of MihI-oC highlights the M_C that seals the I_C in which was accommodated the 3D-hI (c); Comsol simulation indicates the oxygen concentration field in the MihI-oC by using medium flow rate at 30 µl/min into the S_C and N_2 flow rate at 200 µl/min at the inlet of M_C (d); the graph reports the oxygen dissipation along the thickness of MihI-oC from the S_C of the lamina propria to the Luminal side where microbiota grows; the colour map shows the oxygen tension (ranging from 19.9 KPa at Serosal side to 0.13-0.0013 KPa at Lumen side) into MihI tissue depth along the z axis (e); Comsol simulation shows the velocity profile into the entire setup of MihI-oC (f), the color maps indicated the Serosal and the Lumen side, respectively.

CFD fluidodynamic simulation was performed and reported in Supplementary Figure. S3-S4, in order to identify the best medium flow rate to ensure the right oxygen supply to the cells reproducing the physiological oxygen level of the small intestinal wall, which is ~ 0.22 mol/m^3 [1]. CFD simulation

revealed that, when culture medium was flushed at 30 µl/min, a right compromise between oxygen amount in the tissue of MihI-oC (0.22 mol/m^3 at the bottom) and shear stress (0.0267 dyne/cm^2) was obtained (Figure. S3b and e, S4b). Moreover, CFD of the full-assembled MihI-oC was performed to simulate fluid dynamic condition and oxygen provision inside the whole system when oxygenated culture medium was flushed at 30 µl/min in the bottom part of MihI-oC (basolateral channel) and N_2 was injected at 5 µl/min in the M_C (Figure 5.2d-f). In Figure 5.2d, it is showed the oxygen gradient extending from the MihI throughout the mucosal interface into the lumen, whereby microorganisms adjacent to the epithelium of MihI consume most of the available oxygen, keeping the bulk of the lumen deeply hypoxic. We replicated, for the first time, *in vitro*, the physiological oxygen dissipation occurring along the thickness of human small intestine from the serosal side of the lamina propria to the luminal side where microbiota was grown. These conditions provide an environment in which the endogenous ECM produced in our model is able to guarantee the regulatory function of the native lamina propria providing the instructive conditions that *in vivo* maintain the microbiota adhesion and stratification. Figure 5.2e shows the oxygen gradient from the serosal side to the villi tips of the MihI-oC with a hypoxic lumen that host microaerophilic bacteria and the near-anoxic apical side of the M_C in which the obligate anaerobes grow embedded into an endogenously produced mucus layer reproducing the correct extracellular microhabitat of the small intestine. Furthermore, Figure 5.2f, shows that a fully developed Poiseuille velocity profile was established in the S_C and a very low N_2 velocity was recognized in the M_C. These conditions were safe for cell and bacteria viability. In order to demonstrate the M_C functionality in comparison to the conventional culture methods in bacterial glove box, the growth curve of the microaerophilic (*L. rhamnosus*) or anaerobic (*B. longum*) strains cultured in three different conditions for 36 h were estimated: 1) microaerophilic conditions in the AW (micro-AW), 2) anaerobic conditions in the AW (ana-AW), 3) hypoxic environment in the M_C of the MihI-oC (M_C-MihI-oC). Differences between total and viable bacteria were reported compared to the standard curve generated under conventional growth conditions, which are micro-AW for *L. rhamnosus* and ana-AW for *B. longum*, respectively. As pointed out in the inset of Figure 5.3a, differences in the lag phases between the growth condition in micro-AW and the M_C-MihI-oC were displayed, due to the *L. rhamnosus* growth adaptation into the M_C, in which an oxygen gradient from the basal to the apical side, with a progressive reduction of oxygen going upwards, was found. In fact, the bacteria prolonged the lag phase, but subsequently they self-adapted to the oxygen gradient condition in the M_C. Further, once adapted to the growth condition into the M_C, the exponential growth phase was completely superimposed on that of the micro-AW. Additionally, the stationary phase lasts longer in the M_C-MihI-oC before reaching the death phase. *L. rhamnosus* grown under ana-AW showed a growth curve having the same trend but with lower values at each time points

(Figure 5.3a). For *B. longum* cultured in ana-AW, the curve of total bacteria is completely superimposable to that in M_C with slightly higher values of the viable bacteria in M_C-MihI-oC probably due to the CO_2 concentration coming from the basal side or from the exchange of CO_2 in the incubator. It is already known, indeed, that CO_2 although in small percentage can positively influence the growth of the *B. longum* [18], [19].

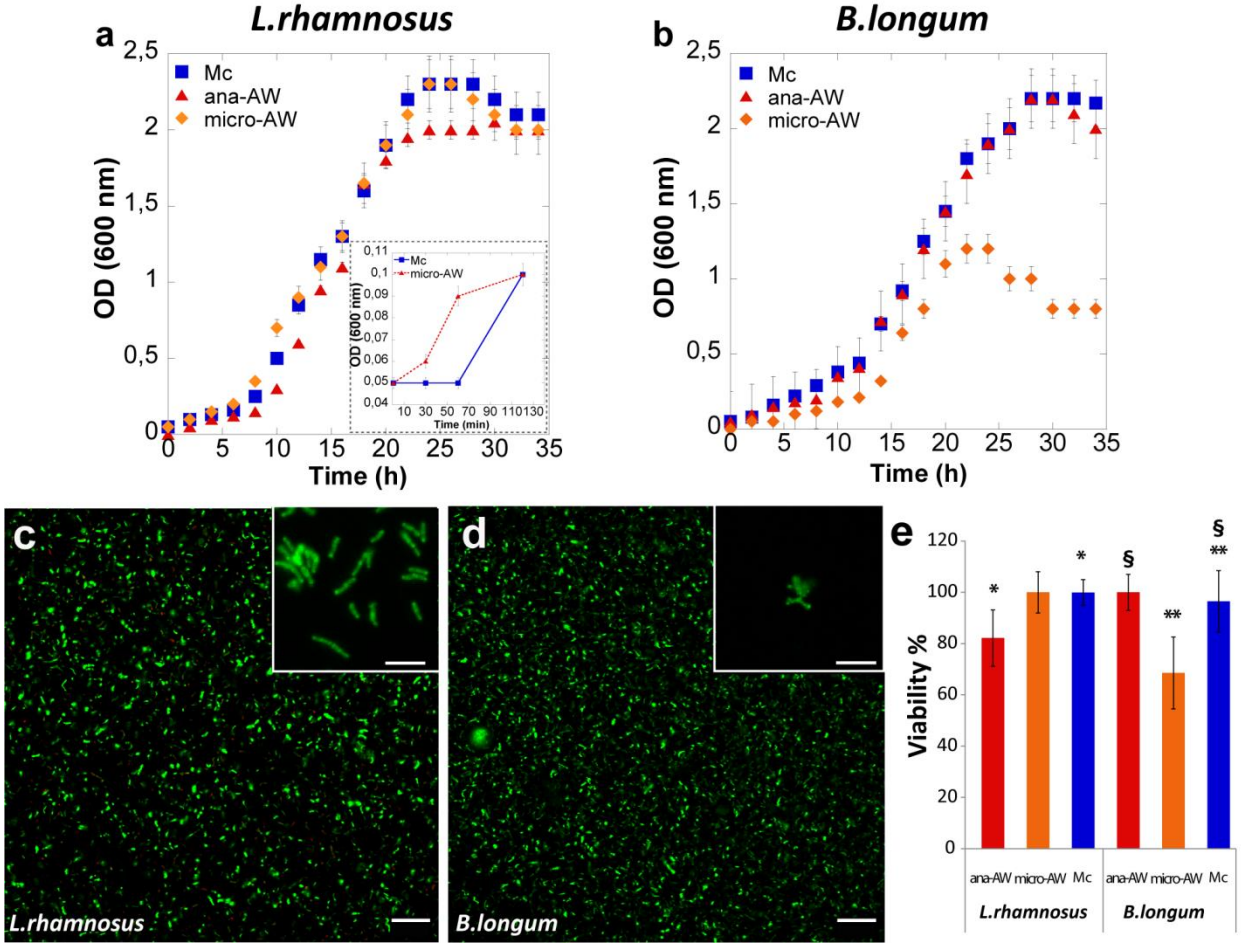

Figure 5.3 Microbiota Chamber (M_C) sustains the microbial strains viability and growth in the MihI-oC lumen. Quantification of total viable bacterial growth - L.rhamnosus (a) and B.longum (b) - on different oxygen microenvironments: microaerophilic conditions in the AW (micro-AW), anaerobic conditions in the AW (ana-AW), hypoxic environment in the M_C of the MihI-oC (M_C-MihI-oC); the inset indicates the Lag phases difference between L. rhamnosus growth in micro-AW vs M_C-MihI-oC (a, inset). Micrographs of the on-line monitoring of viable bacteria (Live/Dead staining) shows the optimal culture conditions for each bacterial species - L.rhamnosus (c) and B.longum (d) with high magnification insets that depict the microbial morphology; scale bar 75 nm for c and d, scale bar 20 nm for insets; the graph reports the quantitative analysis of live bacteria on different oxygen microenvironments, *$p < 0.001$, **$p < 0.01$, §$p < 0.05$ (e).

A strong reduction of total bacteria concentration was reported in micro-AW condition. In ana-AW, the lag phase overlapped with slight differences in the enrichment of the plateau (log phase). Slight increase of the live bacteria in the M_C-MihI-oC compared to ana-AW was shown, due to the optimal microenvironment provided into the M_C of the MihI-oC as showed in the Figure 5.3b. All data were compared with viable count of each strain at different times of culture (Supplementary S5a and b). In aerobic conditions, a significant reduction of *L. rhamnosus* and no colony growth for *B. longum* was

found (data not shown). Finally, the bacterial samples were collected from MihI-oC during the log phase and histological as well as ultrastructural characterization was performed (Supplementary Figure. S5c and d, and insets). The bacteria viability under different culture conditions was also confirmed by on-line measurements of Live/dead staining during log phase of culture. Representative Live/Dead images of single strain grown (*L. rhamnosus* and *B. longum*) in M_C under optimal growth conditions indicated the bacterial growth > 90% for both strains (Figure 5.3c and d, respectively) preserving the bacterial morphology as highlighted by high magnification images (Figure 5.3c and d, insets). Quantitative analysis of Live/Dead staining did not show significant differences when the single bacterial strain in the log phase were grown in M_C-MihI-oC compared to their optimal growth conditions in AW (90±2.2% and 89±2.7 respectively for *L. rhamnosus*; 87±1.5% and 91±2.4% respectively for *B. longum*). A strong significant reduction in cell viability was evidenced for *B. longum* in micro-AW confirming the viable count data (Figure 5.3e).

5.6.3 Establishing physiological vertical localization of microbiota in MihI-oC

Once established the MihI-oC micro-milieu, the in-depth histotypical, molecular and ultra-structural analyses were carried out to deeply investigate the co-culture of 3D-hI with the bacterial strains. Differently from the gut-microbiota on chip models previously proposed [5][7][18], here the 3D-hI is a complex tissue model (Figure 5.4a) composed by an endogenously cell-produced ECM on which intestinal villi-like protrusion covered by a well-polarized epithelium is strictly adhered (Figure 5.4b, *). Recent evidences demonstrated a key role of intestinal lamina propria, not only on the epithelium morphogenesis[8][10][20] but also on microbiota adhesion, distribution and growth [20]. Here, as first step toward the reproduction of intestine-microbiota axis, single bacterial strain was co-cultured on 3D-hI in MihI-oC, and histological characterization (H&E and alcian blue staining) confirmed the correct localization of each strain. We found the microaerophilic *L. rhamnosus* adhered on the polarized microvilli (Figure 5.4b black arrowhead) and the anaerobic *B. longum* vertically distributed far from the epithelium (Figure 5.4c black arrowheads).

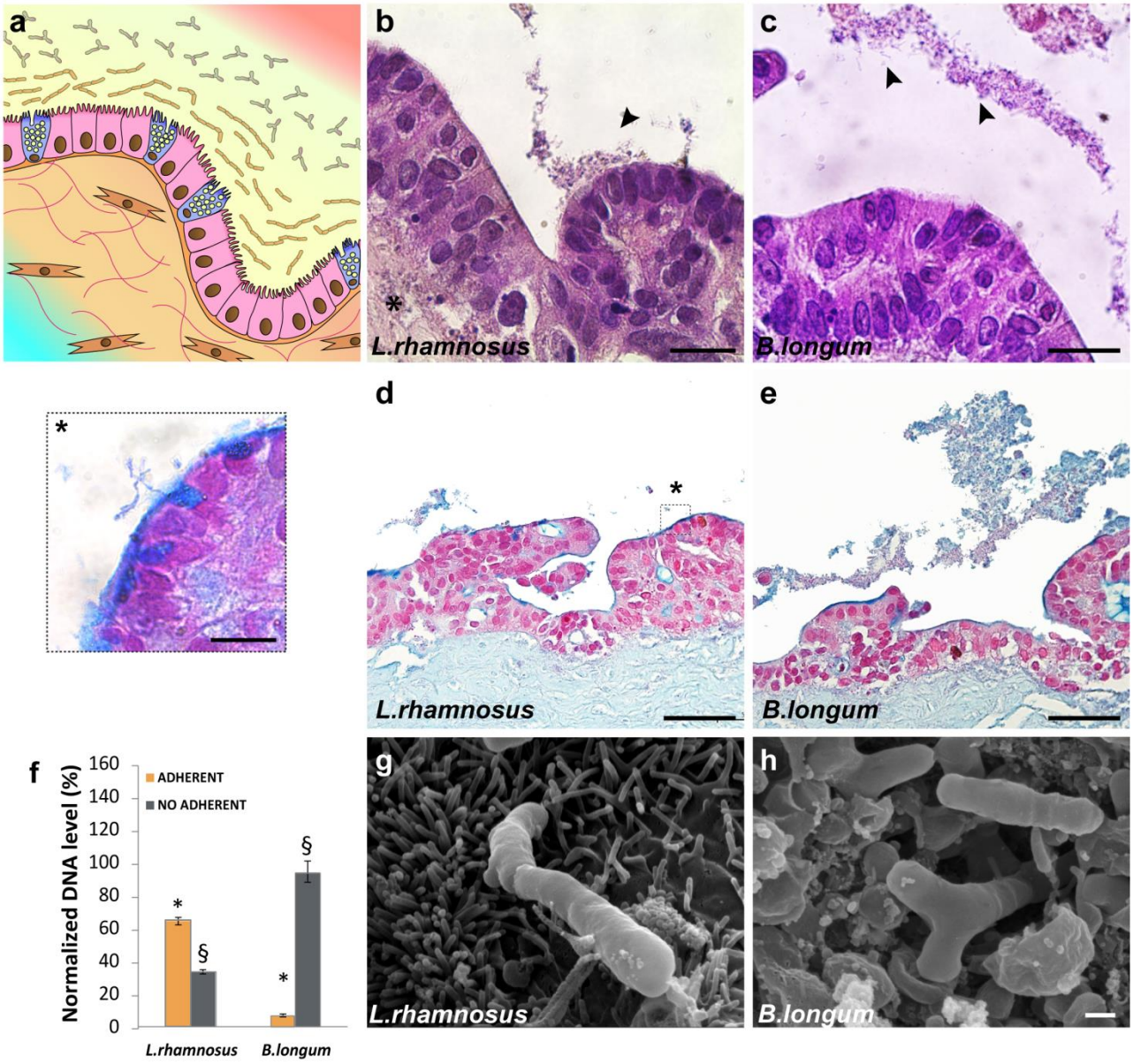

Figure 5.4 Physioxic condition in the lumen of MihI-oC determines the physiological vertical stratification of the microbiota. Schematic representation of villous tip indicates the geographical distribution of the microbial species into the Lumen side of the small intestine (a); representative high magnification H&E images of 3D-hI shows the L. rhamnosus adhesion on the apical side of the epithelial cells (b) and B. longum away from the epithelium (c), scale bar 20 □m; alcian blue stained section of 3D-hI depicts the mucus producing cells and the L. rhamnosus adhesion on mucus that cover the microvilli (d and inset *; scale bar 200 nm and 20 nm, respectively) and B. longum completely embedded into the mucus far from the epithelium (e, scale bar 200 nm); bars diagram indicates the DNA level of two bacterial strains reported as adherent and non-adherent, *$p < 0.001$, §$p < 0.05$ (f); high magnification SEM micrograph evidences the L. rhamnosus adhesion on microvilli structures (g) and B. longum immersed into the mucus (h), scale bar is 200 nm.

Moreover, abundant mucus overlying the intestinal epithelium was detected (Figure 5.4d and e, * inset). Emerging evidences reported the intestinal mucus layer as the first line of defense against the bacterial infiltration and the physical barrier to antigenic substances, digested food particles, enzymes and acids into the lumen [20]. Moreover, the bacterial adhesion to intestinal mucus and epithelia seems to be important for individual stability of the microbial flora [3]. In fact, intestinal bacteria have adapted to colonize the mucus layer by adhering to intestinal mucus components, using mucus-derived nutrients and sensing chemical cues for adaptation. We have previously demonstrated the

relevance of the stromal signals in driving the Caco-2 cells to differentiate in mucus-producing cell phenotype without any exogenous stimulus and the failure of the mucus production in 2D transwell culture [10]. Here, we demonstrated that in our MihI-oC a complex environment was reproduced comprising the mucus layer with embedded bacteria. Transversal section of alcian bue-stained samples confirmed the presence of adherent *L. rhamnosus* on the apical surface of the polarized epithelium as well as in the neo-produced mucus blanket by goblet-like cells as highlighted by the high magnification image (Figure. 4d marked with *). In addition, *B. longum* strain resulted completely embedded into the mucus layer detached from the epithelium stained in blue (Figure 5.4e). In order to prove the topographical distribution of the bacterial strains cultured on the luminal side of the MihI-oC, quantitative analysis of 16S ribosomal DNA (rDNA) from tissue supernatant (reported as adherent) or scratched from the apical surface of the epithelial cells (reported as no-adherent) was assessed. As described in Figure 5.4f, a high amount of the 16S rDNA sequences of *B.longum* was detected into the supernatants that contains unbounded bacteria immersed into the mucus layer. Conversely, a low amount of rDNA of *B. longum* was revealed on scratched supernatants confirming the correct topographical location of this strain, that due to its anaerobic nature is physiologically found far from the oxygen enriched-epithelial cells. In contrast, a small amount (25-35 ± 3.5%) of rDNA of *L. rhamnosus* has been found in the supernatant collected in the lumen of the 3D-hI (no-adherent). In agreement with literature [21], high amount of rDNA sequences of *L. rhamnosus* were found in the scratched supernatants indicating that the *L. rhamnosus* is preferentially localized on the surface of the microvilli of the epithelial cells. In addition, the ultra-structural images showed that the Lactobacilli preserved their morphology and colonized the hI-oC along the Crypt-villous axis. SEM micrograph reported that most microaerophilic bacteria (*L. rhamnosus*) adhered directly on the apical surface of the epithelial cells and are lodged on the brush border structures as showed in Figure 5.4g and Supplementary Figure S6a. Conversely, representative SEM image of *B. longum* demonstrated that the bacteria were completely immersed into the mucus layer produced by the Goblet-like cells of the hI-oC (Figure 5.4h and Supplementary Figure S6b).

5.7 Conclusion

The immune-competent gut-microbiota axis proposed in this work is able to reproduce the architecture and vertical typography of the microbiota with a complex extracellular microenvironment consisting of a responsive ECM and a plethora of immunomodulatory mediators released from different cell populations such as epithelial, stromal, blood and microbial species in homeostatic and non-homeostatic conditions. This system is able to unbundle the single contribution

of each cell and its involvement in the innate and cell-mediated inflammatory response in the onset of the inflammation process. MihI-oC provides a useful platform for inflammation studies such as ileitis, IBD or diseases (Chron disease or leaky gut). By implementing the M_C, MihI-oC favors the cultivation of the various microbial species of the intestinal microbiota (microaerophilic and anaerobic) allowing the vertical stratification of the bacteria species. Furthermore, MihI-oC could be used for future studies of drug testing or active food digestion and could be implemented with other modules that mimic different organs such as the blood brain barrier by reconstructing a microbiota Gut-brain axis, adipose tissue for obesity studies or with the liver to evaluate drug toxicity.

Bibliography

[1] Y. Belkaid and T. W. Hand, “Role of the microbiota in immunity and inflammation,” *Cell*, vol. 157, no. 1, pp. 121–141, 2014, doi: 10.1016/j.cell.2014.03.011.

[2] G. P. Donaldson, S. M. Lee, and S. K. Mazmanian, “Gut biogeography of the bacterial microbiota,” *Nat. Rev. Microbiol.*, vol. 14, no. 1, pp. 20–32, 2015, doi: 10.1038/nrmicro3552.

[3] C. Gusils, V. Morata, and S. González, “Determination of bacterial adhesion to intestinal mucus.,” *Methods Mol. Biol.*, vol. 268, pp. 411–415, 2004, doi: 10.1385/1-59259-766-1:411.

[4] F. L. Hellweger, R. J. Clegg, J. R. Clark, C. M. Plugge, and J. U. Kreft, “Advancing microbial sciences by individual-based modelling,” *Nat. Rev. Microbiol.*, vol. 14, no. 7, pp. 461–471, 2016, doi: 10.1038/nrmicro.2016.62.

[5] M. Marzorati *et al.*, “The HMI^{TM} module: A new tool to study the Host-Microbiota Interaction in the human gastrointestinal tract in vitro,” *BMC Microbiol.*, vol. 14, no. 1, 2014, doi: 10.1186/1471-2180-14-133.

[6] P. Shah *et al.*, “A microfluidics-based in vitro model of the gastrointestinal human-microbe interface,” *Nat. Commun.*, vol. 7, no. May, 2016, doi: 10.1038/ncomms11535.

[7] S. Jalili-Firoozinezhad *et al.*, “A complex human gut microbiome cultured in an anaerobic intestine-on-a-chip,” *Nat. Biomed. Eng.*, vol. 3, no. 7, pp. 520–531, 2019, doi: 10.1038/s41551-019-0397-0.

[8] N. J. Darling, C. L. Mobbs, A. L. González-Hau, M. Freer, and S. Przyborski, “Bioengineering Novel in vitro Co-culture Models That Represent the Human Intestinal Mucosa With Improved Caco-2 Structure and Barrier Function,” *Front. Bioeng. Biotechnol.*, vol. 8, no. August, pp. 1–15, 2020, doi: 10.3389/fbioe.2020.00992.

[9] D. C. Stewart *et al.*, “Quantitative assessment of intestinal stiffness and associations with fibrosis in human inflammatory bowel disease,” *PLoS One*, vol. 13, no. 7, pp. 1–16, 2018, doi: 10.1371/journal.pone.0200377.

[10] V. De Gregorio, G. Imparato, F. Urciuolo, and P. A. Netti, *3D stromal tissue equivalent affects intestinal epithelium morphogenesis in vitro*, vol. 115, no. 4. 2018.

[11] F. Urciuolo *et al.*, “Biophysical properties of dermal building-blocks affect extra cellular

matrix assembly in 3D endogenous macrotissue Biophysical properties of dermal building-blocks affect extra cellular matrix assembly in 3D endogenous macrotissue," 2016.

[12] M. Klinger, L. P. Tolbod, K. V. Gothelf, and P. R. Ogilby, "Effect of polymer cross-links on oxygen diffusion in glassy PMMA films," *ACS Appl. Mater. Interfaces*, vol. 1, no. 3, pp. 661–667, 2009, doi: 10.1021/am800197j.

[13] R. H. W. Lam, M. C. Kim, and T. Thorsen, "Culturing aerobic and anaerobic bacteria and mammalian cells with a microfluidic differential oxygenator," *Anal. Chem.*, vol. 81, no. 14, pp. 5918–5924, 2009, doi: 10.1021/ac9006864.

[14] L. Zheng, C. J. Kelly, and S. P. Colgan, "Physiologic hypoxia and oxygen homeostasis in the healthy intestine. A review in the theme: Cellular responses to hypoxia," *Am. J. Physiol. - Cell Physiol.*, vol. 309, no. 6, pp. C350–C360, 2015, doi: 10.1152/ajpcell.00191.2015.

[15] S. Muenchau *et al.*, "Hypoxic Environment Promotes Barrier Formation in Human Intestinal Epithelial Cells through Regulation of MicroRNA 320a Expression," *Mol. Cell. Biol.*, vol. 39, no. 14, pp. 1–21, 2019, doi: 10.1128/mcb.00553-18.

[16] N. E. Zeitouni, S. Chotikatum, M. von Köckritz-Blickwede, and H. Y. Naim, "The impact of hypoxia on intestinal epithelial cell functions: consequences for invasion by bacterial pathogens," *Mol. Cell. Pediatr.*, vol. 3, no. 1, 2016, doi: 10.1186/s40348-016-0041-y.

[17] M. G. Espey, "Role of oxygen gradients in shaping redox relationships between the human intestine and its microbiota," *Free Radic. Biol. Med.*, vol. 55, pp. 130–140, 2013, doi: 10.1016/j.freeradbiomed.2012.10.554.

[18] K. Ninomiya *et al.*, "Effect of CO2 concentration on the growth and exopolysaccharide production of Bifidobacterium longum cultivated under anaerobic conditions," *J. Biosci. Bioeng.*, vol. 107, no. 5, pp. 535–537, 2009, doi: 10.1016/j.jbiosc.2008.12.015.

[19] S. Kawasaki *et al.*, "Effect of CO2 on colony development by Bifidobacterium species," *Appl. Environ. Microbiol.*, vol. 73, no. 23, pp. 7796–7798, 2007, doi: 10.1128/AEM.01163-07.

[20] W. Shin *et al.*, "A robust longitudinal co-culture of obligate anaerobic gut microbiome with human intestinal epithelium in an anoxic-oxic interface-on-a-chip," *Front. Bioeng. Biotechnol.*, vol. 7, no. FEB, 2019, doi: 10.3389/fbioe.2019.00013.

[21] M. Herath, S. Hosie, J. C. Bornstein, A. E. Franks, and E. L. Hill-Yardin, "The Role of the

Gastrointestinal Mucus System in Intestinal Homeostasis: Implications for Neurological Disorders," *Front. Cell. Infect. Microbiol.*, vol. 10, no. May, 2020, doi: 10.3389/fcimb.2020.00248.

Supplementary

Supplementary Figure. S1

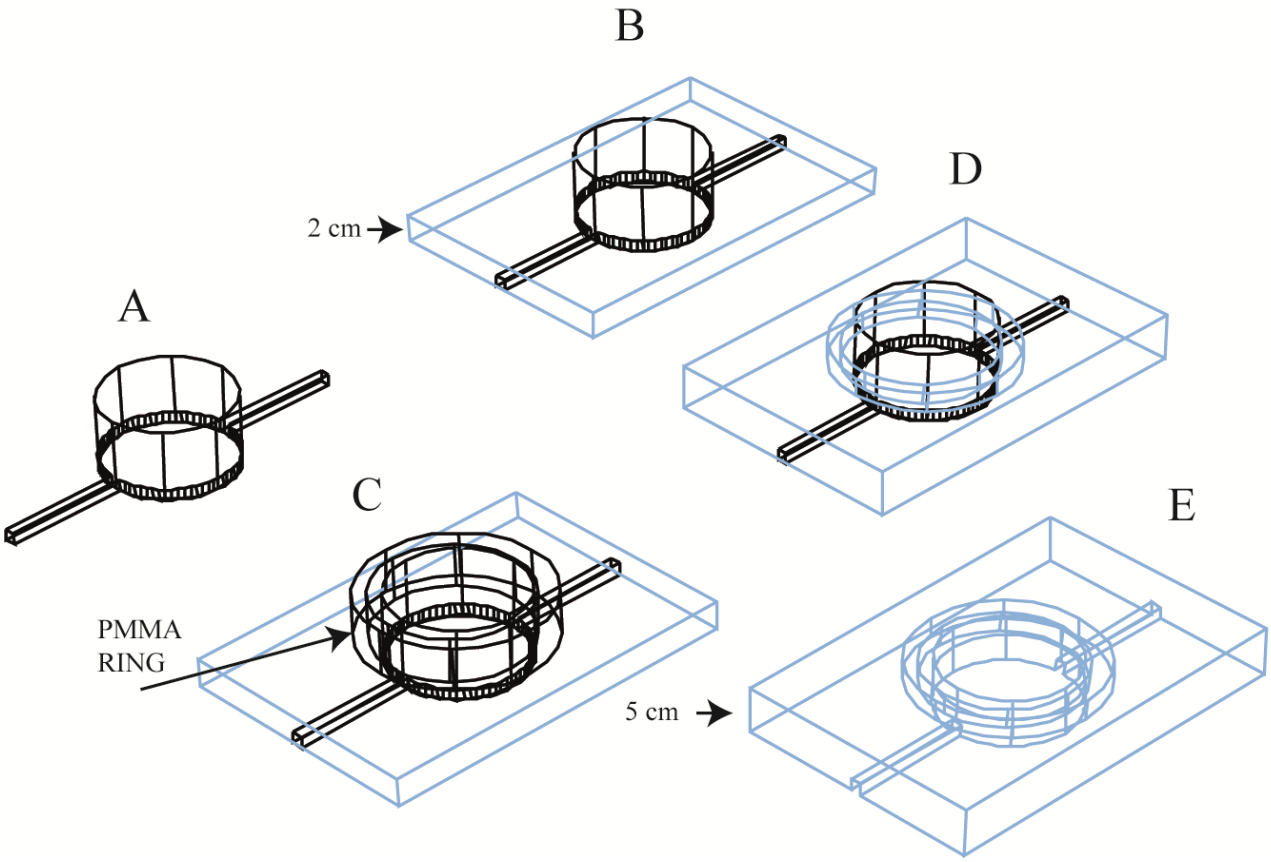

Supplementary Figure. S1 Flow chart of the fabrication process of PMMA snapwell-like structure of MihI-oC. A PMMA snapwell-like structure was glued on the central chamber in order to give the right height to the device (A), and a first layer of PDMS (~ 2 cm in height) was poured and left at 80 °C for 2 h (B). Then, a PMMA ring was put around the central chamber (C), and another PDMS layer (3 cm) was fabricated on it (D). At the end, the ring was removed to have a geometric structure used as a guide for the accommodation of the M_C, guaranteeing its adhesion to the MihI-oC (E).

Supplementary Figure. S2

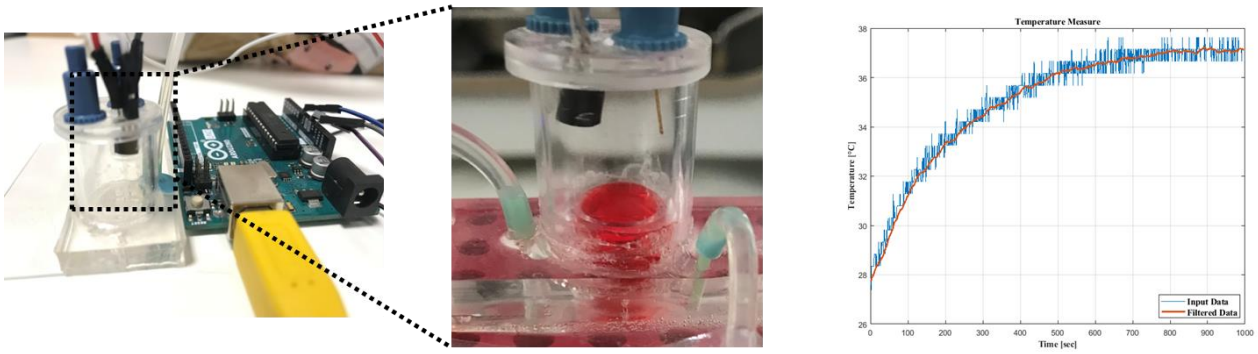

Supplementary Figure. S2 Temperature monitoring into MIhI-oC. The image shows an hand-made Arduino set-up that was used to evaluate the time required from the system to reach the optimal microbiota growth temperature (37°C) (A); high magnification image of the Temperature sensor into the MihI-oC (B); the graph indicates the temperature increase over time (C).

Supplementary Figure S3-S4 Concentration for Different Flow rate

In order to identify the best flow rate to ensure the right supply of oxygen to the cells, CFD simulation was performed. We show the results in terms of oxygen supply and velocity profile in the bottom part of the device for flow rate of 5, 30, and 100 µl/min with a fixed amount of oxygen imposed to the inlet equal to 0.22 mol · L/m^3. For the lowest flow rate (Figure. S3a-b) the amount of oxygen in the S_C is not enough to cells survival (0.14 mol/m^3) while the shear stress (τ), given by $\tau = 6\mu S/WH^2$, where µ is the fluid viscosity, S is the flow rate, and W and H are the width and height of the channel, is 0.00445 dyne/cm^2 (Figure. S4a) similar to the values of the human intestine which have previously been shown to be ~ 0.002–0.08 dyne/cm^2 [1]. Instead, for the highest flow rate, the amount of oxygen that the flow can provide (Figure. S2c-f) 0.22 mol/m^3, as the one imposed to the inlet, is fine, but the shear stress 0.09 dyne/cm^2 is so high determining the cells detachment (Figure. S4c). At 30 µl/min we obtained the right compromise between shear rate 0.00267 dyne/cm^2 (Figure. S4b) and the oxygen amount that uniformly diffuse at the S_C ensuring the appropriate supply of oxygen to the base the base of the 3D-hI (0.22 mol/m^3) [2] (Figure. S1b-c).

Supplementary Figure. S3

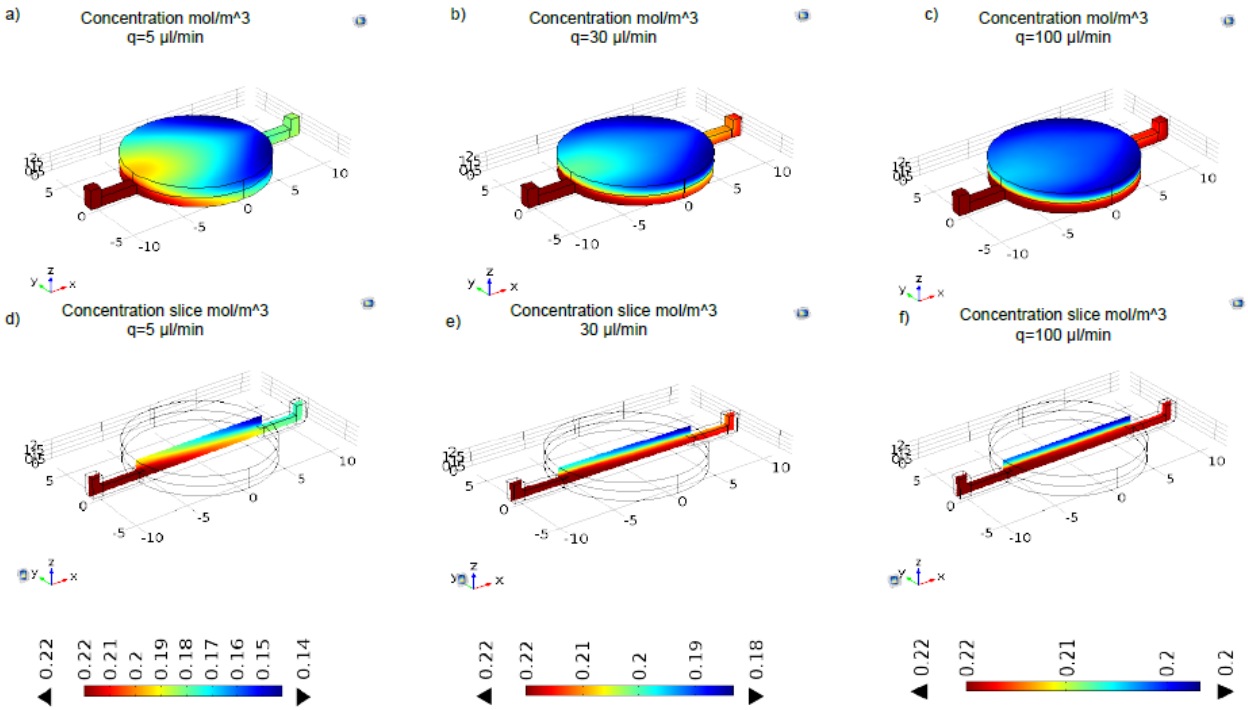

Supplementary Figure. S3 CFD simulations using COMSOL Multiphysics 5.0. Concentration field is reported in a-f, describing the oxygen variation inside the culture chamber reported as surface (a-c) and as section slice (d-f).

Supplementary Figure. S4

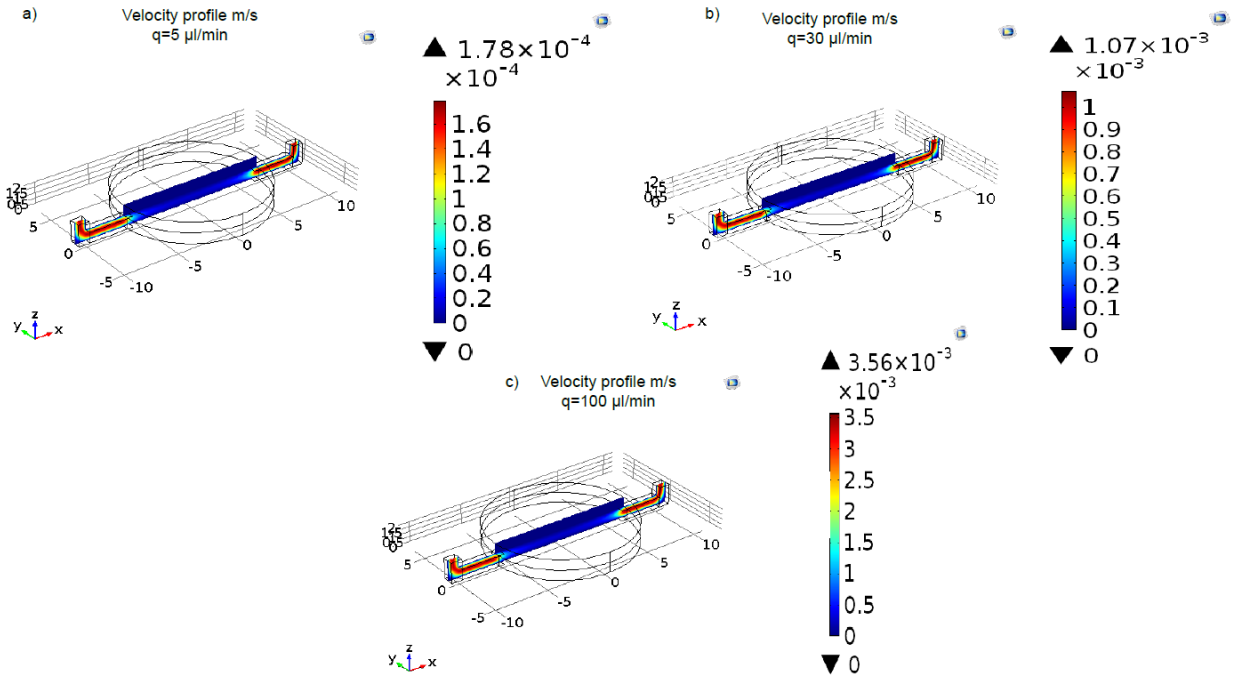

Supplementary Figure S4 Velocity profile for Different Flow. Velocity field is reported in a) whereas oxygen variation inside the culture chamber is reported in b) surface and c) for a section slice

Supplementary Figure. S5 Total count

In order to determine the values of viable bacteria, a serial dilution of the samples at different culture conditions were performed and CFU/ml were reported in the graph (Supplementary Figure S5a and b). Our results indicated that, while at the onset stage of the growth the viability resulted slightly lower, in the exponential phase from 5 to 20 h the data resulted almost superimposable reaching the values of 2.2 * 10^9 CFU/ml viable bacteria in micro-AW and 2.4 * 10^9 in M_C-MihI-oC. Moreover, from 20 to 30 h, although we have a superimposable OD value for bacteria grown in M_C and AW, the number of viable bacteria was preserved up to 30 h in M_C while those in micro-AW are in the initial phase of cell death already at 25 h (Figure. S5b). Representative SEM and gram staining micrographs of *L.rhamnosus* indicated that the lactobacillus phenotypes (gram-positive) with rod shape morphology was preserved (S5c inset). *B.longum* showed the typical Y-shaped morphology in high magnification SEM micrograph and gram-positive staining as highlighted in S5d SEM and inset, respectively.

Supplementary Figure. S5

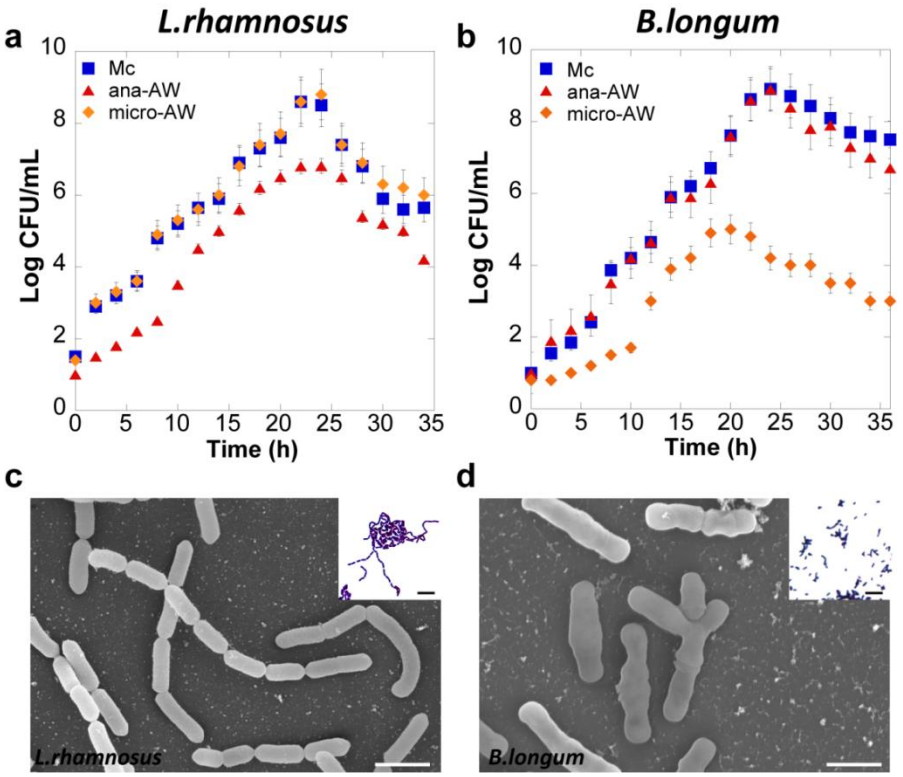

Supplementary Figure. S5 M_C ensures the microbial strains viability and growth in the MihI-oC lumen. Quantification of the viable bacterial growth - L.rhamnosus (a) and B.longum (b) - on different oxygen microenvironments: microaerophilic conditions in the AW (micro-AW), anaerobic conditions in the AW (ana-AW), hypoxic environment in the M_C of the MihI-oC (M_C); SEM micrographs show the microbial morphology of the rod shaped L.rhamnosus (c) and the bifurcated morphology of B.longum (d); insets indicate the gram staining of L. rhamnosus and B.longum, respectively. scale bar 2 nm for c and d, scale bar 20 mm for insets.

Supplementary Figure S6

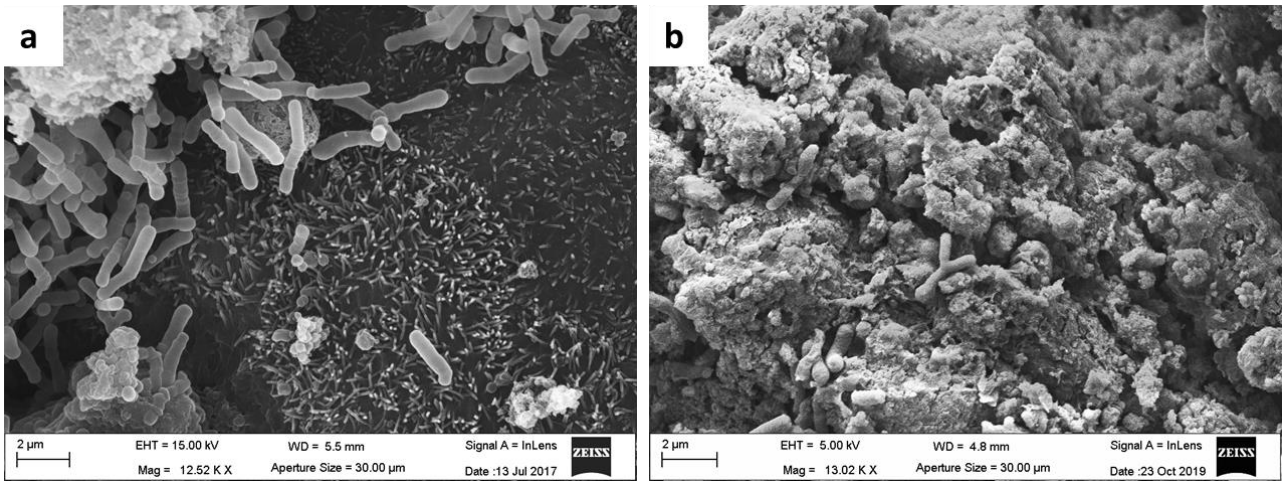

Supplementary Figure S6 Vertical stratification of Microbiota. Low magnification SEM images of L.rhamnosus adherent on the epithelial cells (a) and B. longum (b) embedded into the mucus.

Table 2. Definition of relevant oxygen environments at 37°C into MihI-oC

Localization	**O_2 [mol/m^3]**	**pO_2 [kPa]**
Serosal $_{side}$	0.21	19.9
3D-IS	0.15	7
3D-hI (Crypt-villus)	0.03-0.07	3-0
Lumen $_{side}$	0.001	0.13-0.013

Conclusion

This thesis reports the development of electrical platforms with improved coupling between electronics and biology and their compliant integration within 3D tubular blood brain barrier models. After a short introduction, in chapter 1 we discuss about the technique used to fabricate OECT and their application in the biological applications. We found that the new challenge in the research is the wish to have microfluidic platform that embed, in a simple way, the OECT. In the chapter 2 we discuss the evolution of *in vitro* models for the blood brain barrier, toward 3D configurations, which offer better cell-cell and cell-matrix interactions within a controlled microenvironment. We analyze different devices and we present their limits and the common parameters that everyone need to consider to recreate a blood brain barrier *in vitro* model. In chapter 3, we introduce a fabrication technique to realize a good pattern of PEDOT:PSS without use of Parylene-C in order to integrate OECTs within PDMS microfluidic chambers and with this fabrication technique we assessed a good adhesion between PDMS device and OECTs. In chapter 4, we present a new strategy to make blood brain barrier with an in-line OECT sensor which is a planar sensor integrated in a tubular model. Organ-on-a-chip systems are among the most complex in vitro cell culture platforms and their use for drug testing is on the rise. However, the integration of metal electrodes within micron-size chambers remains challenging. In our platform, 3D vessel is placed on the OECTs for the continuous monitoring of blood brain barrier (BBB) formation and BBB integrity during its use. The BBB regulates ion and solute diffusion within the brain tissue to help maintain its proper functions. However, the BBB prevents the majority of drugs from entering the brain and its disruption is linked to many neurological diseases. At the end of the chapter, we monitored the breakdown and spontaneous reconstruction of the barrier after the passages of the gH625, a peptide able to cross the barrier. In chapter 5, we propose an advanced model of intestine on chip, in which we recreate, through a handmade anaerobic chamber, the oxygen gradient in the gut. As an interesting perspective, we want to combine this gut on chip, with the tubular model of BBB integrating the OECT in order to monitor the effect of the gut on the brain.